

THERMODYNAMICS LABORATORY
AEROSPACE AND MECHANICAL ENGINEERING DEPARTMENT
UNIVERSITY OF LIÈGE

**CONTRIBUTION TO THE CHARACTERIZATION OF SCROLL MACHINES IN
COMPRESSOR AND EXPANDER MODES**

A Thesis

Submitted to the Faculty

of the

University of Liège

by

Vincent LEMORT

In partial Fulfillment of the Requirements for the Degree

of

Doctor of Applied Sciences

Liège, December 19th, 2008

à ma famille

Acknowledgements

I am grateful to Professor J. Lebrun for his trust and supervision. I have learned immensely from his knowledge.

I am also grateful to Professors J. Braun and E. Groll who enabled me to work in their team. I thank them for their trust and the time they devoted to me.

I would also like to thank all the people I had the opportunity to work with. Special thanks to Jules Hannay, Ion Vladut Teodorese, Cristian Cuevas, Ian Bell, Sylvain Quoilin, Stéphane Bertagnolio and Clemens Felsmann.

I want to thank José Concha, Jean-Marie Ralet, Richard Labenda, Frankie Lee, Fritz Peacock, Bob Brown, and Gilbert Gordon for the care they took to prepare test benches.

I thank my family for their support and encouragement. Last but not least a very special word of thanks to Isabelle for her sacrifices and unwavering support.

Chapter Contents

- Chapter 1 General Introduction
- Chapter 2 Modeling Thermal Systems Including Scroll Machines
- Chapter 3 Experimental Investigation on an Air-Cooled Scroll Compressor Chiller
- Chapter 4 Experimental Investigation on a Scroll Expander Integrated into a Rankine Cycle Power System
- Chapter 5 Experimental Investigation on Scroll Machines Integrated into a Liquid Flooded Ericsson Cycle Cooler
- Chapter 6 Development of a Scroll Expander Deterministic Model
- Chapter 7 Validation of the Scroll Expander Deterministic Model
- Chapter 8 General Conclusions and Recommendations
Appendix

Abstract

This thesis contributes to the knowledge and the characterization of scroll machines and their systems. It is based on experimental and modeling works carried out on:

- a) A hermetic scroll compressor used inside an air-cooled water chiller.
- b) An oil-free open-drive scroll expander integrated into an Organic Rankine Cycle (ORC) power system.
- c) Open-drive scroll compressor and expander used in a Liquid Flooded Ericsson Cycle Cooler (LFEC). Such a system uses the liquid flooding of the compressor and of the expander to approach isothermal compression and expansion processes.

New *semi-empirical* models of the scroll compressor and expander were proposed and existing models improved.

A *deterministic model* of the scroll expander was established. The model associates a geometrical description of the machine with a thermodynamic description of the expansion process. This model was validated for the two expanders investigated experimentally. The model validation revealed that the performance of the expanders is mainly affected by the supply pressure drop and by the internal leakages. Using the validated model, parametric studies were carried out to investigate the variation of the performance of both expanders with modification of their design and with the operating parameters.

The thesis also investigated the scroll machines from the point of view of their integration into thermal systems.

A first experimental investigation was carried out on an *air-cooled chiller*. The scroll compressor semi-empirical model, with its parameters identified on the basis of published manufacturer data, was used as a refrigerant flow meter. The analysis of the experimental data allowed a better understanding of the chiller operation and a better identification of its model parameters (such as the fan and the hot gas bypass control models).

A second experimental investigation was carried out on an *ORC power system*, working with R123. In order to select the most appropriate fluid, the performances achieved with four different fluids were compared by simulation. The experimental study confirmed that the scroll expander

is a good candidate for an ORC system: the tested prototype presented a good performance (the maximum global isentropic effectiveness achieved was 68%). Using an ORC simulation model, parametric studies were carried out to investigate the effects of the expander characteristics and operating conditions on the cycle performance. The latter is mainly affected by the expander internal leakage and by the liquid subcooling at the condenser exhaust.

A third experimental investigation was performed on a LFEC working with nitrogen as refrigerant and alkyl-benzene oil as flooding liquid. Experimental data was used to identify the parameters of the scroll compressor and expander semi-empirical models. Parametric studies were performed to identify the different factors affecting their performance. One of the undesirable features of the machines is the increase of the supply and exhaust pressure drops with the increase of oil quantity.

CHAPTER 1

GENERAL INTRODUCTION

1 RESEARCH BACKGROUND

World energy use is today in the center of the climate change debate and an international effort is made to reduce the emissions of carbon dioxide, resulting from the combustion of fossil fuels for energy production, and the emissions of other greenhouse gas.

Compressors consume approximately 17% of the world's electrical output. Most of these compressors are positive displacement machines and are used for compressed air and refrigeration systems (Stošić, 2004). In the refrigeration and air-conditioning industry, scroll compressors are a dominant compression technology. The "popularity" of the scroll compressor is justified by its reliability, low level of noise and vibration, robustness (few moving parts) and high efficiency (Lee, 2002). Research and development is still driven by different challenges: the increase in efficiency, the use of environmental friendly refrigerants, the enlargement of the capacity range and the new applications such as heat pump systems (Elson et al., 2008).

The scroll machine also appears to be a promising candidate as an expansion device for different applications, the most popular of which is the small-scale Rankine cycle power system. Such systems are mainly used for recovering energy from low grade heat sources (such as geothermal heat sources, engine exhaust gas, domestic boilers or cooling down of mechanical equipment). Scroll expanders are also used in CO₂ refrigeration systems in place of expansion valves.

This thesis contributes to the knowledge and to the characterization of scroll machines and of their systems, with a view to increasing their energy efficiency. The thesis is based on experimental and modeling works carried out on different systems using scroll machines.

Both heat engine and heat pump cycles are investigated, giving the opportunity to study the operation of the scroll machine in compressor and in expander modes.

2 RESEARCH OBJECTIVES

The *first* objective of this thesis is to improve existing simulation models of the scroll machines and of their thermal systems. The proposed simulation models must allow:

- 1) Representing the performance of the thermal system as a function of the performance of the scroll machine. This approach is useful for pre-sizing the scroll machine (displacement, built-in volume ratio,...), optimizing the design of the thermal system, defining its control strategies and commissioning existing installations.
- 2) Optimizing the design of the scroll machine for nominal conditions imposed by the thermal system.

The *second* objective of the thesis is to characterize the operation of the scroll machine in expander mode. The different sources of irreversibility of the scroll expander are identified and quantified. The thesis also indicates potential ways to improve the expander's performance.

3 RESEARCH APPROACH

3.1 Investigation of the compressor and expander modes

The investigation is not limited to one mode of operation of the machine, although a larger effort has been put on modeling the expander mode.

Actually, because of the remarkable reversibility of the machine, investigating the compressor mode also allows characterizing the expander mode and vice versa. Similar approaches can be used to model both modes, as shown in *Chapter 6*.

Moreover, most of the expanders tested until now derived from existing compressors. A good understanding of the compressor mode helps to identify possible performance loss and problems associated with the use of the machine in the other mode. Compressor's performance gives a natural frame of comparison in the analysis of the expander's

performance. This will be illustrated in *Chapter 5* presenting an experimental study on oil flooded compressor and expander.

3.2 Modeling the components

New *semi-empirical* models of the scroll compressor and expander will be proposed and existing models be improved (*Chapter 2*). Such modeling only retains the main physical features of the machine, such as the suction and discharge pressure drop, the internal leakage, the suction and discharge heat transfers, electro-mechanical loss, etc.... Each semi-empirical model involves a limited set of equations and hence a limited number of parameters (all of them having a physical meaning). It usually shows reduced computational time and numerical robustness. Hence it is easy to integrate into a whole thermal system simulation model. Semi-empirical models will also be developed for a few other components encountered in the course of this research: compressors, heat exchangers and pumps.

In order to better characterize the use of the scroll machine in expander mode, a comprehensive numerical model of the machine is also developed (*Chapter 6*). This comprehensive, or *deterministic*, model associates a geometrical description of the machine with a thermodynamic model of the expansion process. Such a model is more appropriate for investigating the variation of the expander's performance as function of its geometry.

3.3 Modeling and investigating the thermal systems

This thesis will also propose models for two of the investigated thermal systems: the vapor compression refrigeration system and the Rankine cycle power system.

The modeling approach consists in associating the semi-empirical models of the scroll machines to the sub-models of other components (heat exchangers, pump and/or expansion device).

These models of the thermal systems should allow addressing other specific issues, such as:

1. the pre-sizing of the components of the Organic Rankine Cycle system (*Chapter 4*)
2. the choice of the working fluid for the Organic Rankine Cycle system (*Chapter 4*)
3. the description of the control of the air-cooled water chiller (*Chapter 3*)

3.4 Experimental investigations

A lot of effort has been put into this thesis on the experimental characterization of three scroll machines:

The first one is an expander integrated into an Organic Rankine Cycle (ORC) system working with refrigerant R123. The two other machines are a compressor and an expander, used in a Liquid Flooded Ericsson cycle cooler, working with a mixture of nitrogen and oil.

These experimental investigations aim at measuring performances of the scroll machines and evaluating their variation with operating conditions. Collected data is also used for models validation.

3.5 Model validation

There exist different ways to validate a model. These methods are based on comparison with:

1. experimental data
2. manufacturer data
3. results provided by other simulation models
4. analytical solution

The first method is probably the most reliable. However experimental investigations are time and money consuming.

The second method is very convenient for most of the commercialized components, since performance is usually provided by the manufacturer (e.g. performance maps) and defined according to standards. However, announced performance doesn't necessarily correspond to world operation.

The third method is commonly used for validating building simulation models. However, comparative validation doesn't represent a truth standard. It only gives the opportunity to detect some problems in the model.

The last method is seldom used since in most of the cases, there is no (or no readily available) analytical solution to the physical process currently modeled.

In this thesis, the first three methods are employed.

Manufacturer data is used for validating the models of:

- a) a hermetic scroll compressor designed for heat pumping application (*Chapter 2*)
- b) a hermetic scroll compressor integrated into an air-cooled water chiller (*Chapter 3*)
- c) an air-cooled water chiller (*Chapter 3*)

Experimental data is used for validating the models of:

- a) a prototype of open-drive scroll expander, which is part of an Organic Rankine Cycle system working with R123 (*Chapter 4 and Chapter 7*)
- b) a compressor and an expander integrated into a Liquid Flooded Ericsson Cycle Cooler and fed with a mixture of nitrogen and oil (*Chapter 5 and Chapter 7*)

Results provided by the scroll expander deterministic model are used to validate non-dimensional laws expressing the variation of the semi-empirical model parameters with the expander displacement (*Chapter 7*).

4 ORGANIZATION OF THIS DOCUMENT

This thesis is presented as follows:

Chapter 2 describes the semi-empirical models of the scroll compressor and of the scroll expander. It is shown how the existing model for the scroll compressor can be adapted to account for the discharge valve. This chapter also presents the simulation models for the vapor compression refrigeration system and for the Rankine cycle system.

Chapter 3 presents the validation of an air-cooled scroll compressor water chiller model. Validation is achieved in two steps: first based on manufacturer published data and then based on experimental data collected on a real installation. This study allows validating the

hermetic scroll compressor model, but also better characterizing the chiller (fan control and condenser hot gas bypass).

Chapter 4 presents an experimental investigation carried out on a prototype of Organic Rankine Cycle system working with refrigerant R123. The development of the test bench is described (choice of the components and of the working fluid). The achieved expander's performance is presented and analyzed. Using the experimental results, the scroll expander semi-empirical model is validated and the Rankine cycle simulation model is partially validated. Using both models, parametric studies are performed to investigate expander and cycle performances under variation of the operating conditions and under modification of the expander design.

Chapter 5 presents an experimental study carried out on a Liquid Flooded Ericsson Cooler (*LFEC*). Such a system uses liquid flooding of the compressor and of the expander to approach isothermal compression and expansion processes. Measurements are used to identify the parameters of the compressor and expander semi-empirical models. Measurements as well as parametric studies carried out with validated models help to characterize the evolution of the performance of the scroll machines with the operating conditions.

Chapter 6 details the development of a deterministic model of the scroll expander. This model associates a detailed geometrical description of the expander with a thermodynamic modeling of the expansion process.

Chapter 7 presents the validation of the deterministic scroll expander model for the two expanders investigated experimentally (the expander used in the ORC system and the expander used in the LFEC). The validated models allow checking the physical meaning of the parameters identified for the semi-empirical models. Using these models, parametric studies are carried out in order to investigate the variations of the performances of the expanders with modification of their design.

5 REFERENCES

- Elson, J., N. Kaemmer, S. Wang, and M. Perevozchikov. 2008. Scroll Technology: An Overview of Past, Present and Future Developments. *In Proceedings of the International Compressor Engineering Conference at Purdue*: Paper 1204.
- Lee, G.H.. 2002. Performance simulation of scroll compressors, *Proc Instn Mech Engrs Vol 216 Part A: J Power and Energy*: 169-179.
- Stošić, N. 2004. Screw Compressors in Refrigeration and Air Conditioning. HVAC&R Research, vol 10, 3.

CHAPTER 2

MODELING THERMAL SYSTEMS INCLUDING SCROLL MACHINES

1	INTRODUCTION.....	12
2	MODELING THE COMPONENTS.....	12
2.1	Scroll compressor	13
2.1.1	General description of the model	13
	Heat transfers.....	14
	Internal leakage	15
	Displaced mass flow rate	16
	Pressure drops	17
	(Electro-) mechanical loss.....	18
2.1.2	Description of the compression process in the presence of a discharge valve	18
	Over-compression	20
	Under-compression	21
	Absence of discharge valve	24
2.1.3	Information diagram of the compressor model	24
2.1.4	Validation of the model.....	25
	Prediction of the electrical consumption	26
	Prediction of the displaced mass flow rate and heating capacity.....	28
	Prediction of the isentropic and volumetric effectiveness	28
2.2	Scroll expander	30
2.2.1	Description of the model	30
	Heat transfer, pressure drop and internal leakage	31
	Displaced mass flow rate	31
	Internal power	32
	Mechanical losses.....	32
2.2.2	Information diagram of the expander model	33
2.3	Heat exchangers.....	34
2.3.1	Modeling the evaporator and the condenser of a vapor compression refrigeration system	34
2.3.2	Modeling the evaporator and the condenser of a Rankine cycle power system	35
2.4	Pump	35
3	MODELING THERMAL SYSTEMS.....	36
3.1	Vapor compression refrigeration system.....	36
3.2	Rankine cycle power system.....	37
4	CONCLUSIONS	38

5	REFERENCES.....	39
----------	------------------------	-----------

NOMENCLATURE

A	Area, m ²
AU	Heat transfer coefficient, W/K
c	Specific heat, J/kg-K
C	Clearance volume factor, -
d	Diameter, m
h	Specific enthalpy, J/kg
K	Correction factor, -
\dot{M}	Mass flow rate, kg/s
N	Rotational speed, Hz
\dot{Q}	Heat transfer rate, W
R	Heat transfer resistance, K/W
$r_{v,in}$	Built-in volume ratio, -
s	Specific entropy, J/kg-K
T	Temperature, °C
T	Torque, N-m
u	Specific internal energy, J/kg
v	Specific volume, m ³ /kg
\dot{V}	Volume flow rate, m ³ /s
w	Specific work, J/kg
\dot{W}	Power, W
X	Capacity fraction

Subscripts

0	Constant, clearance
amb	Ambient
calc	Calculated
cd	Condenser, condensing
cp	Compressor
crit	Critical
ex	Exhaust

exp	Expander
in	Internal
loss	Mechanical loss
leak	Leakage
m	Metal
man	Manufacturer
n	Nominal
p	Isobaric
pp	Pump
r	Refrigerant
s	Isentropic, swept
sh	Shaft
sf	Secondary fluid
su	Supply
thr	Throat
tp	Two phase
w	Envelope

Greek and miscellaneous

α	Factor of proportionality for the electromechanical loss, -
Δ	Difference
ε	Effectiveness, -
η	Efficiency, -
γ	Specific heat ratio, -

1 INTRODUCTION

According to Stoecker (1971), the hardware associated with most of thermal systems includes fans, pumps, compressors, engines, expanders, turbines, heat and mass exchangers and reactors, all interconnected with some forms of conduit. Modeling a thermal system is useful for:

- 1) estimating the system performance as a function of the components characteristics,
- 2) evaluating, comparing or defining control strategies of the system and,
- 3) optimizing and sizing the system.

This thesis makes reference to some components and systems models, which are described in this chapter.

The semi-empirical models of the following components are presented: the scroll compressor and expander, the evaporator and condenser and the volumetric pump. The modeling of two different thermal systems is also described: the vapor compression refrigeration system and the Rankine cycle system.

2 MODELING THE COMPONENTS

Literature on semi-empirical models is more abundant for compressors than expanders. Hiller and Glicksmann (1976) seem to be the first ones to propose such a type of modeling in the case of reciprocating compressors.

Haberschill *et al.* (1994) developed models for hermetic scroll, reciprocating and rotary compressor and showed how their parameters can be accurately identified based on a limited number of points. Their model accounts for the built-in volume ratio (for scroll compressor), the re-expansion of the clearance volume (for reciprocating compressors), the internal leakage and the heat transfer to the ambient. Compression is described by an overall polytropic coefficient depending on the heat exchange, i.e. on the mass flow rate of refrigerant and pressure ratio. The model involves 11 parameters in total.

Winandy *et al.* (2002a) developed a model of an open-type reciprocating compressor. The model accounts for supply and exhaust pressure drops and heat transfers, the heat transfer to the ambient, the re-expansion of the clearance volume and the mechanical losses. Based on a similar approach, the same authors (Winandy *et al.*, 2002b) also proposed a hermetic scroll compressor model. The model doesn't account for supply and discharge pressure drops (which are negligible) but describes the electro-mechanical loss and the built-in pressure ratio.

Cuevas *et al.* (2008) modeled an automotive wobble plate compressor. The model describes the suction and discharge heat transfer, the heat transfer to the ambient

The only reference found in literature on scroll expander semi-empirical models is the work carried out by Kane (2002). He investigated and proposed a semi-empirical model of a hermetic scroll expander integrated into an Organic Rankine Cycle system. The model accounts for the supply pressure drop, the built-in volume ratio, the internal leakage the electro-mechanical loss but doesn't account for heat transfer.

2.1 Scroll compressor

The originality of this paragraph is to show how the model proposed by Winandy *et al.* (2002b) could be generalized to scroll compressors using a discharge valve. It will be shown that the modified scroll compressor model is able to predict, with a much better agreement, the electrical consumption. The initial motivation for modifying the scroll compressor model was to improve the modeling of heat pump systems, whose compressors are typically using discharge valves (Cuevas *et al.*, 2008).

2.1.1 General description of the model

The schematic representation of the scroll compressor model proposed here is presented in Figure 2-1. It assumes that the evolution of the refrigerant inside the compressor is decomposed into the following steps:

1. supply heating-up ($su \rightarrow su,1$)
2. mixing with the internal leakage ($su,1 \rightarrow su,2$)
3. adiabatic and reversible compression ($su,2 \rightarrow in$)
4. adiabatic compression at a constant machine volume ($in \rightarrow in^*$)

5. adiabatic and reversible compression ($\text{in}^* \rightarrow \text{ex},2$)
6. exhaust pressure drop ($\text{ex},2 \rightarrow \text{ex},1$)
7. exhaust cooling-down ($\text{ex},1 \rightarrow \text{ex}$)

The modeling of the heat transfers, the internal leakage and the pressure drops is described in this section. Equations describing the compression process are established in the next section.

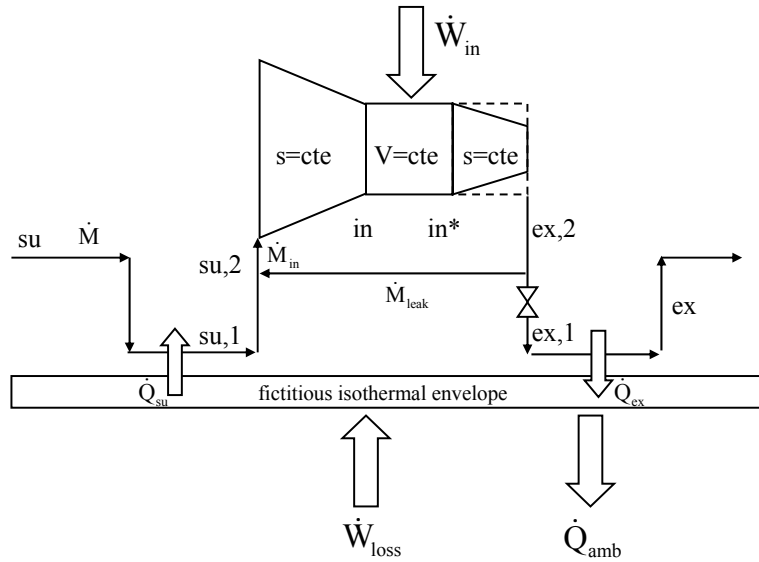


Figure 2-1: Schematic representation of the compressor model

Heat transfers

The main heat transfers in a hermetic scroll compressor occur between:

1. The fluid and the compressor shell during suction and discharge;
2. The fluid and the motor during suction;
3. The fluid and the oil;
4. The fluid and the scrolls during the compression process. These heat transfers have been investigated by Ooi and Zhou (2004) and Jang and Jeong (2006);
5. The shell and the ambient.

In the present modeling, internal heat transfers produce a suction heating-up \dot{Q}_{su} and an exhaust cooling-down \dot{Q}_{ex} . These two heat transfer rates are computed by introducing a

fictitious isothermal envelope at temperature T_w . The ambient loss is computed by introducing a global heat transfer coefficient AU_{amb} between the wall and the ambient:

$$\dot{Q}_{amb} = AU_{amb} \cdot (T_w - T_{amb}) \quad (2-1)$$

Mechanical losses are injected into the envelope under the form of equivalent heat. The steady state balance of this envelope yields

$$\dot{W}_{loss} - \dot{Q}_{su} + \dot{Q}_{ex} - \dot{Q}_{amb} = 0 \quad (2-2)$$

The suction heat transfer is described by a semi-isothermal heat exchanger whose uniform temperature is the envelope temperature

$$\dot{Q}_{su} = \dot{M} \cdot c_p \cdot (T_{su,1} - T_{su}) = \varepsilon_{su} \dot{M} \cdot c_p \cdot (T_w - T_{su}) = \left(1 - e^{\left(\frac{-AU_{su}}{\dot{M} \cdot c_p} \right)} \right) \dot{M} \cdot c_p \cdot (T_w - T_{su}) \quad (2-3)$$

The supply heat transfer coefficient AU_{su} is assumed to vary according to

$$AU_{su} = AU_{su,n} \cdot \left(\frac{\dot{M}}{\dot{M}_n} \right)^{0.8} \quad (2-4)$$

Where $AU_{su,n}$ is the nominal heat transfer coefficient corresponding to the nominal mass flow rate \dot{M}_n . This relationship can be justified by the Reynold's analogy for a turbulent flow through a pipe (Incropera and DeWitt, 2002). An identical relationship is used for the exhaust heat transfer coefficient.

Internal leakage

There are two different leakage paths in a scroll compressor/expander. The radial leakage is due to a gap between the bottom or the top plate and the scrolls. The flank leakage results from a gap between the flanks of the scrolls (Halm, 1997). The leakage flow rate can be

computed by reference to the isentropic flow through a simply convergent nozzle. The fictitious leakage area A_{leak} is assimilated to the nozzle throat and is a parameter of the model to identify. The pressure at the inlet of the nozzle is the compressor exhaust pressure (plus the pressure drop). The flow is restricted by a critical low pressure corresponding to choked flow conditions:

$$P_{thr,leak} = \text{MAX}(P_{su,2}, P_{crit,leak}) \quad (2-5)$$

The critical pressure $P_{crit,leak}$ is computed by considering the refrigerant vapor as a perfect gas:

$$P_{crit,leak} = P_{ex,2} \left[\left(\frac{2}{\gamma + 1} \right)^{\left(\frac{\gamma}{\gamma - 1} \right)} \right] \quad (2-6)$$

The equations of continuity and conservation of enthalpy between the nozzle supply and throat are combined to express the leakage mass flow rate:

$$\dot{M}_{leak} = \frac{A_{leak}}{v_{thr,leak}} \sqrt{2(h_{ex,2} - h_{thr,leak})} \quad (2-7)$$

The specific enthalpy $h_{thr,leak}$ and the specific volume $v_{thr,leak}$ at the throat are computed assuming that the expansion from $P_{ex,2}$ to $P_{thr,leak}$ is isentropic.

Displaced mass flow rate

The internal flow rate is

$$\dot{M}_{in} = \frac{\dot{V}_{s,cp}}{v_{su,2}} \quad (2-8)$$

And the mass flow rate displaced by the compressor is

$$\dot{M} = \dot{M}_{in} - \dot{M}_{leak} \quad (2-9)$$

Pressure drops

Pressure drops can be described by the flow through a system made up of a converging nozzle and an isobaric diffuser. The flow through the nozzle is isentropic; while the one through the diffuser is fully irreversible (all the kinetics energy is destroyed without recovering any static pressure). This modeling is done in two steps:

- 1) an isentropic expansion from the supply to the throat (and eventually further if the critical pressure ratio is reached), followed by
- 2) an isobaric evolution with transformation of the kinematics energy into static enthalpy in the diffuser.

Combining the equation of continuity and conservation of enthalpy (between the nozzle inlet and throat), the mass flow rate exiting the compressor can be expressed as

$$\dot{M} = \frac{\pi d_{ex}^2}{4v_{thr,ex}} \sqrt{2(h_{ex,2} - h_{thr,ex})} \quad (2-10)$$

The specific enthalpy and the specific volume at the throat are function of the pressure $P_{ex,1}$ (if the flow is not choked, which is generally the case) at the throat and of the supply specific entropy $s_{ex,2}$:

$$h_{thr,ex} = f(P_{ex,1}, s_{ex,2}) \quad (2-11)$$

$$v_{thr,ex} = f(P_{ex,1}, s_{ex,2}) \quad (2-12)$$

The system made up of the last three equations must be solved to determine the pressure $P_{ex,1}$.

(Electro-) mechanical loss

The compression power input is equal to the internal power plus the (electro-) mechanical loss. Winandy *et al.* (2002b) proposed to distinguish between a loss proportional to the internal power (α being the factor of proportionality) and a “stand-by” (electro-) mechanical loss $\dot{W}_{\text{loss},0}$:

$$\dot{W}_{\text{cp}} = \dot{W}_{\text{in}} + \dot{W}_{\text{loss}} = (1 + \alpha)\dot{W}_{\text{in}} + \dot{W}_{\text{loss},0} \quad (2-13)$$

The stand-by electro-mechanical loss can be expressed as function of a constant mechanical loss torque, as:

$$\dot{W}_{\text{loss},0} = 2\pi N_{\text{cp}} T_{\text{loss,cp}} \quad (2-14)$$

where $T_{\text{loss,cp}}$ is the mechanical loss torque.

2.1.2 Description of the compression process in the presence of a discharge valve

The discharge valve is particularly important for systems working with pressure ratios of 6-8 or higher. In this case, the internal pressure ratio is significantly below the compressor operating pressure ratio, resulting in an excessive compression work due to gas back flow and recompression (Elson *et al.*, 2008).

The discharge flow in scroll compressors with and without discharge valve has been investigated and modeled in details by several authors, such as Nieter and Gagne (1992) and Myszka (1998). Bush and Lifson (1998) investigated the effect of the geometry of the inner portion of the scrolls and the compressor's operating conditions on the discharge valve's dynamics. The presence of the discharge valve is taken into account in the deterministic models of scroll compressors proposed by Halm (1997), Chen (2000) and Lee (2002). The latter models account for the valve's opening by expressing its forces balance. However, except the recent work of Bukac (2008), no simplified modeling including the discharge valve is found in the literature.

Different technologies of discharge valve have been developed. Among all, the reed valve is the more common. It consists of a thin strip of metal used as a flapper to cover the discharge orifice (Glaeser, 1999). More sophisticated discharge valves can include a reed, a preload member and a stop (Prater, 2003), as shown in Figure 2-3.



Figure 2-2 : Schematic drawing of a reed valve in the open position (Glaeser, 1999)

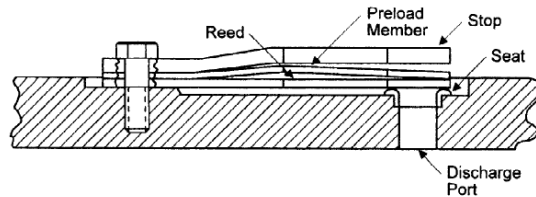


Figure 2-3 : Reed valve with a preload member and a stop (Prater, 2003)

For given refrigerant and operating conditions, there is an internal pressure ratio corresponding to the built in volume ratio. Difference between internal and external pressure ratios yields compression losses (Yanagisawa *et al.*, 1990). Three situations can occur: either the internal pressure ratio is equal to the external pressure ratio (*adapted*), or it is higher (*over-compression*) or it is lower (*under-compression*).

The relative positions of fixed and orbiting scrolls just after the end of the compression (the compression chambers are not sealed off anymore and they communicate with the discharge region) is shown in Figure 2-4. This figure shows the former compression chambers and the clearance volume.

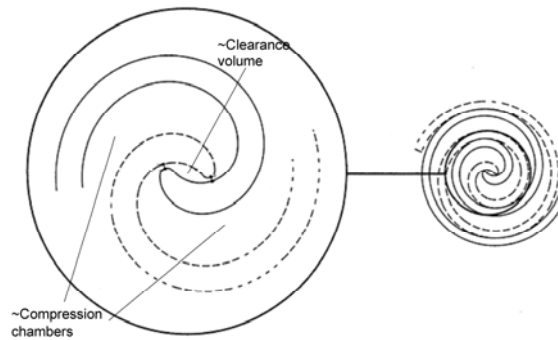


Figure 2-4 : Discharge region of the scroll compressor (right after the end of the compression)

By convention, the clearance volume is defined as the volume of the discharge region at the end of the discharge process. The discharge region comprises the region enclosed by the innermost portions of the scrolls (see Figure 2-4) *plus* the portion of discharge manifold between the scrolls and the discharge valve.

Over-compression

In the case of over-compression, since the pressure in the discharge chamber (the former compression chambers) exceeds the discharge pressure, the valve opens. The flow through the discharge port creates a pressure drop. In the modeling presented here, this pressure drop is computed by describing the flow through an orifice of constant area. Actually, the flow area depends on the distance that the valve has traveled. This distance depends on the spring constant and the difference between the pressure in the discharge region and the discharge pressure (Halm, 1997; Lee, 2002).

The compression is still modeled in two steps, as it was proposed by Sauls (1982). The first part of the compression is assumed to be adiabatic and reversible from the pressure $P_{su,2}$ up to the internal pressure P_{in} . The latter is the pressure in the compression chambers at the end of the compression¹. The second part of the compression is still adiabatic but not reversible and is characterized by a negative work, since the fluid is expanded from the internal pressure down to the discharge pressure (plus the pressure drop) $P_{ex,2}$.

The work associated to the first part of the compression is:

$$w_{in,1} = h_{in}(s_{su,2}, v_{in}) - h_{su,2}(P_{su,2}, T_{su,2}) \quad (2-15)$$

The work associated to the second part of the compression can be written as:

$$w_{in,2} = v_{in} \cdot (P_{ex,2} - P_{in}) \quad (2-16)$$

In the case of *over-compression*, the total internal compression work is then:

¹ Corresponding to the discharge angle, as defined by Halm (1997)

$$W_{in} = W_{in,1} + W_{in,2} \quad (2-17)$$

Since the entire process is assumed to be adiabatic, it follows that the enthalpy at the end of the compression can be computed by:

$$h_{ex,2} = h_{su,2} + W_{in} \quad (2-18)$$

Under-compression

In the eventuality of under-compression, the pressure in the discharge chamber (the former compression chambers) is lower than the pressure in the discharge region (whose volume is the clearance volume). Some fluid has to flow from the discharge region back into the new discharge chamber (that have formerly been the compression chambers) until pressures equalize. In the present model, this phenomenon is assumed to occur instantaneously. Actually, this cannot be achieved immediately, since at the beginning of the discharge process, the flow passage between the discharge chambers and the discharge region is very small (Halm, 1997). This irreversible back-flow process corresponds to the re-expansion of the clearance volume.

The final pressure P_{in}^* in the control volume made up of the discharge chamber and of the discharge region (clearance volume) is calculated by expressing mass and energy balances associated to the mixing processes. The mixing process associated to this re-expansion of the clearance volume is schematically represented in Figure 2-5.

The mass balance can be written as:

$$M_{in}^* = M_{in} + M_{ex,2} = \frac{V_{s,cp}}{V_{su,2}} + \frac{V_0}{V_{ex,2}} = V_{s,cp} \left(\frac{1}{V_{su,2}} + \frac{C}{V_{ex,2}} \right) \quad (2-19)$$

where M_{in} is the fluid mass in the discharge chamber and $M_{ex,2}$ is the fluid mass in the discharge region.

At the time of this mixing (beginning of the discharge process), it is assumed that the state of the fluid in the discharge region is identical to the state at the end of the discharge process (pressure $P_{ex,2}$, and temperature $T_{ex,2}$). This assumption is justified by the cyclic characteristic of the discharge process.

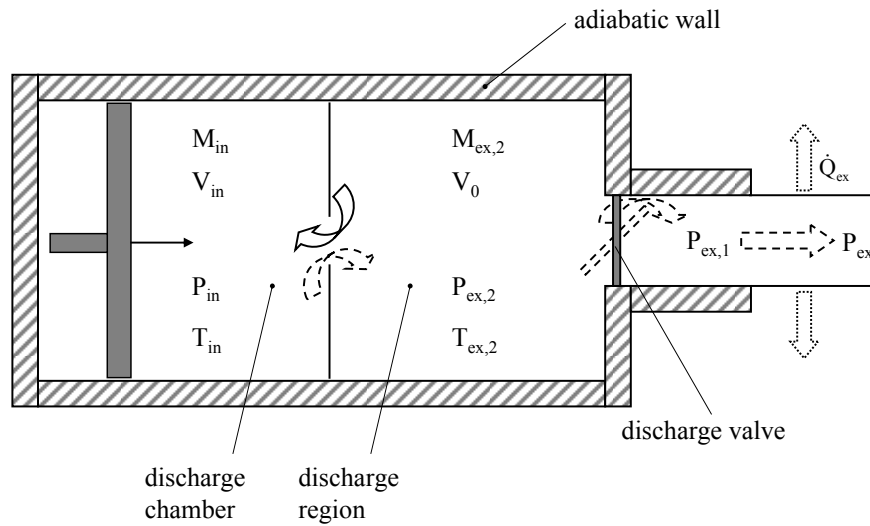


Figure 2-5 : Schematic representation of the re-expansion of the clearance volume at the beginning of the discharge process

The volume V_{in}^* of the resulting chamber, after the discharge chamber (of volume V_{in}) and the discharge region (of clearance volume V_0) have merged, is:

$$V_{in}^* = V_{in} + V_0 = V_{s,ep} \left(\frac{1}{r_{v,in}} + C \right) \quad (2-20)$$

The specific volume of the fluid after mixing can be expressed as:

$$v_{in}^* = \frac{V_{in}^*}{M_{in}^*} = \frac{1/r_{v,in} + C}{1/v_{su2} + C/v_{ex,2}} \quad (2-21)$$

The energy balance describing the mixing can be written as:

$$M_{ex,2} \cdot u_{ex,2} + M_{in} u_{in} = (M_{ex,2} + M_{in}) \cdot u_{in}^* \quad (2-22)$$

Introducing the clearance volume and the compressor displacement and after simplification, the latter expression reduces to:

$$\frac{C}{v_{ex,2}} \cdot u_{ex,2} + \frac{1}{v_{su2}} u_{in} = \left(\frac{C}{v_{ex,2}} + \frac{1}{v_{su2}} \right) u_{in}^* \quad (2-23)$$

The corrected internal pressure P_{in}^* can finally be computed on the basis of the specific volume v_{in}^* and the internal energy u_{in}^* , respectively given by Equations (2-21) and (2-23).

The work fictitiously associated to this back-flow process is given by:

$$w_{in,2,v} = v_{in} \cdot (P_{in}^* - P_{in}) \quad (2-24)$$

As the discharge process continues, the volume of the region made up of the discharge chamber and the discharge region decreases and the corresponding pressure increases until the pressure $P_{ex,2}$ is reached. This evolution is assumed to be adiabatic and reversible. Consequently, the associated work may be expressed as:

$$w_{in,2,s} = h_{ex,2}(P_{ex,2}, s_{in}^*) - h_{in}^*(P_{in}^*, v_{in}^*) \quad (2-25)$$

Hence, in the case of under-compression, the total internal compression work is given by

$$W_{in} = W_{in,1} + W_{in,2} = W_{in,1} + W_{in,2,v} + W_{in,2,s} \quad (2-26)$$

The enthalpy $h_{ex,2}$ at the end of the compression is given by Equation (2-18).

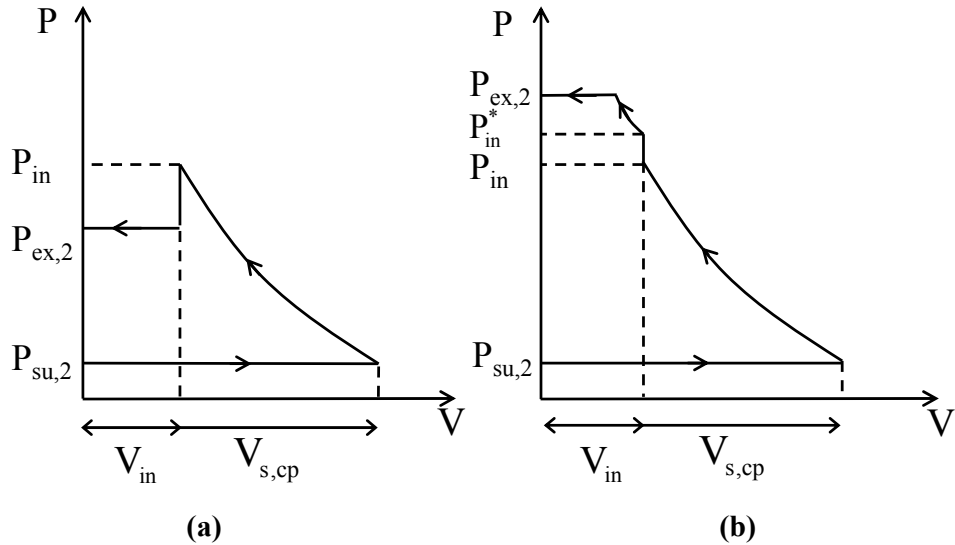


**Figure 2-6 : Representation of the entire compression process in the pressure-volume diagram
((a): over-compression and (b): under-compression)**

Absence of discharge valve

The case where no discharge valve is used corresponds to $C \rightarrow \infty$ (the clearance volume is infinite), yielding $P_{in}^* = P_{ex,2}$. If there was no clearance volume ($C \rightarrow 0$), the isentropic compression would extend from P_{in} to the discharge pressure $P_{ex,2}$.

2.1.3 Information diagram of the compressor model

The information diagram of the scroll compressor model is given in Figure 2-7. The inputs of the model are the supply and exhaust pressures, the supply temperature and the rotational speed. The outputs of the model are the mass flow rate displaced by the compressor, its power consumption and the exhaust temperature. The model necessitates 10 parameters, which are 3 heat transfer coefficients, the swept volume, the built-in volume ratio, the exhaust diameter, the clearance factor, the leakage area, the electro-mechanical loss factor

and the “stand-by” electro-mechanical loss. In general, the swept volume and the built-in volume ratio are given by the manufacturer.

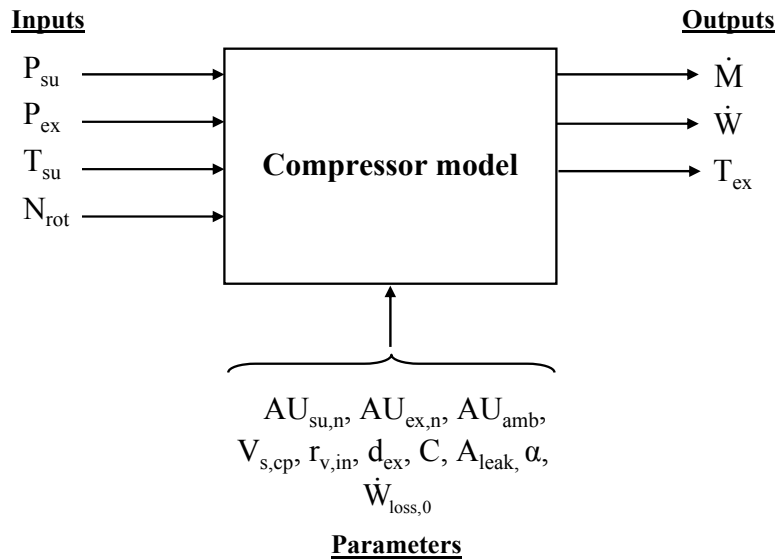


Figure 2-7 : Information diagram of the scroll compressor semi-empirical model

2.1.4 Validation of the model

The compressor model proposed hereunder is validated using performance points given by a compressor manufacturer. The scroll compressor is characterized by a swept volume of 5.92 m³/h and a built in volume ratio of 3.075. The compressor is designed for heat pumping applications and its performances are given for operation with R407C. Figure 2-8 shows the reed valve installed close to the compressor discharge chamber.

Available information consists in 73 operating points characterized by different evaporating and condensing temperatures. Evaporating temperatures range from -25°C to 10°C and condensing temperatures range from 20°C to 65°C. For each point, the following quantities are given: the refrigerant mass flow rate, the electrical consumption, the heating and cooling capacities. The latter are defined for a liquid subcooling of 5K at the condenser exhaust and a vapor superheating of 5K at the evaporator exhaust.



Figure 2-8: View of the discharge reed valve for the compressor under investigation

The identified parameters of the compressor model are given in Table 2-1. The parameter K will be introduced latter.

Table 2-1: Identified parameters of the compressor semi-empirical model

$\dot{V}_{s,cp}$ [m ³ /h]	K [-]	AU _{su} [W/K]	AU _{ex} [W/K]	AU _{amb} [W/K]	r _{v,in} [-]	α [-]	$\dot{W}_{loss,0}$ [W]	d _{ex} [mm]	A _{leak} [mm ²]	C [-]
5.92	0.07	$30\left(\frac{\dot{M}}{0.091}\right)^{0.8}$	$20\left(\frac{\dot{M}}{0.091}\right)^{0.8}$	3	3.075	0.23	100	5.2	0.39	0.45

Prediction of the electrical consumption

Comparison between the electrical consumption predicted by the model and announced by the manufacturer is shown in Figure 2-9. Maximum deviation is 5%. The evolutions of the error on the prediction of the electrical consumption with the pressure ratio is displayed in Figure 2-10, Figure 2-11 and Figure 2-12 for different configurations of the model.

For the initial configuration of the model (no exhaust pressure drop and no taking into account of the discharge valve), the error is increasing with the pressure ratio. The error is largely reduced for over-compression regimes when introducing the exhaust pressure drop². For a given supply pressure, the impact of the pressure drop decreases with the pressure

² Over-compression indicates the situation where $P_{in,cp} > P_{ex2,cp}$, i.e. $r_{p,in,cp} > r_{p,cp}$. Note that for the whole experimental domain, the internal built-in volume ratio ($r_{p,in} = P_{in,cp}/P_{su2,cp}$) is ranging from 3.21 to 3.44.

ratio. The reason is that the mass flow rate exiting the compressor (and hence the pressure drop) decreases with the pressure ratio, due to lower volumetric effectiveness (Figure 2-16).

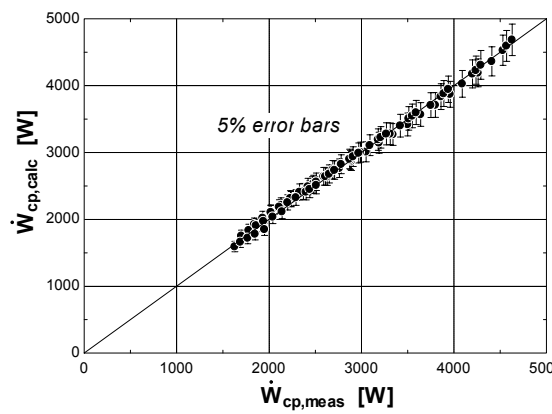


Figure 2-9 : Prediction of the electrical consumption

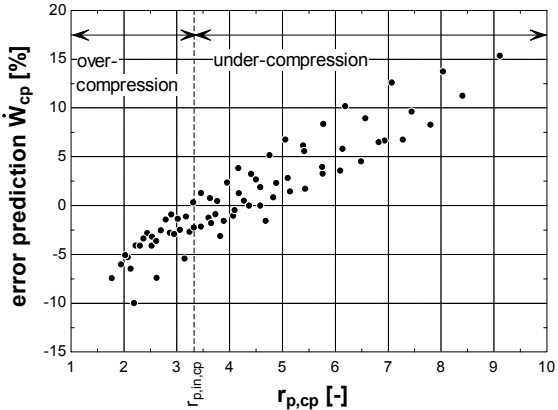


Figure 2-10 : Error on the electrical consumption (model without pressure drop and without discharge valve)

Having introduced the exhaust pressure drop, the error is still increasing with the pressure ratio when the fluid is under-compressed. The model over-predicts the compression work because it still doesn't account for the discharge valve. Figure 2-12 shows that a much better agreement is found when the latter is introduced in the modeling.

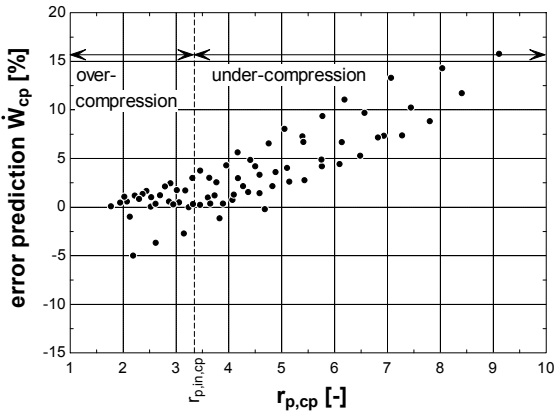


Figure 2-11 : Error on the electrical consumption (model with pressure drop and without discharge valve)

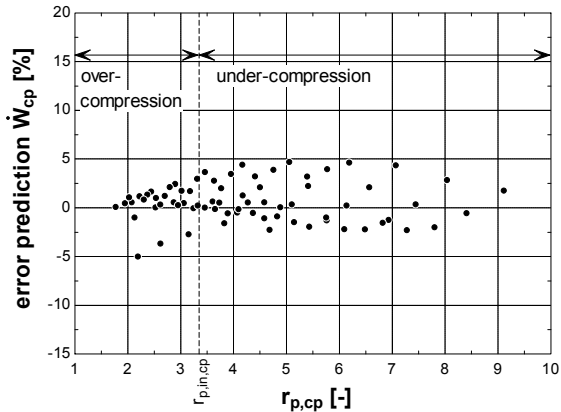


Figure 2-12 : Error on the electrical consumption (model with pressure drop and discharge valve)

Prediction of the displaced mass flow rate and heating capacity

Figure 2-13 compares the mass flow rate predicted by the model and announced by the manufacturer. The maximum deviation is 4.2%. The same comparison is given in Figure 2-14 for the heating capacity. The latter corresponds to a subcooling of 5K at the condenser exhaust. To get the best agreement, the swept volume has to be corrected. The value announced by the manufacturer, $5.92 \text{ m}^3/\text{h}$, has to be increased by 7% (factor K in Table 2-1). This can be explained by the passive supercharging effect described by Nieter (1988). The suction gas may start to be compressed before the end of the suction process, because of the decrease of the volume in the suction pockets near the end of the suction process. In one of the experimental studies on a hermetic scroll he carried out, Winandy (1999) also identified a swept volume higher (6%) than the one given by the manufacturer. According to the author, this can be explained by supercharging effect.

Figure 2-14 compares the heating capacity predicted by the model to the values announced by the manufacturer. This comparison is very satisfactory.

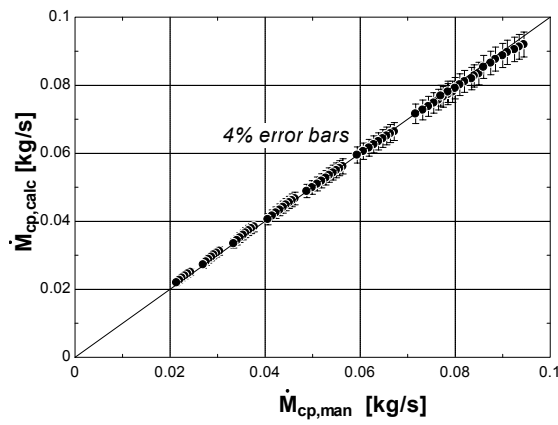


Figure 2-13 : Prediction of the displaced mass flow rate

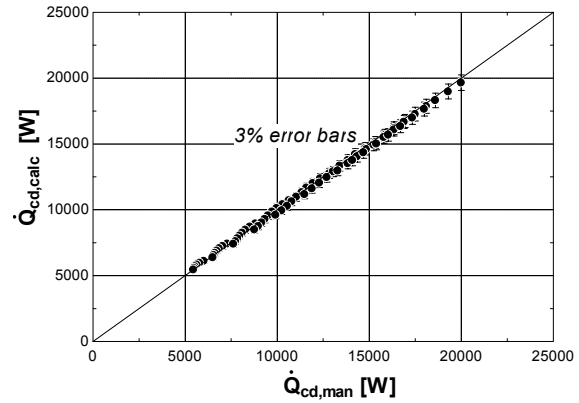


Figure 2-14 : Prediction of the heating capacity

Prediction of the isentropic and volumetric effectiveness

Figure 2-15 and Figure 2-16 compare the isentropic and volumetric effectivenesses predicted by the model to the values announced by the manufacturer. These effectivenesses are given as function of the pressure ratio imposed to the compressor. The model is able to predict the trend with a good agreement. Deviations between model predictions and manufacturer data

for the volumetric effectiveness might be due to fact that the leakage area is actually varying with the pressure ratio, because (among others) of the compliance system. Note also that this model doesn't account for the sliding of the asynchronous motor.

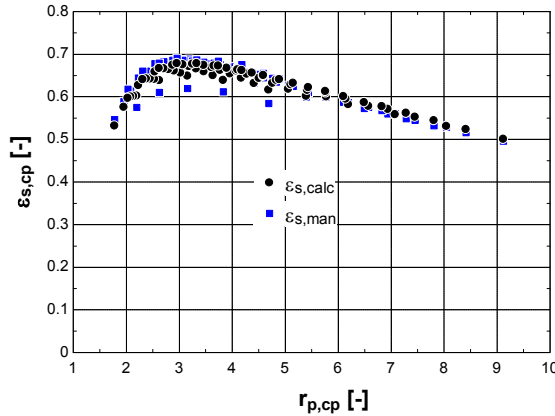


Figure 2-15 : Prediction of the global isentropic effectiveness

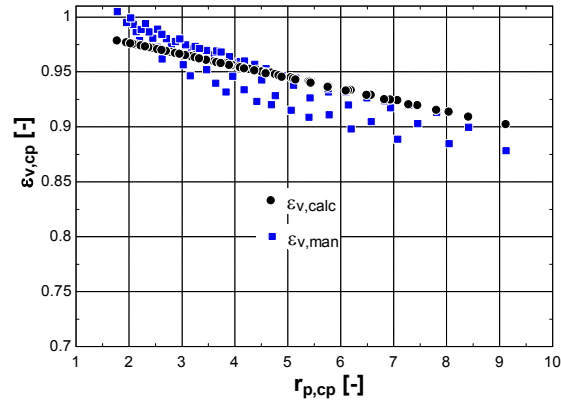


Figure 2-16 : Prediction of the volumetric effectiveness

A large clearance volume has been identified ($V_0 = 0.45V_{s,cp}$). The actual clearance volume has not been measured but is probably smaller. Some of the physical phenomena are probably still escaping (qualitatively or quantitatively) from the modeling. Figure 2-14 shows the impact of the clearance volume on the compressor isentropic effectiveness. The actual (simulated) performance ($C = 0.45$) is compared to the two limiting cases: the isentropic compression from P_{in} to $P_{ex,2}$ ($C = 0$) and the irreversible recompression of the back-flow from P_{in} to $P_{ex,2}$ ($C = 100$). This figure demonstrates the beneficial impact of the discharge valve for high pressure ratios.

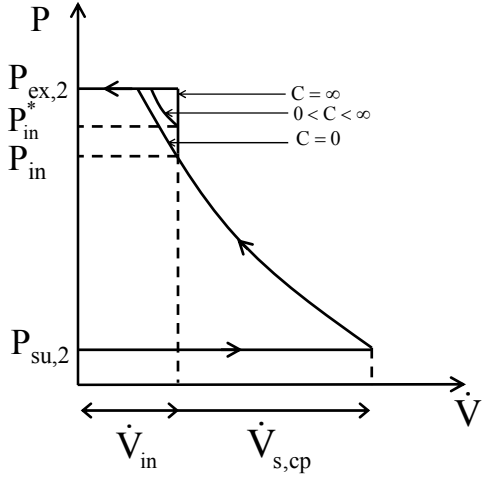


Figure 2-17 : Modification of the P-V diagram with the clearance volume

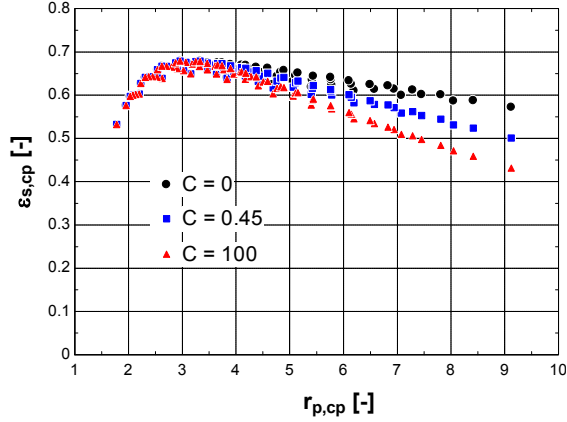


Figure 2-18 : Variation of the global isentropic effectiveness with the clearance volume

2.2 Scroll expander

2.2.1 Description of the model

The expander model is adapted from the model proposed by Winandy *et al.* (2002b) for hermetic scroll compressors. This model has already been partially validated by tests with water steam (Lemort *et al.*, 2006). It is similar from the model of Kane (2002), but requires three additional parameters to describe heat transfers.

The conceptual scheme of the expander model is shown in Figure 2-19. In this model, the evolution of the fluid state through the expander is decomposed into the following consecutive steps:

- supply pressure drop ($\text{su} \rightarrow \text{su},1$)
- supply cooling-down ($\text{su},1 \rightarrow \text{su},2$),
- adiabatic and reversible expansion to the internal pressure ($\text{su},2 \rightarrow \text{in}$),
- adiabatic expansion at a constant machine volume ($\text{in} \rightarrow \text{ex},2$),
- mixing with the internal leakage ($\text{ex},2 \rightarrow \text{ex},1$) and
- exhaust cooling-down or heating-up ($\text{ex},1 \rightarrow \text{ex}$).

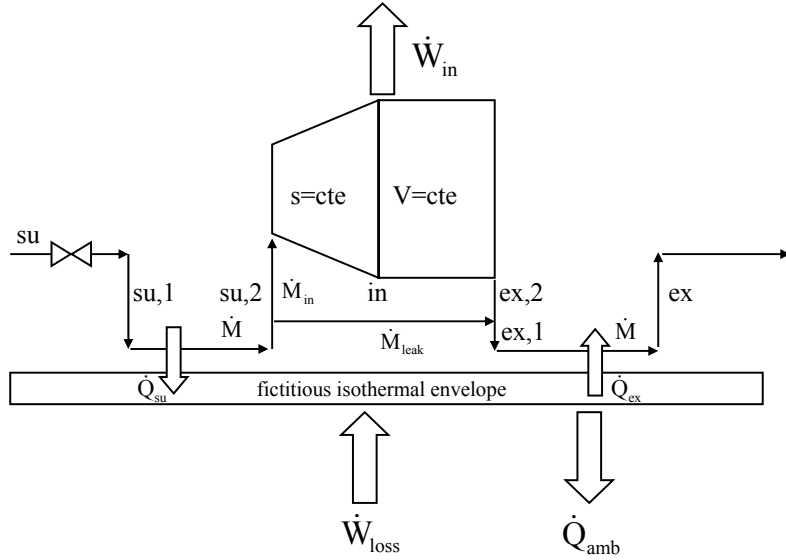


Figure 2-19 : Schematic representation of the expander model

Heat transfer, pressure drop and internal leakage

Heat transfer is described in a way similar to the compressor. The energy balance of the fictitious isothermal envelope is expressed as

$$\dot{W}_{\text{loss}} + \dot{Q}_{\text{su}} - \dot{Q}_{\text{ex}} - \dot{Q}_{\text{amb}} = 0 \quad (2-27)$$

The supply pressure drop is not negligible in the scroll expander: in Chapter 4, it is shown that a better agreement between measurements and model predictions of shaft power is found by introducing this pressure drop in the modeling. The causes are thoroughly investigated in Chapter 7.

The internal leakage is also described in a way similar to the compressor.

Displaced mass flow rate

As shown in Equation (2-28), the internal mass flow rate \dot{M}_{in} is the difference between the mass flow rate \dot{M} entering the expander and the leakage mass flow rate \dot{M}_{leak} . The entering mass flow rate is the volume flow rate $\dot{V}_{\text{s,exp}}$ divided by the specific volume of the fluid $v_{\text{su},2}$

after entering pressure drop and cooling down. The volume flow rate is the swept volume $V_{s,exp}$ multiplied by the expander rotational speed N . The swept volume in expander mode is equal to the one in compressor mode $V_{s,cp}$ divided by the built-in volume ratio of the machine $r_{v,in}$.

$$\dot{M}_{in} = \dot{M} - \dot{M}_{leak} = \frac{\dot{V}_{s,exp}}{v_{su,2}} - \dot{M}_{leak} = \frac{N \cdot V_{s,exp}}{v_{su,2}} - \dot{M}_{leak} = \frac{N}{v_{su,2}} \cdot \frac{V_{s,cp}}{r_{v,in}} - \dot{M}_{leak} \quad (2-28)$$

Internal power

The modeling accounts for the mismatching between the internal pressure ratio and the external pressure ratio. Two situations can occur: either the fluid is under-expanded (Figure 2-20 (a)) or it is over-expanded (Figure 2-20 (b)). This is described by dividing the expansion in two steps: an isentropic expansion to the internal pressure P_{in} imposed by the built-in volume ratio of the machine followed by an adiabatic expansion (or re-compression) at constant machine volume $V_{s,cp}$ to the exhaust pressure.

The internal power is given by

$$\dot{W}_{in} = \dot{M}_{in} (h_{su,2} - h_{in} + v_{in} (P_{in} - P_{ex,2})) \quad (2-29)$$

The development of this relationship is established in the Appendix.

Mechanical losses

Mechanical losses \dot{W}_{loss} are due to friction between the scrolls and losses in the bearings. In the present modeling, all these losses are lumped into one unique mechanical losses torque T_{loss} as proposed by Yanagisawa *et al.* (2001).

$$\dot{W} = \dot{W}_{in} - \dot{W}_{loss} = \dot{W}_{in} - \dot{W}_{loss} = \dot{W}_{in} - 2\pi N T_{loss} \quad (2-30)$$

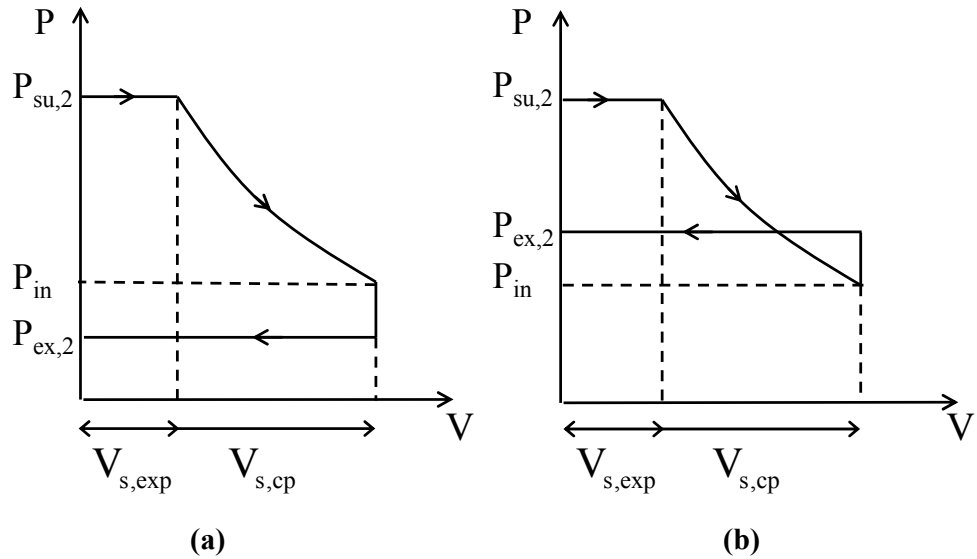


**Figure 2-20 : Representation of the entire expansion process in the pressure-volume diagram
 ((a): under-expansion and (b): over-expansion)**

2.2.2 Information diagram of the expander model

The information diagram of the model is shown in Figure 2-21. The input variables are the supply pressure, the supply temperature, the exhaust pressure, the rotational speed of the expander. The model calculates the following output variables: the mass flow rate displaced by the expander, the delivered mechanical power and the exhaust temperature. The model only necessitates 8 parameters.

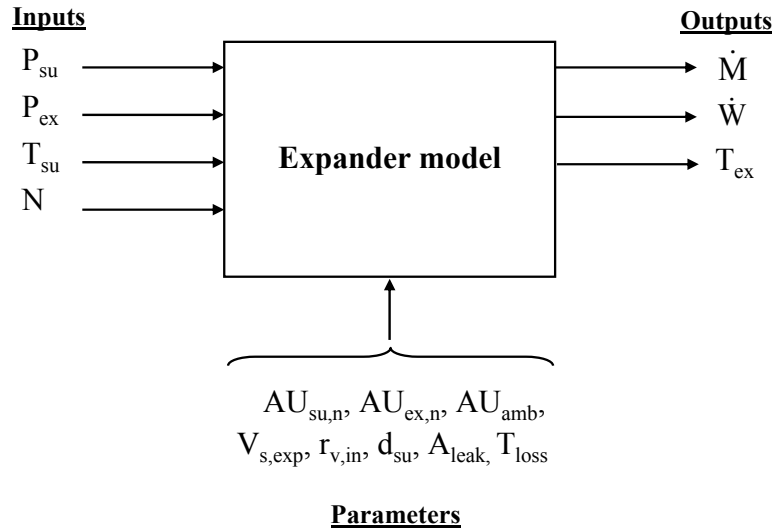


Figure 2-21 : Information diagram of the expander semi-empirical model

2.3 Heat exchangers

According to a very common practice, heat exchangers are modeled by considering three lumped thermal resistance in series: the convective resistance on the *fluid a* side, the metal conductive resistance and the convective resistance on the *fluid b* side. Hence, the global heat transfer coefficient AU is given by

$$AU^{-1} = R_a + R_m + R_b \quad (2-31)$$

2.3.1 Modeling the evaporator and the condenser of a vapor compression refrigeration system

The basic modeling of the evaporator and the condenser consists in assuming that the heat exchanger is semi-isothermal, with the constant temperature equal to the saturation temperature. The single-phase zones of the heat exchanger are neglected and the model reduces to a one-zone heat exchanger. This assumption is acceptable for the evaporator of a chiller, since it presents a large two-phase zone and a small single-phase (superheating) zone.

In order to be more accurate in the condenser modeling, the condensing temperature can be defined as the weighted average of the actual temperatures occurring in the three zones (single-phase desuperheating, two-phase condensation and single-phase undercooling):

$$\bar{t}_{cd} = \left\{ (h_{r,su,cd} - h_{r,su,cd,tp}) \left[\frac{T_{r,su,cd} + T_{cd}}{2} \right] + (h_{r,su,cd,tp} - h_{r,ex,cd,tp}) \cdot T_{cd} \right. \\ \left. + (h_{r,ex,cd,tp} - h_{r,ex,cd}) \left[\frac{T_{r,ex,cd} + T_{cd}}{2} \right] \right\} / (h_{r,su,cd} - h_{r,ex,cd}) \quad (2-32)$$

2.3.2 Modeling the evaporator and the condenser of a Rankine cycle power system

In the modeling of an Organic Rankine Cycle system, due to large liquid and vapor zones, the evaporator and the condenser cannot be accurately described by only one zone (Quoilin *et al.*, 2008).

The condenser and the evaporator are modeled as sets of three counter-flow heat exchangers, each of them being characterized by one heat exchange coefficient AU . The subdivision into zones is shown in Figure 2-22 in the case of the evaporator.

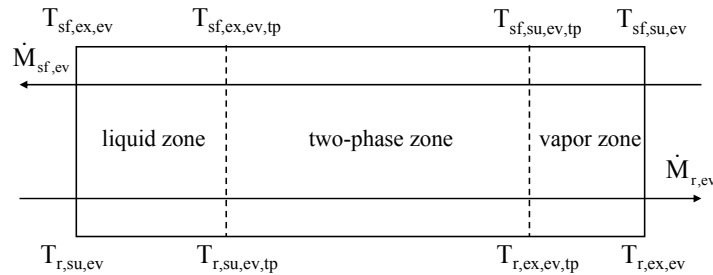


Figure 2-22 : Three-zone evaporator model

2.4 Pump

The volumetric pump is simply modeled by its swept volume and two theoretically constant efficiencies: the isentropic ($\eta_{pp,s}$) and the motor ($\eta_{pp,m}$) efficiencies. The pump electrical consumption and the fluid swept flow rate are given by Equations (2-33) and (2-34).

$$\dot{W}_{pp} = \frac{\dot{W}_{sh,pp}}{\eta_{pp,m}} = \frac{\dot{W}_{pp,s}}{\eta_{pp,s} \cdot \eta_{pp,m}} \quad (2-33)$$

$$\dot{M}_r = \frac{\dot{V}_{s,pp}}{V_{r,su,pp}} = \frac{X_{pp} \cdot \dot{V}_{s,pp,max}}{V_{r,su,pp}} \quad (2-34)$$

3 MODELING THERMAL SYSTEMS

3.1 Vapor compression refrigeration system

The schematic representation of the vapor compression refrigeration system model is shown in Figure 3-1. This model is built by inter-connecting the sub-models of the different components.

The modeling shows the following constraints:

- I. For given supply conditions and exhaust pressure and for a given displacement (or rotational speed), the compressor imposes the mass flow rate through the cycle.
- II. For given secondary fluid mass flow rate and supply temperature, the condenser imposes the condensing pressure. If the condenser model describes the pressure drop on the refrigerant side, both supply and exhaust pressures are determined. The liquid subcooling at the condenser exhaust is here imposed. It is actually a function of the refrigerant charge in the cycle, and could be predicted by introducing void fraction models for the heat exchangers.
- III. The expansion valve model assumes that expansion is isenthalpic, which imposes the vapor enthalpy at the evaporator supply.
- IV. For given secondary fluid flow rate and temperature, the evaporator imposes the evaporating pressure. Here also, provided the pressure drop through the evaporator is described, the model distinguishes between supply and exhaust pressures.

The vapor superheating at the evaporator exhaust is here imposed. It could be determined by introducing a more detailed model of the expansion valve.

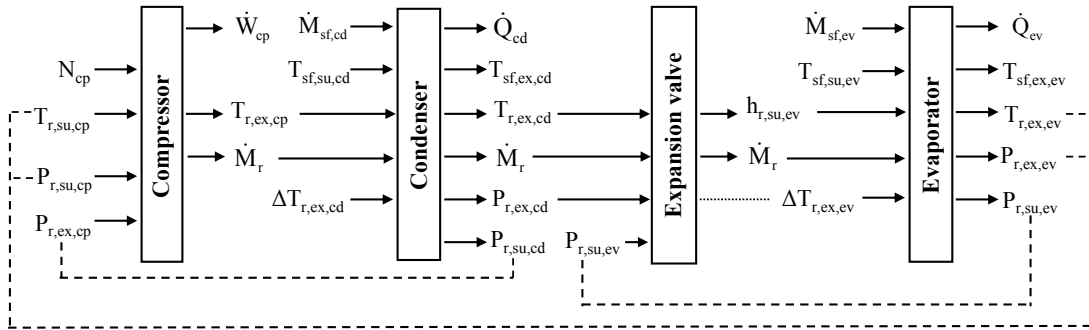


Figure 3-1 : Refrigeration system model (Cuevas, 2006)

3.2 Rankine cycle power system

As shown in Figure 3-2, the Rankine cycle system model has been established adopting the same approach as for the refrigeration system.

Here also, the modeling shows some constraints:

- I. For a given displacement, the pump imposes the refrigerant flow rate.
- II. The evaporator (or “boiler”) imposes the fluid superheating and the pump exhaust pressure.
- III. Provided its rotational speed is fixed, the expander imposes the evaporator exhaust pressure.
- IV. For given secondary fluid flow rate and supply temperature, the condenser imposes the pressures at expander exhaust and pump supply (if its modeling describes the refrigerant pressure drop).

The liquid subcooling at the condenser exhaust is considered as an input of the model, since it is imposed by the refrigerant charge. Here also, it could be determined if void fraction models of the heat exchangers were introduced.

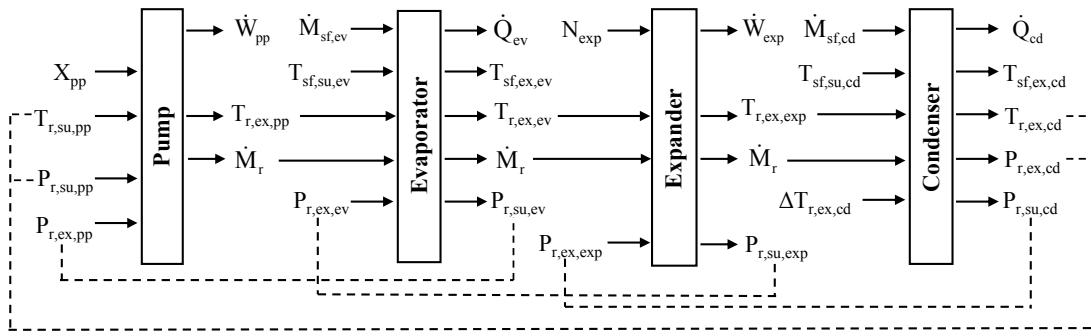


Figure 3-2 : Rankine Cycle System Model

4 CONCLUSIONS

This chapter presented first a semi-empirical model of a scroll compressor that accounts for the eventual discharge valve at the compressor exhaust.

Validation of the model based on published manufacturer data showed that the compressor consumption is more accurately predicted when taking into account the discharge valve. The use of this valve is described in terms of irreversible re-expansion of the clearance volume of the scroll compressor and pressure drop through the discharge opening. Two additional parameters have been introduced in the original model proposed by Winandy *et al.* (2002b). They strongly impact on the prediction of the electrical consumption, but not of the refrigerant mass flow rate. Consequently, introducing these two parameters doesn't increase the complexity of the parameters identification process.

A semi-empirical model of the scroll expander has been derived from the model of the scroll compressor. The model is validated in Chapter 4.

Finally, simulation models for a vapor compression refrigeration system and a Rankine cycle system have been proposed. They associate semi-empirical models of scroll machines, evaporator and condenser. The use of these models is illustrated in Chapters 3 and 4, respectively.

5 REFERENCES

- Bush, J. W., A. Lifson. 1998. Controlling Discharge Valve Closing Impact in Scroll Machines. *Proceedings of the International Compressor Engineering Conference at Purdue*: 631-636.
- Bukac, H. 2008. Analysis of two-stage compression in a scroll compressor. *Proceedings of the International Compressor Engineering Conference at Purdue*: Paper 1363.
- Chen, Y. 2000. Mathematical Modeling of Scroll Compressors. *Ph.D Thesis*, Purdue University.
- Cuevas Baraza, C. 2006. Contribution to the modelling of refrigeration systems. *PhD Thesis*. Université de Liège.
- Cuevas, C., V. Lemort, and J. Lebrun. 2008. Scroll compressor model. *Proceedings of the Heat Pump Symposium at the K.U.L.*
- Elson, J., N. Kaemmer, S. Wang, and M. Perevozchikov. 2008. Scroll Technology: An Overview of Past, Present and Future Developments. *Proceedings of the International Compressor Engineering Conference at Purdue*: Paper 1204.
- Glaeser, W.A. 1999. Failure mechanisms of reed valves in refrigeration compressors. *Wear* vol 225-229: 918-924.
- Haberschill, P., S. Borg, M. Mondot, and M. Lallemand. 1994. Hermetic compressor models determination of parameters from a minimum number of tests. *Proceeding of the International Compressor Engineering Conference at Purdue*: 133-138.
- Halm, N. P. 1997. Mathematical Modeling of Scroll Compressors. *Master Thesis*, Purdue University.
- Hiller, C.C., and L.R. Glicksmann. 1976. Detailed modeling and computer simulation of reciprocating refrigeration compressors. *Proceedings of the International Compressor Engineering Conference at Purdue*: 12-17.
- Incropera, F. P., and D. P. DeWitt. 2002. Fundamentals of Heat and Mass Transfer. *John Wiley & Sons*.
- Jang, K., and S. Jeong. 2006. Experimental investigation on convective heat transfer mechanism in a scroll compressor. *International Journal of Refrigeration* 29: 744-753.

- Kane, El H. 2002. Intégration et optimisation thermoéconomique & environnementale de centrales thermiques solaires hybrides. *PhD Thesis*, Laboratoire d'Energétique Industrielle, Ecole polytechnique Fédérale de Lausanne.
- Lee, G.H.. 2002. Performance simulation of scroll compressors, *Proc Instn Mech Engrs Vol 216 Part A: J Power and Energy*: 169-179.
- Lemort, V., Teodorese, I.V., Lebrun, J. 2006. Experimental study of the integration of a scroll expander into a heat recovery Rankine cycle. *Proceedings of the International Compressor Engineering Conference at Purdue*: C105.
- Myszka, D. H. 1998. An analytical model for the discharge process in scroll compressors, Proc. of the 1998 International Compressor Engineering Conference at Purdue, pp. 625-630.
- Nieter, J. 1988. Dynamic of scroll suction process, *Proceedings of the International Compressor Engineering Conference at Purdue*.
- Nieter, J.J., D. P. Gagne. 1992. Analytical modeling of discharge flow dynamics in scroll compressors, *Proceedings of the International Compressor Engineering Conference at Purdue*: 85-96.
- Ooi, K. T., J. Zhu. 2004. Convective heat transfer in a scroll compressor chamber: a 2-D simulation, *International Journal of Thermal Sciences* 43: 677-688.
- Prater G. Jr. and W. P. Hnat. 2003. Optical measurement of discharge valve modal parameters for a rolling piston refrigeration compressor. *Measurement* 33: 75-84.
- Quoilin, S., M., Orosz, and V., Lemort. 2008, Modeling and Experimental Investigation of an Organic Rankine Cycle System using Scroll Expander for Small Scale Solar Applications, *Proceedings of the First International Conference on Solar Heating, Cooling and Building (EUROSUN)*, Lisboa.
- Sauls, J.R. 1982. Performance characteristics of fixed volume ratio compressors, *Proceedings of the International Compressor Engineering Conference at Purdue*: 201-207.
- Stoecker, W.F. 1971. *Design of Thermal Systems*, McGraw-Hill, New York.
- Winandy, E. L. 1999. Contribution to the performance analysis of reciprocating and scroll refrigeration compressors. PhD Thesis. University of Concepción. Chile.
- Winandy, E., C. Saavedra, and J. Lebrun. 2002a. Simplified modelling of an open-type reciprocating compressor, *International Journale of Thermal Sciecnces* 41: 183-192.

Winandy, E., C. Saavedra, and J. Lebrun. 2002b. Experimental analysis and simplified modelling of a hermetic scroll refrigeration compressor, *Applied Thermal Engineering* 22: 107-120.

Yanagisawa, T., M.C. Cheng, M. Fukuta, T. Shimizu. 1990. Optimum Operating Pressure Ratio for Scroll Compressor. *Proceedings of the Internnatial Compressor Engineering Conference at Purdue*: 425-433.

CHAPTER 3

EXPERIMENTAL INVESTIGATION ON AN AIR-COOLED SCROLL COMPRESSOR CHILLER

1	INTRODUCTION.....	46
2	DESCRIPTION OF THE CHILLER	47
2.1	General description of the chiller	47
2.2	Instrumentation of the chiller	49
3	IDENTIFICATION OF THE CHILLER MODEL PARAMETERS BASED ON MANUFACTURER DATA.....	50
3.1	Procedure for identifying the parameters (at full load).....	50
3.1.1	First step: identification of the parameters of the compressor model	50
3.1.2	Second step: identification of the parameters of the heat exchangers models	54
3.2	Description of part load operation and condenser fans control.....	57
3.2.1	Quasi-static model of the compressor cycling	57
3.2.2	Fan control	59
3.3	Influence of glycol concentration on the chiller performances	61
3.3.1	Summary	63
4	EXPERIMENTAL INVESTIGATION	63
4.1	Simulation with model parameters identified with manufacturer data	63
4.1.1	Description of the simulation	63
4.1.2	Simulation results	65
4.2	Identification of the model parameters based on quasi-steady state points extracted from experimental data.....	66
4.2.1	Definition of quasi-steady state points	66
4.2.2	Verification of the compressor consumption	69
4.2.3	Verification of the cooling power	69
	Higher leakage area	72
	Hot gas bypass	73
4.2.4	Fan control and electrical consumption	75
4.2.5	Identification of the heat exchangers resistances	78
4.2.6	Validation of the model for the quasi-steady state points.....	80
4.3	Simulation with model parameters identification based on quasi-steady state points.....	83

5	CONCLUSIONS	83
6	REFERENCES.....	85

NOMENCLATURE

A	Area, m ²
AU	Heat transfer coefficient, W/K
c	Specific heat, J/kg-K
C	Clearance volume factor, -
d	Diameter, m
h	Specific enthalpy, J/kg
K	Correction factor, -
\dot{M}	Mass flow rate, kg/s
N	Rotational speed, Hz
\dot{Q}	Heat transfer rate, W
R	Heat transfer resistance, K/W
$r_{v,in}$	Built-in volume ratio, -
s	Specific entropy, J/kg-K
T	Temperature, °C
u	Specific internal energy, J/kg
v	Specific volume, m ³ /kg
\dot{V}	Volume flow rate, m ³ /s
w	Specific work, J/kg
\dot{W}	Power, W
X	Capacity fraction

Subscripts

0	Constant, clearance
a	Air
amb	Ambient
aux	Auxiliaries
bp	By-pass
calc	Calculated
cd	Condenser, condensing
cp	Compressor

crit	Critical
ex	Exhaust
exp	Expander
glw	Glycol water
in	Internal
loss	Mechanical loss
leak	Leakage
m	Metal
man	Manufacturer
meas	Measured
n	Nominal
p	Isobaric
r	Refrigerant
s	Isentropic, swept
set	Set point
sh	Shaft
sf	Secondary fluid
su	Supply
thr	Throat
tot	Total
w	Envelope, water

Greek and miscellaneous

α	Factor of proportionality for the electromechanical loss, -
Δ	Difference
ε	Effectiveness, -
γ	Specific heat ratio, -
η	Efficiency, -
θ	Working time fraction, -

1 INTRODUCTION

The hermetic scroll compressor model presented in Chapter 2 has already been validated for different compressor capacities, compressor technologies (with and without liquid or vapor injection) and operating conditions. Among others, Winandy *et al.* (2002) and Cuevas and Lebrun (2008) showed that the model is able to predict variables of first importance with a very good accuracy. This chapter doesn't provide any additional validation of the scroll compressor model, but focuses on the integration of the compressor into a refrigeration system.

The underlying work has been carried out in the frame of a project of the International Energy Agency (Felsmann, 2008). The goal of this project was to undertake pre-normative research to develop testing methods of building energy simulation tools. A part of this project focused on the modeling and the simulation of the performance of certain components that are part of a chilled and/or a heating water system. One of these components is the air-cooled scroll compressor chiller.

The identification of the parameters of the air-cooled scroll compressor model and its validation have been achieved in two steps: on the basis of published manufacturer data and on the basis of experimental results, respectively.

The use of published manufacturer data to identify the parameters of the chiller model is described in the first part of this Chapter. This approach gives better accuracy and better extrapolation capability than polynomial fit models (Jin and Spitler, 2002). Manufacturer data is often the only data available to model HVAC components. Some information is usually lacking to accurately validate the components models. The first part of this chapter will propose rational assumptions and idealizations.

The second part of the chapter presents results of an experimental investigation carried out on the same chiller. This investigation will allow checking assumptions proposed earlier, characterizing better the chiller and improving its modeling.

2 DESCRIPTION OF THE CHILLER

2.1 General description of the chiller

The chiller is part of a chilled water system (shown in Figure 2-1) comprising an air-cooled scroll compressor chiller (ACCH), a cooling coil located inside an air-handling unit (ChW Coil) and a hydraulic network including a circulating pump and a mixing valve. The test facility is installed at the *Energy Resource Station* located at Ankeny, Iowa, USA (Felsmann, 2008).

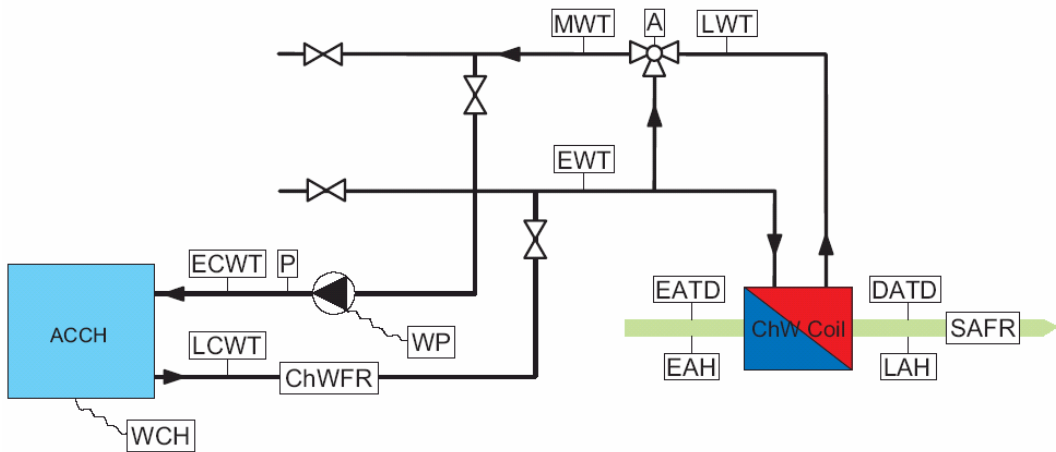


Figure 2-1 : Scheme of the chilled water system (Felsmann, 2008)¹

The chiller consists of *two* air-cooled condensers, *two* hermetic scroll compressors in tandem, *one* brine-heated evaporator and a hot gas by-pass. External views of the chiller are given in Figure 2-2. Its nominal cooling capacity is 34.3 kW in ARI Conditions (ARI Standard 550/590, 1998) for 460 V, 3-phase, 60 Hz regime. These conditions correspond to a 35°C entering air temperature, a brine flow rate of 1.51 l/s (brine is here a 25% in mass aqueous solution of propylene glycol) and a leaving brine temperature of 6.7°C. Full load COP (*Coefficient of Performance*) is 2.84 and part load COP is 3.58.

¹ ChWFR: chilled water flow rate; SAFR: supply air flow rate; ECWT: entering chiller water temperature; LCWT: leaving chiller water temperature; EWT: entering water temperature; LWT: leaving water temperature; MWT: mixing water temperature; EATD: entering air temperature dry; EAH: entering air humidity.



Figure 2-2 : View of the chiller ((a): North facing side, (b): South facing side)

The refrigeration circuit is shown in Figure 2-3.

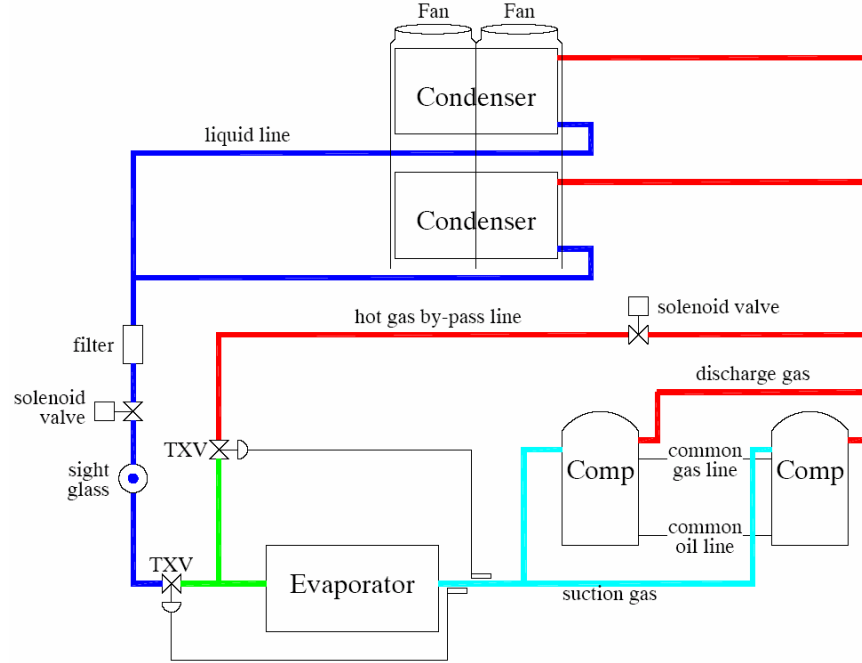


Figure 2-3 : Air-cooled chiller refrigeration circuit (Felsmann, 2008)

The evaporator is a stainless steel plate heat exchanger insulated with 19 mm thick closed-cell polyurethane insulation.

The condenser is a plate fin heat exchanger. The tubes are in copper and located in staggered pattern. The fins are constructed of aluminum.

Each compressor has a swept volume of 93.013 cm^3 per revolution. This swept volume corresponds to a displaced volume flow rate of $16.183 \text{ m}^3/\text{h}$ at 50 Hz operation and of $19.533 \text{ m}^3/\text{h}$ at 60 Hz operation.

2.2 Instrumentation of the chiller

The following instrumentation has been installed on the air-cooled brine chiller:

- *On brine side*: flow rate and evaporator supply and exhaust temperatures.
- *On air side*: condenser supply and exhaust temperatures (average of four RTD sensors) and separate fans consumptions. Supply air RTD sensors are shown in Figure 2-2. There is no measurement of the air flow rate. The test rig is equipped with a pressure differential sensor on the condenser. The condenser pressure drop could have been used to estimate the air flow rate. Unfortunately, this pressure drop is not available in the experimental data provided to the modelers.
- *On refrigerant side*: pressures at the supply and at the exhaust of the compressor.
- *On the compressor*: its electrical consumption.

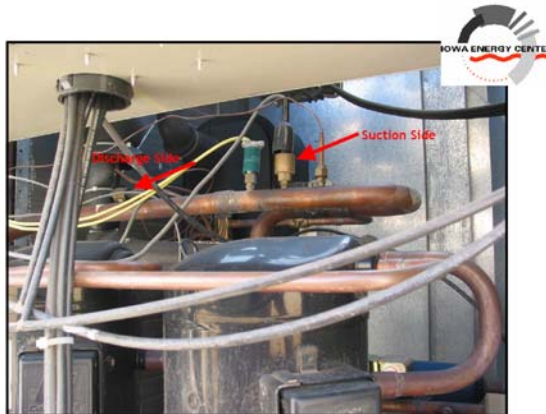


Figure 2-4 : Location of the pressure sensors

Shrestha (2006) carried out a validation of the chiller model implemented in *EnergyPlus* by using experimental data collected on the chiller investigated here. For all the tests, the model under-predicts the chiller consumption and the cooling capacity. According to the author, the disagreement could be due to the fact that the temperature of the air entering the condenser is higher than the measured ambient temperature (considered as the entering air temperature in the simulation). Actually, the chiller is located in an outside area surrounded with concrete

walls (Felsmann, 2008). During periods of strong irradiations, this area is heated. Hence, the condenser supply temperature is higher than the temperature measured at the weather station. This may explain the under-prediction of the chiller consumption but not of the cooling capacity.

3 IDENTIFICATION OF THE CHILLER MODEL PARAMETERS BASED ON MANUFACTURER DATA

3.1 Procedure for identifying the parameters (at full load)

The identification of the parameters of the model is achieved in two steps:

- 1) The parameters of the compressor model are first identified, according to the *compressor* performance data.
- 2) The parameters of the evaporator and the condenser are then identified, according to *chiller* performance data.

3.1.1 First step: identification of the parameters of the compressor model

Polynomial equations are given by the manufacturer to describe the compressor cooling capacity, electrical consumption and mass flow rate. These polynomial equations are given in the form $X=f(T_{ev}, T_{cd})$:

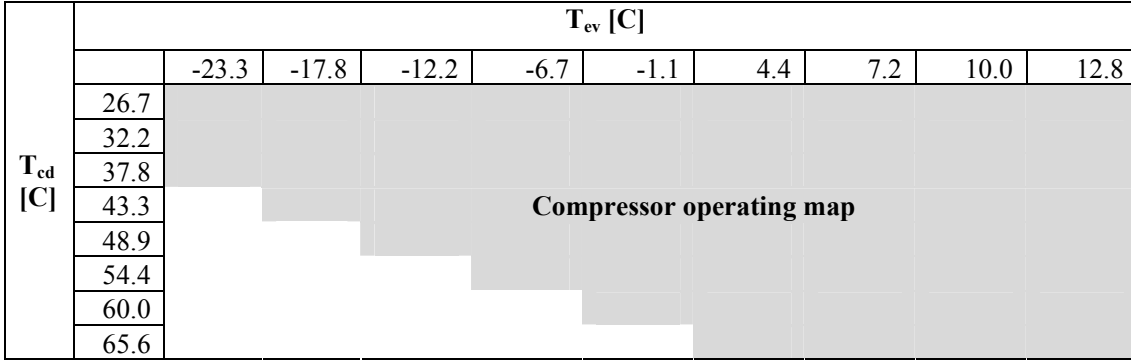
$$X = C_0 + C_1 T_{ev} + C_2 T_{cd} + C_3 T_{ev}^2 + C_4 T_{ev} T_{cd} + C_5 T_{cd}^2 + C_6 T_{ev}^3 + C_7 T_{cd} T_{ev}^2 + C_8 T_{ev} T_{cd}^2 + C_9 T_{cd}^3 \quad (3-1)$$

Coefficients of this equation for the cooling capacity, electrical consumption and mass flow rate are given in the Appendix. The validity of these polynomial equations is limited to the operating map defined in Table 3-1.

Rating conditions are:

- superheat at the compressor inlet: 11.11°C (20°F)
- subcooling at the condenser outlet: 8.33°C (15°F)
- ambient air temperature: 35°C (95°F)
- 50Hz operation
- Refrigerant : HCFC R-22

Table 3-1: Compressor operating map



The compressor model has been described in Chapter 2. Its parameters are tuned in order to bring the values of the refrigerant mass flow rate, power consumption and cooling capacity predicted by the model as close as possible to the values announced by the manufacturer. Figure 3-1 shows that the evaporating and condensing temperatures as well as the suction superheat and the condenser subcooling are the inputs of the model, while the model calculates the mass flow, the power consumption, the cooling capacity and the heat rejection. Identified parameters are given in the information diagram shown in Table 3-2.

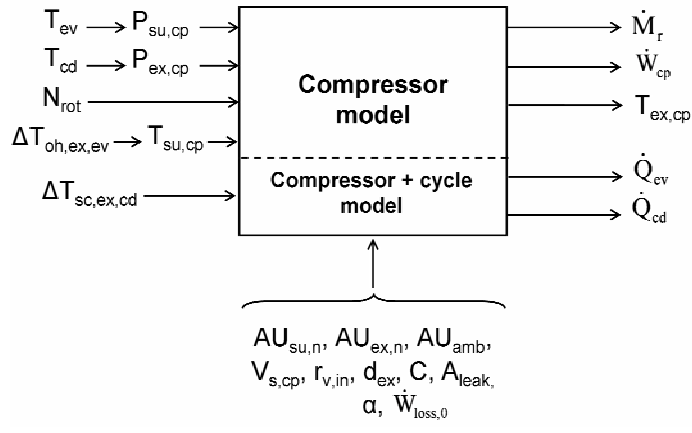


Figure 3-1: Information diagram of the scroll compressor model

Table 3-2 : Parameters of the compressor model

Parameter	Value
AU_{amb}	10 W/K
$AU_{su,n}$	18 W/K
$AU_{ex,n}$	35 W/K
\dot{M}_n	0.091 kg/s
A_{leak}	0.599 mm ²
$r_{v,in}$	2.55
$\dot{V}_{s,cp}$	16.183 m ³ /h
d_{ex}	0.0075 m
$\dot{W}_{loss,0}$	150 W
α	0.2
κ	0.06

Prediction by the model of the refrigerant mass flow rate, power consumption and cooling capacity are compared to the values given by the manufacturer in Figure 3-2, Figure 3-3 and

Figure 3-4. It can be observed that the agreement is fairly good. However, the model doesn't seem to predict correctly the lowest mass flow rates. The deviation between calculation and manufacturer data for the cooling capacity is consistent with the deviation for the mass flow rate. Figure 3-5 compares the evolution of the global isentropic effectiveness predicted by the model and announced by the manufacturer with the pressure ratio imposed to the compressor. This global isentropic effectiveness is defined by:

$$\varepsilon_{s,cp} = \frac{\dot{M}_r (h_{r,ex,cp,s} - h_{r,su,cp})}{\dot{W}_{cp}} \quad (3-2)$$

The disagreement between the values predicted by the model and announced by the manufacturer is obviously related to the disagreement in the refrigerant mass flow rate (lowest and highest mass flow rates are under- and over-predicted respectively). This is confirmed in Figure 3-6 which shows the isentropic effectiveness predicted by the model with the mass flow rate announced by the manufacturer. One reason for the deviation between prediction by the model and manufacturer data for the low flow rate could be that the compressor cannot be characterized by a unique leakage area. This may be due to the axial and radial compliance features.

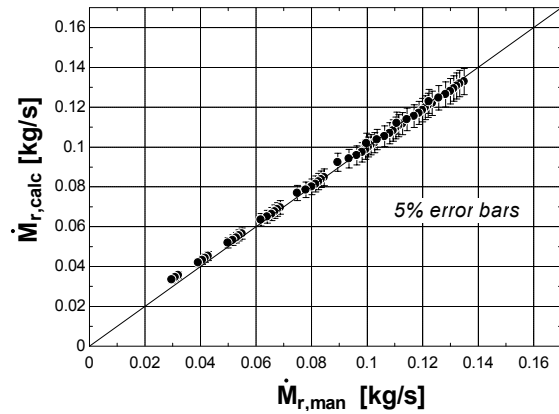


Figure 3-2: Prediction of the compressor displaced refrigerant mass flow rate

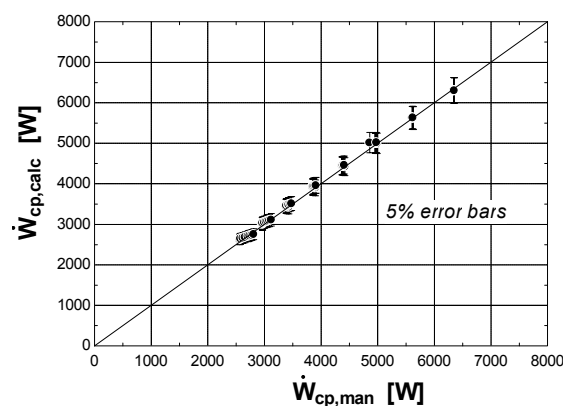


Figure 3-3: Prediction of the compressor electrical consumption

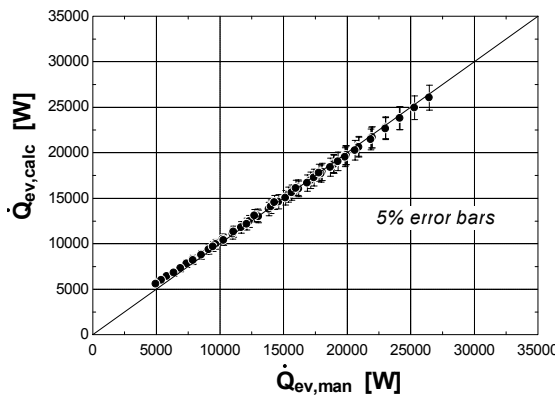


Figure 3-4: Prediction of the compressor cooling capacity

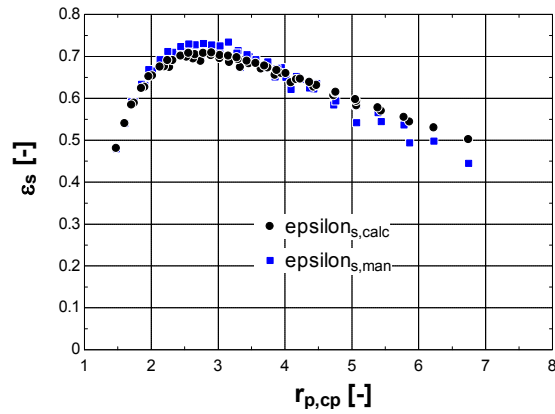


Figure 3-5: Prediction of the compressor global isentropic effectiveness

It should be mentioned to conclude that the heat rejection at the condenser \dot{Q}_{cd} was not given by the manufacturer. Usually, it is part of the available performance data and can be used to deduce the compressor discharge temperature (which allows a more accurate identification of the heat transfer coefficients).

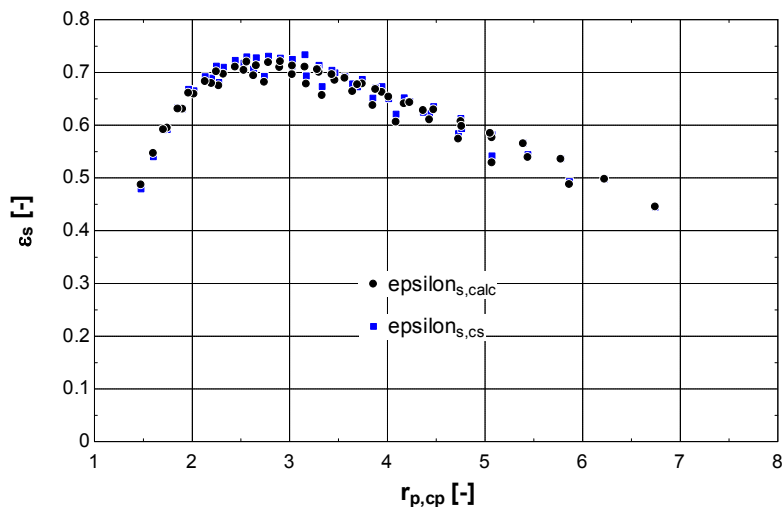


Figure 3-6 : Prediction of the compressor global isentropic effectiveness, when the mass flow rate is imposed equal to the mass flow rate given by the manufacturer

3.1.2 Second step: identification of the parameters of the heat exchangers models

Thirty performance points are given by the chiller manufacturer (Table 3-3). These performance data are presented as function of the leaving water temperature (evaporator exhaust temperature $T_{w,ex,ev}$, LWT) and the ambient air temperature (condenser supply temperature $T_{a,su,cd}$), according to ARI (ARI Standard 550/590, 1998)

Table 3-3 : Chiller performance data (the red framed point is the closest to ARI standard)

LWT (°C)	Ambient Air Temperature (°C)											
	25			30			35			40		
	Unit kW	PWR kW	Unit COP	Unit kW	PWR kW	Unit COP	Unit kW	PWR kW	Unit COP	Unit kW	PWR kW	Unit COP
5	35	8	3.4	33.7	8.8	3.03	32.3	9.7	2.7	30.9	10.7	2.38
6	36.2	8.1	3.49	34.9	8.9	3.12	33.5	9.8	2.78	32.1	10.8	2.46
7	37.5	8.2	3.59	36.2	9	3.21	34.8	9.9	2.86	33.3	10.9	2.53
8	38.9	8.3	3.68	37.5	9.1	3.3	36	9.9	2.94	34.5	10.9	2.61
9	40.2	8.4	3.78	38.8	9.1	3.39	37.3	10	3.02	35.7	11	2.68
10	41.6	8.4	3.87	40.1	9.2	3.48	38.6	10.1	3.11	36.9	11.1	2.75

The electrical input is for the compressor only. The COP corresponds to the entire unit (it accounts for the fans' electrical consumption).

The parameters of the heat exchangers models are first identified on the basis of one point. Among all points available, the one closest to ARI Standard (entering air dry and wet bulb temperature: 35°C and 23.9°C; leaving water temperature: 6.67°C; water flow rate: 0.043 L/s per kW) has been selected (red framed point in Table 3-3).

The parameters of the condenser and the evaporator models (three resistances and two nominal flow rates) are identified by imposing the cooling capacity and the compressor consumption calculated by the model equal to the values announced by the manufacturer.

This makes only *two* information for a total of six resistances to be identified. The following four hypothetical relationships are also imposed:

- For the plate heat exchanger, the metal resistance is neglected.
- As a first guess, resistances on the water side and on the refrigerant side are assumed equal.

$$R_{w,ev,n} = R_{r,ev,n} \quad (3-3)$$

$$R_{m,ev} = 0 \quad (3-4)$$

- For the plate fin heat exchanger, by similarity to the cooling coils (Homes, 1988), the three resistances were given the same weight.

$$R_{a,cd,n} = R_{r,cd,n} = R_{m,cd} \quad (3-5)$$

The latter ratios between the resistances are proposed here as a first estimate. They can be tuned afterwards to get a better agreement between predictions by the model and measurements.

Fans

The chiller investigated here comprises two fans. The condenser nominal airflow rate given by the manufacturer is 23700 m³/h for the two fans (it is defined by convention at condensers exhaust). In nominal conditions (red frame point in Table 3-3), it corresponds to a mass flow rate of 7.201 kg/s. It is assumed that the fans operate at their maximum flow rate for all the points given in Table 3-3, since it gives the best results for the prediction of the total electrical consumption.

The identified parameters of the model are given in Table 3-4. The identified fan consumption is 1100 W.

Table 3-4 : Parameters of the evaporator and condenser models identified based on published manufacturer data

Evaporator		Condenser	
$R_{w,ev,n}$	0.0001308 [K/W]	$R_{a,cd,n}$	0.00006849 [K/W]
$R_{m,ev}$	0 [K/W]	$R_{m,cd}$	0.00006849 [K/W]
$R_{r,ev,n}$	0.0001308 [K/W]	$R_{r,cd,n}$	0.00006849 [K/W]
$\dot{M}_{w,ev,n}$	1.499 [kg/s]	$\dot{M}_{a,cd,n}$	7.201 [kg/s]
$\dot{M}_{r,ev,n}$	0.2191 [kg/s]	$\dot{M}_{r,cd,n}$	0.2191 [kg/s]
$\Delta T_{oh,ex,ev}$	5 [K]	$\Delta T_{sc,ex,cd}$	5 [K]
$\dot{W}_{fan,n}$			1100 [W]
\dot{W}_{aux}			200 [W]

The agreement between predicted and measured performances is shown in Figure 3-7, Figure 3-8 and Figure 3-9. In these figures, the ratios between the resistances (for both the condenser and the evaporator) have not been retuned and are those given in Equations (3-3) to (3-5).

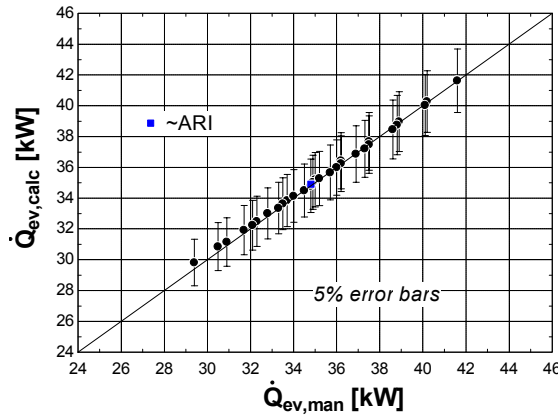


Figure 3-7 : Prediction of the chiller cooling capacity

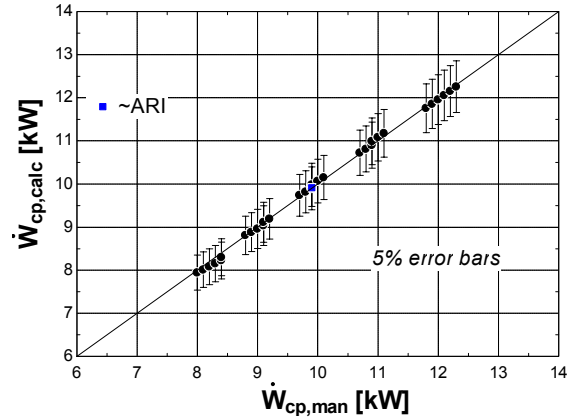


Figure 3-8: Prediction of the chiller electrical consumption

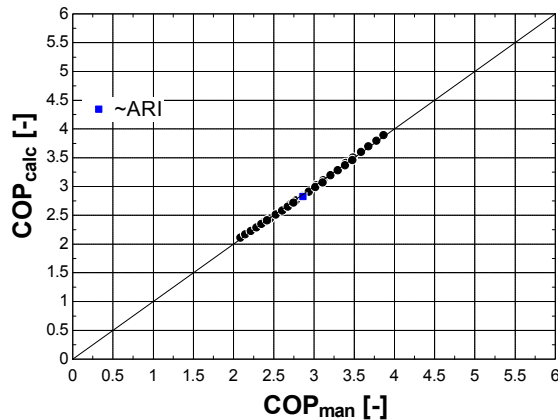


Figure 3-9 : Prediction of the chiller overall COP (including fans consumption)

3.2 Description of part load operation and condenser fans control

The chiller part load performances are described by four points given in Table 3-5. These data are certified according to ARI (ARI Standard 550/590, 1998). The air temperature is missing for the 75%, 50% and 25% points. It is assumed that this temperature is in accordance with the ARI Standard (26.7°C, 18.3°C and 12.8°C).

Table 3-5 : Chiller part load data

Chiller Performance (Water Application)			
Percent of Rated Capacity	100 %	75 %	50 %
Capacity kW	34.5	25.7	17.2
Unit kW Input	12.1	7.4	4.6
COP	2.84	3.49	3.69
Entering Liquid Temp °C	12.22	10.83	9.44
Leaving Liquid Temp. °C	6.67		
Liquid Flow l/s	1.48		
Entering Air Temp. °C	35	26.7	18.3
			12.8

3.2.1 Quasi-static model of the compressor cycling

During part load operation, the chiller is controlled by cycling its two compressors in order to maintain a set point on the leaving water temperature.

This control is simulated in the following way:

- when only one compressor is working, the leaving water temperature is $t_{w,ex,ev,1}$;
- when two compressors are working, this temperature is $t_{w,ex,ev,12}$;
- when no compressor is working, the water leaving temperature is the entering water temperature $t_{w,su,ev}$.

These three temperatures must be weighted to reach (if there is enough available capacity) the water leaving temperature set point. The working time fractions $\theta_{cp,1}$ and $\theta_{cp,2}$ of the two compressors are calculated by solving successively the two following equations:

$$\theta_{cp,2} = \text{MAX}\left[0, \text{MIN}\left(1, \frac{T_{w,ex,ev,set} - T_{w,ex,ev,1}}{T_{w,ex,ev,12} - T_{w,ex,ev,1}}\right)\right] \quad (3-6)$$

$$\theta_{cp,1} = \text{MIN}\left[1, \frac{T_{w,ex,ev,set} - T_{w,su,ev}}{T_{w,ex,ev,1} - T_{w,su,ev}}\right] \quad (3-7)$$

The achieved leaving water temperature is given by:

$$T_{w,ex,ev} = (1 - \theta_{cp,1})T_{w,su,ev} + \theta_{cp,1}((1 - \theta_{cp,2})T_{w,ex,ev,1} + \theta_{cp,2}T_{w,ex,ev,12}) \quad (3-8)$$

The cooling capacity is given by:

$$\dot{Q}_{ev} = (1 - \theta_{cp,2})\theta_{cp,1}\dot{Q}_{ev,1} + \theta_{cp,2}\dot{Q}_{ev,12} \quad (3-9)$$

The compressor consumption, the fan consumption, the total consumption and the COP are given by:

$$\dot{W}_{cp} = \theta_{cp,1}((1 - \theta_{cp,2})\dot{W}_{cp,1} + \theta_{cp,2}\dot{W}_{cp,12}) \quad (3-10)$$

$$\dot{W}_{fan} = \theta_{cp,1} ((1 - \theta_{cp,2}) \dot{W}_{fan,1} + \theta_{cp,2} \dot{W}_{fan,12}) \quad (3-11)$$

$$\dot{W}_{tot} = \dot{W}_{cp} + \dot{W}_{fan} + \dot{W}_{aux} \quad (3-12)$$

$$COP = \frac{\dot{Q}_{ev}}{\dot{W}_{tot}} \quad (3-13)$$

3.2.2 Fan control

According to manufacturer submittal, condenser fan motors are automatically cycled in response to the condenser pressure by a standard method of head pressure control. The second fan cycles in order to maintain the head pressure, which allows the unit to run at low ambient air temperature down to 1.7°C. The first fan modulates its motor speed in response to condenser pressure, which allows the unit to operate down to -18°C.

This control could be described by the following set of equations. The fan control variable is proportional to the difference between the actual condensing temperature and the condensing temperature set point

$$X_{contr,fan} = MAX(0, gain_{fan}(t_{cd} - t_{cd,set})) \quad (3-14)$$

The air flow rate through the condenser is adjusted by means of the control variable

$$\dot{V}_{a,cd,set} = \dot{V}_{a,cd,min} + (\dot{V}_{a,cd,max} - \dot{V}_{a,cd,min}) X_{contr,fan} \quad (3-15)$$

However, the air flow rate is limited by a maximal value:

$$\dot{V}_{a,cd} = MIN(\dot{V}_{a,cd,set}, \dot{V}_{a,cd,max}) \quad (3-16)$$

The fan capacity fraction is defined as

$$x_{fan} = \frac{\dot{V}_{a,cd}}{\dot{V}_{a,cd,n}} \quad (3-17)$$

The total fan consumption is the summation of the consumption of each fan

$$\dot{W}_{fan} = \dot{W}_{fan,1} + \dot{W}_{fan,2} \quad (3-18)$$

Since the first one is a variable speed fan, its consumption varies with its capacity fraction $x_{fan,1}$ according to

$$\dot{W}_{fan,1} = x_{fan,1}^3 \dot{W}_{fan,n} \quad (3-19)$$

Since the second fan cycles, its consumption can be expressed as a function of its capacity fraction $x_{fan,2}$ (here defined as the working time fraction of the fan) according to

$$\dot{W}_{fan,2} = x_{fan,2} \dot{W}_{fan,n} \quad (3-20)$$

The control variables of both fans are defined by

```

if (2 xfan ≤ 1),
    xfan,1=2 xfan
    xfan,2=0
else
    xfan,1=1
    xfan,2=2 xfan-1
end

```

(3-21)

The prediction by the model of the electrical consumption at part load is shown in Figure 3-10. It appeared that the best agreement was found for a fan operating all the time at its

nominal volume flow rate ($x_{fan}=1$), i.e. without control. However, it is not known how these points are defined by the manufacturer.

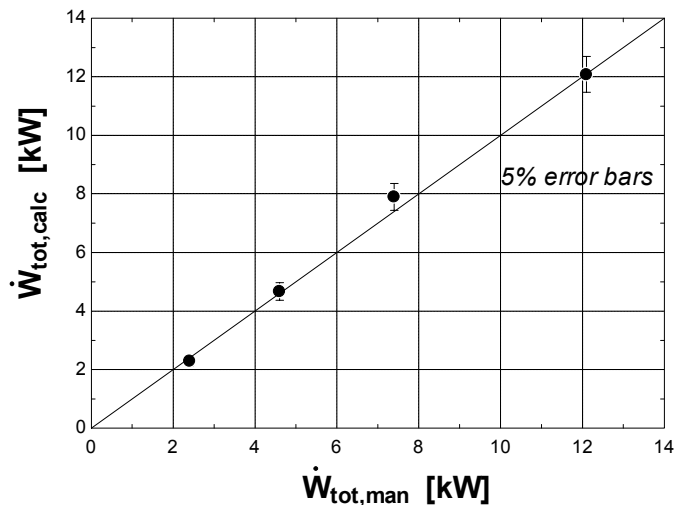


Figure 3-10 : Prediction by the model of the chiller total consumption (compressors + fans) at part load

3.3 Influence of glycol concentration on the chiller performances

Chiller capacity is reduced when glycol is added to the water. This is taken into account in the model by re-identifying the water-side nominal resistance in the evaporator model.

Adjustment factors given by the manufacturer for the use of (propylene) glycol is given in Table 3-6. These factors give an estimate of the cooling capacity increase, electrical consumption decrease and mass flow rate decrease. It is assumed that these values correspond to ARI conditions (entering air temperature: 35°C, leaving water temperature: 6.67, temperature difference over the evaporator: 5.55 K).

Table 3-6 : Adjustment factors for use of propylene glycol and anti-freeze fluids

Glycol [%]	$X_Q = \frac{\dot{Q}_{ev}}{\dot{Q}_{ev,n}}$	$X_W = \frac{\dot{W}_{cp}}{\dot{W}_{cp,n}}$	$X_M = \frac{\dot{M}_{w,ev}}{\dot{M}_{w,ev,n}}$
10	0.987	0.992	1.01
20	0.975	0.985	1.028
30	0.962	0.978	1.05
40	0.946	0.971	1.078
50	0.929	0.965	1.116

The correction factor $K_{w,ev}$ on the water-side resistance (defined in Equation (3-22)) has been identified by imposing the adjustment factor X_Q given in Table 3-6 as an input of the chiller model.

$$R_{w,ev} = R_{w,ev,n} K_{w,ev} \left(\frac{\dot{M}_{w,ev,n}}{\dot{M}_{w,ev}} \right)^{0.8} \quad (3-22)$$

Evolution of the water-side resistance correction factor with the glycol concentration is given in Figure 3-11. It can be observed that the water-side resistance only increases by 15% when adding 20% in mass of glycol in the water (concentration of glycol for the experimental study presented in §4). Figure 3-12 shows that the adjustment factor for the mass flow rate is fairly well predicted (assumption of the 5.55K temperature difference over the evaporator is plausible). By contrast, the reduction in the chiller electrical consumption predicted by the model is lower than the one given in Table 3-6.

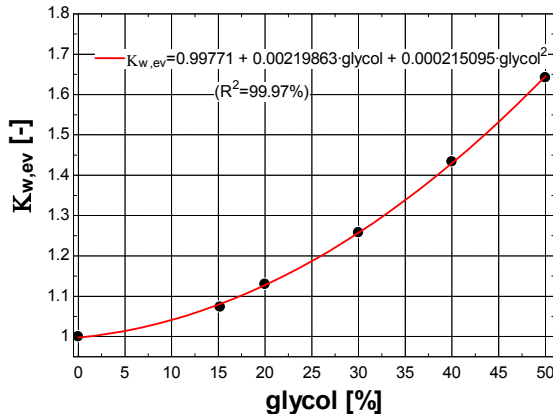


Figure 3-11 : Evolution of the correction factor on the water-side resistance with the glycol concentration

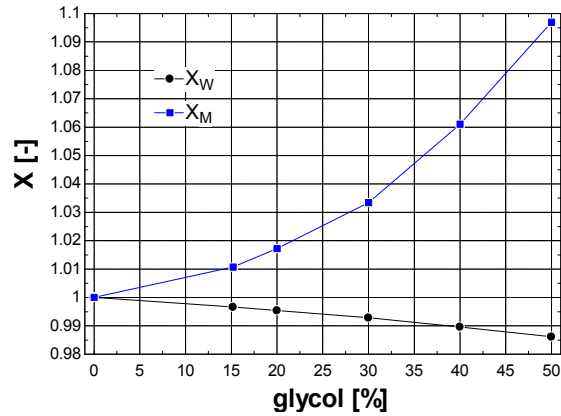


Figure 3-12 : Evolution of the reduction factors for the chiller electrical consumption and the water mass flow rate with the glycol concentration

3.3.1 Summary

Results of the identification of the chiller model parameters based on published manufacturer data can be summarized as follows. The compressor model parameters can be accurately identified using the compressor performance points.

Parameters of the evaporator and the condenser have been identified using only one of the chiller performance points and introducing rational assumptions about heat transfer resistances. Predictions by the model of the compressor consumption, cooling capacity and total electrical consumption agree very well with manufacturer data.

For full load and part load operation, the best agreement between the model's predictions and the measurements is found when imposing the fan to operate at its maximum capacity. Available manufacturer data has not allowed the identification of the fan control model's parameters.

4 EXPERIMENTAL INVESTIGATION

4.1 Simulation with model parameters identified with manufacturer data

4.1.1 Description of the simulation

A simulation has been carried out using the model with its parameters identified based on manufacturer data (see §3). The goal of this empirical test is to predict chiller cooling power,

electric power consumption as well as the temperature of glycol water leaving the chiller. Input data come from an experiment which was conducted at the ERS from August 8-23, 2006 and divided in 4 periods of time. For convenience, the thesis will only compare simulation results with empirical data for the first period of time (August 8-11, 2006). This simulation period corresponds to the *Empirical Test II Cold Dry*² of the IEA-ECBCS Annex 43, Subtask D, Chiller Exercise (Felsmann, 2008).

The chilled water temperature is set at 4.4°C (40°F) and the chilled water pump speed is kept constant. Brine is an aqueous solution of propylene glycol 18% in mass. Glycol water flow rate was around 5.5m³/h (24.3gpm).

The inputs of the simulation are the number of working compressors (0, 1 or 2), the glycol water flow rate, the evaporator supply glycol water temperature and the condenser supply air temperature. In the initial exercise (Felsmann, 2008) the exhaust glycol water temperature was imposed as an input, instead of the number of working compressors. However, in order to better analyze what causes the predictions by the model to deviate from the measurements, it appears to be more convenient not to represent the chiller control. The number of working compressors can be easily identified from the measurement of the chiller power consumption (Figure 4-1).

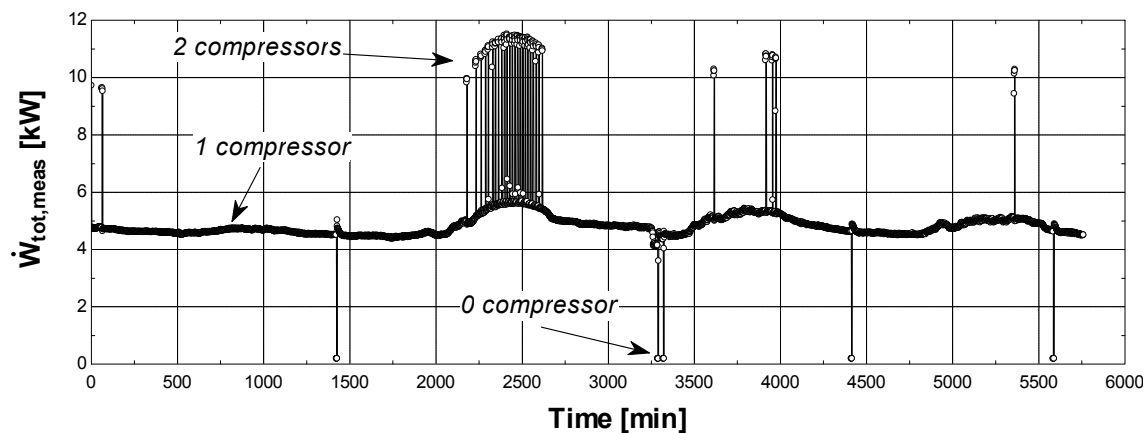


Figure 4-1 : Time evolution (minute by minute) of the measured chiller power consumption (Empirical Test II Cold dry)

² “Cold dry” refers to the conditions of the air entering the cooling coil. This cooling coil was tested successively cold dry, hot dry, hot humid and cold humid.

Since it was not possible to identify the parameters of the fan control model based only on manufacturer data, the simulation is carried out by imposing the number of fans (1 fan for the entire simulation, since according to measurements only 1 fan was in operation), operating at maximum capacity ($x_{fan}=1$).

The outputs of the simulation are the exhaust glycol water temperature, the exhaust air temperature, the compressors consumption and the fan consumption. Parameters of the chiller model are those presented in §3. A simulation is carried out on a period of 5760 minutes (August 8, 2006 to August 11, 2006). The time step is one minute.

4.1.2 Simulation results

The total cooling and electrical energies (integration of the cooling power and chiller electrical consumption over the entire simulation period) measured and predicted by the model are shown in Figure 4-2. Deviation between measurements and model prediction is 27.8% for the cooling energy and 5.2% for the electrical energy.

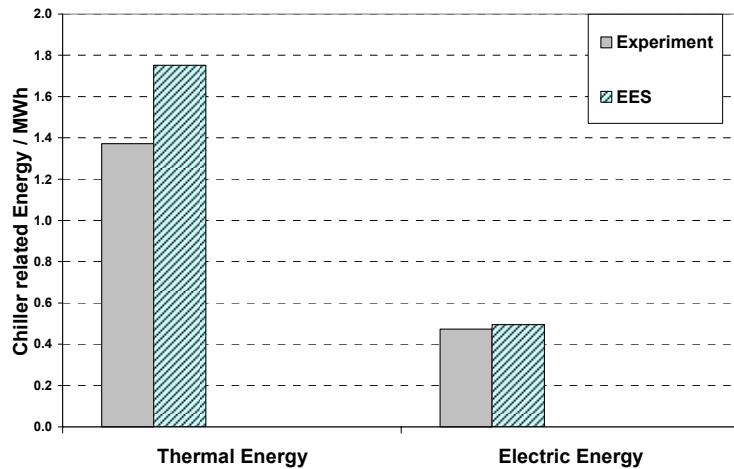


Figure 4-2 : Chiller Total cooling and electrical energies (parameters identified based on manufacturer)

The total electrical consumption is fairly well predicted by the model. However, the model with its parameters identified based on manufacturer data appears to not predict correctly the cooling power. The objective of the next paragraph is to identify the underlying reasons.

4.2 Identification of the model parameters based on quasi-steady state points extracted from experimental data

4.2.1 Definition of quasi-steady state points

In order to allow a better identification of the chiller model parameters, 10 quasi-steady state points have been extracted from experimental data. These points correspond to quasi-stabilized air and water temperatures. To increase the accuracy of the heat balances across the evaporator and the condenser, points characterized by large enough supply/exhaust temperature differences are selected. For each of the 10 points, measurements are averaged over a period of 5 minutes. These 10 points are given in Table 4-1.

Three of these points are indicated in Figure 4-3, Figure 4-4 and in Figure 4-5 by the vertical red line. They have been extracted from the measurements conducted over the period August 8-11, 2006. The 7 other points have been extracted from the measurements conducted over the period August 12-23, 2006 and are described in the Appendix.

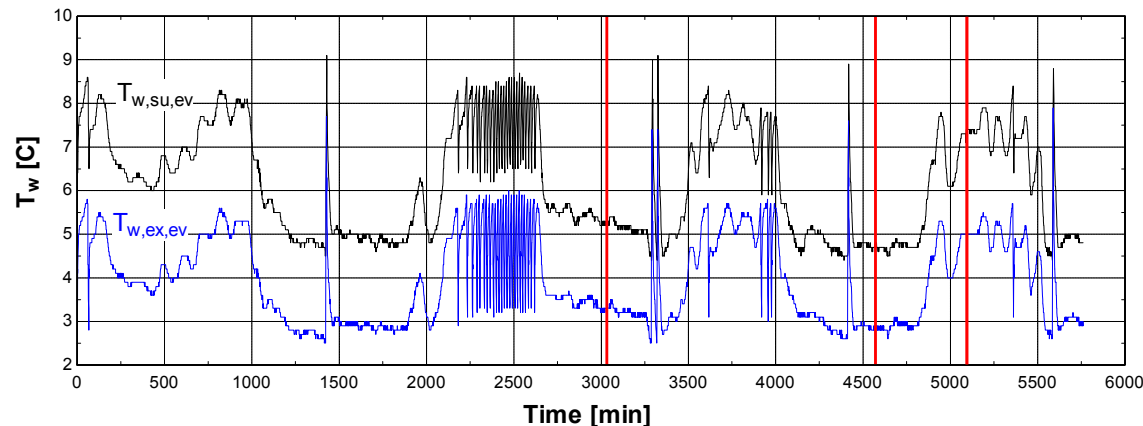
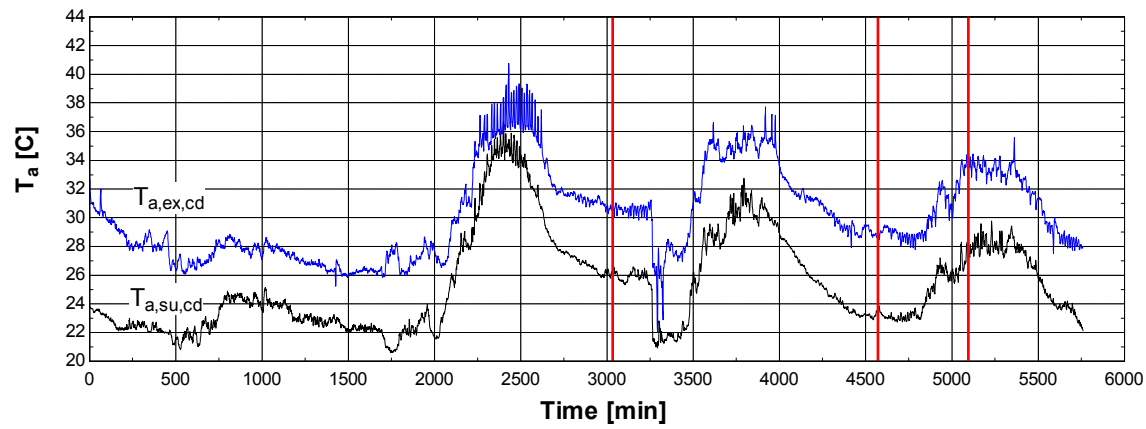
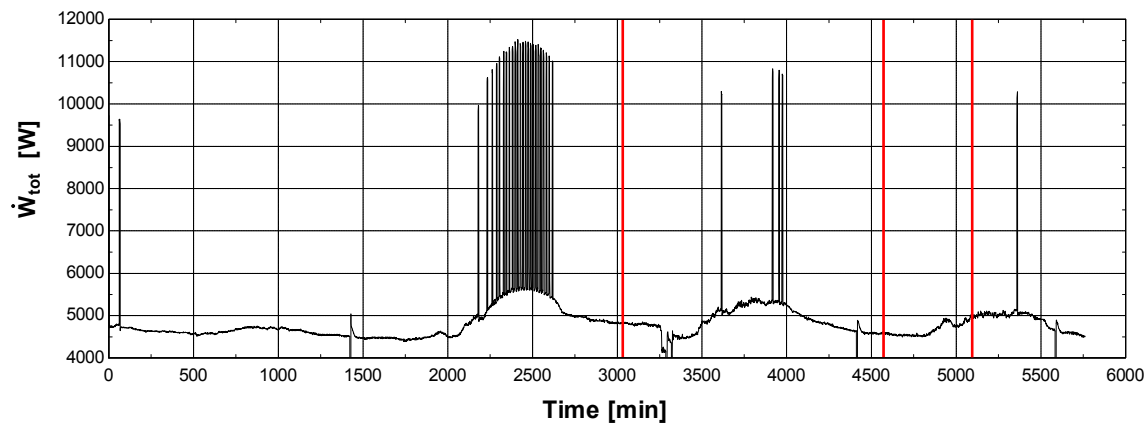


Figure 4-3 : Time evolution of the evaporator measured glycol water supply and exhaust temperatures (Empirical test II Cold Dry)



**Figure 4-4 : Time evolution of the condenser measured air supply and exhaust temperatures
(Empirical test II Cold Dry)**



**Figure 4-5 : Time evolution of the measured chiller electrical consumption (Empirical test II
Cold Dry)**

Table 4-1: Quasi-steady points extracted from experimental data

	P_{atm}	P_{cd}	P_{ev}	$T_{a,ex,cd}$	$T_{a,su,cd}$	$T_{w,ex,ev}$	$T_{w,su,ev}$	$\dot{V}_{w,ev}$	\dot{W}_{fan}	\dot{W}_{tot}	$w_{su,cd}$
	[kPa]	[kPa]	[kPa]	[C]	[C]	[C]	[C]	[l/s]	[W]	[kW]	[kg/kg]
1	98.67	1241.0	412.3	27.8	20.2	3.6	5.9	1.592	460.5	4.534	0.01036
2	98.29	1240.0	407.6	29.0	23.3	2.9	4.8	1.615	494.9	4.581	0.01547
3	98.94	1233.0	416.5	27.0	20.1	4.1	6.7	1.609	492.9	4.540	0.013
4	98.48	1349.0	429.0	34.2	27.8	5.0	7.4	1.597	652.4	4.987	0.01405
5	98.56	1256.0	419.9	28.1	21.7	4.1	6.6	1.611	526.4	4.616	0.01238
6	97.96	1304.0	415.1	30.9	26.0	3.3	5.3	1.614	587.2	4.818	0.01809
7	98.6	1452.0	396.9	32.8	25.0	3.3	7.3	1.562	861.5	9.792	0.01302
8	98.75	1624.0	410.0	38.8	31.6	3.5	7.2	1.559	1002	10.730	0.01075
9	98.82	1684.0	413.4	40.0	33.0	3.5	7.2	1.572	1005	11.080	0.01294
10	98.07	1754.0	417.9	41.7	34.9	3.7	7.3	1.572	1002	11.430	0.01334

The measured cooling power can be evaluated based on measurement of the glycol water flow rate and the evaporator supply and exhaust glycol water temperatures:

$$\dot{Q}_{ev,meas} = \dot{M}_{glw,meas} \cdot c_{glw} \cdot (T_{glw,su,ev,meas} - T_{glw,ex,ev,meas}) \quad (4-1)$$

There is no measurement of the air flow rate through the condenser. The heat rejected at the condenser is roughly estimated by a heat balance over the chiller (Equation (4-2)). The two first terms of this equation are measurements, while the last term is determined by the compressor model.

$$\dot{Q}_{cd,meas} = \dot{Q}_{ev,meas} + \dot{W}_{cp,meas} - \dot{Q}_{amb,cp,tot} \quad (4-2)$$

Condenser supply and exhaust air temperatures are the average of four RTD sensors located at the condenser inlet and outlet respectively. The air flow rate through the condenser is estimated by:

$$\dot{M}_{a,\text{meas}} = \frac{\dot{Q}_{cd,\text{meas}}}{c_{p,a,cd} (T_{a,ex,cd,\text{meas}} - T_{a,su,cd,\text{meas}})} \quad (4-3)$$

4.2.2 Verification of the compressor consumption

The compressors are “dissociated” from the heat exchangers by imposing the evaporating and the condensing pressures as inputs of the simulation. Parameters of the compressor model are those given in Table 3-4. Comparison between the compressor electrical consumption predicted by the model and the measured one is given in Figure 4-6. Deviation between the prediction by the model and the measurements is lower than 5%.

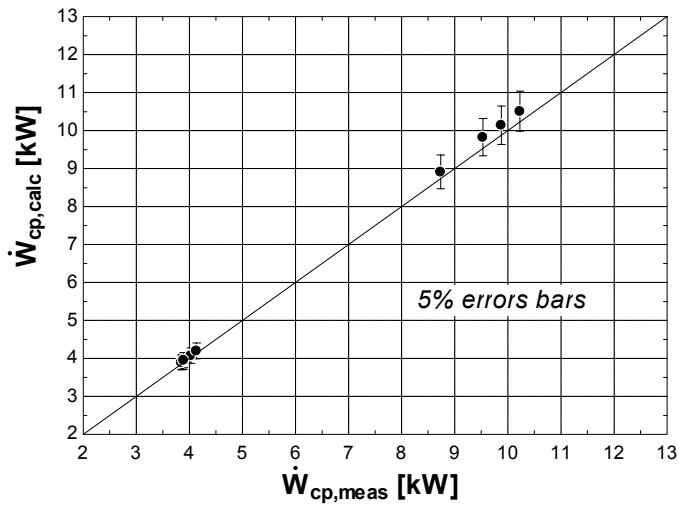


Figure 4-6 : Verification of the compressor electrical consumption (with parameters identified based on manufacturer data)

4.2.3 Verification of the cooling power

Figure 4-7 compares the cooling power predicted by the model with the measured cooling power (Equation (4-1)). The evaporating pressure and the condensing pressure are still imposed as inputs of the simulation. As anticipated by Figure 4-2, deviations between the prediction by the model and the measurements are very large.

These deviations cannot be explained by heat accumulation in the evaporator. For the point encircled in Figure 4-7, the deviation is approximately 10 kW. If the evaporator is

represented by a mass of steel of 20 kg, this would give a rate of increase of the evaporator temperature of approximately 1 K/s. Such a temperature variation rate would be detectable in the evolution of the glycol water temperatures. Figure 4-8 displays the time evolution of the glycol water supply and exhaust temperatures for the period of time around the point encircled in Figure 4-7. It can be observed that the temperatures are quasi-stabilized.

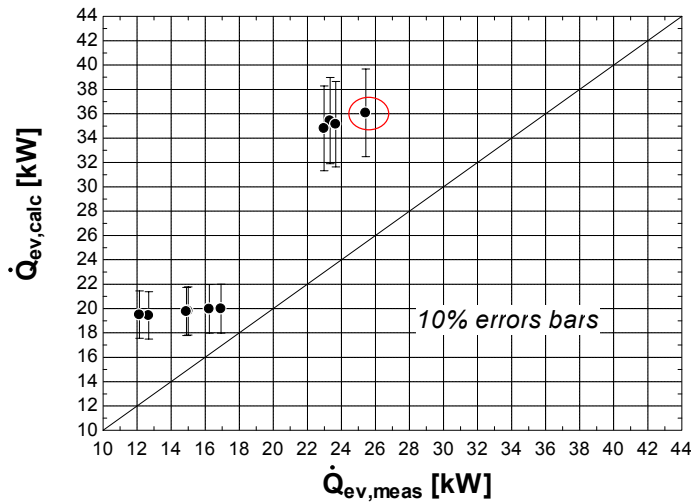


Figure 4-7 : Verification of the chiller cooling power (with parameters identified based on manufacturer data)

Figure 4-8 and Figure 4-9 also show the control strategy for the compressors. This control strategy is described in the Appendix. The number of compressor cycles in order to maintain the evaporator glycol water exhaust temperature around a set point (4°C).

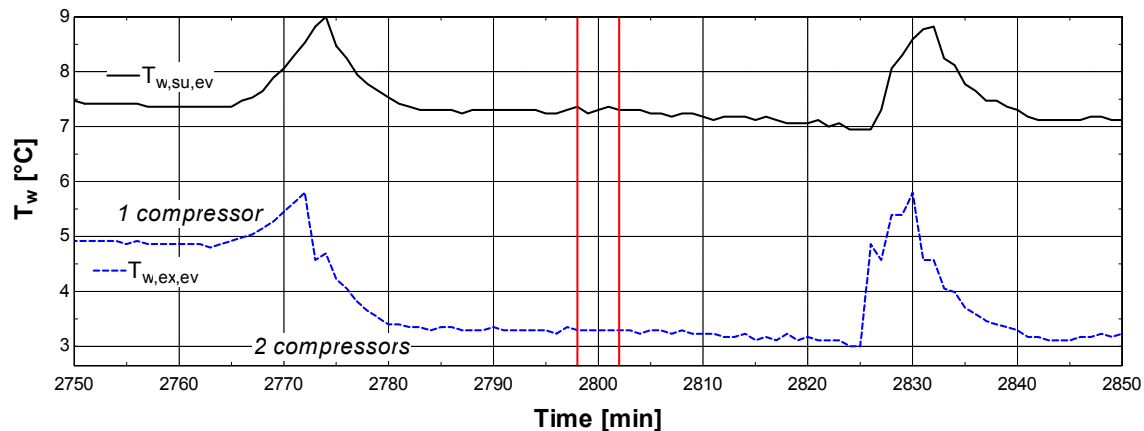


Figure 4-8 : Time evolution of the evaporator measured glycol water supply and exhaust temperatures

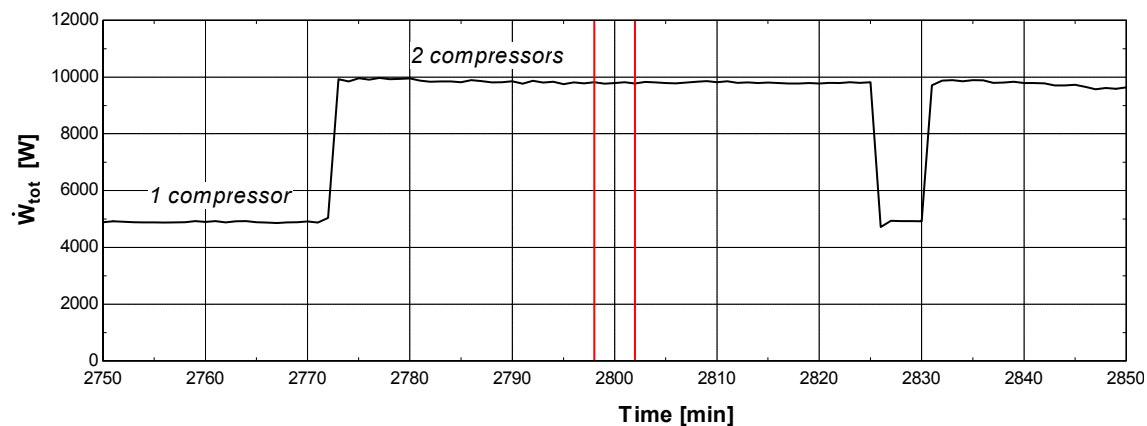


Figure 4-9 : Time evolution of the chiller measured electrical consumption

The time evolution of the condenser air supply and exhaust temperatures is given in Figure 4-10. As mentioned previously, in order to increase the accuracy of the energy balance given in Equation (4-3), points characterized by a large supply-exhaust temperature difference has been selected.

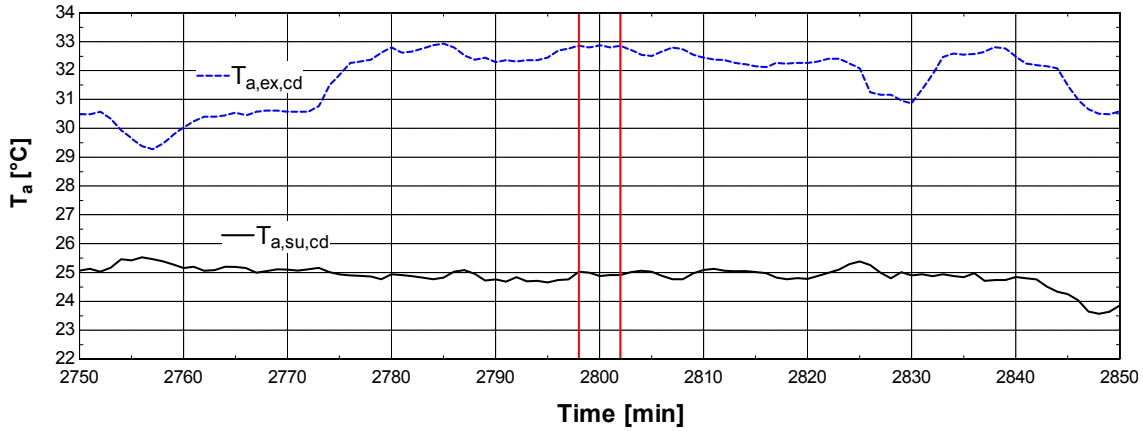


Figure 4-10 : Time evolution of the condenser measured air supply and exhaust temperatures

Higher leakage area

Since we are confident on the information about the number of compressor in use, the first explanation for this large discrepancy was that the *compressor internal leakage* area is larger than that identified based on manufacturer data (due to aging of the compressor). Results of a simulation with a much larger leakage area (4.6 mm^2 instead of 0.599 mm^2) are given in Figure 4-11 and Figure 4-12. It can be observed that the compressor electrical consumption is still predicted with a very good accuracy and the cooling power is now predicted within 10%. However, such a large increase of the internal leakage seems unlikely.

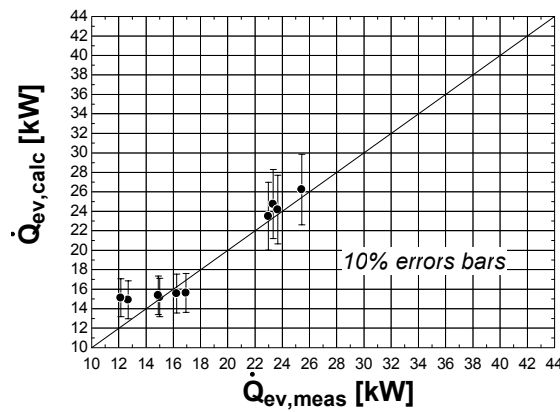


Figure 4-11 : Verification of the chiller cooling power (with a larger compressor leakage area)

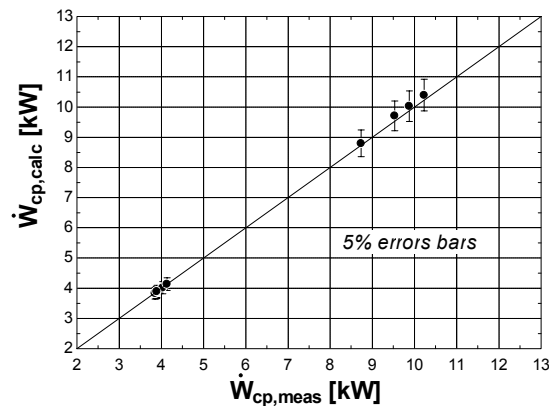


Figure 4-12 : Verification of the compressor electrical consumption (with a larger compressor leakage area)

Hot gas bypass

The second explanation might be that the *hot gas bypass* (HGBP) of the condenser is in use. HGBP is used to maintain the compressor supply pressure above a minimal value by bypassing hot gas from the compressor exhaust to the evaporator supply. This system prevents evaporator frosting and compressor flooding and excessive cycling at low load operation (down to 10% of unit full load) (Solberg and Bradley, 2003). Also, it maintains the refrigerant velocity in the evaporator high enough for proper oil return to the compressor. Finally, it allows instantaneous matching between chiller capacity and cooling load. In the case of the chiller investigated in this chapter, the HGBP valve is pressure-actuated, which means that its opening increases with the difference between the valve's suction pressure setpoint and the actual suction pressure. The pressure at which the valve begins opening is a function of the temperature the bulb is sensing (the bulb is represented in Figure 2-3). The valve is factory-set to begin opening at 58 psig (400 kPa gauge) when the air-charge bulb is in a 26.67°C ambient temperature.

The time evolution of the compressor supply pressure (gauge) for the *Empirical Test II Cold Dry* is shown in Figure 4-13. The supply pressure is constantly maintained above 400 kPa. Incursions below 400 kPa correspond to the shut-down of the last compressor. The evolution of the pressure shown in this figure tends to confirm that the hot gas bypass is actually working in order to maintain the compressor supply pressure above the lower limit (approximately 400 kPa).

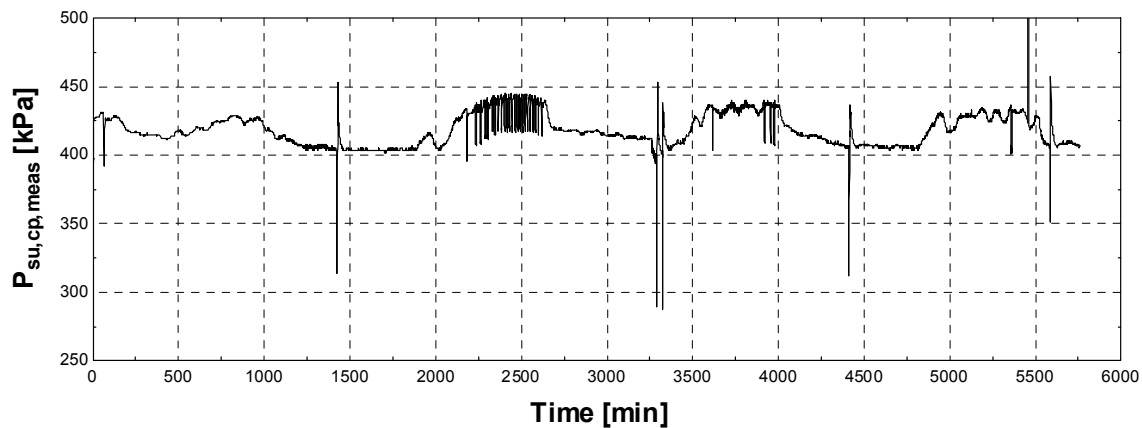


Figure 4-13 : Time evolution of the compressor measured supply pressure (gauge) (Empirical Test II Cold Dry)

The mass flow rate bypassing the condenser can be calculated by equaling the cooling capacities predicted by the model and measured. Saturation pressures are still imposed as input of the simulation. Equations of conservation of mass and energy describing the hot gas bypass are

$$\dot{M}_{r,cd} h_{r,ex,cd} + \dot{M}_{r,bp} h_{r,ex,cp} = \dot{M}_{r,ev} h_{r,su,ev} \quad (4-4)$$

$$\dot{M}_{r,cd} + \dot{M}_{r,bp} = \dot{M}_{r,ev} \quad (4-5)$$

The fraction of gas bypassing the condenser is defined as

$$X_{bp} = \dot{M}_{r,bp} / \dot{M}_{r,ev} \quad (4-1)$$

The time evolution of the identified mass fraction of bypass gas for Empirical Test II Cold Dry is shown in Figure 4-14. The evolution of the evaporator glycol water supply temperature is shown in the same figure. The fraction of bypass gas increases when the return water temperature decreases (reduction of the cooling capacity) and inversely.

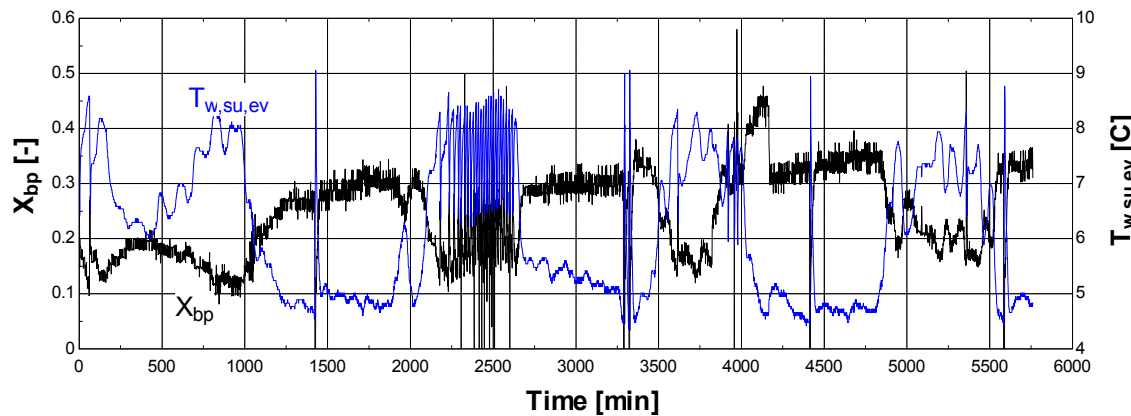


Figure 4-14 : Time evolution of the fraction of hot gas bypassed and of the evaporator measured supply water temperature (Empirical Test II Cold Dry)

The evolution of the mass fraction of gas bypassing the condenser with the pressure difference between the exhaust and the supply of the compressor is shown in Figure 4-15, for the 10 quasi steady state points extracted from manufacturer data. Up to 30% of the refrigerant mass flow rate is bypassing the condenser, which is consistent with the deviation between model's predictions and measurements shown in Figure 4-2 and Figure 4-7. Since the compressor supply and exhaust pressures are still imposed as inputs of the simulation, the predicted compressor electrical consumption is the one shown in Figure 4-6.

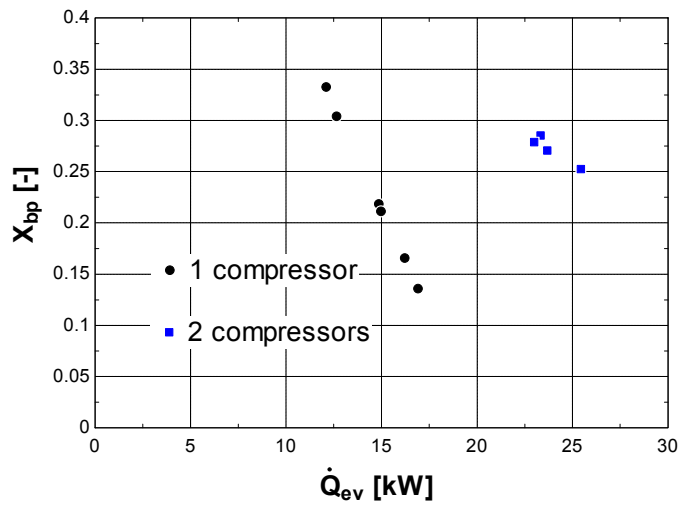


Figure 4-15 : Evolution of bypass mass flow rate fraction with the cooling power

4.2.4 Fan control and electrical consumption

The evolution of the measured fan electrical consumption with the condensing pressure (more precisely, the pressure at the compressor exhaust) is shown in Figure 4-16. In the available measurement data, only one fan is working (the variable speed one). Evolution of the measured electrical consumption indicates that above approximately 1600 kPa (gauge) the fan is operating at maximum speed, while below 1600 kPa it reduces its speed.

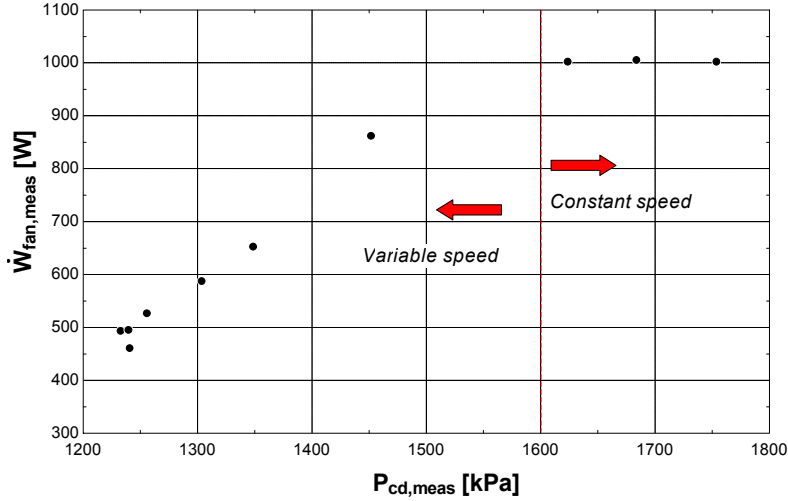


Figure 4-16 : Evolution of the measured fan electrical consumption with the condensing pressure (gauge)

The evolution of the measured air volume flow rate with the condensing pressure is shown in Figure 4-17. The measured air volume flow rate (defined at the condenser exhaust) is the product of the measured air mass flow rate (Equation (4-3)) and the air specific volume at the condenser exhaust. The evolution shown in Figure 4-17 is consistent with Figure 4-16: the volume flow rate is increasing with the condensing pressure, due to the increase of the fan speed. The maximal volume flow rate (for pressure higher than 1600 kPa) is around $4 \text{ m}^3/\text{s}$. This value is of the same order of magnitude as the nominal volume flow rate given by the manufacturer ($11850 \text{ m}^3/\text{h}$, i.e. $3.30 \text{ m}^3/\text{s}$), which tends to confirm that the air flow rate through the condenser is correctly estimated. At this point, it should be stressed that the “measured” air flow rate is roughly estimated by a heat balance and not directly measured. However the identified evolution of the measured air flow rate is consistent with the fan consumption. As shown in Figure 4-18, the fan consumption increases more or less linearly with the air volume flow rate. At maximal fan speed (for pressure higher than 1600 kPa) the fan electrical consumption is close to 1000 W, what is close to the value identified based on manufacturer data (1100 W).

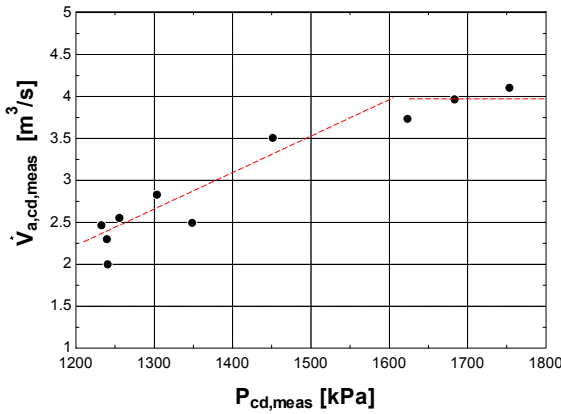


Figure 4-17 : Evolution of the measured air volume flow rate (defined at the condenser exhaust) with the condensing pressure (gauge)

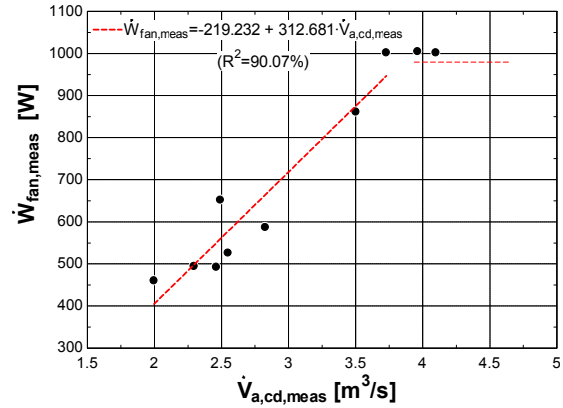


Figure 4-18 : Evolution of the fan electrical consumption with the air volume flow rate (defined at the condenser exhaust)

Parameters of the fan control model introduced in §3.2 can be roughly estimated from the 10 quasi-steady state points. This is shown in Figure 4-19, which gives the evolution of the fan control variable with the difference between the actual condensing temperature and the condensing temperature set point (for the points where the fan is not working at maximum speed). For an arbitrary condensing temperature set point of 25°C, the identified gain is 0.0500566 K^{-1} .

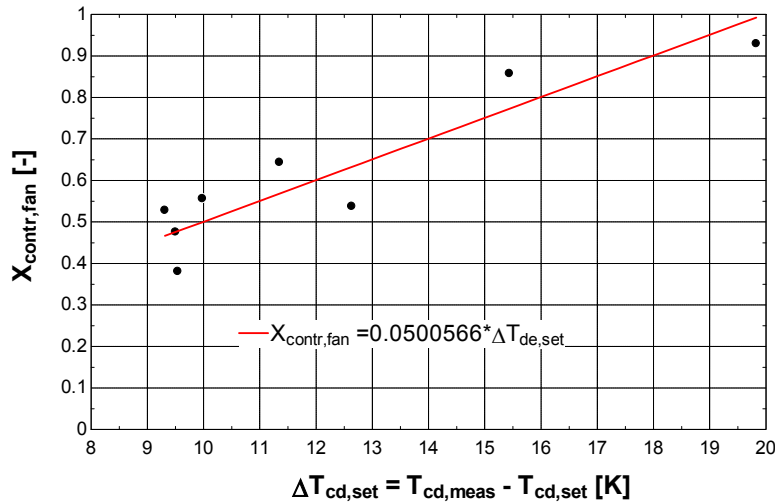


Figure 4-19 : Evolution of the fan control variable with the difference between the condensing temperature and condensing temperature set point (arbitrarily set to 25°C)

4.2.5 Identification of the heat exchangers resistances

The Wilson-plot method (Wilson, 1915) can be used to approximate the evaporator refrigerant-side resistance. This method consists in plotting the overall heat transfer resistance as a function of $\dot{M}_{r,ev}^{-n}$ for a constant glycol water mass flow rate \dot{M}_{glw} . Provided the exponent n is chosen correctly, the points should fall on a straight line.

From the 10 experimental points, 7 points with similar glycol water flow rates (ranging 1.592 to 1.646 kg/s) are extracted. They are characterized by refrigerant flow rates ranging from 0.1143 to 0.2238 kg/s (with two main groups of points, corresponding to either 1 or 2 working compressors). The evolution of the overall heat transfer resistance with $\dot{M}_{r,ev}^{-0.8}$ for these points is given in Figure 4-20. Two sources of information can be drawn from the Wilson-plot method:

1. If the line is extrapolated to $\dot{M}_{r,ev}^{-0.8} = 0$ ($\dot{M}_r \rightarrow \infty, R_{r,ev} \rightarrow 0$), the intersection with the R-axis gives the value of the metal plus water-side resistance ($R_{w,ev} + R_{m,ev}$). Drawing a linear regression, the metal plus water-side resistance appears to be close to 0.0000964881 K/W. For a nominal water flow rate of 1.616 kg/s (average value for the 7 points), the nominal water-side resistance is given by

$$R_{w,ev,n} = \frac{0.0000964881}{K_{w,ev}} = \frac{0.0000964881}{1.107} = 0.00008716 \text{ [K/W]} \quad (4-6)$$

The correction factor $K_{w,ev}$ (to account for the glycol) is given in Figure 3-11.

The range of water mass flow rates is not wide enough to identify clearly any dependency between this total resistance and the water mass flow rate. Consequently, it is not possible to distinguish between the water-side and metal resistance. Moreover, for a plate heat exchanger, the metal resistance is usually negligible compared to the two other resistances. Hence, the metal resistance is imposed to 0 and the water-side resistance to 0.00008716W/K.

2. The nominal refrigerant-side resistance can be identified from the slope of the linear regression:

$$R_{r,ev,n} = \frac{0.0000265094}{\dot{M}_{r,ev,n}^{0.8}} = 0.00008931 \text{ [K/W]} \quad (4-7)$$

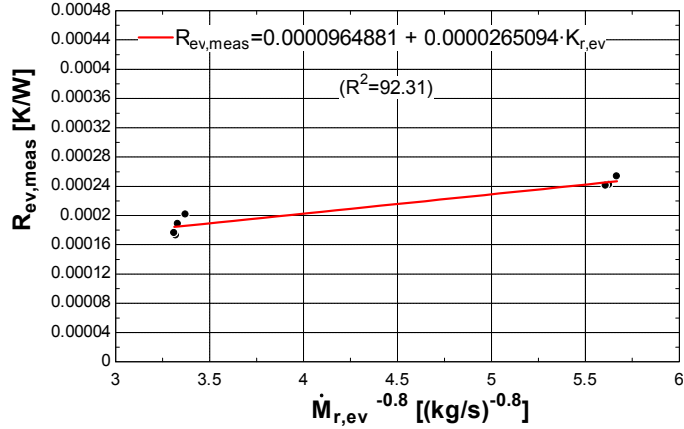


Figure 4-20 : Wilson plot method applied to the evaporator

There are not enough points characterized by similar air flow rate to accurately determine the condenser refrigerant side resistance by means of the Wilson plot method. The three resistances of the condenser model are tuned to get the best agreement between the measurements and prediction by the model for the condensing pressure. Identified resistances are given in Table 4-2.

Comparison between predictions by the model and measurements for the *evaporating* and *condensing* pressures are shown in Figure 4-21 and Figure 4-22. Both pressures are predicted within 5%.

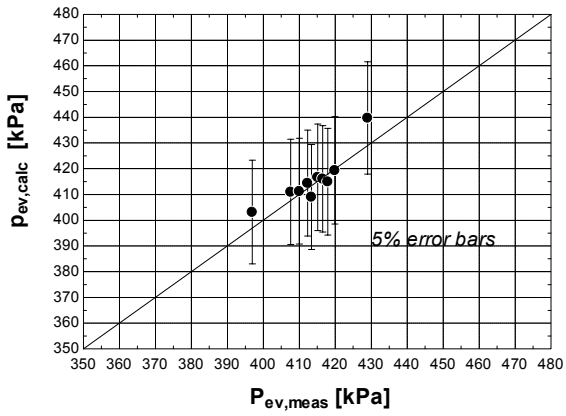


Figure 4-21 : Prediction of the evaporating pressure

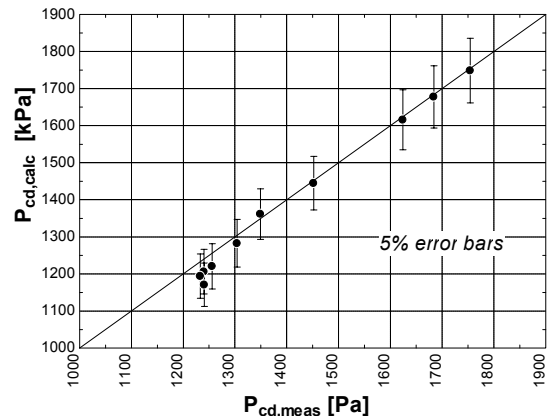


Figure 4-22 : Prediction of the condensing pressure

4.2.6 Validation of the model for the quasi-steady state points

The hot gas bypass is described by means of a quasi-static model similar to the fan control model. Equations governing its modeling are given hereunder. The hot gas bypass control is proportional to the difference between the evaporating pressure (compressor supply pressure) set point and the actual evaporating pressure

$$X_{\text{contr,bp}} = \text{MAX}(0, \text{gain}_{\text{bp}}(P_{\text{ev,set}} - P_{\text{ev}})) \quad (4-8)$$

The fraction of bypass gas is adjusted by means of the bypass control variable

$$X_{\text{bp,set}} = X_{\text{bp,min}} + (X_{\text{bp,max}} - X_{\text{bp,min}})X_{\text{contr,bp}} \quad (4-9)$$

$$X_{\text{bp}} = \text{MIN}(X_{\text{bp,set}}, X_{\text{bp,max}}) \quad (4-10)$$

The gain in Equation (4-8) is adjusted in order to get a good agreement between model predictions and measurements for the cooling power. The identified gain is $0.000006132 \text{ Pa}^{-1}$. Predictions of the cooling power and the compressor consumption are shown in Figure 4-23 and Figure 4-24. With this simple model of the hot gas bypass control, the cooling power is predicted within 10% (for most of the points) and the compressor consumption within 5%.

Note that the disagreement for the compressor consumption is mainly due to inaccuracies in the prediction of the compressor supply pressure.

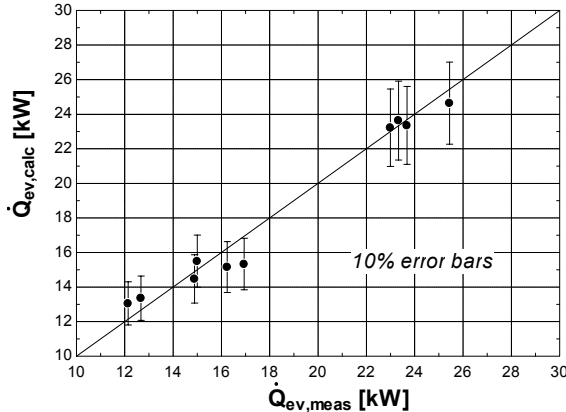


Figure 4-23 : Prediction of the cooling power

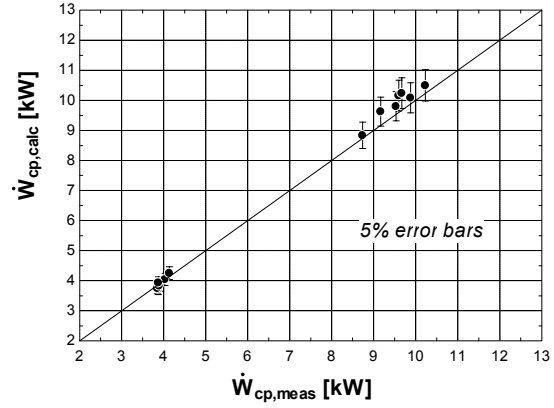


Figure 4-24 : Prediction of the compressors electrical consumption

Figure 4-25 compares the air volume flow rate predicted by the model to the measured one. Both predicted and measured flow rates are given as function of the measured condensing pressure. It can be observed that the model correctly predicts the high air flow rates (close to the maximal fan speed) and only roughly estimates the air flow rate for lower fan speeds, but predicts correctly the trend. Comparison between predicted and measured fan electrical consumption is shown in Figure 4-26. Deviations between the prediction and the measurements at lower fan speeds are due to discrepancies in the air flow rate predictions.

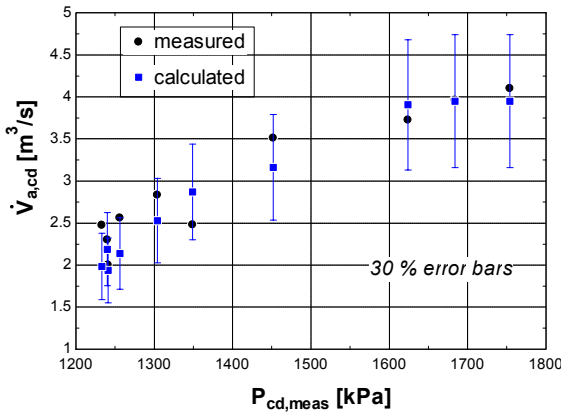


Figure 4-25 : Prediction of the air volume flow rate (defined at the condenser exhaust)

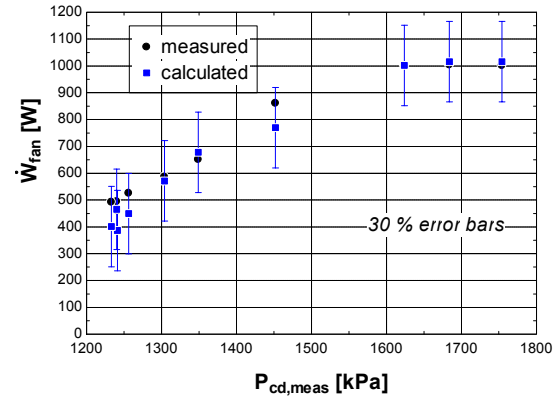


Figure 4-26 : Prediction of the fan electrical consumption

Parameters of the evaporator and the condenser models identified based on the 10 quasi steady state points extracted from experimental data are summarized in Table 4-2.

Table 4-2: Parameters of the evaporator and condenser models identified based on experimental data

	Evaporator	Condenser
$R_{w,ev,n}$	0.00005825 [K/W]	$R_{a,cd,n}$ 0.000095 [K/W]
$R_{m,ev}$	0 [K/W]	$R_{m,cd}$ 0.000095 [K/W]
$R_{r,ev,n}$	0.0001218 [K/W]	$R_{r,cd,n}$ 0.000095 [K/W]
$\dot{M}_{w,ev,n}$	1.608 [kg/s]	$\dot{M}_{a,cd,n}$ 7.201 [kg/s]
$\dot{M}_{r,ev,n}$	0.2191 [kg/s]	$\dot{M}_{r,cd,n}$ 0.2191 [kg/s]
$\Delta T_{oh,ex,ev}$	5 [K]	$\Delta T_{sc,ex,cd}$ 5 [K]
$gain_{bp}$	0.000006974 [Pa ⁻¹]	$\dot{W}_{fan,n}$ 1100 [W]
		\dot{W}_{aux} 200 [W]
		$gain_{fan}$ 0.0500924 [K ⁻¹]

4.3 Simulation with model parameters identification based on quasi-steady state points

The same simulation as in §4.1 is carried out with the chiller model parameters identified based on the 10 quasi steady state points. The number of working compressors is still imposed.

The total cooling and electrical energies (integration of the cooling power and chiller electrical consumption over the entire simulation period) measured and predicted by the model are shown in Figure 4-27. Deviation between measurements and model prediction is only 3.7 % for the cooling energy and 0.49 % for the electrical energy.

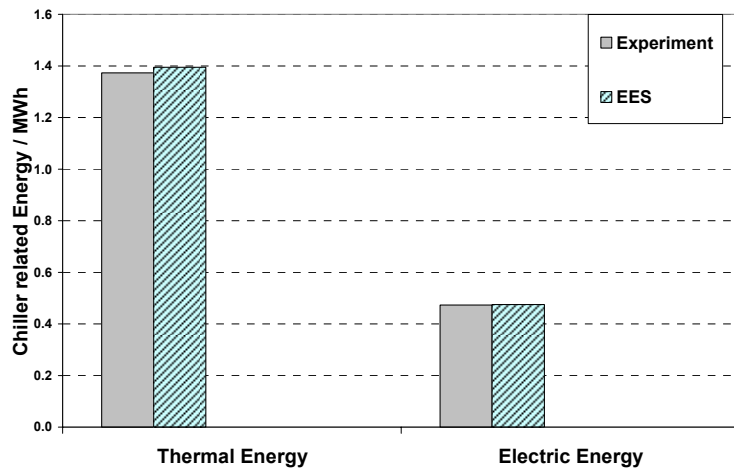


Figure 4-27 : Chiller Total cooling and electrical energies (parameters identification based on quasi steady state points)

5 CONCLUSIONS

This Chapter showed how the parameters of a chiller model can be identified based on published manufacturer data. This identification process can be achieved in two steps. First the compressor model parameters are identified using compressor's performance. Then the heat exchangers models parameters are identified on the basis of the chiller's performance. The only encountered difficulty was the characterization of the fan control model: information was lacking to identify its parameters.

An experimental investigation has been carried out on the same chiller, integrated into an existing cooling plant. Its instrumentation is mainly limited to simple measurements: the secondary fluids temperatures, the water flow rate, the compressor suction and discharge pressures and the chiller electrical consumption (with distinction between fan and compressors consumption). There is neither any measurement of the refrigerant flow rate, nor of the air flow rate through the condenser. The validated compressor model is “used” as a refrigerant flow meter and the air flow rate is determined by expressing the heat balance across the condenser.

Comparison between simulation and experimental data revealed that the chiller model with its parameters identified based on manufacturer catalog data was not able to correctly predict the cooling power (deviations up to almost 30%).

Detailed analysis of experimental data showed that the compressor model is able to correctly predict its electrical consumption.

Analysis of the chiller’s performance based on the 10 quasi steady-state points extracted from experimental data has allowed a better understanding of the chiller operation (fan control and Hot Gas Bypass) and a better identification of the model’s parameters.

The proposed fan control model is able to predict the air flow rate through the condenser and the fan electrical consumption with a good accuracy.

A simple but realistic model of the Hot Gas Bypass has been proposed. However, a more detailed model could be introduced in order to better predict the evaporating pressure and cooling power.

6 REFERENCES

- ARI Standard 550/590. 1998. Water Chilling Packages using the Vapor Compression Cycle, Air-Conditioning and Refrigeration Institute, 4301 North Fairfax Drive, Suite 425, Arlington, VA 22203, U.S.A.
- Cuevas, C., and J. Lebrun. 2008. Testing and modelling of a variable speed scroll compressor, *Applied Thermal Engineering*
- Felsmann, C. 2008. Mechanical Equipment & Control Strategies for a Chilled Water and a Hot Water System. A Report for the International Energy Agency's SHC Task 34/ECBCS Annex 43 Subtask D.
- Holmes, M. J. 1988. ECBCS Annex 10 Report, System Simulation, Heating and Cooling Coils.
- Jin, H., and J. Spitler. 2002. Parameters Estimation Based Model of Water-to-Water Heat Pumps with Scroll Compressors and Water/Glycol Solutions, *Proceedings of the Sixth International Conference on System Simulation in Buildings*.
- Klein, S.A. 2008, *Engineering Equation Solver*, F-Chart Software, Middleton, WI.
- Lemort, V., A. Rodríguez, and J. Lebrun. 2008. Simulation of HVAC Components with the Help of an Equation Solver. A Report for the International Energy Agency's SHC Task 34/ECBCS Annex 43 Subtask D. Iowa State University, Ames, Iowa, USA.
- Shrestha, S.S. 2006. Empirical validation of building energy simulation software: EnergyPlus, *MsC Thesis*. Volume 32, No.2
- Solberg, P., and B. Bradley. 2003. Blessing or curse? Hot Gas Bypass, *Trane Engineers newsletteri*. Volume 32, No.2.
- Wilson, E.E. 1915. A Basis for Rational Design of Heat Transfer Apparatus, *ASME Transactions*, Vol. 37: 47-70.
- Winandy, E., C. Saavedra, and J. Lebrun. 2002. Experimental analysis and simplified modelling of a hermetic scroll refrigeration compressor, *Applied Thermal Engineering* 22: 107-120.

CHAPTER 4

EXPERIMENTAL INVESTIGATION ON A SCROLL EXANDER INTEGRATED INTO A RANKINE CYCLE POWER SYSTEM

1	INTRODUCTION.....	90
2	DEVELOPMENT OF THE TEST BENCH.....	91
2.1	Choice of the working fluid	91
2.1.1	Literature survey.....	91
2.1.2	Selected fluids for the comparison	93
2.1.3	Cycle efficiency	95
2.1.4	Operating Pressures	97
2.1.5	Pump consumption	98
2.1.6	Charge of fluid.....	98
2.1.7	Expander Characteristics	99
2.1.8	Environmental impact.....	100
2.1.9	Resource utilization	101
2.1.10	Vapor superheating at the boiler exhaust.....	103
2.1.11	Conclusions.....	105
2.2	Choice of the expansion device.....	106
2.3	Description of the Test Rig	109
2.3.1	Description of the components.....	109
2.3.2	Instrumentation	110
3	DESCRIPTION AND ANALYSIS OF THE TESTS	112
3.1	Description.....	112
3.2	Expander performance	112
3.2.1	Isentropic effectiveness	112
3.2.2	Volumetric effectiveness	113
3.3	Cycle performance.....	114
4	VALIDATION.....	115
4.1	Validation of the expander model.....	115
4.1.1	Identification of the parameters of the model	115
4.1.2	Validation of the model	116
4.2	Validation of the cycle model	120
4.2.1	Boiler.....	120

4.2.2	Condenser	122
5	PARAMETRIC STUDIES.....	123
5.1	Parametric study on the expander	123
5.2	Parametric study on the cycle	125
6	CONCLUSIONS	127
7	REFERENCES.....	128

NOMENCLATURE

A	Area, m ²
AU	Heat transfer coefficient, W/K
bwr	Back work ratio, -
d	Diameter, m
h	Specific enthalpy, J/kg
h	Convective heat transfer coefficient, W/m ² -K
\dot{H}	Enthalpy flow rate, W
v	Specific volume, m ³ /kg
V	Volume, m ³
\dot{V}	Volume flow rate, m ³ /s
\dot{M}	Mass flow rate, kg/s
N	Rotational speed, Hz
\dot{Q}	Heat transfer rate, W
q	Heat, J/kg
R	Heat transfer resistance, K/W
$r_{v,in}$	Built-in volume ratio, -
s	Specific entropy, J/kg-K
T	Temperature, °C
T	Torque, N-m
w	work, J/kg
\dot{W}	Power, W
X	Capacity fraction, -

Subscripts

a	air
amb	Ambient
boil	Boiler
calc	Calculated
cp	Compressor

cd	Condenser
ex	Exhaust
exp	Expander
ev	Evaporator, evaporating
in	Internal
l	Liquid
loss	Mechanical loss
leak	Leakage
meas	Measured
n	Nominal
net	Net power
oh	Superheating
pp	Pump
r	Refrigerant
reg	Regenerator
s	Isentropic, swept
sat	Saturation
sc	Subcooling
sh	Shaft
sf	Secondary fluid
su	Supply
tp	Two phase
v	Volumetric
v	Vapor
w	Water
I	First law
II	Second law

Greek and miscellaneous

Δ	Difference
ϵ	Effectiveness, -
η	Efficiency, -

1 INTRODUCTION

Due to environmental constraints, the interest for low grade heat recovery has grown dramatically in the past decades. An important number of new solutions have been proposed to generate electricity from low grade heat sources and are now applied to diverse fields such as solar thermal power, geothermal heat sources, engine exhaust gas, domestic boilers, cooling down of mechanical equipment, etc.

Among the proposed solutions, the heat recovery Rankine Cycle system is the most widely used. Its main advantages are its simplicity and its commonly available components. Unlike with traditional power cycles, local and small scale energy production is made possible with this technology (Kane, 2002 and Quoilin, 2007).

In such a cycle, the working fluid is either water or an organic fluid. Systems using water have been described by Platell (1993), Lemort *et al.* (2006), Aoun *et al.* (2008). They are particularly suitable for recovering energy from engine exhaust gas. Systems using an organic fluid (called *Organic Rankine Cycles*) are more appropriate for lower temperature heat sources.

An experimental study has been performed on a prototype of a Rankine cycle power system working with refrigerant R123 and using an open-drive scroll expander. The investigated system is characterized by a thermal power at the boiler ranging from 10 to 20 kW. The first objective of this study was to show the feasibility of the system and to evaluate its performance. The second objective was to collect data for validating the expander and the entire system simulation models. The third objective was to highlight the main sources of inefficiency of the expander and of the whole system and to propose potential improvements.

This chapter is organized as follows:

First the development of the test bench is described. This comprises the choice of the working fluid, the selection of the expansion machine and a brief description of all the components of the test rig.

The achieved tests are then described and analyzed. Expander performance is described in terms of isentropic and volumetric effectiveness.

Based on collected experimental data, the expander semi-empirical model is validated. The cycle simulation model is only partly validated.

Using the expander and the cycle models, parametric studies are performed in order to investigate the expander and the cycle performance under the variation of operating conditions or under the modification of the expander design.

2 DEVELOPMENT OF THE TEST BENCH

2.1 Choice of the working fluid

The selection of the working fluid is extensively discussed in this paragraph. This is actually one of the major factors affecting the design and the performance of the ORC.

The fluids can be compared according to the following criteria:

- 1) The achieved performance of the cycle: appropriate indices of performance must be defined.
- 2) The operating conditions (such as pressures, temperatures): they have a significant impact on the design of the components.
- 3) The environmental impact of the fluid: it is evaluated in terms of *Ozone Deplating Potential* (ODP) and *Global Warming Potential* (GWP).
- 4) Safety: corrosive, flammable and toxic fluids may be forbidden for some ORC applications.
- 5) The cost of the fluid: systems characterized by smaller fluid charge may be preferred.

2.1.1 Literature survey

Hung *et al.* (1997) investigated benzene (C_6H_6), R113, R11, R12, R134a and ammonia as working fluids for Organic Rankine Cycles. Benzene was found to provide the highest efficiency. They also compared the fluids in terms of types of vapor saturation curve in the T-s diagram: dry fluids with positive slope (benzene, R113), wet fluids with negative slope

(water and ammonia) and isentropic fluids with nearly infinite slope (R11, R12, R134a). They observed that water and ammonia show an efficiency increasing with the turbine supply temperature. In contrary, except at high system pressure, dry fluids show decreased efficiency as the turbine supply temperature is increased.

Angelino and Colonna di Paliano (1998) showed that the performance of the ORCs may be improved by adopting multicomponent, zeotropic working fluids. They are particularly suitable when the heat source and sink exhibit marked temperature difference.

Yamamoto *et al.* (2001) compared both theoretically and experimentally the performance of a Rankine cycle working with water and R123. Analysis of experimental results demonstrated that the performance of the turbine is better with R123 than with water. According to the authors, friction loss in the turbine may be dominant when working with water.

Maizza and Maizza (2001) investigated the thermodynamic and physical properties of some unconventional fluids by means of numerical simulation. The modeled cycle was characterized by a boiler exhaust temperature ranging from 80 to 110°C and a condenser supply temperature ranging from 35 to 60°C. Among the fluids analyzed in their study, R123 and R600a (isobutane) coupled good system performance with high operation flexibility.

Hung (2001) compared the efficiencies and irreversibilities of the ORCs using various dry fluids, such as benzene (C_6H_6), toluene (C_7H_8), p-xylene (C_8H_{10}), R123 and R113. Dry fluids are better adapted to the use of a turbine, since the fluid remains in vapor state throughout the expansion. Lower efficiencies are achieved with refrigerants, because they exhibit relatively higher vaporization pressures and hence lead to smaller cycle area on the T-s diagram. Refrigerant fluids usually require three times as much flow rate than $C_{6+n}H_{6+2n}$ fluids (for a given power at the boiler and evaporating pressure). Since refrigerants are more expensive than $C_{6+n}H_{6+2n}$, it is not economical to use them for systems of large capacity. Among the selected $C_{6+n}H_{6+2n}$ fluids, C_8H_{10} has the best performance and among the refrigerants, R123 is better than R113.

Brasz and Bilbow (2004) compared the performance of R245fa, R134a, R236fa and R123. Their comparison included two different heat source temperatures (high/low), air-cooled/water-cooled options, cycles with/without regenerator and “ideal”/“realistic” component efficiencies. In the case of high temperature waste heat streams, much higher

thermal efficiency can be achieved when working with fluids of high critical temperatures. This is due to the reduction of the temperature difference between the heat source and the refrigerant in the evaporator.

More recently, Brasz (2008) investigated the performance of C6F, an ORC working fluid having a critical temperature similar to R245fa. C6F has very attractive environmental properties (zero-ODP, zero-GWP) and is non-flammable and non-toxic. C6F is characterized by a smaller slope of the saturated liquid line on the T-s diagram. This allows increasing both the thermal efficiency (pinch point occurs at higher temperature) and the resource utilization (larger preheating section of the boiler). However, C6F presents a larger de-superheating loss than R245fa, which could be overcome by the use of a regenerator. Finally, because of its lower density, C6F would require larger and therefore more costly equipment than R245fa.

2.1.2 Selected fluids for the comparison

Four different fluids have been considered as candidates for the experimental study presented hereafter: HFC-134a, HCFC-123, HFC-245fa and n-pentane.

Table 2-1 gives the critical temperatures and pressures, the saturation pressures (at 25°C) and the saturation temperatures (at 1 bar) of the four fluids. With regards to these characteristics, all these fluids are “good” candidates (with a temperature of the heat source varying between 130°C and 170°C), except R134a whose critical temperature (101°C) is a bit too low.

Table 2-1: Critical and saturation (@ 25°C and 1 bar) pressures and temperatures of the four fluids under consideration

	R245fa	R134a	R123	n-pentane
T_{crit} [°C]	154.1	101	183.7	196.5
$T_{sat,amb}$ [bar]	14.58	-26.37	27.4	35.49
P_{crit} [bar]	36.39	40.59	36.68	33.64
$P_{sat,amb}$ [bar]	1.493	6.658	0.915	0.6892

In order to select the most appropriate fluid, cycle’s performance and operating conditions have been compared by simulation. The environmental impact is only briefly described. Cost

and safety aspects are not covered in this paragraph. However, it should be mentioned that n-pentane is flammable.

For each of the fluids, the cycle's performances are evaluated by imposing the evaporating and the condensing temperatures. Refrigerants used in refrigeration cycles are currently compared in a same way (Calm, 2006). This comparison doesn't include the performances of the heat exchangers. The simple cycle model is schematically represented in Figure 2-1. The description of the heat exchangers will be taken into account when evaluating the resource utilization and discussing the impact of the vapor superheating at the boiler exhaust.

The comparison presented hereunder is based on the following hypothetical characteristics of the cycle:

- expander isentropic effectiveness: 70%
- pump efficiency: 60%
- regenerator effectiveness: 80%
- condensing temperature: 35°C
- vapor superheating at the boiler exhaust: 10K
- liquid subcooling at the condenser exhaust: 5K

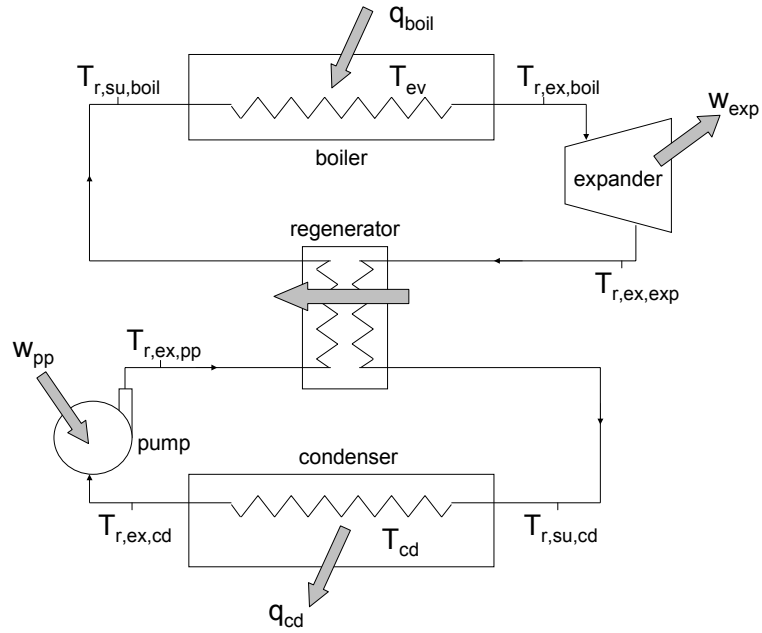


Figure 2-1: Representation of the simple ORC system model used for the fluid comparison

2.1.3 Cycle efficiency

Figure 2-2 shows the evolution of the thermal efficiency of the cycle with the evaporating temperature ((a): without a regenerator; (b): with a regenerator). The cycle thermal efficiency is classically defined as

$$\eta_I = \frac{W_{\text{exp}} - W_{\text{pp}}}{q_{\text{boil}}} \quad (2-1)$$

As it is well known, the thermal efficiency increases with the evaporating temperature, which justifies working with as high as possible heat source temperature and increasing as much as possible the boiler effectiveness. The highest efficiencies are achieved with R123 and n-pentane, and the lowest with R134a. Introducing a regenerator in the cycle substantially increases its efficiency.

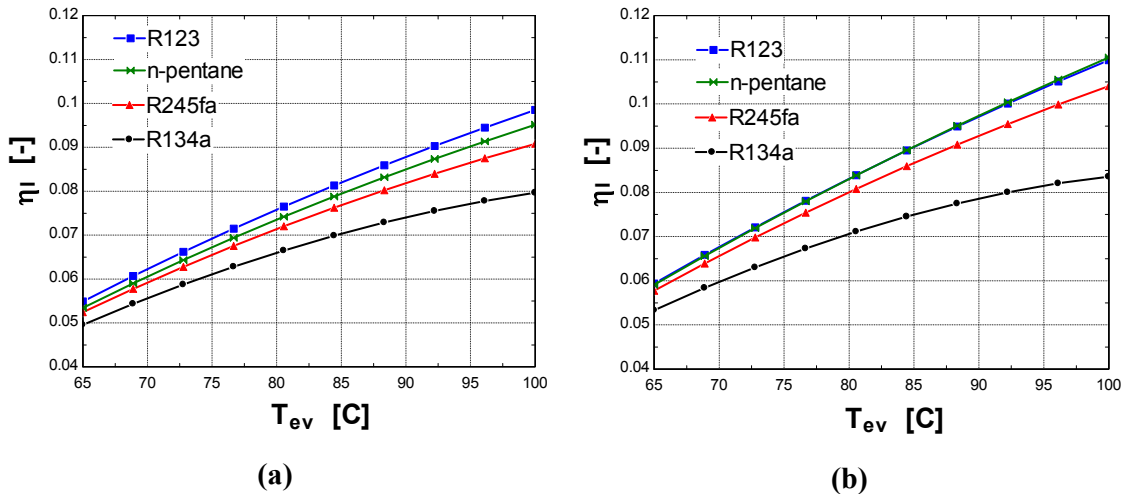


Figure 2-2: Evolution of the cycle efficiency with the evaporating temperature ((a): without a regenerator; (b): with a regenerator)

The levels of temperature achieved in the heat exchangers impose a limit to the cycle efficiency, which is the *Carnot efficiency*.

$$\eta_{\text{carnot}} = 1 - \frac{\bar{T}_{\text{cd}}}{\bar{T}_{\text{boil}}} \quad (2-2)$$

Since the evolutions of the fluid in both the boiler and the condenser are not isothermal, the Carnot efficiency has to be defined on the basis of mean equivalent temperatures (Angelino and Colonna di Paliano, 1998):

$$\bar{T}_{\text{boil}} = \frac{h_{r,\text{ex,boil}} - h_{r,\text{su,boil}}}{s_{r,\text{ex,boil}} - s_{r,\text{su,boil}}} \quad (2-3)$$

$$\bar{T}_{\text{cd}} = \frac{h_{r,\text{su,cd}} - h_{r,\text{ex,cd}}}{s_{r,\text{su,cd}} - s_{r,\text{ex,cd}}} \quad (2-4)$$

The ratio between the actual cycle efficiency and the Carnot efficiency, also called *second law efficiency*, gives an indication about how far from ideality the cycle is.

$$\eta_{II} = \frac{\eta_I}{\eta_{carnot}} \quad (2-5)$$

Figure 2-3 shows the evolution of the cycle second law efficiency as function of the evaporating temperature (with a regenerator). The efficiency achieved with R123 is the closest to the maximal efficiency. For R134a and R245fa, the ratio clearly decreases with the evaporating temperature. This is due to the increasing pump specific work, as demonstrated in Figure 2-5, which shows the corresponding evolution of the “back work ratio” (defined in §2.1.5).

2.1.4 Operating Pressures

The evolution of the evaporating pressure as function of the evaporating temperature is given in Figure 2-4. The highest pressures are reached with R134a. The design of the main components (expander, heat exchangers and pump) should account for these high pressures. Condensing pressures corresponding to a saturation temperature of 35°C are respectively 8.88, 1.31, 2.13 and 0.98 bar for the R134a, R123, R245fa and n-pentane.

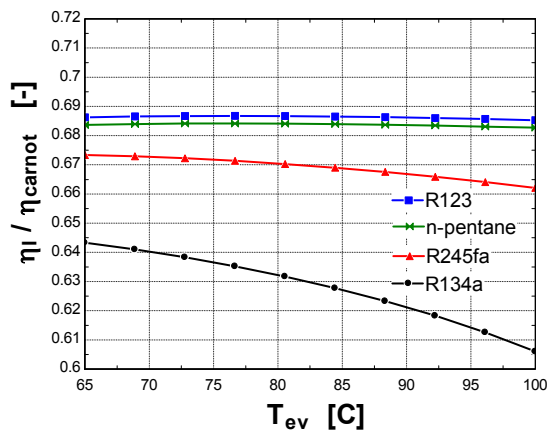


Figure 2-3: Evolution of the cycle second law efficiency with the evaporating temperature (with a regenerator)

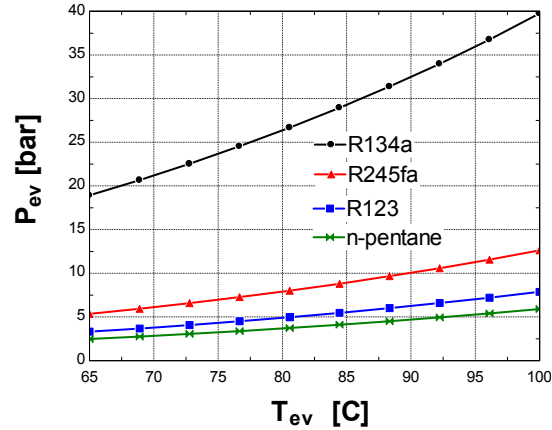


Figure 2-4: Evolution of the evaporating pressure with the evaporating temperature

2.1.5 Pump consumption

A parameter commonly used to describe power plant performance, which could be usefully employed for small scale Rankine cycles, is the *back work ratio* (bwr). It is defined as the ratio of the pump work input to the work developed by the expander (Moran *et al.*, 2003).

$$bwr = \frac{W_{pp}}{W_{exp}} \quad (2-6)$$

The evolution of the back work ratio with the evaporating temperature is shown in Figure 2-5. The cycle working with R134a is characterized by a back work ratio much larger than the other ones. In contrast, the cycles working with n-pentane and R123 are characterized by the smallest back work ratios. The larger pump consumption encountered with R134a is due to the large pressure difference between the condenser and the boiler.

2.1.6 Charge of fluid

Figure 2-6 gives the evolution of the boiler specific heat flow rate q_{boil} [J/kg] as function of the evaporating temperature (cycle without regenerator). The cycle working with n-pentane presents the highest specific heat flow rate. This also means that, for a given power, the cycle working with n-pentane requires the smallest charge of fluid.

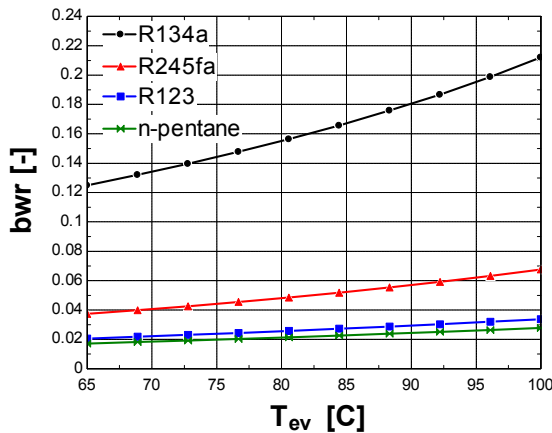


Figure 2-5: Evolution of the back work ratio with the evaporating temperature

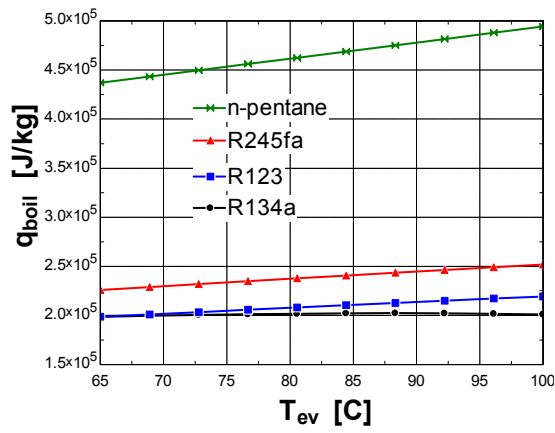


Figure 2-6: Evolution of the boiler specific heat flow rate with the evaporating temperature

2.1.7 Expander Characteristics

The expander swept volume is given by:

$$V_{s,exp} = \frac{1}{N_{exp}} \dot{M}_r \cdot V_{r,su,exp} = \frac{1}{N_{exp}} \frac{\dot{Q}_{boil}}{q_{boil}} \cdot V_{r,su,exp} = \frac{\dot{Q}_{boil}}{N_{exp}} \cdot V_{s,exp}^* \quad (2-7)$$

For a given thermal power (\dot{Q}_{boil}) recovered at the boiler and for a given expander rotational speed (N_{exp}), the swept volume of the expander is proportional to the ratio $v_{r,su}/q_{ev}$ [m^3/J]. This latter quantity is called *specific displacement* $V_{s,exp}^*$. Figure 2-7 shows the evolution of the specific displacement with the evaporating temperature. The specific displacement decreases with the evaporating temperature, due to the increase of the fluid density. The use n-pentane will require the largest displacement, while the use of R134a will require the smallest displacement. The size of the expander could be a particularly important factor in some ORC applications, such as automotive applications.

Another main characteristics of the expander design is its built-in volume ratio $r_{v,in}$. The evolution of the *ideal* built-in volume ratio with the evaporating temperature is shown in Figure 2-8. R134a and R245fa require respectively the smallest and the largest built-in volume ratio. Note that for a given expander displacement, the larger its built-in volume ratio the larger its external dimension. This will be discussed in Chapter 6.

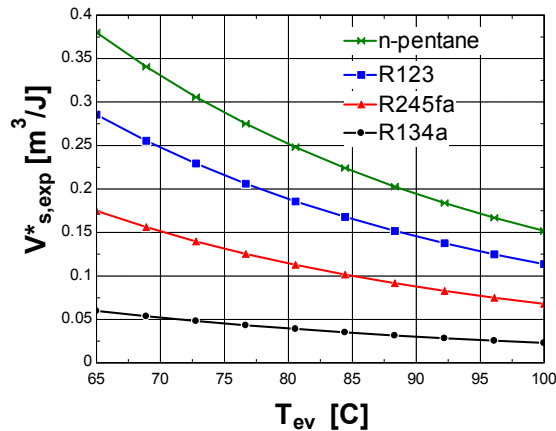


Figure 2-7: Evolution of the expander specific displacement with the evaporating temperature

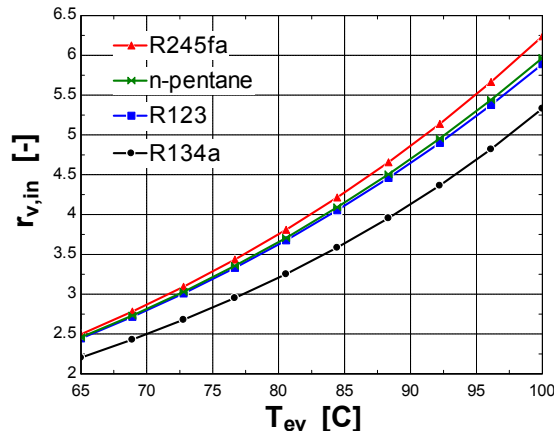


Figure 2-8: Evolution of the expander ideal built-in volume ratio with the evaporating temperature

2.1.8 Environmental impact

ODP and GWP of the four fluids are given in Table 2-2. R123 will be phased out around 2030, because of its non-zero ODP. R134a and R245fa will probably be sooner or later forbidden, due to their high GWP. N-pentane has ODP and GWP close to zero. However, its main drawback is its flammability.

Table 2-2: ODP and GWP of the four fluids

	R134a	R123	R245fa	n-pentane
ODP	0	0.012	0	~0
GWP	1320	53	1020	~0

In conclusion, all the fluids exhibit pros and cons. However, since ORCs appear to be a promising technology, it could be expected that Industry will develop appropriate fluids. For instance, as mentioned previously, Brasz (2008) investigated the performance of C6F, a non-flammable and non-toxic fluid with zero-ODP and zero-GWP.

2.1.9 Resource utilization

In the case of a heat recovery Rankine cycle system, the index of performance can be the net power generated by the system, provided the heat source is “free”. In order to compute the net power (or “resource utilization”) for given characteristics of the heat source, the model is modified to describe the heat exchanges in the boiler and the condenser. The modified ORC system simulation model is shown in Figure 2-9.

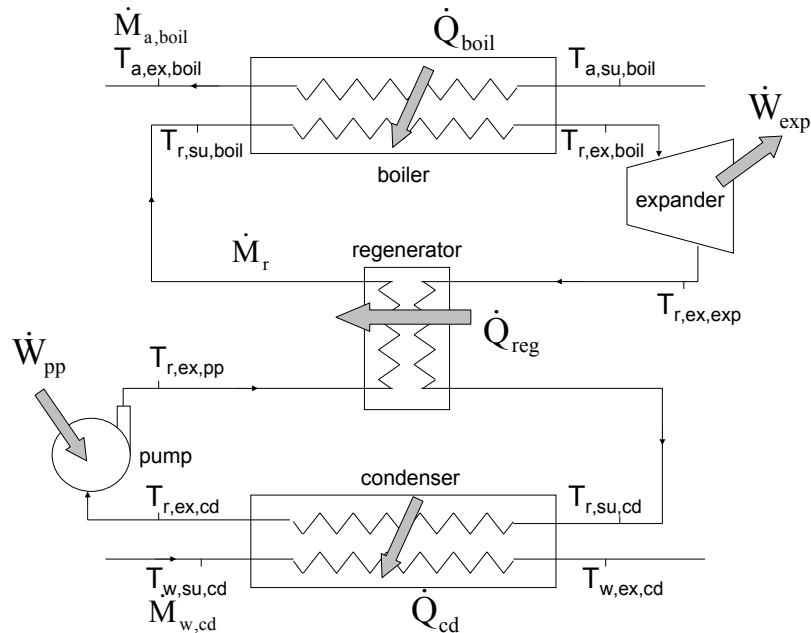


Figure 2-9: Representation of the modified ORC system model used for the fluid comparison

The comparison among the fluids refers to the following system characteristics:

- Air flow rate: 0.2 kg/s; boiler air supply temperature: 150°C.
- Evaporating temperature: 90°C; condensing temperature: 35°C
- Vapor superheating at the boiler exhaust: 10K; liquid subcooling at the condenser exhaust: 5K.
- Pump efficiency: 60%; regenerator effectiveness: 80%.
- Temperature pinch in the boiler: 10K and temperature pinch in the condenser: 5K
- Condenser water supply temperature: 20°C
- Expander isentropic effectiveness: 70%.

Table 2-1 compares the performance of the cycle achieved with each of the four fluids. As demonstrated previously, the best efficiencies are achieved with R123 and n-pentane. The poorest efficiency and the largest pump power consumption are achieved with R134a. However, the largest net power (difference between the expander power output and pump power input) is obtained with R134a.

Table 2-1 : Comparison of the ORC system performance for each of the four fluids

	<i>R134a</i>	<i>R123</i>	<i>R245fa</i>	<i>n-pentane</i>
$P_{r,su,exp}$ [bar]	32.47	6.252	10.04	4.688
$P_{r,ex,exp}$ [bar]	8.875	1.307	2.129	0.9835
\dot{Q}_{boil} [W]	18613	13253	13996	12933
$\dot{W}_{sh,exp}$ [W]	1786	1326	1380	1291
\dot{Q}_{reg} [W]	1150	1408	1901	1886
\dot{W}_{pp} [W]	322	39	79	31
\dot{W}_{net} [W]	1464	1287	1301	1260
η_{carnot} [%]	12.66	14.15	13.94	14.25
η_I [%]	7.863	9.713	9.297	9.745
η_I / η_{carnot} [%]	62.12	68.62	66.72	68.39
$V_{s,exp}$ [cm ³]	11.17	38.55	24.55	50.32
$r_{v,in}$	4.125	4.643	4.859	4.688
\dot{M}_r [g/s]	97.7	68.6	65.0	31.0
$\dot{M}_{w,cd}$ [g/s]	409.8	283.3	299.2	274.4

The swept volumes necessary for the expander to rotate at 3000 rpm are also given in Table 2-1. As already mentioned, the smallest and the largest swept volumes are obtained with R134a and n-pentane respectively. R134a and R245fa necessitate the smallest and largest built-in volume ratio respectively. The largest and lowest refrigerant mass flow rates are required with R134a and n-pentane respectively. This has already been demonstrated in §2.1.6.

2.1.10 Vapor superheating at the boiler exhaust

A frequently asked question when designing a heat recovery ORC is whether the vapor superheating at the boiler exhaust benefits to the cycle's performances. Yamamoto *et al.* (2001) showed that, for a given evaporator thermal power and with water, the turbine shaft power increases with the supply temperature, even if the mass flow rate decreases. However, with R123, the turbine shaft power decreases as the supply temperature increases, because the mass flow rate decreases too rapidly. They concluded that, if a working fluid with a low latent heat is used, the saturated vapor at the turbine supply would give the best operating conditions. This is explained in Table 2-2 which compares the performance of the cycle in the case of using R123 with vapor superheating (40 K) and without (0.1 K for the numerical convergence). Configurations with and without regenerator are also compared.

Table 2-2 : Comparison of the ORC system performance for R123 with and without vapor superheating

	0.1 K w/o regenerator	40 K w/o regenerator	0.1 K with regenerator	40 K with regenerator
\dot{Q}_{boil} [W]	14936	13992	13904	11660
q_{boil} [J/kg]	205006	239864	190837	199888
\dot{M}_r [g/s]	72.9	58.3	72.9	58.3
$\dot{W}_{sh,exp}$ [W]	1352	1256	1352	1256
w_{exp} [J/kg]	18559	21531	18559	21531
\dot{W}_{net} [W]	1311	1223	1311	1223
η_I [%]	8.78	8.74	9.43	10.49

Even if the boiler specific heat flow rate (q_{boil}) and the expansion specific work (w_{exp}) increase, the thermal power recovered at the boiler (\dot{Q}_{boil}) and the shaft power ($\dot{W}_{sh,exp}$) decrease with the superheating, because of the rapid decrease of the refrigerant mass flow rate. If a regenerator is used, the cycle efficiency increases with the superheating, because of the large superheating obtained at expander exhaust.

Based on the cycle model established in the previous paragraph, performances of the system have been computed as function of the vapor superheating at boiler exhaust. The evolution of

the net power is given in Figure 2-10. According to these results, superheating should be minimized to maximize the net power.

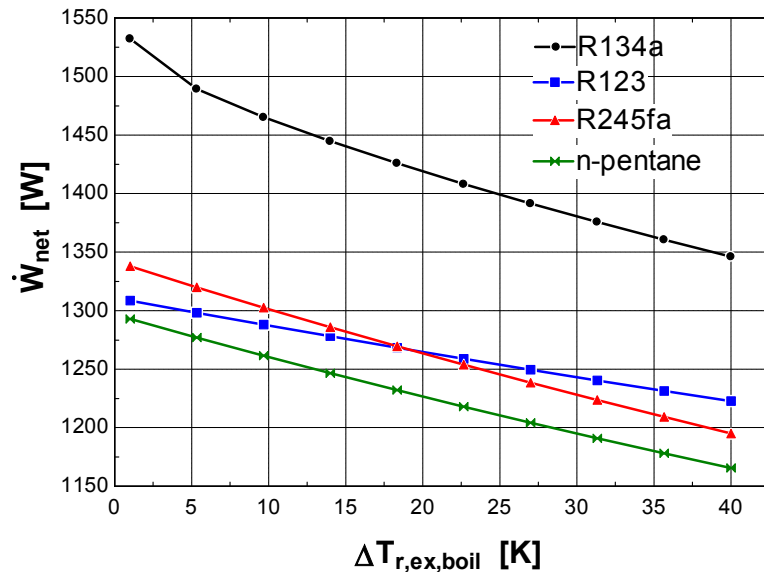


Figure 2-10: Evolution of the net power with the vapor superheating at the boiler exhaust

Temperature profiles in the boiler achieved with and without vapor superheating are compared in Figure 2-11 and Figure 2-12. In these figures, the x-axis represents the thermal power exchanged between the air and the refrigerant. The figures show the different zones in the boiler (liquid, two-phase and vapor) as well as the temperature pinch point (between the liquid and two-phase zones). Note that the spatial division of the boiler into zones is purely fictitious, since practically different zones coexist in the same section of the boiler.

For wet and isentropic fluids, expansion from saturated state may lead to a two-phase state at the end of the expansion. Figure 2-13 and Figure 2-14 give a representation of the cycle in the T-s diagram for an isentropic (R134a) and a dry (R123) fluid, in the case of a saturated cycle. Note that scroll expanders tolerate the presence of liquid. In contrary, this could cause damage to *turbo*-expanders.

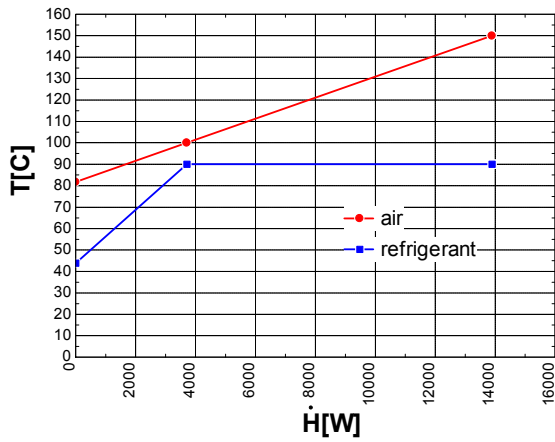


Figure 2-11: Temperature profiles in the boiler (without vapor superheating)

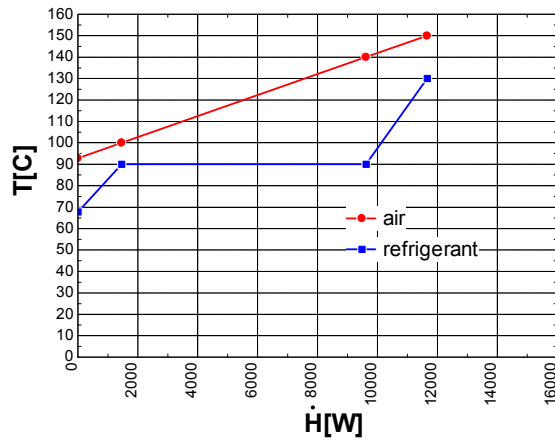


Figure 2-12: Temperature profiles in the boiler (with vapor superheating)

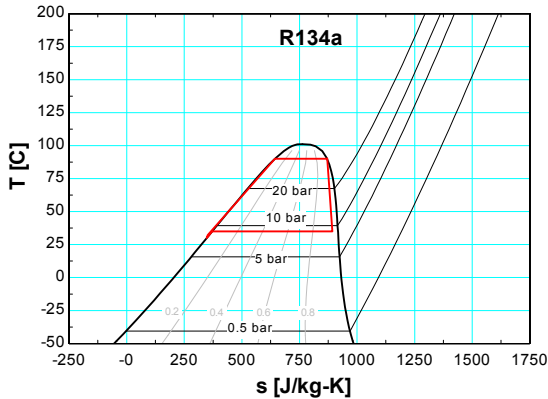


Figure 2-13: Representation of the cycle in the T-s diagram for R134a

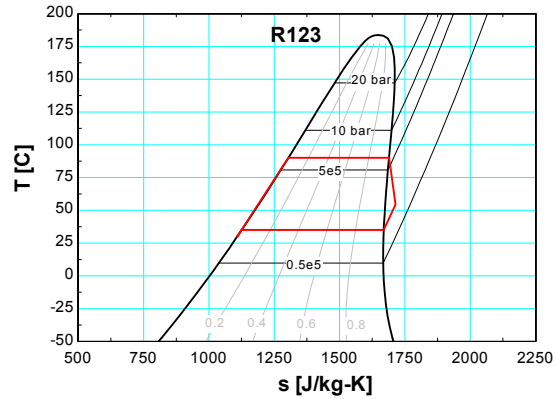


Figure 2-14: Representation of the cycle in the T-s diagram for R123

2.1.11 Conclusions

The comparisons among the four fluids presented here above can be summarized as follows. In terms of thermal efficiency, R123 and n-pentane exhibit the best performance. Poorest performance is achieved with R134a. However, R123 will be phased out around 2030 due to its non-zero ODP. N-pentane is flammable, which prevents its use in some applications. This risk is however limited by the fact that the system requires a small charge of fluid. It should be mentioned that the use of n-pentane in domestic refrigerators has become common practice.

Provided the heat source is free, the best resource utilization (net delivered power) will be achieved with R134a, even if the fluid is characterized by a large back work ratio. The smallest expander size is required with R134a. But, the latter fluid exhibits a critical temperature much lower than the three other ones, which would limit its use to moderate heat source temperatures (supercritical state might actually be achieved).

From the latter remarks, it is concluded that R134a is well adapted to the heat recovery from the cooling water jacket of a car engine (low temperature free heat source + compact expander).

For the ORC system built in the frame of this research project, R123 appears to be the most appropriate fluid: it presents the highest performance, n-pentane has to be rejected for its flammability and the expander is not adapted to the high pressure (maximum acceptable pressure of 10 bar).

Other aspects should be taken into account in these comparisons, such as the heat transfer coefficients and pressure drops in the heat exchangers. Such comparative analysis could also be extended to other fluids.

2.2 Choice of the expansion device

The expander is a key element of the ORC power system. The choice of the expander strongly depends on the operating conditions and on the size of the facility. Two main types of machines can be distinguished: the “dynamic” (“turbo” or “negative displacement”) and “positive displacement” (or “volumetric”) type. The positive displacement type machine is more appropriate to the small scale ORC power systems for the following reasons:

1. A positive displacement machine is characterized by a lower flow rate and a higher pressure ratio than a turbo-machine (polystaging can be used with turbo-machines, but it makes it heavier and more expensive).
2. Each type of expander shows an optimal peripheral speed, fairly independent from the expander size (Persson, 1990). Since the optimum tip speed is usually much higher for turbo machines than for positive displacement machines, small turbo machines must run at very high shaft speeds, which produces high mechanical stresses (e.g. due to centrifugal loading), bearing friction losses, reduction of the bearing lifetime, necessity for higher reduction gear, etc (Persson, 1990).

3. Positive displacement machines are able to support two-phase conditions, which may appear at the end of the expansion in some operating conditions.

Among positive displacement machines, the scroll machine is a good candidate for the ORC application, because of its reduced number of moving parts, reliability, wide output power range, and broad availability (Zanelli and Favrat, 1994). Moreover, it appears to be a proven technology, thanks to the experience already gained when using this machine in compressor mode for refrigeration and air-conditioning. However, up to now, the use of scroll machines in expander mode has been mainly limited to experimental work.

Zanelli and Favrat (1994) carried out an experimental investigation on a hermetic scroll expander-generator fed with refrigerant R134a. The machine produced a power ranging from 1.0 to 3.5 kW with a maximal isentropic efficiency of 65%.

For instance, Yanagisawa *et al.* (2001) carried out an experimental study on an oil-free scroll-type air expander. They observed that the performances can be lowered greatly by the mechanical loss and that leakage loss becomes significant as the rotational speed decreases. Maximal achieved volumetric and isentropic effectiveness are 76% and 60% respectively.

Kane (2002) designed, built and tested a prototype of hybrid solar thermal power plant associating solar collectors, cogeneration engines and two superposed Organic Rankine Cycles. Each cycle was equipped with a hermetic scroll expander (which is originally a scroll compressor adapted in expander mode).

Manzagol *et al.* (2002) studied a cryogenic scroll expander used for a 10 L/h helium liquefier. The expander was tested on a Brayton cycle refrigerator and reached an isentropic efficiency of 50 to 60% for supply gas conditions of 35 K and 0.7 MPa.

Xiaojun *et al.* (2004) investigated the possibility to recover work in a fuel cell by means of a scroll expander.

Hugenroth (2006) developed a novel approach to implementing a gas Ericsson cycle heat pump, using liquid flooding of the compressor and expander to approach isothermal compression and expansion process. Scroll machines were selected due to their ability to compress and expand a mixture of oil and gas.

Aoun and Clodic (2008) investigated the same expander as Yanagisawa *et al.* (2001), but operating with steam. In order to improve the volumetric effectiveness, original tip seals were replaced by PTFE tip seals, better adapted for high temperature applications and presenting lubricating properties. Maximal achieved volumetric and isentropic effectiveness were respectively 63% and 48%.

Other types of positive-displacement machines were investigated. For instance, Gnutek *et al.* (2001) studied the performances of a multicycle ORC. The authors proposed to combine all the different expanders of the cycle into one unique machine, consisting of several sliding vane expansion devices which are placed on the common drive shaft and are separated from each other by partitions. Baek *et al.* (2005) studied a prototype derived from a four-cycle two-piston gasoline engine and used it in place of the throttling valve in a transcritical CO₂ refrigeration cycle. Kovacevic *et al.* (2006) proposed to combine the compressor and the expander of a CO₂ cycle in one unique machine, which uses a single pair of screw rotors.

In the present study, the expander was selected among off-the-shelf compressors readily available. It is originally an oil-free open-drive *air* scroll compressor (Figure 2-15). This scroll machine is characterized by a large built-in volume ratio (close to 4.0), which makes it adapted to the higher pressure ratios than *refrigeration* scroll compressors. The swept volume of this machine is 148 cm³ in compressor mode. The fact that the expander doesn't need to be lubricated was also an important selection criterion. Lubrication of the expander would have required an oil separator and an oil pump, what would have increased the cost and the complexity of the system. The only modification made to the original compressor was to remove the cooling fan.



Figure 2-15: Fixed and orbiting scrolls of the investigated expander

2.3 Description of the Test Rig

2.3.1 Description of the components

As shown in Figure 2-16, the expander drives an asynchronous machine through two belt-and-pulley couplings and a torque-meter (see Figure 2-16). The asynchronous machine imposes the expander rotational speed. The latter is set to different values by modifying the pulley ratio.

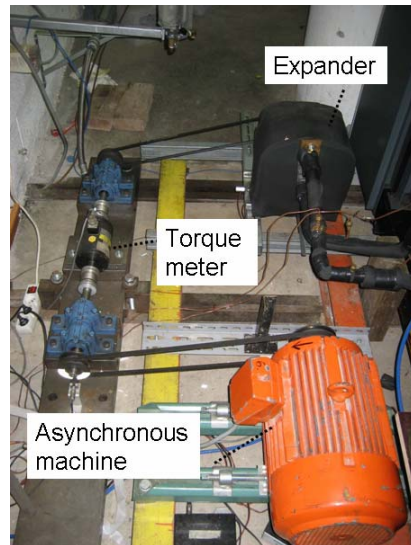


Figure 2-16: The expander, the torque meter and the asynchronous machine

The boiler is made up of three plate heat exchangers HX1, HX2 and HX3 in series supplied with hot air. The condenser is made up of two plate heat exchangers in parallel, supplied with cold water (Figure 2-17). A diaphragm pump with a maximum displacement of 210 l/h drives

the refrigerant through the cycle (Figure 2-18). Its swept volume can be adjusted to control the refrigerant flow rate.

A schematic representation of the whole test rig is given in Figure 2-19.



Figure 2-17: Plate heat exchangers used for the condenser



Figure 2-18: The diaphragm pump

2.3.2 Instrumentation

The expander mechanical power is determined by measuring simultaneously the rotational speed and the torque developed on the torque-meter shaft.

The refrigerant flow rate is measured in liquid phase by a Coriolis flow meter, located at the exhaust of the pump.

Temperatures and pressures are measured at the main points of the cycle. Temperatures are measured with T-type thermocouples (copper/copper-nickel) of Class 1 with a reference temperature of 0°C obtained by a water/ice mixture.

Pressures are measured with 0-5 bar and 0-10 bar pressure sensors (with an accuracy of $\pm 0.5\%$ full scale). A differential pressure transducer 0-10 bar is also used to measure the pressure differential over the expander (with an accuracy of $\pm 0.5\%$ full scale).

The expander shaft power is determined from the measurements of the torque and the speed at the torque-meter shaft (with an estimate of the transmission belt efficiency of 95%). The accuracy of the torque-meter is 0.1 N-m.

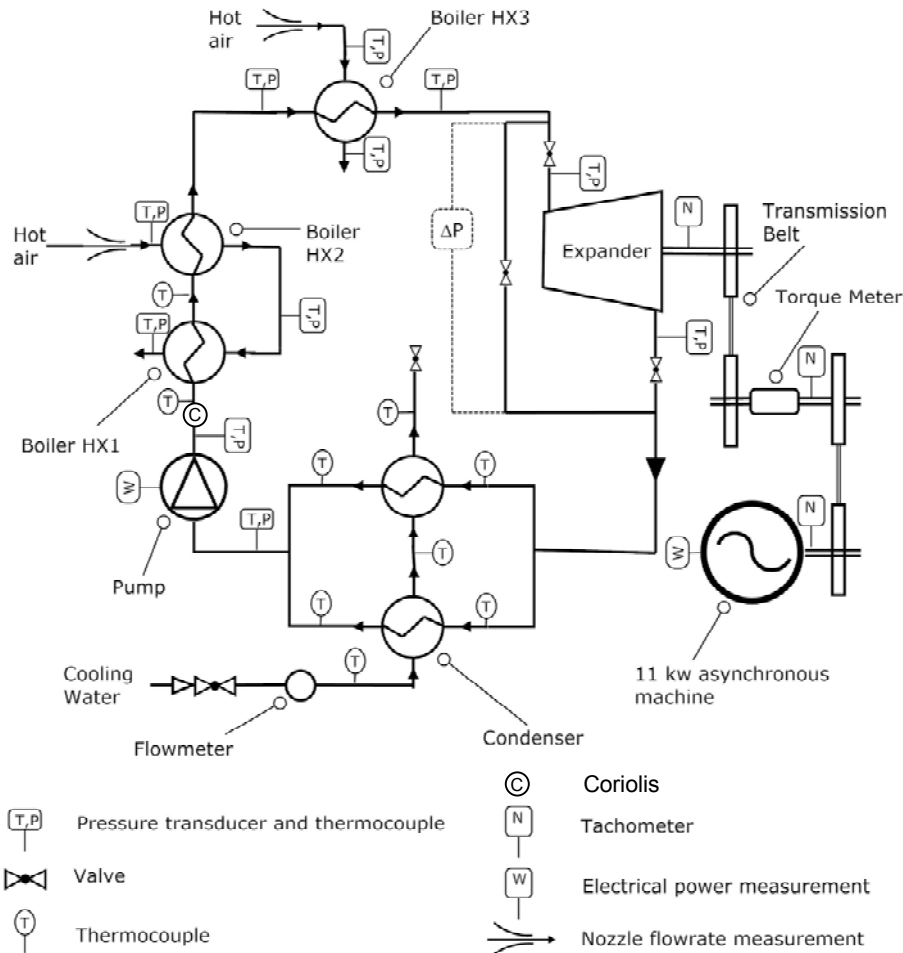


Figure 2-19: Schematic representation of the Rankine cycle test rig

Rotational speeds of the expander and of the torque-meter shaft are measured by means of proximity sensors. The accuracy of the measurements needed for the expander analysis is given in Table 2-3.

Table 2-3: Accuracy of the measurement devices

<i>Torque</i>	0.1 N.m
<i>Temperatures</i>	0.3 K
<i>Expander supply pressure</i>	0.05 bar
<i>Expander exhaust pressure</i>	0.025 bar
<i>Refrigerant flow rate</i>	1%

3 DESCRIPTION AND ANALYSIS OF THE TESTS

3.1 Description

The experimental data covers a wide range of operating conditions (Quoilin, 2007). A total of 39 points were achieved. The influence of the following variables and parameters were investigated: the expander supply temperature and pressure (by controlling the refrigerant flow rate displaced by the pump, as well as the hot air flow rates and temperatures), the expander exhaust pressure (by adjusting the water flow through the condenser) and the expander rotational speed (set to 3 different values: 1771, 2296, 2660 rpm).

3.2 Expander performance

3.2.1 Isentropic effectiveness

The maximum shaft power is 1.82 kW and the maximum achieved global isentropic effectiveness is 68%. This effectiveness is defined by the ratio between the measured shaft power and the isentropic power. The latter is the product of the measured flow rate by the expansion work associated to an isentropic expansion from supply conditions to the exhaust pressure.

$$\varepsilon_{s,exp,meas} = \frac{\dot{W}_{exp,meas}}{\dot{M}_{r,meas} (h_{r,su,exp} - h_{r,ex,exp,s})} \quad (3-1)$$

The evolution of the overall isentropic effectiveness with the pressure ratio imposed to the expander is given in Figure 3-1 for the three rotational speeds. It can be observed that this effectiveness drops at low pressure ratios due to over-expansion losses. Error bars are associated with calculated uncertainties, given by Equation (3-2). Provided measurements are

uncorrelated and random, the uncertainty U_Y on the variable Y is calculated as function of the uncertainties U_{X_i} on each measured variables X_i by (Klein, 2008)

$$U_Y = \sqrt{\sum_i \left(\frac{\partial Y}{\partial X_i} \right)^2 U_{X_i}^2} \quad (3-2)$$

3.2.2 Volumetric effectiveness

The volumetric effectiveness is defined as the ratio between the mass flow rate theoretically displaced by the expander and the measured mass flow rate:

$$\varepsilon_{v,meas} = \frac{\dot{V}_s}{\dot{M}_{r,meas} \cdot V_{su}} \quad (3-3)$$

The evolution of the volumetric effectiveness with the expander supply pressure is given in Figure 3-2, for the same three rotational speeds as in Figure 3-1. The volumetric effectiveness could be expected to decrease with the supply pressure due to larger internal leakage flows. However, this trend cannot be observed, due to the simultaneous effect of supply pressure drop. It can be observed that the lower the rotational speed, the lower the volumetric effectiveness, due to the larger relative impact of the internal leakage and due to smaller supply pressure drop.

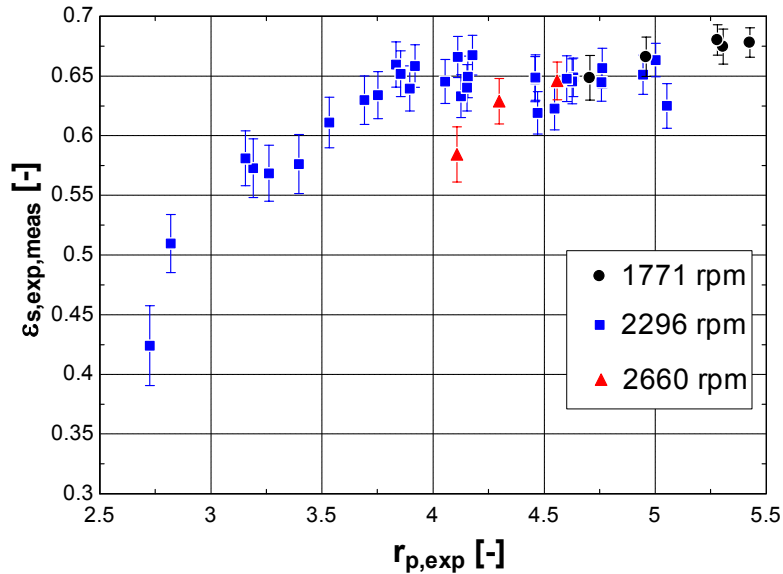


Figure 3-1: Evolution of the global isentropic effectiveness with the pressure ratio

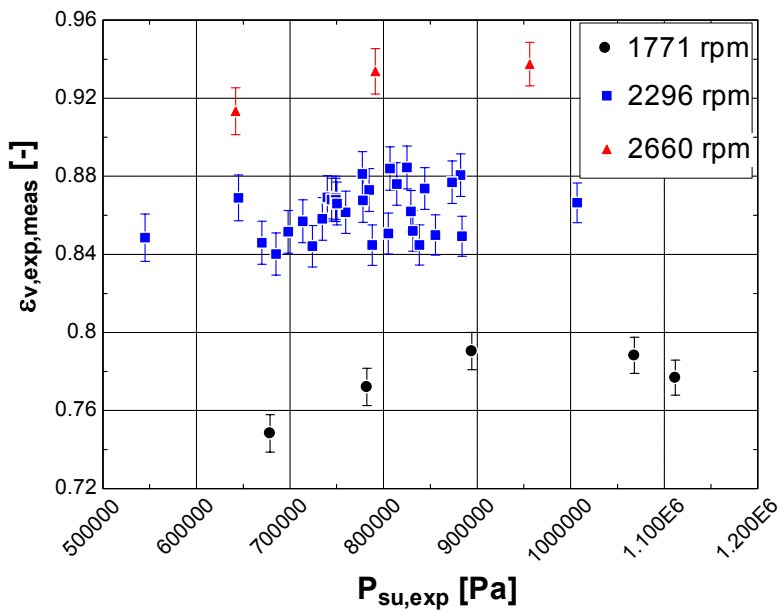


Figure 3-2: Evolution of the volumetric effectiveness with the pressure at the expander supply

3.3 Cycle performance

The maximum achieved cycle and second law efficiencies are 7.2% and 21.2% respectively. The cycle efficiency is calculated on the basis of the thermal power measured on the air side.

$$\eta_I = \frac{\dot{W}_{exp,meas} - \dot{W}_{pp,meas}}{\dot{Q}_{a,ev,meas}}$$

The pump power has only been measured for two points, which permitted the identification of a global efficiency ($\eta_{pp,s} \cdot \eta_{pp,m}$) of 15%. The pump consumption has been extrapolated for the other points assuming a constant efficiency. For the whole points, the back work ratio ranges from 13% to 30%.

The second law efficiency is computed as follows:

$$\eta_{II} = \frac{\eta_I}{\eta_{carnot}} = \frac{\eta_I}{1 - \frac{T_{w,su,cd}[K]}{T_{a,su,ev}[K]}}$$

4 VALIDATION

4.1 Validation of the expander model

The validation of the expander model is achieved in two steps. First, the values of the 8 parameters of the model are identified on the basis of the measurements. Then, predictions by the model are compared to measurements. Relative deviations are then used to determine the quality of the fit.

4.1.1 Identification of the parameters of the model

The parameters of the model are identified by minimizing a global error function ε accounting for the individual errors on the mass flow rate, shaft power and discharge temperature predictions. The global error function is defined by:

$$\varepsilon = \frac{1}{3} \left(\sqrt{\sum_1^{N_{tests}} \left(\frac{\dot{M}_{r,calc} - \dot{M}_{r,meas}}{\dot{M}_{r,calc}} \right)^2} \right) + \frac{1}{3} \left(\sqrt{\sum_1^{N_{tests}} \left(\frac{\dot{W}_{exp,calc} - \dot{W}_{exp,meas}}{\dot{W}_{exp,calc}} \right)^2} \right) + \frac{1}{3} \left(\sqrt{\sum_1^{N_{tests}} \left(\frac{T_{ex,calc} - T_{ex,meas}}{60} \right)^2} \right) \quad (4-1)$$

The same weight is given arbitrarily to each of the three individual errors. For the error in the temperature prediction, the value of the denominator (60) is the difference between the highest and lowest measured exhaust temperatures.

This minimization process is carried out by means of a genetic algorithm available in the EES software (Klein, 2008). The identified parameters are listed in Table 4-1.

Table 4-1: Identified parameters of the expander model

AU_{amb}	6.4 W/K
AU_{su}	21.2 W/K
AU_{ex}	34.2 W/K
\dot{M}_n	0.12 kg/s
A_{leak}	4.6 mm ²
$r_{v,in}$	4.05
V_s	36.54 cm ³
d_{su}	5.91 mm
T_{loss}	0.47 N-m

4.1.2 Validation of the model

Figure 4-1 compares the evolutions of the mass flow rate measured and predicted by the model with the expander supply specific volume, for the three different rotational speeds. The mass flow rate decreases with the specific volume of the refrigerant and increases with the rotational speed. It can be observed than the agreement between the measurement and the prediction by the model is good. The maximum deviation is 2.5%.

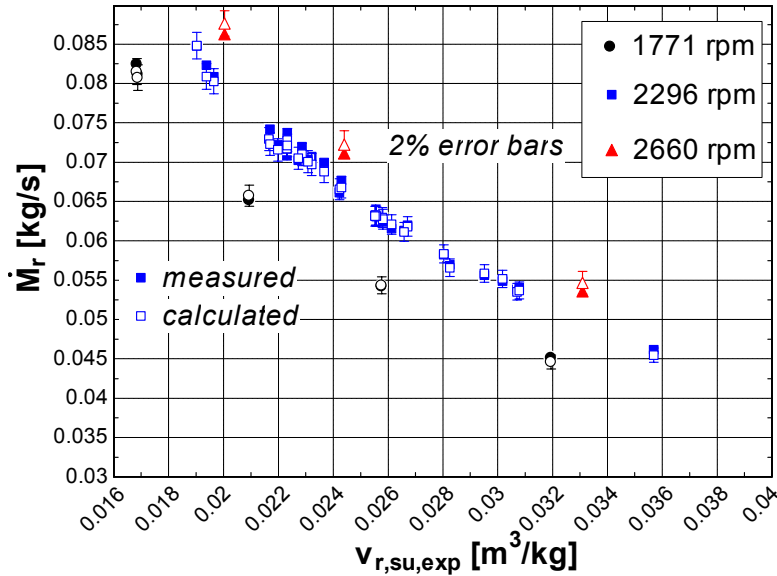


Figure 4-1: Evolution of the mass flow rate (predicted and measured) with the specific volume at the expander supply

The evolutions of the shaft power, measured and predicted by the model, with the pressure ratio are compared in Figure 4-2. Here also, it can be observed that the agreement is good. For most of the points, the shaft power is predicted within 5%.

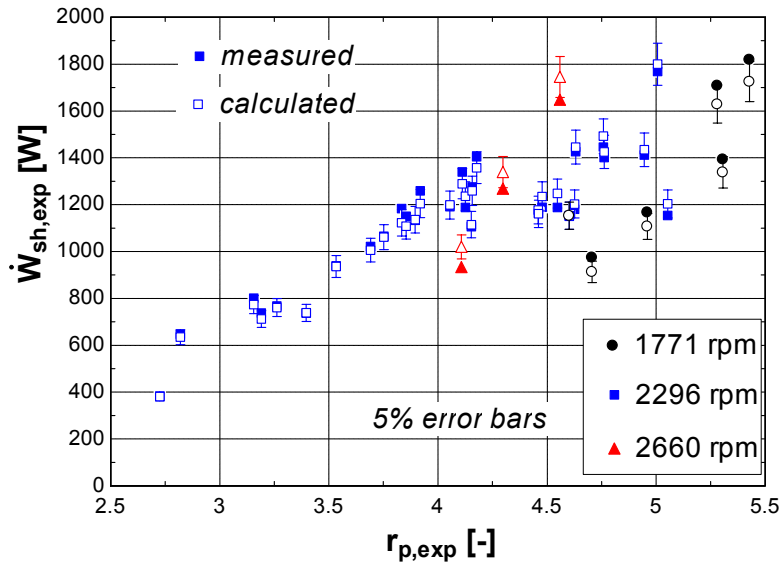


Figure 4-2: Evolution of the shaft power (predicted and measured) with the pressure ratio

Figure 4-3 compares the evolutions of the measured and predicted exhaust temperatures as function of the mean temperature between the supply and the exhaust of the expander:

$$\bar{T}_{r,exp,meas} = \frac{T_{r,su,exp} + T_{r,ex,exp,meas}}{2} \quad (4-2)$$

For most of the points, the model predicts the exhaust temperature within 3K (the maximal deviation is 4.1K). However, the model seems to slightly overestimate the exhaust temperature for high expander mean temperatures and slightly underestimate it for the lower mean temperatures.

This figure shows also the evolution of the exhaust temperature predicted by the model without ambient loss. The deviation between the predicted exhaust temperature and the measured one increases as the mean temperature (and thus the ambient loss) increases. This analysis confirms that the model must take the ambient loss into account in order to predict correctly the exhaust temperature.

Figure 4-4 shows the evolution of the ambient losses measured and predicted by the model with the mean temperature of the refrigerant.

The measured ambient loss is evaluated as follows:

$$\dot{M}_{r,meas} \cdot (h_{r,su,exp,meas} - h_{r,ex,exp,meas}) = \dot{W}_{sh,exp,meas} + \dot{Q}_{amb,exp,meas} \quad (4-3)$$

Figure 4-4 shows that the model slightly over-predicts the ambient loss at low mean temperatures and slightly under-predicts it at high mean temperatures. Hence, the model under-estimates the wall temperature for the lower mean temperatures and over-estimates it for the higher mean temperatures. This is the reason why higher discharge temperatures are over-predicted and lower discharge temperatures under-predicted. The underlying reason might be the internal and external heat transfers cannot be described by one unique uniform wall temperature.

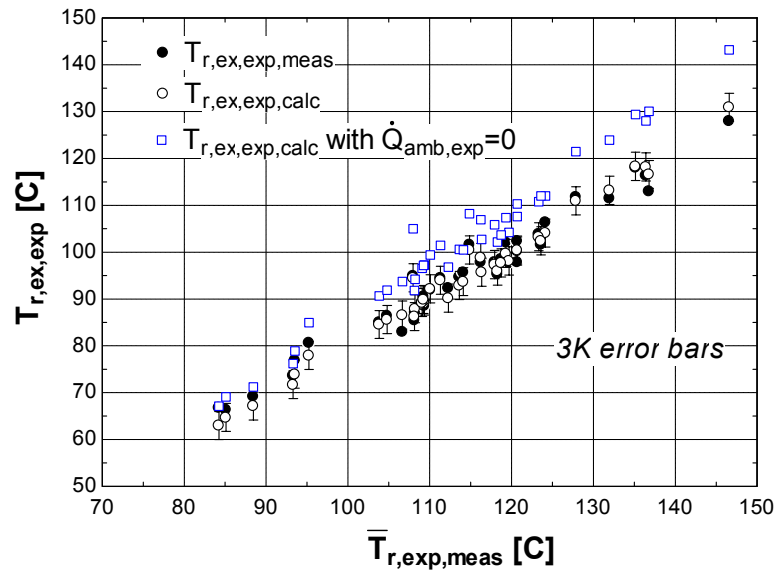


Figure 4-3: Evolution of the (predicted and measured) exhaust temperature with the mean measured temperature of the fluid between the expander supply and exhaust

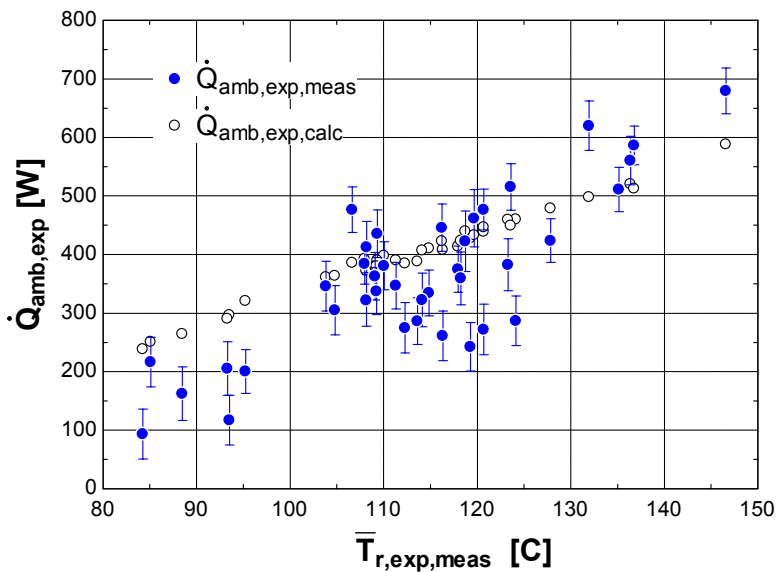


Figure 4-4: Evolution of the ambient losses (measured and predicted by the model) with the mean measured temperature of the fluid between the expander supply and exhaust

4.2 Validation of the cycle model

Validation of the cycle simulation model consists in identifying the parameters of the models of the boiler, the condenser and the pump. The information diagram of the Rankine cycle simulation model is shown in Figure 4-5. This model has been described in Chapter 2.

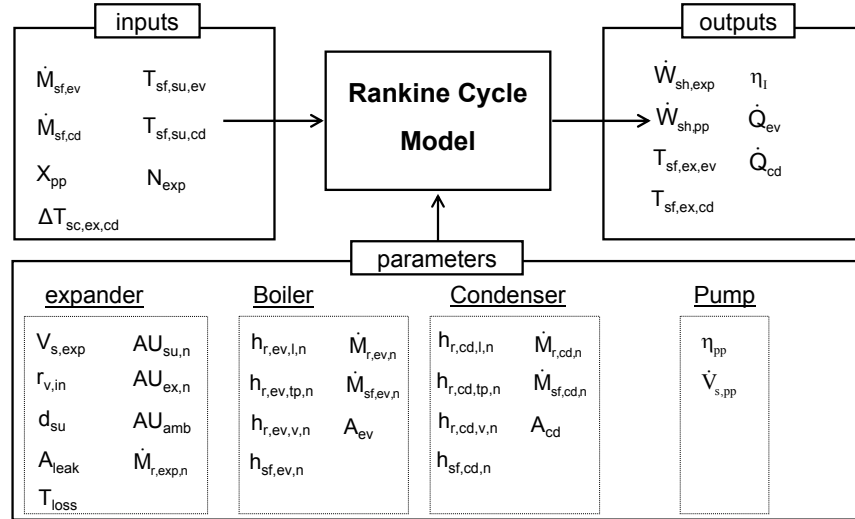


Figure 4-5: Information diagram for the ORC system model

The study presented here doesn't focus on the validation of the heat exchangers' models. This validation has been detailed by Quoilin *et al.* (2008).

However, one of the objectives of the present study is to analyze the dependency between the cycle and the expander performance. In order to roughly determine the parameters of the boiler and the condenser models, they are estimated on the basis of only one performance point.

4.2.1 Boiler

The main difficulty encountered when modeling the boiler is that the latter is made up of three different heat exchangers: HX1, HX2 and HX3 (see Figure 2-19). These heat exchangers are in series on the refrigerant side. However, on the air side only HX1 and HX2 are in series and HX3 is fed independently (but with the same air mass flow rate). As shown in Figure 4-6, the vaporization of the refrigerant is achieved successively in HX2 and HX3.

In order to simplify its modeling, the boiler is represented by one unique heat exchanger. A fictitious air supply temperature is defined by energy balance:

$$T_{sf,su,ev} = T_{sf,ex,ev} + \frac{\dot{Q}_{sf,ev,meas}}{\dot{M}_{sf,ev} \cdot c_{p,sf,ev}} = T_{sf,ex,HX1} + \frac{\dot{Q}_{sf,HX1} + \dot{Q}_{sf,HX2} + \dot{Q}_{sf,HX3}}{\dot{M}_{sf,ev} \cdot c_{p,sf,ev}} \quad (4-4)$$

The model, already presented in Chapter 2, distinguishes the three different zones of the refrigerant (liquid, two-phase and vapor) but doesn't account for the pressure drops.

The orders of magnitude of the heat transfer convective coefficients on refrigerant and air sides have identified by Quoilin *et al.* (2008) are given in Table 4-1. The remaining parameter to identify is the heat exchange area A_{ev} of the equivalent heat exchanger.

Table 4-1: Identified parameters of the ORC system model

Expander		Boiler		Condenser		Pump	
$V_{s,exp}$	36.54 cm ³	$h_{r,ev,l,n}$	50 W/m ² -K	$h_{r,cd,l,n}$	76 W/m ² -K	η_{pp}	0.15
$r_{v,in}$	4.05	$h_{r,ev,tp,n}$	650 W/m ² -K	$h_{r,cd,tp,n}$	174 W/m ² -K	$\dot{V}_{s,pp}$	210 l/h
A_{leak}	4.6 mm ²	$h_{r,ev,v,n}$	22 W/m ² -K	$h_{r,cd,v,n}$	67 W/m ² -K		
T_{loss}	0.47 N-m	$\dot{M}_{r,ev,n}$	0.080 kg/s	$\dot{M}_{r,cd,n}$	0.046 kg/s		
d_{su}	5.91 mm	$h_{sf,ev,n}$	644 W/m ² -K	$h_{sf,cd,n}$	2000 W/m ² -K		
$AU_{su,n}$	21.2 W/K	$\dot{M}_{sf,ev,n}$	0.100 kg/s	$\dot{M}_{sf,cd,n}$	0.719 kg/s		
$AU_{ex,n}$	34.2 W/K	A_{ev}	9.483 m ²	A_{cd}	3.974 m ²		
AU_{amb}	6.4 W/K						
$\dot{M}_{r,exp,n}$	0.120 kg/s						

The measured and calculated temperature profiles in the boiler are compared in Figure 4-6. The boiler model is able to predict correctly the thermal power. The expander supply pressure, and hence the saturation temperature T_{ev} , is predicted by the cycle simulation model with a very good agreement.

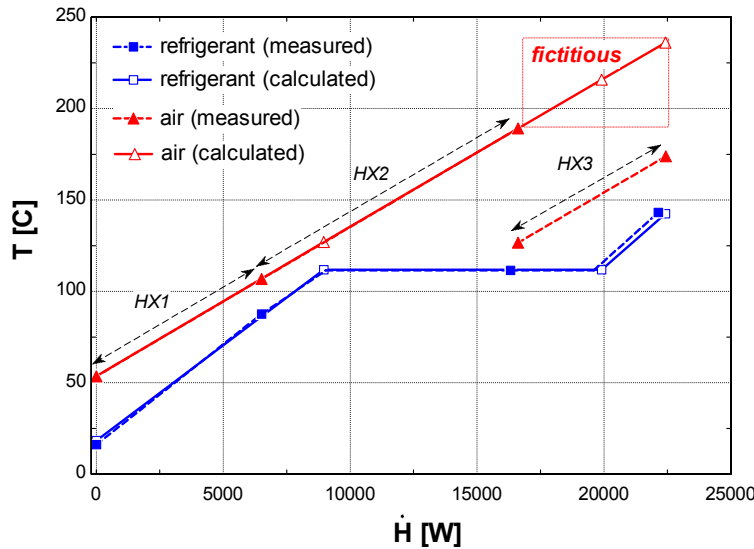


Figure 4-6: Temperature evolutions of the refrigerant and of the air in the boiler

4.2.2 Condenser

The modeling of the condenser is simplified by merging the two heat exchangers shown in Figure 2-19 into one unique heat exchanger. The convective heat transfer coefficients related to the condenser are given in Table 4-1. The liquid subcooling is imposed as equal to its measured value. The only parameter to identify is the equivalent heat transfer area A_{cd} .

Here also, the condenser model is able to predict accurately the thermal power. The saturation temperature is predicted by the cycle model with a very good accuracy.

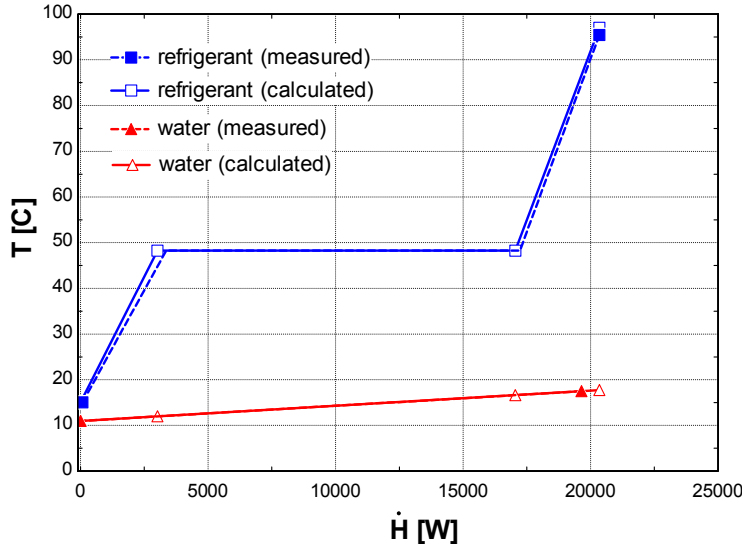


Figure 4-7: Temperature evolutions of the refrigerant and of the water in the condenser

5 PARAMETRIC STUDIES

5.1 Parametric study on the expander

A parametric study is conducted in order to investigate the expander performance as function of some of the parameters introduced previously. This study aims at indicating how the expander design might be altered to achieve better performance.

Figure 5-1 shows the evolution of the predicted global isentropic effectiveness with the values of some of the modeling parameters introduced in § 4.1.1. This figure shows the sensitivity of the expander performance with these parameters.

For one selected operating point (supply pressure of 10.03 bar, exhaust pressure of 2.01 bar, supply temperature of 141.6°C and rotational speed of 2296 rpm), it can be observed that the expander is rather well adapted in term of built-in volume ratio. The performance can be slightly improved by reducing even more the mechanical loss. The impact of the ambient loss on the performance is weak.

The performance could be improved by increasing by 50% the equivalent supply port diameter. As it will be shown in Chapter 7, this could be achieved by increasing the size of the actual supply port, but also by limiting the effect of supply port blockage by the tip of the

orbiting scroll. The performance could also be largely improved by decreasing the leakage area. For example, by increasing by 50% the equivalent supply port diameter and decreasing by 50% the equivalent leakage area, the global isentropic effectiveness from 67.4% to 79.6%.

Note that the large internal leakage may be due to the behavior of the tip seals. The latter are probably not adapted to the use of refrigerant (instead of air) and they may not lift. This will be investigated in Chapter 7. Aoun and Clodic (2008) carried out an experimental study on a similar expander fed with water steam. They replaced the original seals by better adapted Teflon seals, which yielded a substantial increase of the volumetric effectiveness of the expander.

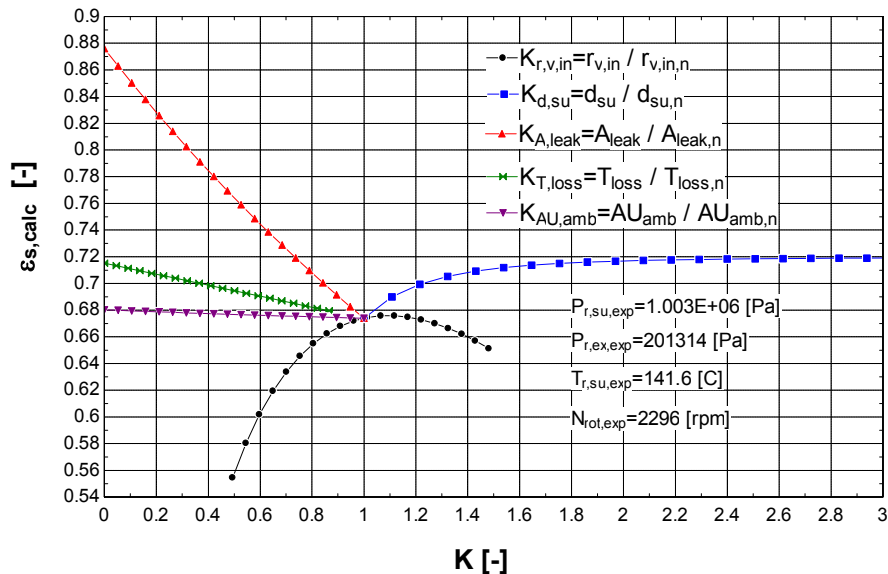


Figure 5-1: Improvement of the expander performance: evolution of the (predicted) global isentropic effectiveness with the values of the different parameters (K) of the expander model

The evolution of the predicted shaft power with some of the model parameters is given in Figure 5-2. It can be observed that the shaft power could be largely increased by reducing the supply pressure drop. This is due to the double effect of the pressure drop: the latter tends to decrease the internal flow rate \dot{M}_{in} and to decrease the specific expansion work w_{in} .

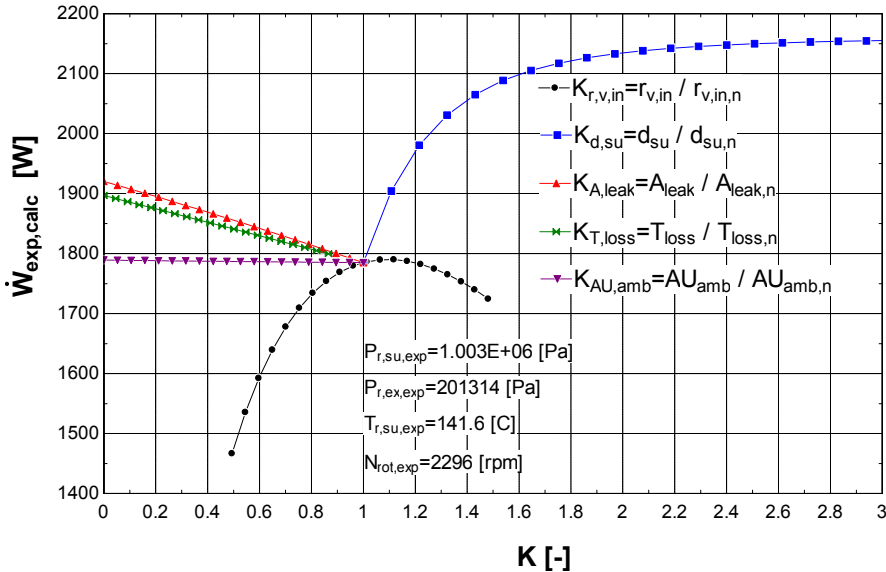


Figure 5-2: Improvement of the expander performance: evolution of the (predicted) shaft power with the values of the different parameters (K) of the expander model

5.2 Parametric study on the cycle

From Figure 5-3, it can be observed that the expander leakage area has a major impact on the net delivered power. Actually, for a given refrigerant mass flow rate (imposed by the pump), increasing the leakage area will simultaneously reduce the internal working mass flow rate ($\dot{M}_{in,exp}$) and reduce the expander supply pressure.

It can also be observed that there is an optimal built-in volume ratio maximizing the shaft power. This optimal built-in volume ratio is a function of the pressure ratio imposed to the expander.

In a similar way, for a given built-in volume ratio, there exists an optimal rotational speed leading to the adapted pressure ratio over the expander.

It is interesting to observe that reducing the suction pressure drop does not yield a substantial power increase. The reason is that the refrigerant working flow rate is imposed by the pump (the leakage flow rate is more or less unchanged). Increasing the suction diameter will simultaneously decrease the suction pressure P_{su} and suction pressure drop, so that the pressure $P_{su,l}$ remains almost unchanged.

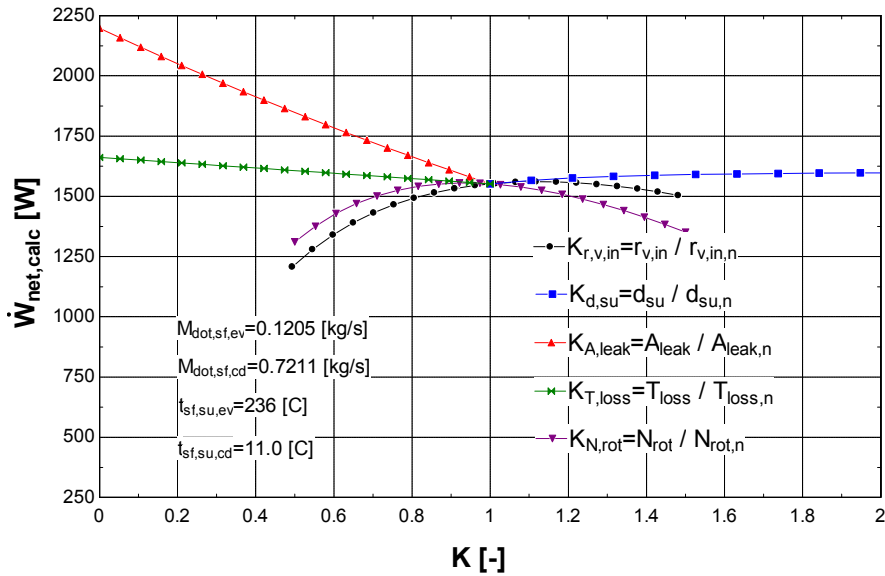


Figure 5-3: Improvement of the cycle performance: evolution of the (predicted) power with the values of the different parameters (K) of the expander model

The influence of the expander model parameters on the cycle efficiency is shown in Figure 5-4. By reducing to zero the expander internal leakage, the cycle efficiency would increase by almost 3%.

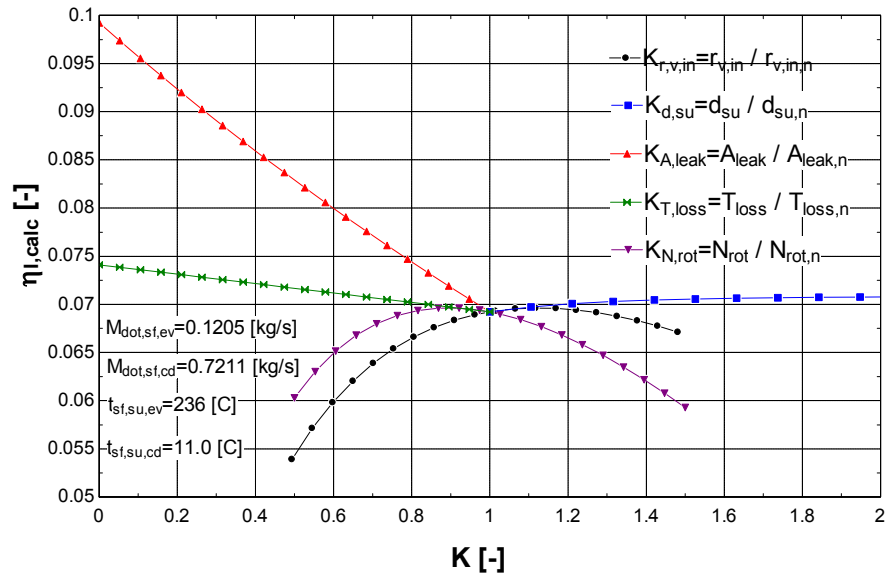


Figure 5-4: Improvement of the cycle performance: evolution of the (predicted) cycle efficiency with the values of the different parameters (K) of the expander model

Figure 5-5 shows the evolution of the net delivered power with the cycle model parameters or operating conditions. As expected, the net power increases with the pump displacement. The heat exchangers are already oversized, so there is no need to increase even more the heat exchange area.

The more substantial power gain will be achieved by decreasing the liquid subcooling at the condenser exhaust. This could be achieved by reducing the charge of refrigerant inside the system. As shown in Figure 4-7, since the pinch point is located at the condenser exhaust, decreasing the subcooling would allow the expander exhaust pressure to be lowered.

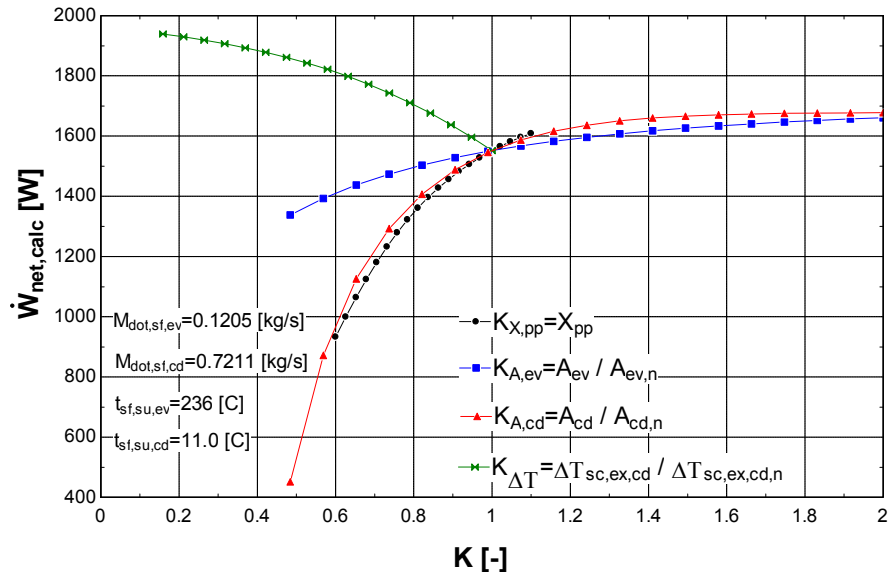


Figure 5-5: Improvement of the cycle performance: evolution of the (predicted) power with the values of the different parameters (K) of the cycle model

6 CONCLUSIONS

The experimental study confirms that the scroll expander is a good candidate for an Organic Rankine Cycle application. The tested prototype presents good performances: the maximum global isentropic effectiveness achieved is 68%.

The proposed modeling of the scroll expander predicts with a very good agreement the variables of first importance such as the mass flow rate, the shaft power and the discharge

temperature. The model involves a limited number of parameters which describes the main physical features of the expander. Due to its accuracy, low computational time and robustness, the model can be easily associated to the models of other components (such as heat exchangers) in order to describe the whole cycle system.

A parametric study was conducted to both investigate the expander and the cycle performances under the variation of operating and design parameters. It was shown that the performance of the expander could be largely improved by reducing both the internal leakage and the suction pressure drop.

The performances of the cycle mainly suffer from the expander internal leakage and liquid subcooling. The latter could be reduced by decreasing the charge of refrigerant inside the cycle. Reducing the liquid subcooling would actually lower the condensing pressure, increasing in the mean time the pressure ratio over the expander.

The expander and cycle models can therefore be used as pre-design tools to define the optimal main characteristics of the expander and operating conditions of the cycle.

7 REFERENCES

- Angelino, G., and P. Colonna di Paliano. 1998. Multicomponent working fluids for organic Rankine cycles (ORCs), *Energy* (23): 449–463.
- Aoun, B., and D. Clodic. 2008. Theoretical and experimental study of an oil-free scroll type vapor expander, *Proceedings of the International Compressor Engineering Conference at Purdue*: paper 1188.
- Baek, J.S., E.A. Groll, and P.B. Lawless. 2005. Piston-cylinder work producing expansion device in a transcritical carbon dioxide cycle. Part I: experimental investigation, *International Journal of Refrigeration* 28: 141-151.
- Brasz, L.J., and W.M. Bilbow. 2004. Ranking of working fluids for organic Rankine cycle applications, *Proceedings of the International Refrigeration and Air-Conditioning Conference at Purdue*: Paper R068.

- Brasz, L.J., and W.M. Bilbow. 2004. Ranking of working fluids for organic Rankine cycle applications, *Proceedings of the International Refrigeration and Air-Conditioning Conference at Purdue*: Paper R068.
- Calm, J. M. 2006. Comparative efficiencies and implications for greenhouse gas emissions of chiller refrigerants, *International Journal of Refrigeration* (29): 833–841.
- Gnutek, Z., A Bryszewska-Mazurek. 2001. The thermodynamic analysis of multicycle ORC engine. *Energy* 26: 1075-1082.
- Hugenroth, J. J. 2006. Liquid Flooded Ericsson Cycle Cooler. *PhD Thesis*, Purdue University.
- Hung, T.C., T.Y. Shai, and S.K. Wang. 1997. A review of Organic Rankine Cycles (ORCs) for the recovery of low-grade waste heat. *Energy* Vol. 22, No. 7: 661-667.
- Hung, T.-C. 2001. Waste heat recovery of organic Rankine cycle using dry fluids. *Energy Conversion and Management* 42: 539-553.
- Kane, El H. 2002. Intégration et optimisation thermoéconomique & environnementale de centrales thermiques solaires hybrides. *PhD Thesis*, Laboratoire d'Energétique Industrielle, Ecole polytechnique Fédérale de Lausanne, Suisse.
- Klein, S.A. 2008, *Engineering Equation Solver*, F-Chart Software, Middleton, WI.
- Kovacevic, A., N. Stosic, and I. K. Smith. 2006. Numerical simulation of combined screw compressor-expander machines for use in high pressure refrigeration systems, *Simulation Modelling Practice and Theory* 14: 1143-1154.
- Lemort, V., Teodorese, I.V., Lebrun, J. 2006. Experimental study of the integration of a scroll expander into a heat recovery Rankine cycle. *Proceedings of the International Compressor Engineering Conference at Purdue*: C105.
- Lemort, V., C. Cuevas, J. Lebrun, and I.V. Teodorese. 2007, Contribution à l'étude des cycles de Rankine de récupération de chaleur. *Colloque Interuniversitaire Franco-Québécois sur la Thermique des Systèmes à Montréal*.
- Maizza, V., and A. Maizza. 2001. Unconventional working fluids in organic Rankine-cycles for waste energy recovery systems. *Applied Thermal Engineering* 21: 381-390.
- Manzagol, J., P. d'Harbouillé, G. Claudet, and G. Gistau Baguer. 2002. Cryogenic scroll expander for claude cycle with cooling power of 10 to 100 watts at 4.2 K. *Advances in Cryogenic Engineering*. Proceedings of the Cryogenic Engineering Conference - CEC AIP Conference Proceedings 613: 267-274.

- Moran M., H. N. Shapiro, B. R. Munson, and D. P. DeWitt. 2003. Introduction to Thermal Systems Engineering. John Wiley & Sons: 189.
- Persson, J.-G. 1990. Performance mapping vs design parameters for screw compressors and other displacement compressor types, *VDI Berichte*, nr. 859, Düsseldorf.
- Platell, P. 1993. Displacement expanders for small scale cogeneration, *Licentiate Thesis*, Department of Machine Design, Royal Institute of Technology, Stockholm.
- Quoilin, S. 2007. Experimental Study and Modeling of a Low Temperature Rankine Cycle for Small Scale Cogeneration. *Master Thesis*, Université de Liège.
- Quoilin, S., M. Orosz, and V. Lemort. 2008, Modeling and Experimental Investigation of an Organic Rankine Cycle System using Scroll Expander for Small Scale Solar Applications, *Proceedings of the First International Conference on Solar Heating, Cooling and Building (EUROSUN)*, Lisboa.
- Xiaojun, G., L. Liansheng, Z. Yuanyang, S. Pengcheng. 2004. Research on a Scroll Expander Used for Recovering Work in a Fuel Cell. *International Journal of Thermodynamics* 7:1-8.
- Yamamoto, T., T. Furuhata, N. Arai and K. Mori. 2001. Design and testing of the Organic Rankine Cycle. *Energy* 26: 239-251.
- Yanagisawa, T., M. Fukuta, Y. Ogi, and T. Hikichi. 2001. Performance of an oil-free scroll-type air expander. *Proc. Of the ImechE Conf. Trans. On compressors and their systems*: 167-174.
- Zanelli R., D. Favrat. 1994. Experimental Investigation of a Hermetic Scroll Expander-Generator. Proceedings 12th Internnatiional Compressor Engineering Conference at Purdue: 459-464.

CHAPTER 5

EXPERIMENTAL INVESTIGATION ON SCROLL MACHINES INTEGRATED INTO A LIQUID FLOODED ERICSSON CYCLE COOLER

1	INTRODUCTION.....	135
2	DESCRIPTION OF THE TEST RIG	137
2.1	System operation	137
2.2	Recommendations from previous work	138
2.3	Components.....	139
2.3.1	Compressor and expander	139
2.3.2	Liquid separators	140
2.3.3	Heat exchangers and regenerator	141
2.3.4	Hydraulic motor and pump.....	141
2.3.5	Electrical motors.....	141
2.3.6	Gas and oil	142
2.3.7	Chiller	142
2.4	Measurement devices	142
2.5	Control of the test rig	143
3	TESTS DESCRIPTION AND ANALYSIS	144
3.1	Description of the tests	144
3.2	Fluid properties	145
3.3	Measurement post-processing.....	147
3.4	Expander performance	148
3.4.1	Gas flow rate displaced by the expander	148
3.4.2	Shaft power	150
3.4.3	Global isentropic effectiveness	151
	Internal isentropic effectiveness	152
	Volumetric effectiveness.....	153
3.4.4	Exhaust temperature	153
3.5	Compressor performance.....	155
3.5.1	Displaced mass flow rate.....	155

3.5.2	Shaft power	155
3.5.3	Exhaust temperature	156
3.5.4	Global isentropic effectiveness	157
	Global isentropic effectiveness	157
	Internal isentropic and volumetric effectiveness	157
3.6	Performance of the cycle.....	158
4	VALIDATION OF THE SCROLL MACHINES SEMI-EMPIRICAL MODELS	
	159	
4.1	General equation for compressible two-phase flow across an orifice	159
4.2	Expander model.....	161
4.2.1	Prediction of the mass flow rate	162
4.2.2	Prediction of the shaft power.....	163
4.2.3	Prediction of the exhaust temperature.....	165
4.3	Compressor model.....	165
4.3.1	Prediction of the mass flow rate	166
4.3.2	Prediction of the shaft power.....	166
4.3.3	Prediction of the exhaust temperature.....	167
5	PARAMETRIC STUDY OF THE COMPRESSOR AND EXPANDER PERFORMANCES.....	168
5.1	Expander performance	168
5.2	Compressor performance	169
5.3	Concluding remarks.....	170
6	CONCLUSIONS	171
7	REFRENCES	172

NOMENCLATURE

A	Area, m ²
AU	Heat transfer coefficient, W/K
C _d	Discharge coefficient, -
C _{ratio}	Capacitance ratio, -
c	Specific heat, J/kg-K
d	Diameter, m
h	Specific enthalpy, J/kg
\dot{H}	Enthalpy flow rate, kg/
k	Thermal conductivity, W/m-K
k	Specific heat ratio, -
K	Slip ratio, -
\dot{M}	Mass flow rate, kg/s
N	Rotational speed, Hz
P	Pressure, Pa
r _p	Pressure ratio, -
r _{v,in}	Built-in volume ratio, -
\dot{Q}	Heat transfer rate, W
s	Specific entropy, J/kg-K
T	Temperature, °C
T	Torque, N-m
x	Mass fraction, -
v	Specific volume, m ³ /kg
U	Velocity, m/s
\dot{V}	Volume flow rate, m ³ /s
\dot{W}	Power, W

Subscripts

amb	Ambient
c	Cold

calc	Calculated
cp	Compressor
e	Effective
ex	Exhaust
exp	Expander
g	Gas
glw	Glycol water
h	Hot
hex	Heat exchanger
in	Internal
l	Liquid
leak	Leakage
loss	Mechanical loss
m	Mixture
meas	Measured
mot	Motor
p	Isobaric
pp	Pump
s	Isentropic, swept
sh	Shaft
su	Supply
th	Theoretical
v	Volumetric

Greek and miscellaneous

α	Void fraction, -
Δ	Difference, -
ϵ	Effectiveness, -
ψ	Entrainment mass fraction, -
μ	Viscosity, Pa-s
ρ	Density, kg/m ³
*	Effective

1 INTRODUCTION

Under environmental pressure, conventional refrigerants are, or will be, phased out, because of their *direct impact* on the environment (associated to the release of refrigerant from equipments to the atmosphere). This explains the increase of interest for alternative refrigeration cycles in the last 20 years.

One of these alternative systems is the Ericsson cycle heat pump, which can use any non-condensable gas (air, helium, nitrogen,...) as refrigerant. The principle of the Ericsson cycle is given in the Appendix. For such a system, the direct impact on the environment is eliminated. However, its *indirect impact* must compete with that of vapor compression systems. The indirect impact is the CO₂ emission associated to the power production to drive the system. The indirect impact of the refrigeration system decreases with its Coefficient of Performance (COP).

The system investigated in this Chapter is the Liquid Flooded Ericsson Cycle Cooler (*LFEC*). Such a system uses liquid flooding of the compressor and the expander to approach isothermal compression and expansion processes. Hugenroth *et al.* (2007) were the first to investigate this cycle. They modeled the system in such a way to evaluate the variation of its performance with the main operating parameters. They also carried out an experimental study in order to prove the feasibility of the concept. The experimental set-up used nitrogen as the refrigerant and alkyl-benzene oil as the liquid to flood the compressor and the expander. The LFEC system is schematically represented in Figure 1-1. It mainly comprises a scroll compressor and expander, “cold” and “hot” heat exchangers (heat source and heat sink of the cycle) and a regenerator. As explained more in details in §2.1, two oil separators are installed at the heat exchangers’ exhaust. Separated oil is driven to the compressor and expander supplies by means of a hydraulic motor and a pump respectively. Scroll compressor and expander are selected for their ability to tolerate the large amount of liquid flooding inherent to this application.

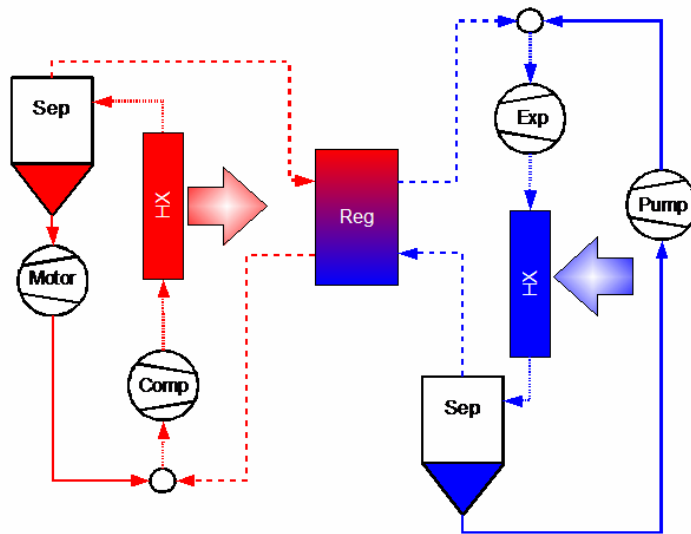


Figure 1-1: Representation of the Liquid Flooded Ericsson Cycle Cooler

Another way to approach isothermal compression and expansion has been investigated by Kim *et al.* (2004). They suggested using a heat-pipe heating structure to keep the scroll expander at a uniform temperature. According to the authors a considerable quantity of heat can be added to the working fluid through the scroll wrap.

Hugenroth *et al.* (2007) showed that the performance of the LFEC strongly correlates with that of the compressor and the expander. Therefore, the design of these machines has to be optimized for this application.

The work presented in this chapter mainly focuses on the expander. However, for comparison, some results related to the compressor are also presented. The objective of the experimental study was to collect detailed experimental data for evaluating the impact of operating conditions on the expander performance and for validating a comprehensive (deterministic) model of the liquid flooded scroll expander model (Chapter 7). Analysis of the flooded compression has been carried out in parallel by Bell *et al.* (2008b).

2 DESCRIPTION OF THE TEST RIG

The test rig employed by Hugenroth *et al.* (2007) was modified to account for recommendations from its work. A detailed schematic of the rig with all the major components and the instrumentation is shown in Figure 2-1. The system was set up using mostly off-the-shelf components with little modification.

2.1 System operation

The system operation can be described according to the following steps (see Figure 2-1):

- a) The mixture of nitrogen and oil enters the compressor at low temperature and pressure.
- b) After compression, the mixture at high pressure is cooled through a (“hot”) heat exchanger.
- c) At the exhaust of the heat exchanger, oil is separated from the nitrogen by means of an oil separator and sent to a hydraulic motor. Further separation of the oil is achieved in a second stage separator, which can optionally be bypassed.
- d) Gas coming from the regenerator is mixed with oil coming from the hydraulic motor.
- e) Heat is transferred from the gas at higher temperature coming from the “hot”-side of the system to the gas at lower temperature coming back from the “cold”-side.
- f) Gas at lower temperature is then mixed with oil discharged from the pump.
- g) The mixture is expanded through the expander and then heated through a (“cold”) heat exchanger, producing the cooling effect of the cycle.
- h) At the exhaust of this heat exchanger, oil is extracted from the gas by means of a first stage separator and circulated by the pump. Further separation is achieved by means of a second stage separator.
- i) Gas, at low temperature and pressure, flows through the regenerator to the hot-side of the system, where it is mixed with oil coming from the hydraulic motor.

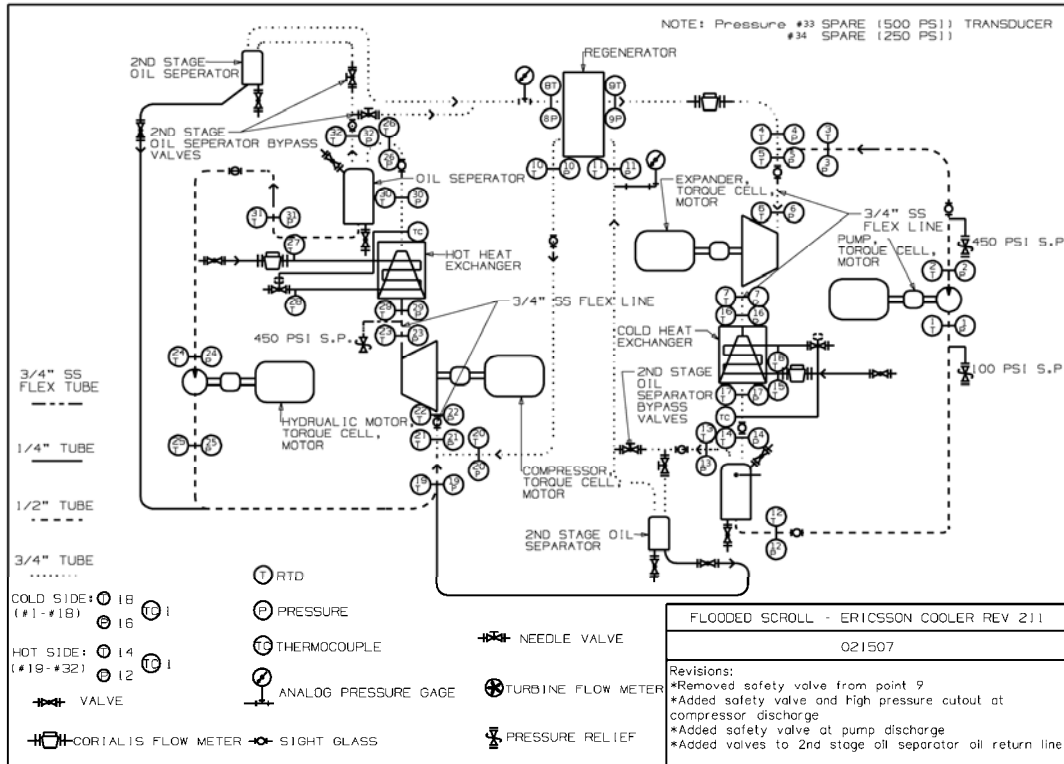


Figure 2-1: Schematic of the LFEC test rig

2.2 Recommendations from previous work

Hugenroth *et al.* (2007) presented data from 70 experimental runs. The achieved efficiency was very poor, due to the fact that only off-the-shelf components had been selected. Moreover, this performance was reduced because of large pressure drops in the piping. Reducing these pressure drops was one of the main improvements of the new test bench.

The test rig employed by Hugenroth lacked the instrumentation to adequately measure the heat losses and gains through the system (whose physical size is large, compared to cooling capacity). Additional instrumentation has been installed on the new test bench.

Flow and temperature measurement errors played a significant role in difficulties encountered while analyzing the experimental data. The ± 0.5 K uncertainty in temperature measurements proved to be significant and detrimental for data analysis. Thermocouples have been replaced by Resistance Temperature Detectors (RTD's) Pt-100.

The location of the heat exchangers has been modified, following one of the conclusions of Hugenroth's work, arguing that the heat exchangers should be put directly downstream of the compressor and expander exhaust, in order to improve the performance.

Hugenroth encountered some trouble with measuring the oil mass flow rate with a Coriolis flowmeter, because of the presence of entrained gas bubbles. The Coriolis flowmeters have been removed from the oil lines and are presently used to measure the secondary fluid flow rates through the heat exchangers.

2.3 Components

2.3.1 Compressor and expander

As mentioned previously, scroll machines are used for their ability to tolerate large amounts of oil without excessive loading on the elements. This is mainly due to the fact that scroll machines do not use valves to control suction and discharge flows. The timing of suction and discharge is purely determined by the scroll geometry (Preissner, 2001). By contrast, in reciprocating machines, these processes are externally controlled by valves. Hence, oil entrapped in the dead volume may damage the compressor elements at the end of the piston motion.



Figure 2-2: Scroll compressor and expander housing (Hugenroth, 2006)



Figure 2-3: View of the orbiting scroll (left) and the fixed scroll (right) (Hugenroth, 2006)

In the system considered, the compressor and the expander are originally the same automotive open-drive scroll compressor designed for use in vapor compression systems using R-134a refrigerant. Their displacement $V_{s,cp}$ (in compressor mode) is equal to 104.8 cm³ and their built-in volume ratio $r_{v,in}$ is close to 1.6. This value has been calculated by Bell *et al.* (2008a), based on the measurements of the scroll geometry. Note that Hugenroth *et al.* (2007) measured a volume ratio of 1.8, what introduces a considerable difference in terms of expander displacement.

Two modifications were made to the original machines. For both of them, the discharge valve was removed: in expander mode, it would have prevented the liquid to enter the suction chamber and, in compressor mode, it might have been broken by the large amount of liquid. The second modification consisted in removing the radial compliance system. This system allows the orbiting and the fixed scroll to separate in the presence of contamination or large liquid slugs. It however imposes a minimal rotational speed to ensure the contact between the wraps by centrifugation and to ensure flank sealing.

2.3.2 Liquid separators

Oil separation from the gas is achieved by means of two different liquid separators in series (on both the cold- and the hot-sides of the system). In the *first stage separators*, liquid and gas are separated by gravity. Remaining oil mist is removed from the gas by centrifugation in the *second stage separators* (located downstream of the first stage on the gas line). Service valves are installed at the bottom of both first stage separators. They are used to charge the system with oil and nitrogen. Two sight glasses are located on the first stage separators. The sight glasses allow visual inspection of the oil levels on both sides of the rig.

2.3.3 Heat exchangers and regenerator

The cold- and hot-side heat exchangers and the regenerator are brazed stainless plate heat exchangers. The cold- and hot-side heat exchangers are fed with almost pure ethylene glycol.

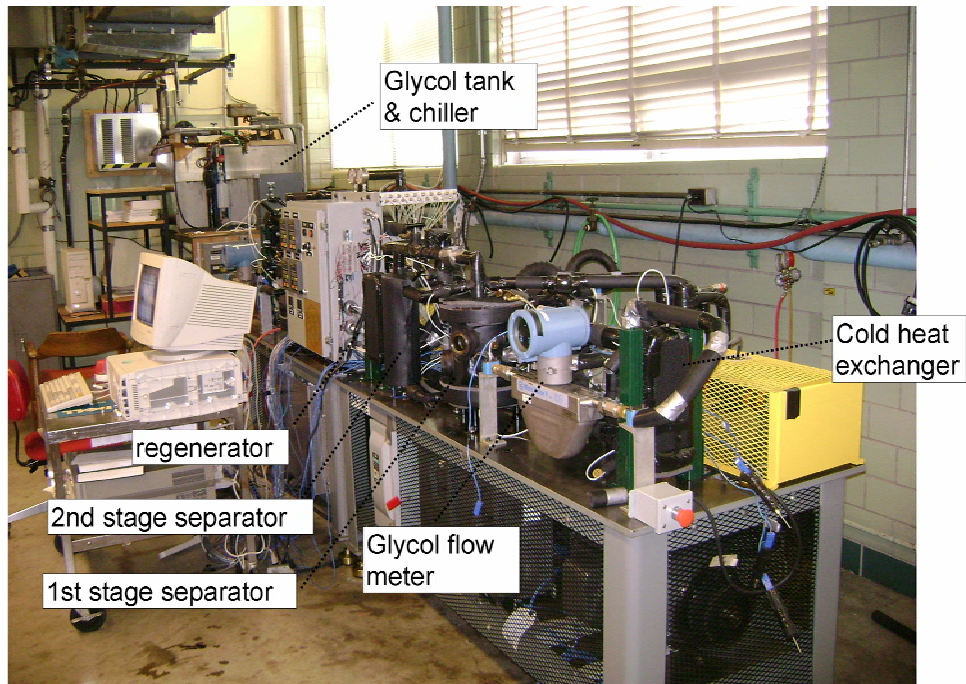


Figure 2-4 View of the "cold"-side of the Liquid Flooded Ericsson Cooler test rig

2.3.4 Hydraulic motor and pump

A vane-type pump and a hydraulic motor are used on the cold- and hot-liquid loops respectively. The hydraulic motor has a displacement of $18.0 \text{ cm}^3/\text{rev}$, while that of the pump is $17.2 \text{ cm}^3/\text{rev}$. The pressure limit is 275 bar, which is well above the operating pressure of the rig. However, the lower pressure of the pump could not exceed 7 bar, in order to avoid damage to the pump seal. This restriction also limits the low-side pressure of the system.

2.3.5 Electrical motors

Four 230 V three-phase 10 HP electrical motors were used to operate the compressor, expander, pump and hydraulic motor. The speed of each of the four machines can be controlled (in the range of 0-5000 rpm, with an accuracy of 1 rpm) by means of motor

controllers. The shafts of the electrical motors are coupled to the shafts of the rotating machinery via toothed pulleys and belts. Under normal operation, the motor associated to both the expander and the hydraulic motor work in generator mode. Generated electrical power is transferred to the controllers of the compressor and the pump motors.

2.3.6 Gas and oil

As mentioned previously, the selected gas for this application is nitrogen and the liquid is Zerol 60 alkyl-benzene oil. This is a synthetic refrigeration oil with properties similar to mineral oils. The lowest available viscosity (60 SUS) has been chosen in order to minimize pressure drops in the liquid loops (Hugenroth, 2006).

2.3.7 Chiller

A recirculating water cooled chiller is used to provide a heat source and a heat sink to the cold and to the hot heat exchangers respectively. The heat transfer fluid is (almost) pure ethylene glycol (Dowtherm SR-1). In order to be accurate on the specific heat of the glycol, its density is regularly measured so that the water content (a few percent) could be determined. Actually, the ethylene glycol (which is in a tank opened to the ambient) is highly hygroscopic.

2.4 Measurement devices

The following instrumentation was initially installed on the test rig (see Figure 2-1):

- Thirty two Pt-100 Resistance Temperature Detectors (RTDs): located at the main points of the system.
- Twenty eight pressures transducers (0-250 psig and 0-500 psig, i.e. 0-17.24 bar and 0-34.48 bar): also located at the main points of the system.
- Four thermocouples: at the supply and exhaust of the compressor and the expander.
- Four 200 in-lbf (0-22.60 N-m) torque meters
- Four motor speed output from the motor controllers
- Three Coriolis mass flow meters: on the gas line and on the glycol loops feeding both “cold” and “hot” heat exchangers.

All instrumentation data was collected by an HP 75000 data acquisition system. An Agilent VEE program was written to display performance data during the tests. An EES program was built to analyze the data relative to all the tests.

Accuracy of the measurement devices is given in Table 2-1.

Table 2-1: Measurement devices accuracy

RTD	Thermocouple	Low Pressure	High Pressure	Coriolis flow meters	Torque
±0.2 K	±0.5 K	±2.24 kPa	±4.48 kPa	±1%	±0.0136 N.m

There is no direct measurement of the oil flow rates through the compressor and the expander. Previous work (Hugenroth, 2006) showed that the presence of remaining gas in the oil (in the oil lines) does not make the use of a Coriolis flow-meter possible. As explained latter, the oil flow rates will be estimated by means of energy balances across the compressor and across the expander.

2.5 Control of the test rig

Before each test, the system is evacuated by means of a vacuum pump. Oil is then charged through the service valve of the first stage separators on both the hot and cold sides. Nitrogen is finally charged (up to 60 psig, i.e. 4.14 bar relative) through the service valve of the first stage separator on the cold side. The chiller is switched on. The speeds of the compressor, the expander, the pump and the hydraulic motor are set on the control panel. These machines are started simultaneously. The oil circulation rate in both the compressor and the expander is controlled by adjusting the rotational speed of the motor and the pump. The pressure level at one reference point of the system is controlled by varying the nitrogen charge. If charge is added during the test in order to increase the pressures, it has to be removed before stopping the test, so that a pressure lower than 100 psig (6.89 bar gauge) is maintained at the pump supply.

3 TESTS DESCRIPTION AND ANALYSIS

3.1 Description of the tests

The experimental program is described in the test matrix given in Table 3-1. The compressor speed is maintained constant. Four different speed ratios between the compressor and the expander are achieved, by imposing four different expander speeds. The pump and the hydraulic motors are run at three different speeds. Finally, three different levels of pressure are imposed by varying the nitrogen charge in the system. A total of 27 tests is defined by combining some of these operating conditions.

Table 3-1: Test Matrix

	N_{cp} [rpm]	N_{exp} [rpm]	N_{mot} [rpm]	N_{pp} [rpm]	Pressure
1	3500	865	120	60	Low
2	3500	865	240	120	Low
3	3500	865	480	240	Low
4	3500	865	120	60	Medium
5	3500	865	240	120	Medium
6	3500	865	480	240	Medium
7	3500	865	120	60	High
8	3500	865	240	120	High
9	3500	865	480	240	High
10	3500	1155	120	60	Low
11	3500	1155	240	120	Low
12	3500	1155	480	240	Low
13	3500	1155	120	60	Medium
14	3500	1155	240	120	Medium
15	3500	1155	480	240	Medium
16	3500	1155	120	60	High
17	3500	1155	240	120	High
18	3500	1155	480	240	High
19	3500	1751	120	60	Low
20	3500	1751	240	120	Low
21	3500	1751	480	240	Low
22	3500	1751	120	60	Medium
23	3500	1751	240	120	Medium

24	3500	1751	480	240	Medium
25	3500	1751	120	60	High
26	3500	1751	240	120	High
27	3500	1751	480	240	High

Three series of additional tests were performed:

- one series of tests at higher temperatures,
- one series of tests with constant rotational speed, low expander supply temperature, high expander supply pressure and pump speed varying from 39 to 216 rpm,
- one series of tests with constant rotational speed, low expander supply temperature, low expander supply pressure and pump speed varying from 39 to 216 rpm.

In total, 59 tests have been performed.

3.2 Fluid properties

This paragraph gives the expression used for calculating the properties of the mixture of oil (called “liquid” hereunder) and gas.

The mixture density ρ_m can be expressed as a function of the void fraction α and the densities of the gas ρ_g and liquid ρ_l .

$$\rho_m = \alpha \rho_g + (1 - \alpha) \rho_l \quad (3-1)$$

The void fraction is the ratio of the gas flow cross section to the total cross section. It can be written as a function of the gas mass dryness x_g , the slip ratio K and the specific volumes of each fluid v_l and v_g :

$$\alpha = \frac{x_g v_g}{x_g v_g + K(1 - x_g)v_l} \quad (3-2)$$

The slip ratio (also called “velocity ratio”) is the ratio between the mean velocities U_g of the gas to the mean velocity U_l of the liquid:

$$K = \frac{U_g}{U_l} \quad (3-3)$$

Combining the last two equations gives:

$$\rho_m = \frac{x_g + K(1-x_g)}{x_g/\rho_g + K(1-x_g)/\rho_l} = \frac{1}{v_m} \quad (3-4)$$

Except for the suction, discharge and leakage flows, the homogeneous density, which is actually considered in this modeling, assumes that both phases have the same velocity ($K=1$), giving

$$\rho_h = \frac{1}{x_g/\rho_g + (1-x_g)/\rho_l} = \frac{1}{v_h} \quad (3-5)$$

The mixture viscosity and thermal conductivity are given as (Levy, 1999)

$$\mu = \left(\frac{1}{\mu_l} x_l + \frac{1}{\mu_g} x_g \right)^{-1} \quad (3-6)$$

$$k_h = k_l(1-\alpha_h) + k_g \alpha_g \quad (3-7)$$

The enthalpy of the mixture is calculated by:

$$h_m = x_g h_g + x_l h_l = (1-x_l)h_g + x_l h_l \quad (3-8)$$

The mixture specific internal energy u_m , mixture specific entropy s_m , and mixture constant pressure specific heat $c_{p,m}$ are defined in a similar way.

As mentioned previously, in the case of the oil-flooded system currently investigated, the mixture is made up nitrogen and alkyl-benzene oil. Nitrogen is considered as an ideal gas. Hence, its enthalpy is only a function of its temperature. The heat capacity is given by a polynomial expression of the temperature, whose coefficient can be found in thermodynamics textbooks. Thermal properties of alkyl-benzene oil are derived from polynomial functions of the temperature. The latter have been identified in laboratory and are given in the Appendix. Properties of nitrogen and oil at 25°C and 1 bar are summarized in Table 3-2.

Table 3-2: Noticeable properties of nitrogen and oil at 25°C and 1 bar

	Nitrogen	Oil
ρ [kg/m ³]	1.13	851.99
μ [kg/m-s]	0.00001814	0.0102
c_p [J/kg-K]	1042	1883
k [W/m-K]	0.02575	0.1153

3.3 Measurement post-processing

As mentioned previously, the *gas flow rate* is measured by means of a Coriolis flow meter installed on the gas line between the hot side of the second stage separator and the regenerator (see Figure 2-1). Note that the same flow rate is flowing through the compressor and the expander. It is assumed that the first and second stage separators remove almost all the oil from the gas. As a limit case, it is assumed that only pure gas is flowing through the gas flow meter. Actually, inspection through a sight glass installed between the exhaust of the heat exchanger and the expander supply revealed that little or no liquid is entrained by the gas.

The *oil flow rates* through the compressor and expander are not directly measured. They can only be estimated on the basis of:

- energy balances on the hot and cold heat exchangers;
- energy balances on the compressor or expander;
- pump and motor displacement.

In the early stage of the project, heat balances on the heat exchangers were considered. It appeared that this method was largely inaccurate, due to problems of temperature measurements for two phase flows.

Estimating the oil mass flow rates based on the pump or motor displacement assumes that the volumetric effectiveness is 100%. Actually, this effectiveness may be lower due to internal leakages.

The oil mass flow rates are finally estimated by expressing the energy balances across the compressor and the expander with an estimate of the global heat transfer coefficient between the machines and the ambient (Figure 3-1):

$$\dot{Q}_{\text{amb}} = AU_{\text{amb}}(T_{\text{ex,meas}} - T_{\text{amb}}) \quad (3-9)$$

The heat transfer coefficient is estimated to 1W/K for each machine (Hugenroth *et al.*, 2007).

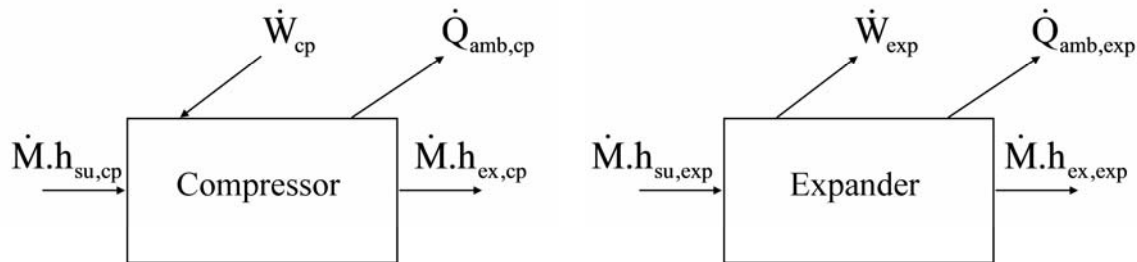


Figure 3-1: Energy balance on the compressor and on the expander

3.4 Expander performance

3.4.1 Gas flow rate displaced by the expander

Figure 3-2 shows the evolution of the measured gas flow rate with the specific volume of the gas at the supply of the expander for the three different expander speeds (first series of tests). The gas mass flow rate increases with the expander speed, due to the increase of its

displacement. As it was to be expected, the gas mass flow is also a decreasing function of the specific volume of the gas, because of the volumetric characteristic of the machine. Note that the oil phase never occupies more than 7% of the expander displacement.

Analysis of the measurements made also appear that, for a given level of pressure (low, medium or high), the expander supply pressure decreases (and hence the specific volume of the gas increases) as the oil flow rate is increased (by increasing the pump rotational speed). This is probably explained by the increase of the pressure drops along the piping.

Under the following assumptions:

- composition of the internal leakage equal to that of the mixture entering the expander,
- no suction pressure drop,
- no suction heat transfer,

the following relationship can be established:

$$\dot{M}_{\text{gas}} = \dot{M}_{\text{gas,th,exp}} + \dot{M}_{\text{gas,leak,exp}} = (1 - x_{l,\text{exp}}) \frac{\dot{V}_{s,\text{exp}}}{V_{\text{mix,su,exp}}} + \dot{M}_{\text{gas,leak,exp}} \quad (3-10)$$

The first term is the theoretical gas flow rate computed based on the expander displacement¹. The second term is the gas leakage flow rate. The evolution of the measured gas flow rate and theoretical mass flow rate are compared in Figure 3-3. The gas leakage flow rate can be estimated by difference.

¹ This displacement has been computed based on the compressor displacement (104.8 cm^3) and an internal built-in volume ratio of 1.6. Considering an internal built-in volume ratio of 1.8 wouldn't change qualitatively the results.

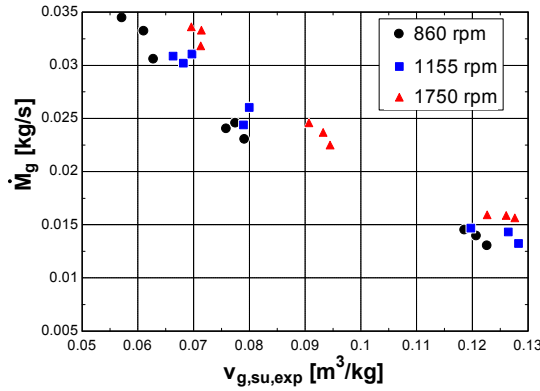


Figure 3-2: Evolution of the gas flow rate with the gas specific volume at the expander supply

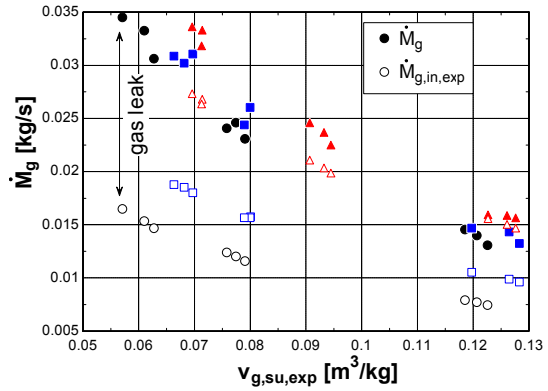


Figure 3-3: Estimation of the gas leakage flow rate in the expander

Figure 3-3 demonstrates the magnitude of the internal leakage. Surprisingly, the leakage flow rate seems to decrease with the expander speed. The large internal leakage explains the low volumetric effectiveness (see Figure 3-7). Note that, a smaller internal leakage was actually expected given the amount of oil displaced in the expander. Possible explanations will be discussed latter.

3.4.2 Shaft power

The evolution of the expander shaft power as function of the gas flow rate (first series of tests) is shown in Figure 3-4. For each pressure level and each rotational speed, the shaft power is a decreasing function of the oil flow rate. This is partially explained by the decrease of the expander pressure ratio with the oil flow rate (due to the larger pressure drop through the piping and the cold heat exchanger), what is an undesirable feature of the investigated system.

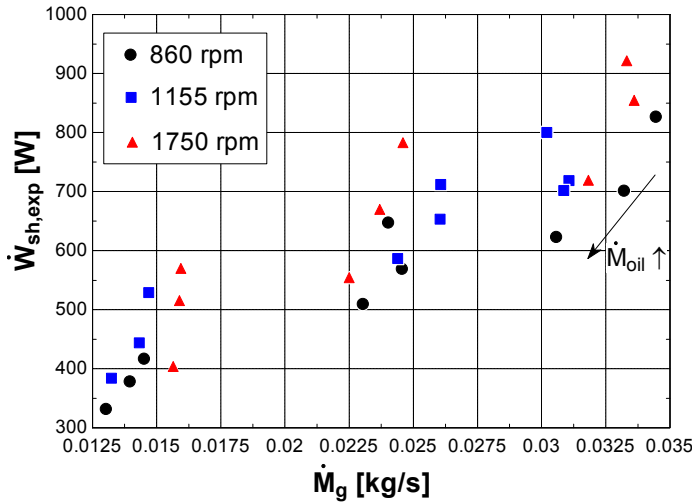


Figure 3-4: Evolution of the expander shaft power with the gas flow rate

3.4.3 Global isentropic effectiveness

The *global isentropic* effectiveness, defined in Equation (3-11), can be decomposed into the *internal isentropic* effectiveness and *volumetric* effectiveness (Kohsokabe *et al.*, 2008). To a first approximation, the internal isentropic effectiveness only depends on suction pressure drop, mechanical loss and under- or over-expansion loss.

$$\varepsilon_{s,\text{exp}} = \frac{\dot{W}_{\text{exp,meas}}}{\dot{M}_{\text{exp,meas}} \cdot (h_{\text{su,exp}} - h_{\text{ex,exp,s}})} = \frac{\dot{W}_{\text{exp,meas}}}{\dot{M}_{\text{exp,th}} \cdot (h_{\text{su,exp}} - h_{\text{ex,exp,s}})} \cdot \frac{\dot{M}_{\text{exp,th}}}{\dot{M}_{\text{exp,meas}}} = \varepsilon_{s,\text{in,exp}} \varepsilon_{v,\text{exp}} \quad (3-11)$$

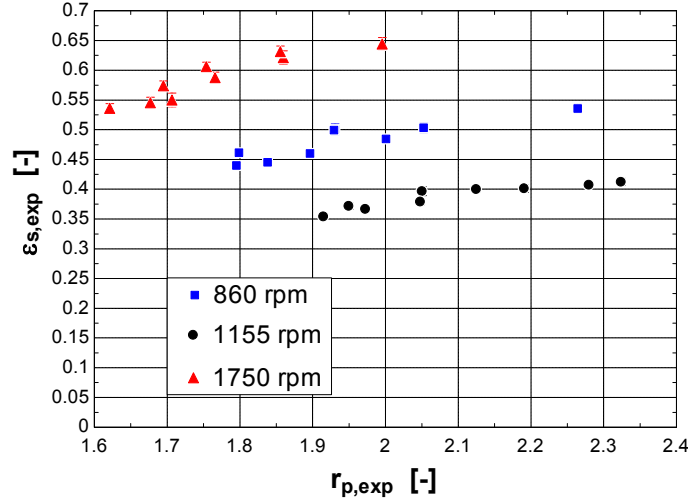


Figure 3-5: Evolution of the measured expander global isentropic effectiveness with the pressure ratio

Internal isentropic effectiveness

Figure 3-6 shows that, in the first test series, the internal volumetric effectiveness is a decreasing function of the oil mass fraction. This can be due to an increase of the expander suction pressure drop and an increase of the mechanical loss. The decrease of the expander performance with the oil mass fraction also partly explains the decrease of shaft power already observed in Figure 3-4.

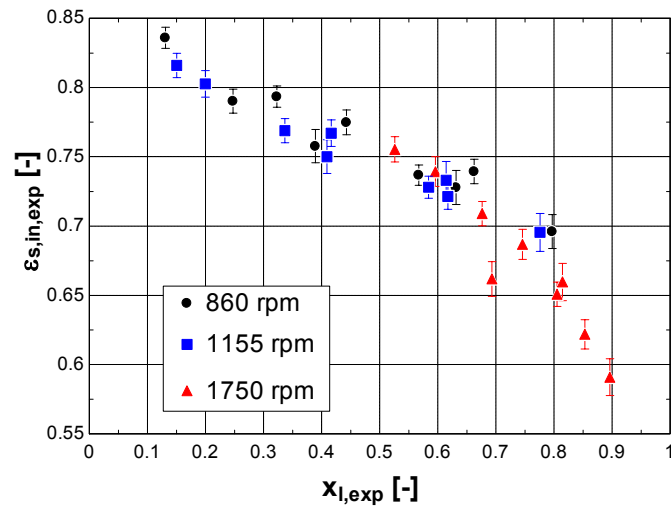


Figure 3-6: Evolution of the expander internal isentropic effectiveness with the oil mass fraction

Volumetric effectiveness

Figure 3-7 shows the expander volumetric effectiveness as a function of the pressure differential over the expander, for the first series of tests. The volumetric effectiveness clearly improves as the expander speed is increased. Values close to 1 could be due to excessive suction pressure drop associated to the large amount of oil. The increase of the volumetric effectiveness with increasing rotational speeds is consistent with the relative decrease in the internal leakage and the increase of suction pressure drop.

As mentioned before, the achieved volumetric effectiveness appears to be very poor, given the amount of oil displaced through the expander. Hugenroth (2006) observed a similar behavior and assumed that this can be due to excessive clearance between the fixed and the orbiting scrolls, since the radial compliance feature was removed from the expander (and the compressor).

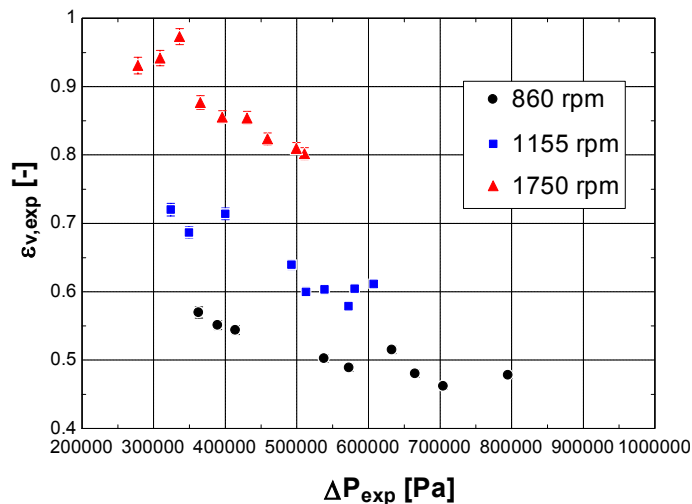


Figure 3-7: Evolution of the expander volumetric effectiveness with the pressure differential over the expander

3.4.4 Exhaust temperature

Figure 3-8 shows the evolution of the effective isentropic exponent k^*_{exp} and of the reduced exhaust temperature with the capacitance ratio C_{ratio} . This ratio, introduced by Hugenroth (2006), is defined as

$$C_{ratio,exp} = \frac{\dot{M}_{l,exp} c_1}{\dot{M}_g c_{p,g}} \quad (3-12)$$

This parameter eliminates the need to consider the flow rates and specific heat values of the fluid independently.

The exhaust temperature is nondimensionalized with respect to the supply temperature

$$T_{ex,exp}^* = \frac{T_{ex,exp} + 273.15}{T_{su,exp} + 273.15} \quad (3-13)$$

The effective isentropic exponent k_{exp}^* is defined as

$$k_{exp}^* = \frac{\dot{M}_g c_{p,g} + \dot{M}_{l,exp} c_1}{\dot{M}_g c_{v,g} + \dot{M}_{l,exp} c_1} \quad (3-14)$$

This figure shows that the slope of both the effective isentropic exponent and the discharge temperature is very steep for lower C_{ratio} values.

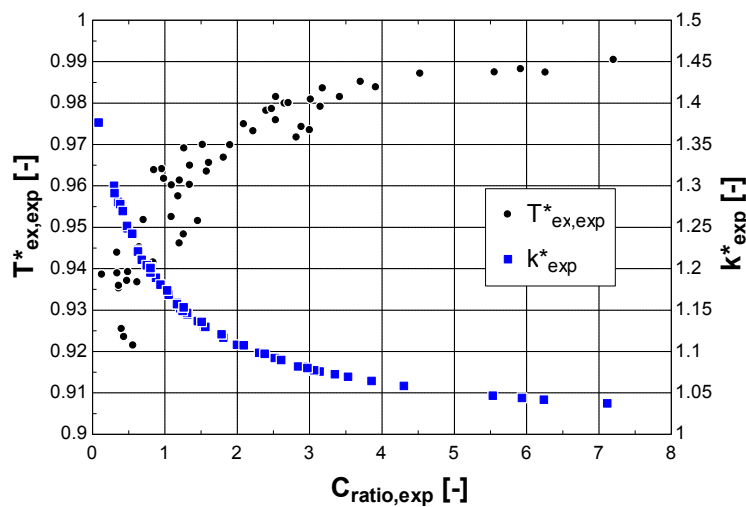


Figure 3-8: Variation of the reduced discharge temperature and effective isentropic exponent with the expander C_{ratio}

3.5 Compressor performance

The initial objective of the present work was to focus on the expander. However, analyzing the performance of the compressor could help better understanding the expander performance. The same approach will be adopted for the semi-empirical modeling of the machines: parameters identified for the expander will be compared to those identified for the compressor.

3.5.1 Displaced mass flow rate

Figure 3-9 shows the evolution of the measured gas flow rate with the gas specific volume at the compressor supply. The hyperbolic evolution is due to the volumetric characteristics of the machine. The three groups of points correspond to the three levels of pressure. Also the compressor was run at the unique speed of 3500 rpm. As a difference with the expander mode, the measured gas flow rate and the internal mass flow rate are very close from each other. This means that internal leakages are much more limited than in expander mode.

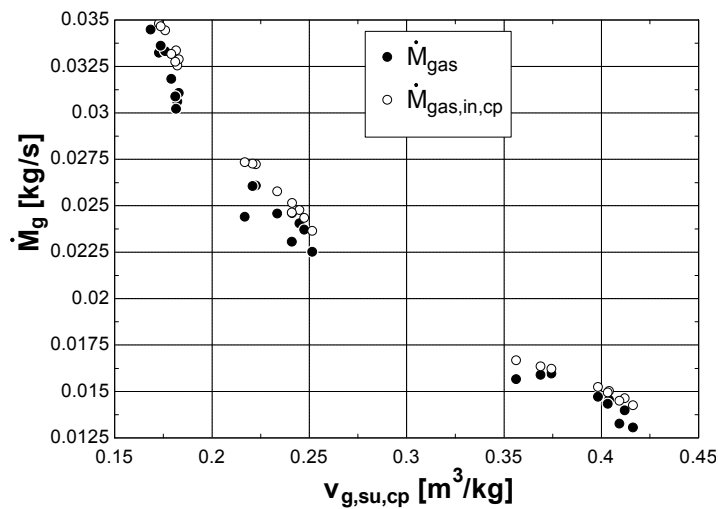


Figure 3-9: Evolution of the gas flow rate with the gas specific volume at the compressor supply

3.5.2 Shaft power

The evolution of the compressor shaft power with the gas flow rate, for the first series of tests, is shown in Figure 3-10. The power increases with the gas flow rate with scattering due to variation of the pressure ratio and the oil flow rate.

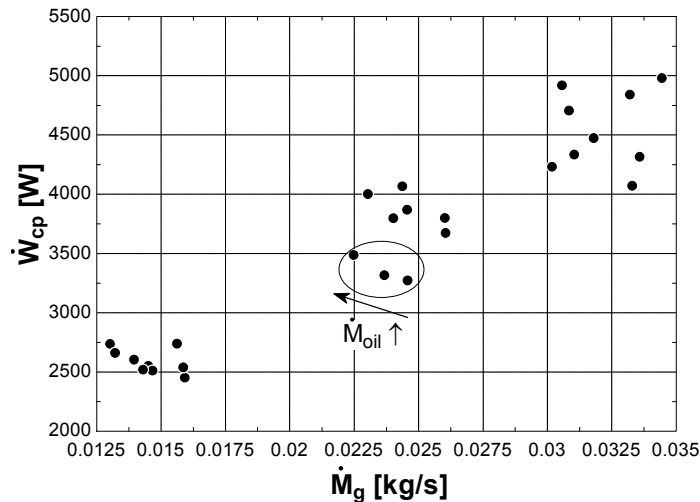


Figure 3-10: Evolution of the compressor shaft power with the gas mass flow rate

3.5.3 Exhaust temperature

The evolution of the effective isentropic exponent and the reduced exhaust temperature with the capacitance ratio is given in Figure 3-11.

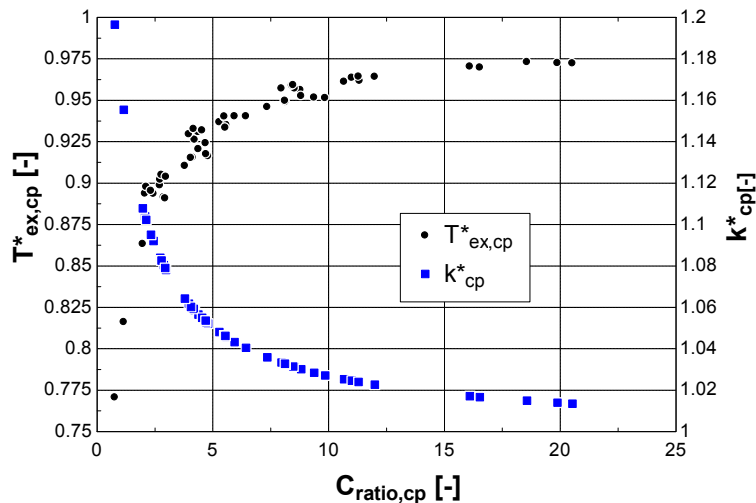


Figure 3-11: Variation of the reduced discharge temperature and effective isentropic exponent with the expander C_{ratio}

3.5.4 Global isentropic effectiveness

As for the expander, the isentropic effectiveness can be split into internal isentropic effectiveness and volumetric effectiveness.

$$\varepsilon_{s,cp} = \frac{\dot{M}_{cp,meas} \cdot (h_{ex,cp,s} - h_{su,cp})}{\dot{W}_{cp,meas}} = \frac{\dot{M}_{cp,th} \cdot (h_{ex,cp,s} - h_{su,cp})}{\dot{W}_{cp,meas}} \frac{\dot{M}_{cp,meas}}{\dot{M}_{cp,th}} = \varepsilon_{s,in,cp} \varepsilon_{v,cp} \quad (3-15)$$

Global isentropic effectiveness

Figure 3-12 shows that the global isentropic effectiveness decreases with the oil mass fraction, which is an undesirable feature of the machine.

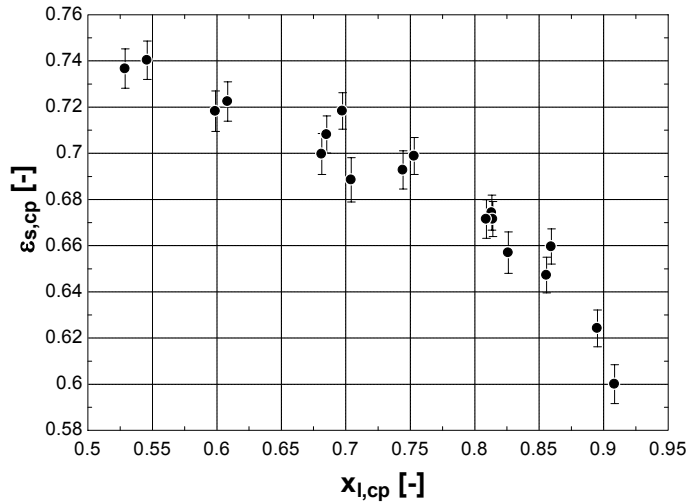


Figure 3-12: Evolution of the compressor global isentropic effectiveness with the oil mass fraction

Internal isentropic and volumetric effectiveness

Figure 3-13 and Figure 3-14 show that the decrease of the global isentropic effectiveness with the oil mass fraction is actually due to the decrease of the internal isentropic effectiveness. At this point of the analysis, it is not possible to identify with certainty the underlying reason. However, it might be explained by suction and discharge pressure drops as well as mechanical loss increasing with the oil mass fraction.

The achieved volumetric effectiveness is much larger than for the expander. Moreover, it does not present large variations as for the expanders (for the 59 achieved points, it varies between 89 and 98%).

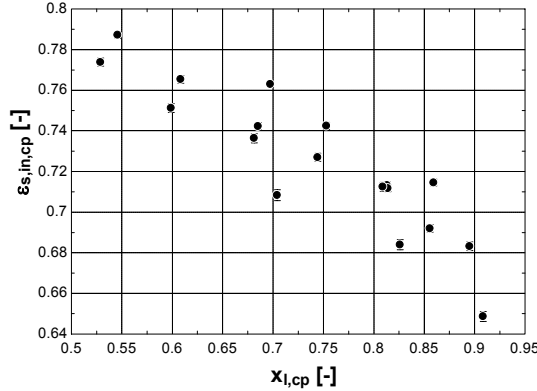


Figure 3-13: Evolution of the compressor internal isentropic effectiveness with the oil mass fraction

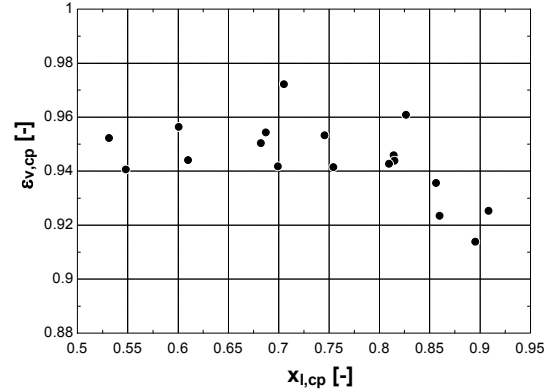


Figure 3-14: Evolution of the compressor volumetric effectiveness with the oil mass fraction

3.6 Performance of the cycle

The variation of the LFEC performance with operating parameters has already been investigated by Hugenroth *et al.* (2007). For the tests presented hereunder the maximal cycle COP (Coefficient of Performance) was 0.22. This COP is defined as

$$\text{COP} = \frac{\dot{H}_{\text{glw,hex,c}}}{\dot{W}_{\text{net}}} \quad (3-16)$$

where

$$\dot{W}_{\text{net}} = \dot{W}_{\text{cp}} - \dot{W}_{\text{exp}} + \dot{W}_{\text{pp}} - \dot{W}_{\text{mot}} \quad (3-17)$$

The maximal cooling ($\dot{H}_{\text{glw,hex,c}}$) and heating ($\dot{H}_{\text{glw,hex,h}}$) capacities were 609W and 4331W respectively.

4 VALIDATION OF THE SCROLL MACHINES SEMI-EMPIRICAL MODELS

The validation of the compressor and expander models in the case of flooded compression and expansion is presented in this section. The identification of the model parameters should be helpful to better evaluate the effect of the different sources of irreversibility and better understand the measured performance presented in §3.4 and 3.5. Among others, the following questions might be addressed:

- Could the decrease in both the compressor and the expander performance with the increase of oil mass fraction be explained by suction and discharge pressure drops?
- What would be the leakage area necessary to predict the measured volumetric effectiveness?
- What is the order of magnitude of the mechanical loss?

4.1 General equation for compressible two-phase flow across an orifice

In both the semi-empirical model and the deterministic models, flow across different orifices will be described. Among others, the latter are the suction and discharge ports, the leakage flow passages and the opening between the chambers.

Models available to describe the flow of a two-phase mixture through nozzles, orifice and other flow elements can essentially be classified between those accounting for the compressibility of the gas and those assuming no gas density change. With respect to the pressure differential characteristics of suction, discharge and leakage flow, the former models should be considered.

Among other models, Chisholm (1983) derived an expression for calculating the flow rate of a compressible gas-liquid mixture through an orifice, based on conservation of momentum:

$$\dot{M} = C_d A_2 \sqrt{\frac{-2 \int_{P_1}^{P_2} v_e dP}{v_{e,2}^2 \left[1 - \left(\frac{A_2 v_{el}}{A_1 v_{e2}} \right)^2 \right]}} \quad (4-1)$$

Subscripts 1 and 2 refer to the upstream and downstream conditions respectively. Unless some assumptions are made (Morris, 1991), there is no analytical solution to this equation and it must be solved numerically. Note that choking conditions occurs when further decrease in the downstream pressure yields an increase of the mass flow rate.

Different expressions of the effective specific volume v_e (also called *momentum* specific volume) have been proposed according to the flow pattern (Chisholm, 1983 and Morris, 1991). In the most general case of a separated-phase flow with some liquid entrained in the gas (and flowing at the gas velocity), the following equation can be established:

$$v_e = \left[x_g v_g + K_e (1 - x_g) v_1 \left[x_g + \frac{1 - x_g}{K_e} \right] \right] \quad (4-2)$$

The effective slip ratio is given by

$$K_e = \left[\psi + \frac{(1 - \psi)^2}{K - \psi} \right]^{-1} \quad (4-3)$$

where ψ is the fraction of liquid that travels in the gas phase at the gas velocity. The entrainment slip ratio K is evaluated from:

$$K = \psi + (1 - \psi) \sqrt{\frac{1 + \psi[(1 - x_g)/x_g] v_1 / v_g}{1 + \psi(1 - x_g)/x_g}} \sqrt{\frac{v_g}{v_1}} \quad (4-4)$$

The two limiting case of this model correspond to $\psi=0$ and $\psi=1$. In the former case, the two phases are purely separated. In the latter case, the mixture is homogeneous and equation (4-2) reduces to equation (3-5)².

² Note that in the case of $x_l=0$, Equation (4-1) reduces to the equation for the isentropic flow through a converging nozzle.

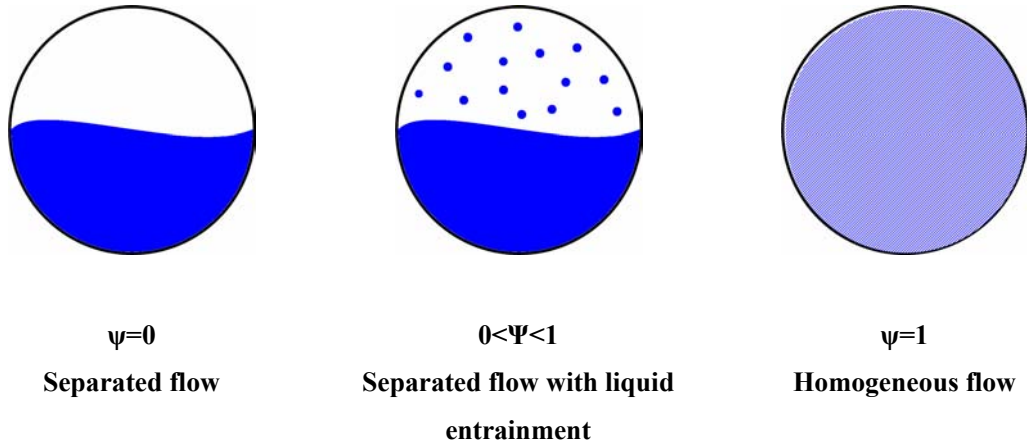


Figure 4-1: Two-phase flow patterns

4.2 Expander model

The inputs of the model are the supply pressure, the supply temperature, the exhaust pressure, the oil mass fraction in the mixture, the expander rotational speed and the ambient temperature.

Parameters must be identified in order to bring the mechanical power, the displaced mass flow rate and the discharge temperature predicted by the model as close as possible to measurements. Identified parameters are given in Table 4-1. Both suction and discharge pressure drops have been introduced in the modeling.

It was observed that the built-in volume ratio has to be tuned in order to get the best agreement between measurements and predictions by the model. The identified built-in volume ratio is 1.7. The volume ratio calculated based on measurements was 1.6. This represents a difference of 6.25% between the expander displacement considered in the semi-empirical model and in the deterministic model.

Table 4-1: Identified parameters of the expander semi-empirical model

$V_{s,exp}$ [cm ³]	$AU_{su,exp}$ [W/K]	$AU_{ex,exp}$ [W/K]	$AU_{amb,exp}$ [W/K]	$r_{v,in,exp}$ [-]	$T_{loss,exp}$ [N·m]	$d_{su,exp}$ [mm]	$d_{ex,exp}$ [mm]	$A_{leak,exp}$ [mm ²]
61.65	$20\left(\frac{\dot{M}}{0.012}\right)^{0.8}$	$20\left(\frac{\dot{M}}{0.012}\right)^{0.8}$	1.5	1.7	0.7	12	13	§4.2.1

4.2.1 Prediction of the mass flow rate

It was not possible to identify one unique leakage area. This has been anticipated by the evolution of the gas leakage flow rate given in Figure 3-3. The leakage area has been identified by imposing the calculated gas mass flow rate to be equal to the measured one.

Figure 4-2 shows the evolution of the identified leakage area with the pressure ratio for the three different achieved rotational speeds. It appears that the leakage area strongly correlates with the pressure ratio and the rotational speed.

The maximal leakage area is around 7 mm^2 , which is a fairly large value. For comparison, the leakage area identified for the Rankine Cycle expander is 4.6 mm^2 (corresponding to a displacement of 36.34 cm^3).

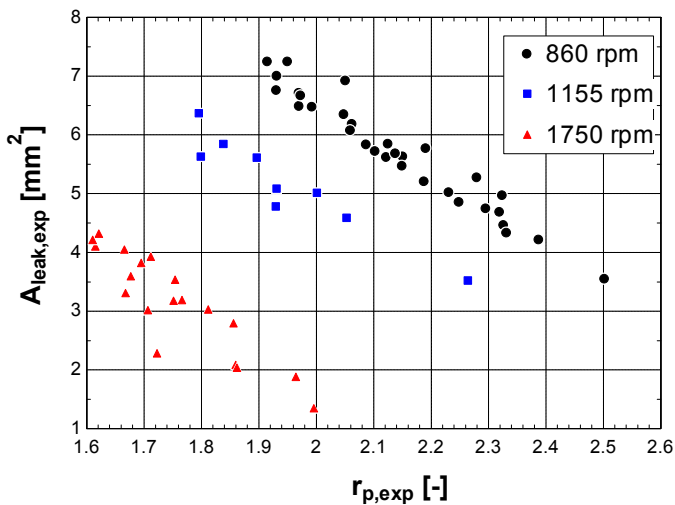


Figure 4-2 : Variation of the identified leakage area with the pressure ratio imposed to the expander (expander model)

With the available measurements, it doesn't seem possible to explain the variation of the leakage area given in Figure 4-2. More intrusive measurements, such as pressure measurements in the working chambers, might be useful to better understand the observed evolution. However, two potential explanations are listed hereunder:

- 1) Hugenroth (2006) mentioned that the radial compliance mechanism has been removed, what could have caused an excessive flank gap. The large amount of oil was

supposed to seal the flank leakage paths. However, the ability of oil to seal these gaps may vary with the operating conditions.

- 2) The tip seals might not be working correctly under the operating conditions imposed to the expander.

The following relationship has been drawn from the identified leakage area given in Figure 4-2.

$$A_{\text{leak}} = 2.23005992 \cdot 10^{01} - 5.43121354 \cdot 10^{-03} N_{\text{rot}} - 5.56821478 r_p \quad [\text{mm}^2] \quad (4-5)$$

Considering this relationship, the gas flow rate predicted by the model is compared to the measured one in Figure 4-3.

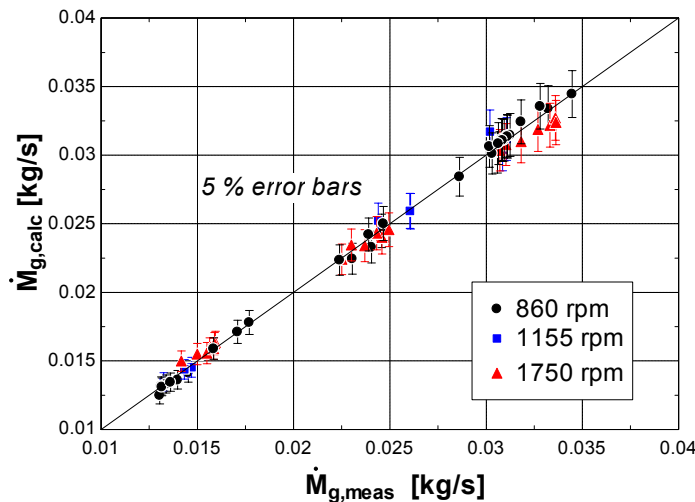


Figure 4-3: Prediction of the gas mass flow rate (expander model)

4.2.2 Prediction of the shaft power

The identified mechanical loss torque appears to slightly correlate with the expander supply temperature and the oil mass fraction. The decrease of the torque with the increase of temperature might be explained by the decrease of the oil viscosity.

$$T_{\text{loss}} = 8.97739572 \cdot 10^{-1} - 1.79686553 \cdot 10^{-2} T_{\text{su}} + 3.33144515 \cdot 10^{-1} x_{\text{l,su}} \quad [\text{N-m}] \quad (4-6)$$

The evolution of the identified mechanical loss torque is found to slightly correlate with the expander supply temperature and the oil mass fraction.

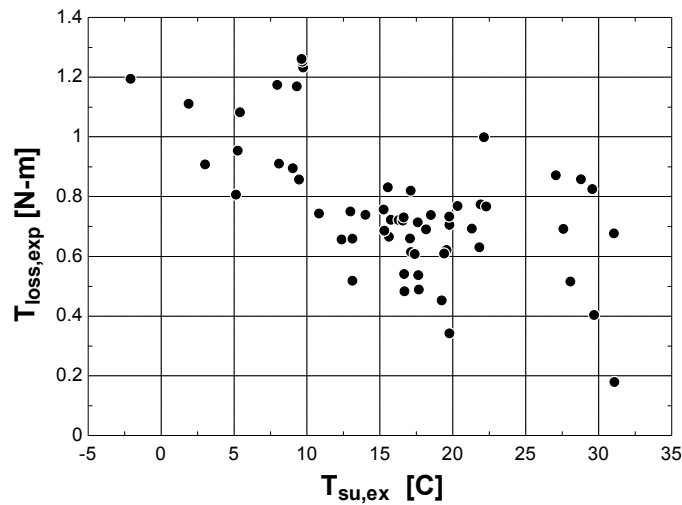


Figure 4-4: Variation of the identified mechanical loss torque with the supply temperature

The comparison between the shaft power predicted by the model and the measured shaft power is shown in Figure 4-5. The shaft power is computed by considering a mechanical loss torque varying according to Equation (4-6).

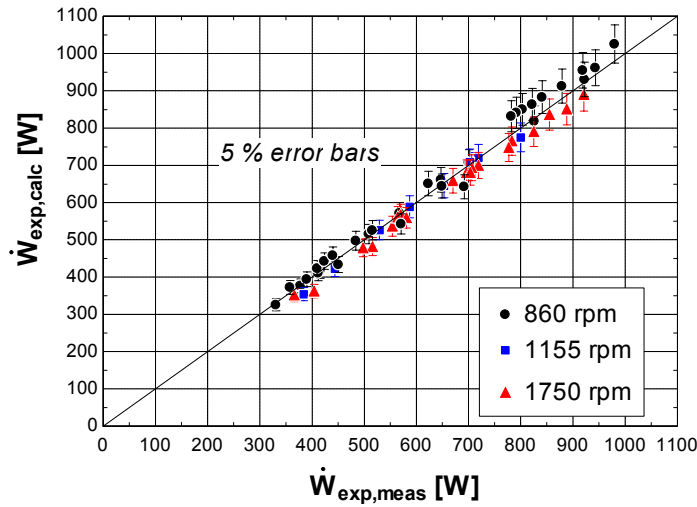


Figure 4-5: Prediction of the shaft power (expander model)

4.2.3 Prediction of the exhaust temperature

Figure 4-6 compares the predicted exhaust temperature to the measured one. The very good correlation is not surprising, since the oil mass flow rate has been identified by performing a energy balance. This energy balance involves the shaft power, the mixture flow rate and the ambient loss or gain. The shaft power and the mixture flow rate are predicted with a good agreement and the heat exchange with the ambient has been evaluated on the basis of a slightly retuned heat transfer coefficient AU_{amb} .

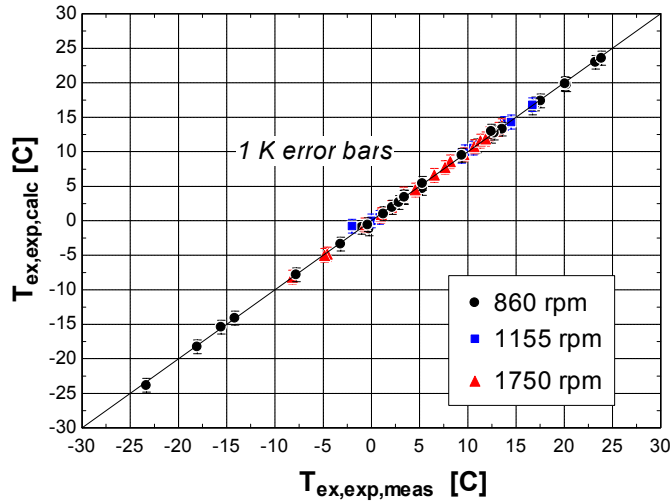


Figure 4-6: Prediction of the discharge temperature (expander model)

4.3 Compressor model

The inputs of the model are the same as for the expander. Parameters of the compressor semi-empirical model, given in Table 4-2, have been more readily identified. They were tuned in order to get the best agreement between predictions by the model and measurements for the gas flow rate, the shaft power and the exhaust temperature.

Table 4-2: Identified parameters of the compressor semi-empirical model

$V_{s,cp}$ [cm ³]	$AU_{su,cp}$ [W/K]	$AU_{ex,cp}$ [W/K]	$AU_{amb,cp}$ [W/K]	$r_{v,in,cp}$ [-]	$T_{loss,cp}$ [N-m]	$d_{su,cp}$ [mm]	$d_{ex,cp}$ [mm]	$A_{leak,cp}$ [mm ²]
104.8	$20\left(\frac{\dot{M}}{0.012}\right)^{0.8}$	$20\left(\frac{\dot{M}}{0.012}\right)^{0.8}$	1	1.7	0.8	13.5	5.8	0.5

4.3.1 Prediction of the mass flow rate

A constant leakage area of 0.5 mm^2 is found to yield a very good prediction of the gas mass flow rate which is shown in Figure 4-7. The identified leakage area is much smaller than the values identified for the expander model.

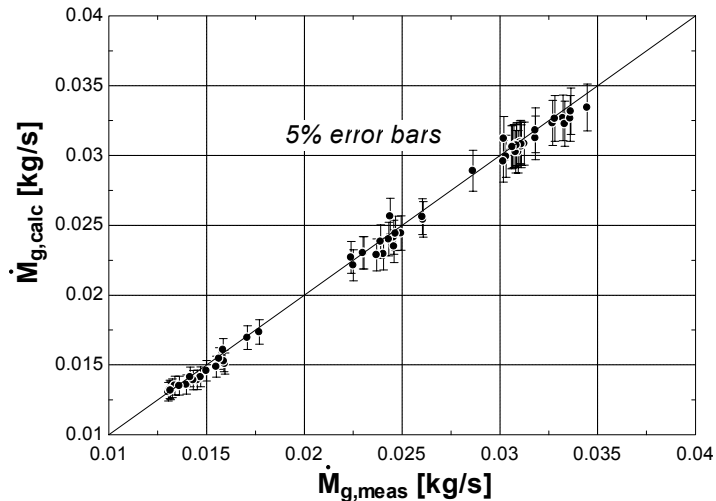


Figure 4-7: Prediction of the gas flow rate (compressor model)

The smaller leakage area could also be explained by the sealing mechanisms of the leakage gaps by the oil. Oil builds-up more easily at the contact points in compressor mode than expander mode, since in the former case leakage flow is opposite to internal flow (Peterson *et al.*, 2008).

4.3.2 Prediction of the shaft power

Figure 4-8 compares the predicted shaft power to the measured one. No strong correlation was found between the identified mechanical loss torque and the operating parameters. A constant torque of $0.8 \text{ N}\cdot\text{m}$ is found to yield good results.

The fictitious compressor supply diameter is of the same order of magnitude as the fictitious expander exhaust diameter. In contrary, the compressor exhaust diameter is much smaller than the expander supply diameter. The large identified expander supply diameter might correlate with the large internal leakage area. Actually, as explained more in detailed in Chapter 7, increasing the leakage paths between the suction chamber and the adjacent expansion chambers attenuates the suction pressure drop.

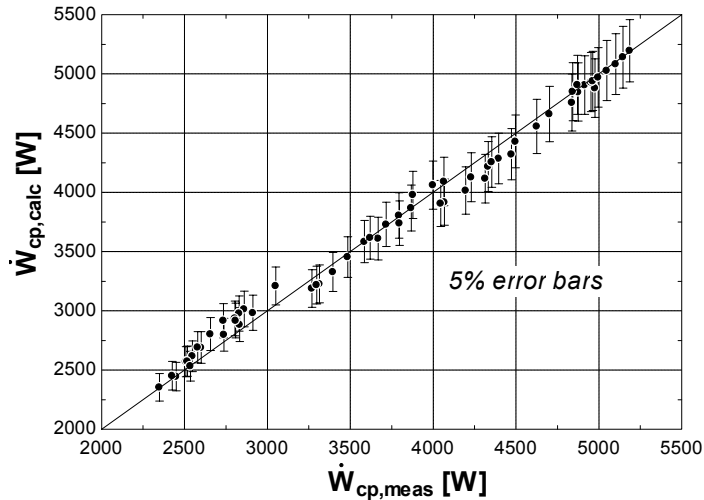


Figure 4-8: Prediction of the shaft power (compressor model)

4.3.3 Prediction of the exhaust temperature

As for the expander (§ 4.2.3), the very good agreement between the calculated exhaust temperature and the measured exhaust temperature is simply due to the fact that the oil mass flow rate has been determined from the compressor energy balance.

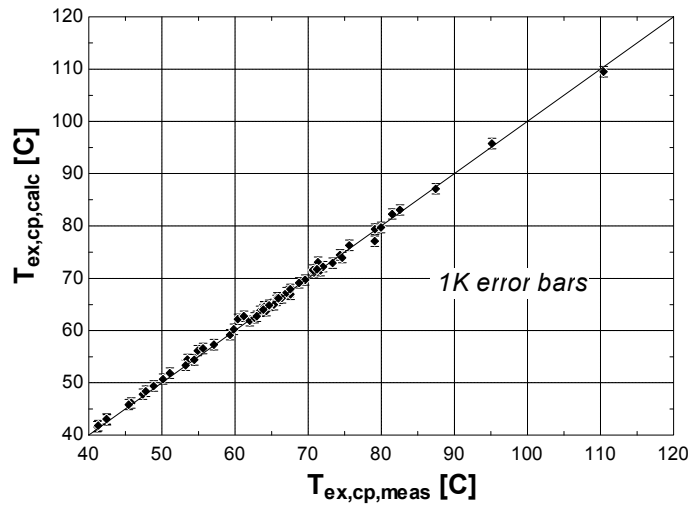


Figure 4-9: Prediction of the exhaust temperature (compressor model)

5 PARAMETRIC STUDY OF THE COMPRESSOR AND EXPANDER PERFORMANCES

Using both the compressor and expander semi-empirical models, parametric studies are carried to evaluate the impact of the different sources of irreversibility on the global performance of the machines.

5.1 Expander performance

Figure 5-1 shows the evolution of the shaft power predicted by the model with the oil mass fraction in the mixture. Operating conditions are $P_{su,exp}=15$ bar, $P_{ex,exp}=5$ bar, $T_{su,exp}=10^\circ\text{C}$, $\text{rpm}_{exp}=1750 \text{ min}^{-1}$. The corresponding global isentropic effectiveness is given in Figure 5-2.

Parameters of the model are those given in Table 4-1. The mechanical loss torque is set to 0.7 N-m and the leakage area to 1 mm².

The evolution at the top of Figure 5-1 assumes that the expansion is fully isentropic from the supply conditions to the exhaust pressure. The evolution goes through a maximum, which is due to the fact that the expander displacement is imposed. On one hand, increasing the oil mass fraction increases the gas expansion work because the polytropic exponent n for the gas (in $Pv_g^n = C$) decreases. On the other hand, the gas mass flow rate decreases because the volume of the oil phase increases. Hence the gas expansion power goes through a maximum.

The effect of the mismatching between the internal pressure ratio and the external pressure ratio is to decrease the shaft power and hence the isentropic effectiveness. For the operating point under consideration, the expansion is characterized by under-expansion losses: the internal pressure P_{in} is higher than the exhaust pressure $P_{ex,exp}$. An expander characterized by a larger built-in volume ratio should be used. Figure 5-2 shows that the isentropic effectiveness goes through a minimum. Actually, the internal pressure $P_{in,exp}$ and the under-expansion loss increase with the oil mass fraction (because the polytropic exponent n increases). In the mean time, the gas volume ratio increases with the oil mass fraction, because the latter is uncompressible (Hugenroth, 2006). The gas volume ratio is defined as

the ratio between the volumes of the gas phase at the end and at the beginning of the expansion.

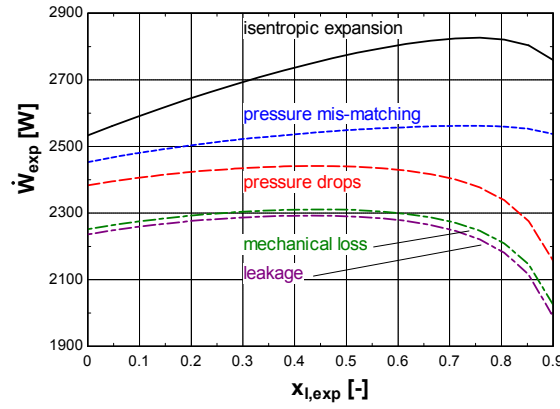


Figure 5-1: Evolution of the predicted expander shaft power with the oil mass fraction

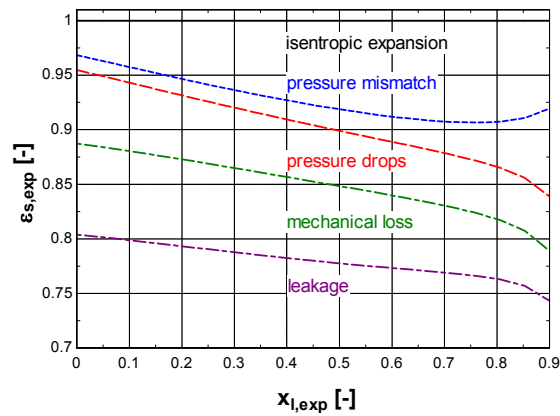


Figure 5-2: Evolution of the predicted expander global isentropic effectiveness with the oil mass fraction

Supply and exhaust pressure drops strongly reduce the expander performance. Moreover, they shift the optimum oil mass fraction to the left because pressure drops become especially severe for the larger oil quantities.

As shown in Figure 5-1 and Figure 5-2, mechanical loss strongly reduces the expander performances.

Internal leakages reduce the expander shaft power because the supply and exhaust pressure drops increase with the mixture flow rate. Isentropic and isothermal effectiveness drop sharply because of the increase of the denominators of Equation (3-11).

5.2 Compressor performance

Figure 5-3 displays the evolution of the compressor shaft power with the oil fraction. From the bottom to the top of the figure, the modeling progressively accounts for the different sources of irreversibility. The corresponding evolutions for the global isentropic effectiveness are given in Figure 5-4.

Parameters of the model are those given in Table 4-2. The operating conditions for the simulation are $P_{su,cp}=5$ bar, $P_{ex,cp}=20$ bar, $T_{su,cp}=25^\circ\text{C}$, $\text{rpm}_{cp}=3500 \text{ min}^{-1}$.

The evolution of the shaft power corresponding to an isentropic compression goes through a minimum. This has already been discussed by Hugenroth *et al.* (2007): the gas compression power decreases with the oil mass fraction, but in the mean time the power necessary to pump the liquid phase increases.

The pressure mismatching is a considerable source of irreversibility. For this operating point, the mixture is under-compressed. A compressor with a higher built-in volume ratio would be more appropriate.

Pressure drops decrease the compressor's performance. The performance drop increases with the high oil mass fractions. As for the expander, mechanical loss and internal leakage strongly penalize the compressor's performance.

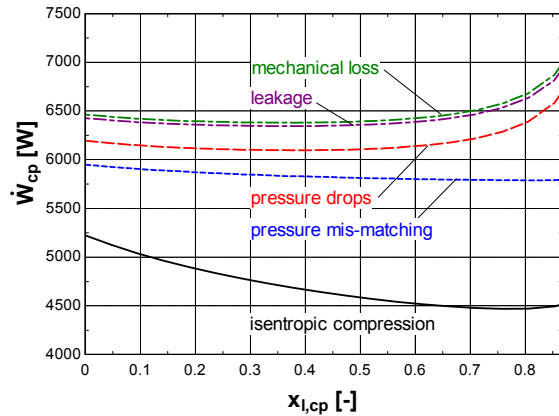


Figure 5-3: Evolution of the predicted compressor shaft power with the oil mass fraction

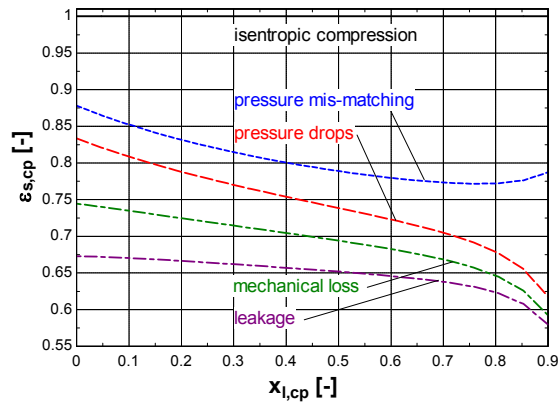


Figure 5-4: Evolution of the global compressor isentropic effectiveness with the oil mass fraction

5.3 Concluding remarks

For both the expander and the compressor, the main sources of irreversibility are the pressure mismatching and the pressure drops. At this point it is not possible to determine whether the pressure drops can be reduced. This necessitates a more detailed modeling of the machines,

accounting for their geometry. In the case of the expander, this model will be established and validated in Chapter 6 and 7.

On the other hand, a scroll machine with an appropriate built-in volume ratio can certainly be designed. For instance, for the same operating point as in §5.1, the expander ideal built-in volume ratio as a function of the oil mass fraction is given in Figure 5-5. The presence of a maximum is due to the fact that the oil phase slightly increases the gas volume ratio.

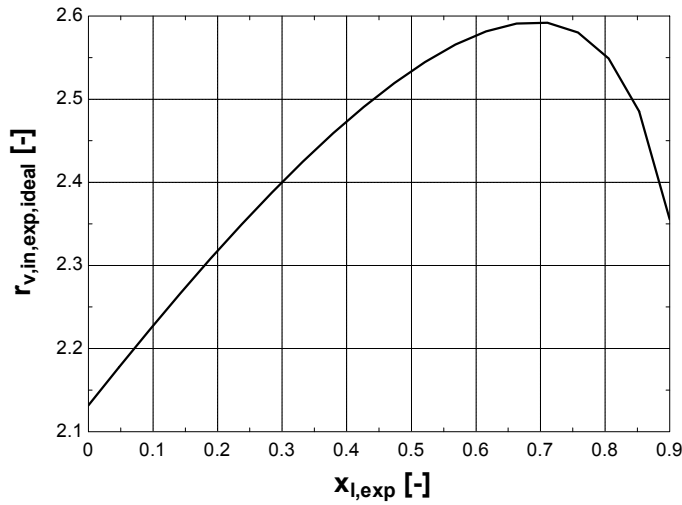


Figure 5-5: Evolution of the expander ideal built-in volume ratio with the oil mass fraction

6 CONCLUSIONS

The purpose of this work was to study a Liquid Flooded Ericsson Cycle cooler, and more especially to focus this study on the performance of the scroll machines integrated into this system.

An experimental study on a prototype of a Liquid Flooded Ericsson Cycle cooler has been carried out in order to characterize the evolution of the performance of the scroll machines with the operating conditions. The following observations have been made: 1) both machines show an internal isentropic effectiveness decreasing with the oil mass fraction; 2) the volumetric effectiveness of the expander is very low compared to the effectiveness achieved with the compressor.

From the work of Hugenroth *et al.* (2007), one step forward was made by trying to identify and quantify the different sources of irreversibility. This has been achieved through the validation of the semi-empirical models of both the compressor and the expander.

While the parameters of the scroll compressor model have been readily identified, this was not the case for the expander model. Actually, it was not possible to identify one unique leakage area for the expander. It appears that the leakage area is a decreasing function of the rotational speed and of the pressure ratio. Moreover, the maximal leakage area is much larger than the one identified for the compressor, what explains the lower volumetric performance. At this point, it is not possible to determine the underlying reason (mechanical deformation, play in the orbiting scroll, problems with the tip seals,...).

Using the semi-empirical models, parametric studies have been carried out to evaluate the performance of the machines as a function of the oil mass fraction. It appears that the main factors affecting the compressor and the expander performance is the mismatching between internal and external pressure ratios as well as the supply and exhaust pressure drops. Machines with adapted built-in volume ratios can certainly be designed. However, a detailed modeling of the machine is necessary to determine whether pressure losses can be reduced. Such a model, applicable to the expander, will be presented in Chapters 6 and 7.

7 REFERENCES

- Bell, I., V. Lemort, J. Braun, and E. Groll. 2008a. Development of Liquid-Flooded Scroll Compressor and Expander Models. *Proceedings of the International Compressor Engineering Conference at Purdue University*: Paper 1283.
- Bell, I., V. Lemort, J. Braun, E. Groll. 2008b. Analysis of Liquid-Flooded Compression Using a Scroll Compressor. *Proceedings of the International Compressor Engineering Conference at Purdue University*: Paper 1263.
- Çengel, Y. A., and M.A. Boles. 2006. Thermodynamics, An engineering Approach, *Mc Graw Hill*.

- Chisholm, D. 1983. Two-phase flow in pipelines and heat exchangers. *George Godwin*, London.
- Hugenroth, J.J. 2006. Liquid Flooded Ericsson Cycle Cooler. *PhD Thesis*, Purdue University.
- Hugenroth, J., J.E. Braun, E.A. Groll, and G.B. King. 2007. Thermodynamic analysis of a liquid-flooded Ericsson cycle cooler, *Int. J. Refrig.*, Vol. 30, No. 7: 1176-1186.
- Kim, Y. M., D. K. Shin, and J. H. Lee. 2004. A scroll expander with heating structure and their systems, *Proceedings Internnatiional Compressor Engineering Conference at Purdue*: paper C024.
- Kohsokabe, H., M. Koyama, K. Tojo, M. Matsunaga, and S. Nakayama. 2008. Performance characteristics of scroll expander for CO₂ refrigeration cycles. *Proceedings of International Compressor Engineering Conference at Purdue*: paper 1239.
- Levy, S. 1999. *Two-phase flow in complex systems*, John Wiley & Sons, New York: 104-105.
- Morris, S.D. 1991. Compressible Gas-Liquid Flow Through Pipeline Restrictions. *Chem. Eng. Process.* 30: 39-44.
- Peterson, R.B., H. Wang, and T. Herron. 2008. Performance of a small-scale regenerative Rankine power cycle employing a scroll expander. *Proc. IMechE Vol. 222 Part A: J. Power and Energy*: 271-282.
- Preissner, M. 2001. Carbon Dioxide Vapor Compression Cycle Improvements with Focus on Scroll Expanders. *Ph.D. Thesis*. University of Maryland. College Park

CHAPTER 6

DEVELOPMENT OF A SCROLL EXPANDER DETERMINISTIC MODEL

1	INTRODUCTION.....	179
1.1	Why a deterministic model?.....	179
1.2	Literature review	180
1.2.1	Compressors.....	180
1.2.2	Expanders.....	181
1.3	Development of the model	182
1.4	Investigated expanders.....	182
2	MODELING THE GEOMETRY.....	183
2.1	General geometrical consideration.....	183
2.1.1	Principle of operation of a scroll machine	183
2.1.2	Description of the Scroll Involute	184
2.1.3	Conjugacy points	185
2.1.4	Ending angle of the involutes.....	186
2.1.5	Orbiting angle	186
2.2	Parameters identification	186
2.3	Definition of various expander chambers.....	188
2.4	Calculation of various chamber areas and volumes.....	190
2.4.1	Suction chambers.....	190
2.4.2	Expansion chambers	191
2.4.3	Discharge chambers.....	192
2.4.4	Summary	192
2.5	Suction chamber supply port and discharge chambers' opening area	194
2.5.1	Calculation of the suction chamber supply port area.....	194
2.5.2	Calculation of discharge chamber's opening area	194
2.6	Calculation of leakage areas.....	195
3	MODELING THE THERMODYNAMICS PROCESSES.....	196
3.1	Differential equations governing the expansion process.....	196
3.2	Modeling the suction, expansion and discharge processes	200
3.2.1	Suction process	200

3.2.2	Expansion process	201
3.2.3	Discharge process	201
3.3	Internal leakages.....	202
3.4	Thermal model.....	203
3.4.1	Definition of the lumped elements	203
3.4.2	Heat transfer between the fluid and the metal mass of the expander	204
3.4.3	Mechanical loss	208
3.4.4	Heat transfer in the plenum	208
3.4.5	Energy balances	209
3.5	Calculating the mass flow rate.....	210
3.6	Calculating the average discharge temperature and enthalpy	210
3.7	Calculating the expansion work rate and the shaft power	211
3.8	Numerical solution.....	212
4	CONCLUSIONS	215
REFERENCES.....		216

NOMENCLATURE

A	Area, m ²
A	Oscillation amplitudes, m
AU	Heat transfer coefficient, W/K
C _d	Discharge coefficient, -
\dot{C}	Capacity flow rate, W/K
d	Diameter, m
E	Total internal energy, J
f	Frequency, Hz
h	Scroll height, m
h	Specific enthalpy, J/kg
h _c	Convective heat transfer coefficient, W/m ² -K
k	Specific heat ratio, -
L	Length, m
M	Mass, kg
\dot{M}	Mass flow rate, kg/s
MAXN	Number of steps, -
N	Rotational speed, Hz
NEXP	Number of pair of expansion chambers, -
Nu	Nusselt number, -
P	Pressure, Pa
\dot{Q}	Heat transfer rate, W
r	Radius, m
r _{v,in}	Built-in volume ratio, -
s	Specific entropy, J/kg-K
t	Scroll thickness, m
T	Temperature, °C
u	Specific internal energy, J/kg
U	Internal energy, J
U	Mean Velocity, m/s
\dot{V}	Volume flow rate, m ³ /s

V	Volume, m ³
\dot{W}	Power, W
z	Height, m

Subscripts

amb	Ambient
b	Base circle
c	Curvature
chan	Channel
conj	Conjugate
cp	Compressor
CV	Control volume
d	Discharge
DB	Dittus Boelter
e	Ending
elec	Electrical
ex	Exhaust
exp	Expander
fix	Fixed
h	Height, hydraulic
i	Initial
l	Low
leak	Leakage
loss	Mechanical loss
mot	Motor
o	Outer, orbiting radius
orb	Orbiting
plen	Plenum
rad	Radial
s	Starting, swept, suction

St	Strouhal
su	Supply
v	Constant volume

Greek and miscellaneous

ε	Effectiveness, -
δ	Gap, m
Δ	Difference
ω	Rotational speed, rad/s
φ	Involute angle, rad
ρ	Density, kg/m ³
θ	Orbiting (crank) angle, rad
0	Initial

1 INTRODUCTION

1.1 Why a deterministic model?

The first objective of establishing a deterministic model of a component is to better understand all the inherent physical processes. As few parameters as possible should be tuned. First, because tuning a parameter means missing an opportunity to better characterize a physical feature of the component. Then there is a risk to give a fictitious value to the parameter, which could actually compensate a weakness in the modeling.

However, a model is seldom purely deterministic and, in most cases, some parameters still need to be tuned. First of all, some compromise has to be found between the model complexity (and hence development time and computational time) and its accuracy. Also, there could be no sense to continue refining a model if there is no measurement (or other information) available for detailed validation.

A deterministic model is not supposed to yield a better accuracy than a semi-empirical model. Actually, it is found that it could be easier (and less time consuming) to increase the accuracy of the semi-empirical model by tuning its parameters. Actually in both models some physical features of the machines are probably being neglected. This could be “balanced” by fictitiously tuning some of the parameters. In the semi-empirical model, there are more parameters to identify. Hence the latter model offers more degrees of freedom to decrease the deviations between the model’s predictions and the measurements.

In this work, the deterministic model of the expander is presented after the semi-empirical model (introduced in Chapter 2). This actually corresponds to the chronology of this research project. The main reasons for developing a scroll expander deterministic model were:

- to check whether the parameters identified in the semi-empirical model have a physical meaning;
- to evaluate the technical feasibility of the solutions suggested in Chapter 4 for improving the expander’s performance (decrease of the suction pressure drop and of the internal leakage);

- to develop an appropriate tool for investigating the variation of the expander's performance with modification of its geometry. The deterministic model actually accounts for the exact description of the geometry of the machine.

The deterministic model can also be used to generate performance map, the data of which can then be employed to identify the parameters of the semi-empirical model. This is justified by the fact that experimental data are not always readily available for identifying the parameters of the semi-empirical model (experimental investigations are expensive and time-consuming).

1.2 Literature review

Most of the literature dealing with the modeling of scroll machines concerns compressors. However, most of the results found in the literature on compressors can be also applied to the modeling of the expanders.

1.2.1 Compressors

The first technical paper on scroll compressor is the patent taken out by Creux (1905) on his *Rotary Engine*. Sixty years were necessary for industry to provide machining tools with small enough tolerances (such as NC machines) appropriate to manufacture scroll compressors and the latter came onto the market in the 70's. Since then, the technical paper activity increased.

Morishita *et al.* (1984) seem to be the first authors to give an analytical expression for the volume of the suction, compression and discharge chambers.

Nieter (1988) investigated in detail the suction process in scroll compressors. He showed that the suction gas may start to be compressed before the end of the suction process. Four years later, Nieter and Gagne (1992) proposed an analytical model for the discharge flow.

Caillat *et al.* (1988) developed one of the first global simulation models of the scroll compressor in order to analyze geometric, dynamic, thermodynamic and heat transfer characteristics under different conditions.

Two years later, Yanagisawa *et al.* (1990) developed another simulation model for investigating more in details the influence of flow resistance, leakage and rotational speed on the compressor's performance.

Halm (1997) summarized most of the previous works and established a very detailed model of the scroll compressor, associating a mathematical description of its geometry and a thermodynamic description of the entire compression process. Later, Wang *et al.* (2005) generalized all the different proposed analytical descriptions of the scroll geometry.

Similar models, also based on control volumes analysis, have been developed by Chen (2000), Schein and Radermacher (2001), Lee (2002) for an air-conditioning hermetic compressor, Huff and Radermacher (2003) for CO₂ application, and Wang *et al.* (2007) for investigating refrigerant injection.

More recently, advances have been made in the understanding of the heat transfers inside the scroll working chambers. Ooi and Zhu (2004) developed a two-dimensional model to study the fluid flow and heat transfer in the working chambers of a scroll compressor. Jang and Jeong (2006) experimentally investigated the convective heat transfer inside the scroll compressor.

1.2.2 Expanders

One of the first works on scroll expander modeling was presented by Yanagisawa *et al.* (2001). They modeled an oil-free scroll-type air expander, describing the crank angle evolution of the pressure and temperature in the expander pockets. They were able to experimentally validate their model, using internal measurements of the pressures in the pockets.

A few other papers dealing with scroll expander modeling based on control volume analysis were found. Xiaojun *et al.* (2004) numerically simulated a scroll expander used to recover work in a fuel cell. The model ignores heat transfer as well as suction pressure losses. The model accounts for radial and flank leakage and represents the mechanical losses by introducing a mechanical efficiency. Yuanyang *et al.* (2006) investigated a scroll

compressor/expander module used in an automotive fuel cell. The modeling accounts for under-over compression-expansion and leakages.

1.3 Development of the model

The model is based on a previously existing refrigeration scroll compressor model (Halm, 1997 and Chen, 2000). It has been adapted to represent the expander operation and to account for a larger number of working chambers.

The proposed modeling approach is to follow a series of control volumes in transient regimes over one entire revolution of the crankshaft, discretized in a number of time steps.

The development of this model is done in two steps. First, a *model describing the geometry* of the expander is built. This model determines the evolution of the volumes (and their derivatives) with the crank angle, but also the evolution of the internal leakage paths and the evolution of heat transfer areas. The model also accounts for other geometrical peculiarities of the machines (such as the dimension of the ports and the presence of a plenum between the inlet port and the suction chamber).

Results generated by the geometrical model are then used in the *expansion process model*. This model describes the evolution of the temperature and the pressure in all the chambers of the expander with the crank angle. In the expansion process model, equations of conservation of energy and mass are established and numerically solved for each chamber.

1.4 Investigated expanders

The deterministic model presented in this chapter has been adapted to describe two different scroll expanders. Results are presented in a chronological way.

The first expander which has been model was integrated inside an Ericsson cycle cooler. It is originally an automotive scroll compressor adapted to be run in expander mode. This machine has been introduced in Chapter 5. In the following paragraphs, it will be called *LFEC expander*.

The developed model was then adapted to describe the scroll expander introduced in Chapter 4. This second expander was originally an open-drive oil free air compressor. It will be called *ORC expander*.

For convenience, in this Chapter, only modeling features related to the Ericsson expander will be presented. The adaptation of the model in order to describe the ORC expander will be covered in Chapter 7.

The validation of the deterministic model for both expanders will be detailed in Chapter 7.

2 MODELING THE GEOMETRY

The geometrical model calculates volumes and areas associated with the different chambers in the expander, since these volumes and areas and their derivatives determine the expansion process. This model also describes geometrical peculiarities which should be taken into account in the expansion process description.

2.1 General geometrical consideration

2.1.1 Principle of operation of a scroll machine

A scroll machine consists of two scrolls (see Figure 2-1). One scroll is stationary (fixed scroll) and the other is submitted to an orbital motion around the shaft center (orbiting scroll). The two elements are identical spirals that are assembled at 180° phase difference. The magnitude of the orbital motion depends on the base circle radius r_b and the scroll flange thickness t defined later.

During operation, the two scroll elements make contact at several points, forming an independent series of two pockets at each orbital position. These two pockets progressively decrease (or increase) in size toward the center. The compression (or expansion) process of a scroll compressor (or expander) is defined as a positive displacement process. This type of process increases (or decreases) the pressure of the fluid by reducing (or increasing) the internal volume of the compression (or expansion) chambers.

Scroll machines do not require active valves to control suction and discharge processes. The timing of these processes is imposed by the scroll geometry and the orbital motion.

By design, a scroll compressor (expander) has a fixed built-in volume ratio $r_{v,in}$. In compressor mode, this is the ratio between the suction chambers volume at the end of the suction and the discharge chambers volume at the beginning of the discharge.

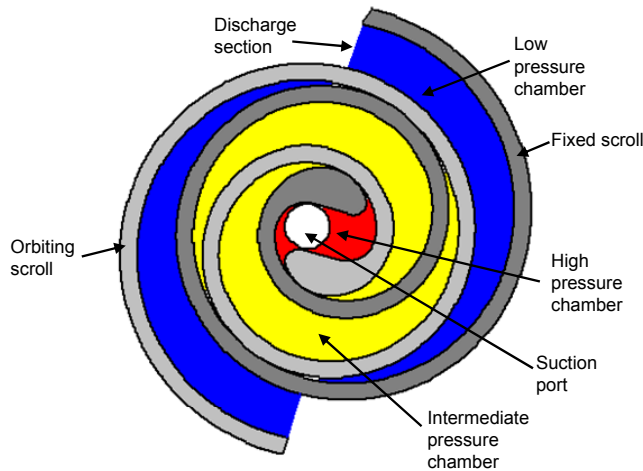


Figure 2-1 : Representation of the fixed and orbiting scrolls and the different chambers (expander mode)

2.1.2 Description of the Scroll Involute

The geometry of a scroll machine is defined by two involutes that develop around a common basic circle and are offset by a constant distance. This pair of involutes can be described in polar coordinates by the following equations (see Figure 2-2):

$$L_i = r_b \cdot (\varphi - \varphi_{i0}) \quad (2-1)$$

$$L_o = r_b \cdot (\varphi - \varphi_{o0}) \quad (2-2)$$

where,

L_i is the length of the inner involute

- L_o is the length of the outer involute
- φ_{i0} is the initial angle of the inner involute
- φ_{o0} is the initial angle of the outer involute

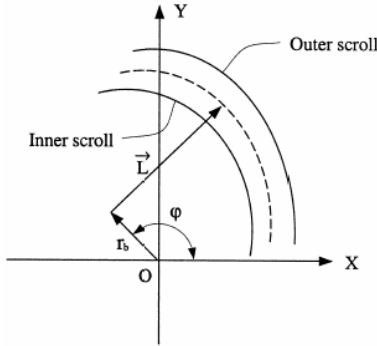


Figure 2-2: General relations of a scroll (Chen, 2000)

The thickness t of the scroll is given by:

$$t = L_o - L_i = r_b \cdot (\varphi_{i0} - \varphi_{o0}) \quad (2-3)$$

2.1.3 Conjugacy points

The fixed and the orbiting scrolls are in contact at different points of conjugacy defined as a function of the conjugate angles φ_k .

These conjugacy points are (here conventionally) defined on the fixed scroll as a function of the orbiting angle θ (or “crank angle”) defined in the next paragraph.

The k -th point of conjugacy is determined by:

$$\varphi_{\text{conj},i,k} = \varphi_e - \theta_d + \theta - 2\pi(k-1), \text{ on the } \textit{inner involute} \quad (2-4)$$

$$\varphi_{\text{conj},o,k} = \varphi_e - \theta_d + \theta - 2\pi(k-1) - \pi, \text{ on the outer involute} \quad (2-5)$$

with $k \in [1, N_{\text{exp}} + 1]$ for the scroll expander investigated here. N_{exp} is the number of pairs of expansion chambers.

2.1.4 Ending angle of the involutes

Another main parameter of the scroll geometry is the different angles φ_e at which the inner and the outer involutes of both the fixed and the orbiting scrolls end. For the scroll machines investigated in this work, both the outer and the inner involutes end at the same angle (which is also the same for both the fixed and the orbiting scrolls).

2.1.5 Orbiting angle

The orbiting angle θ is defined such that at $\theta = 0 \text{ rad}$, the suction chamber has its minimal volume and starts to increase again. The discharge angle θ_d is defined such that at this angle the expansion chamber has just opened and is in communication with the discharge port of the expander. The discharge angle is given by:

$$\theta_d = \varphi_e - \varphi_{os} - 3\pi \quad (2-6)$$

2.2 Parameters identification

Geometrical parameters of the scroll compressor/expander have been retrieved by means of a reverse engineering method consisting of the following steps. The orbiting scroll is first scanned and imported in MATLAB (see Figure 2-3). The scroll shape described by the model is superimposed on this figure. Parameters are tuned to match the shape described by the model to the figure. These parameters are finally refined in order to get the desired compressor displacement volume $V_{s,cp}$ (given by the manufacturer) and equal to 104.8 cm^3 .

Figure 2-3 compares the shape of the orbiting scroll as described by the model to the actual shape. Parameters of the scroll geometry are summarized in Table 2-1.

Table 2-1: Main geometrical parameters of the LFEC Expander

r_b	h	$\varphi_{o,0}$	$\varphi_{i,0}$	$\varphi_{o,s}$	$\varphi_{i,s}$	φ_e	r_o
[mm]	[mm]	[rad]	[rad]	[rad]	[rad]	[rad]	[mm]
3.522	32.89	-1.1248	0.1983	4.70	1.80	15.5	6.4

As shown in Figure 2-3, the shape of the tip of the scroll cannot be described anymore by the involute of a circle. Actually, the involutes forming the scroll start at an inner starting angle φ_{is} and an outer starting angle φ_{os} . These starting points can be bridged by different geometries. The simplest is the circular arc (Halm 1997).

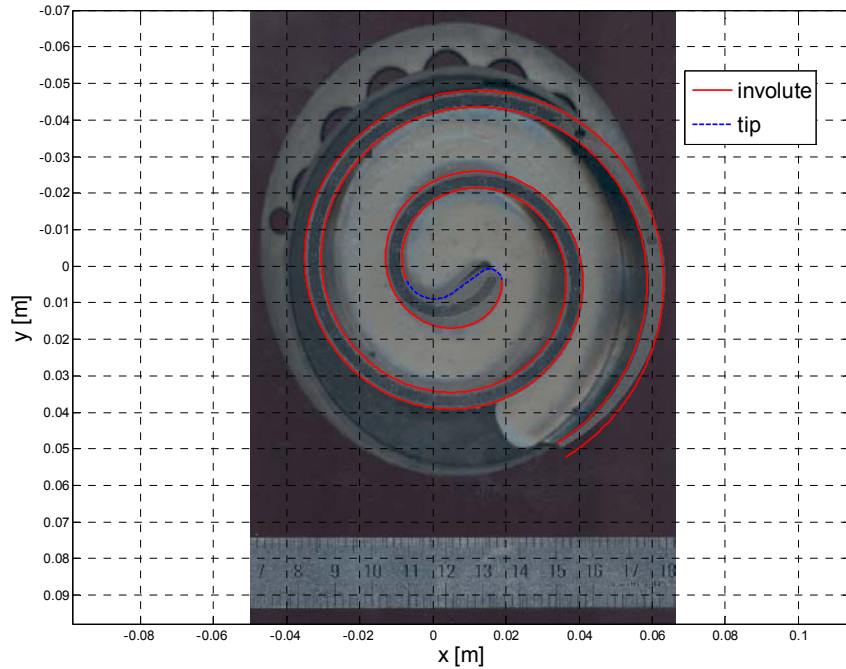


Figure 2-3 : View of the orbiting scroll (LFEC expander)

However, different geometries are produced. In order to achieve easy paths for the machining tools, these geometries are usually composed of straight lines and circular arcs. These geometries are designed to increase the material strength for high pressure operation or reducing the clearance volume (called *Perfect Meshing Profile*). For the expander under

investigation, the tip of the scroll can be very accurately described by a line, a circular arc and a second line in series. Note that an accurate description of the innermost portion of the scroll is crucial to correctly represent the suction process.

2.3 Definition of various expander chambers

The relative position of the fixed and the orbiting scrolls defines different chambers which are referred to by numbers in Figure 2-4.

The suction chamber, which is in communication with the suction chamber supply port (located close to the center of the scrolls in Figure 2-4) is labeled *chamber 6*. As explained hereunder, this chamber can be fictitiously divided into *chambers 1, 2 and 3* ($V_6 = V_1 + V_2 + V_3$).

It is actually useful to impose this subdivision of the suction chamber, since the different sub-chambers may be in communication only by small gaps (depending on the orbiting angle); which leads to pressure differences between the different sub-chambers. Such a situation is depicted in Figure 2-4 where *chamber 1* is in communication with *chamber 2* and *chamber 3* through the small opening between the tip of each scroll and the inner involute of the opposite scroll. Note that this opening is well known in compressor operation and accentuates the discharge pressure drop (Yanagisawa, 1990). Different chambers could be merged and treated as one unique control volume, provided the pressures in these chambers are equalized.

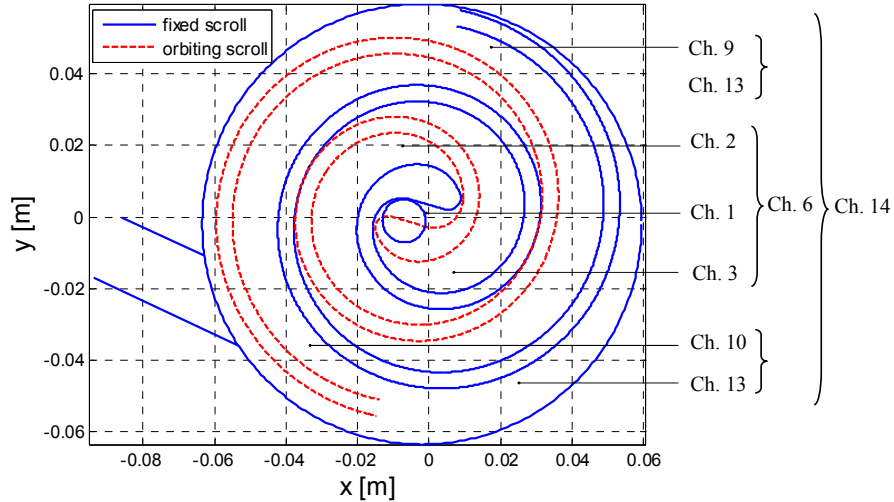


Figure 2-4: Definition of various expander chambers (at position $\theta/2\pi = 0.9$)

Chamber 7 and *8* are the expansion chambers that develop from *chambers 3* and *2* respectively.

Chamber 9 and *10* are the discharge chambers that develop from *chamber 7* and *8* respectively. *Chamber 9* and *chamber 10* are opened up to the discharge region, called *chamber 13*. In the case that the pressures in all three *chambers 9*, *10* and *13* are equalized, the entire control volume is treated as *chamber 14* (called also exhaust channel). The exhaust channel is in communication with the exhaust port.

The different chambers are represented in Figure 2-5 at four different steps during one entire revolution ((a) at the beginning; (b) at the middle; (c) at the discharge angle; (d) at the end).

It should be mentioned that during a short part of the suction process, *chamber 6* is divided into 2 chambers which communicate only through a small opening between the two straight lines forming the tip of the scroll. This situation is depicted in Figure 2-5 (c). In the early stage of the simulation code, *chamber 6* was divided into *chambers 4* and *5* for a short period. The two latter chambers were merged again into *chamber 6* to be finally divided into *chambers 1*, *2* and *3*. This description largely increased the complexity of the code without improving significantly the accuracy of the model.

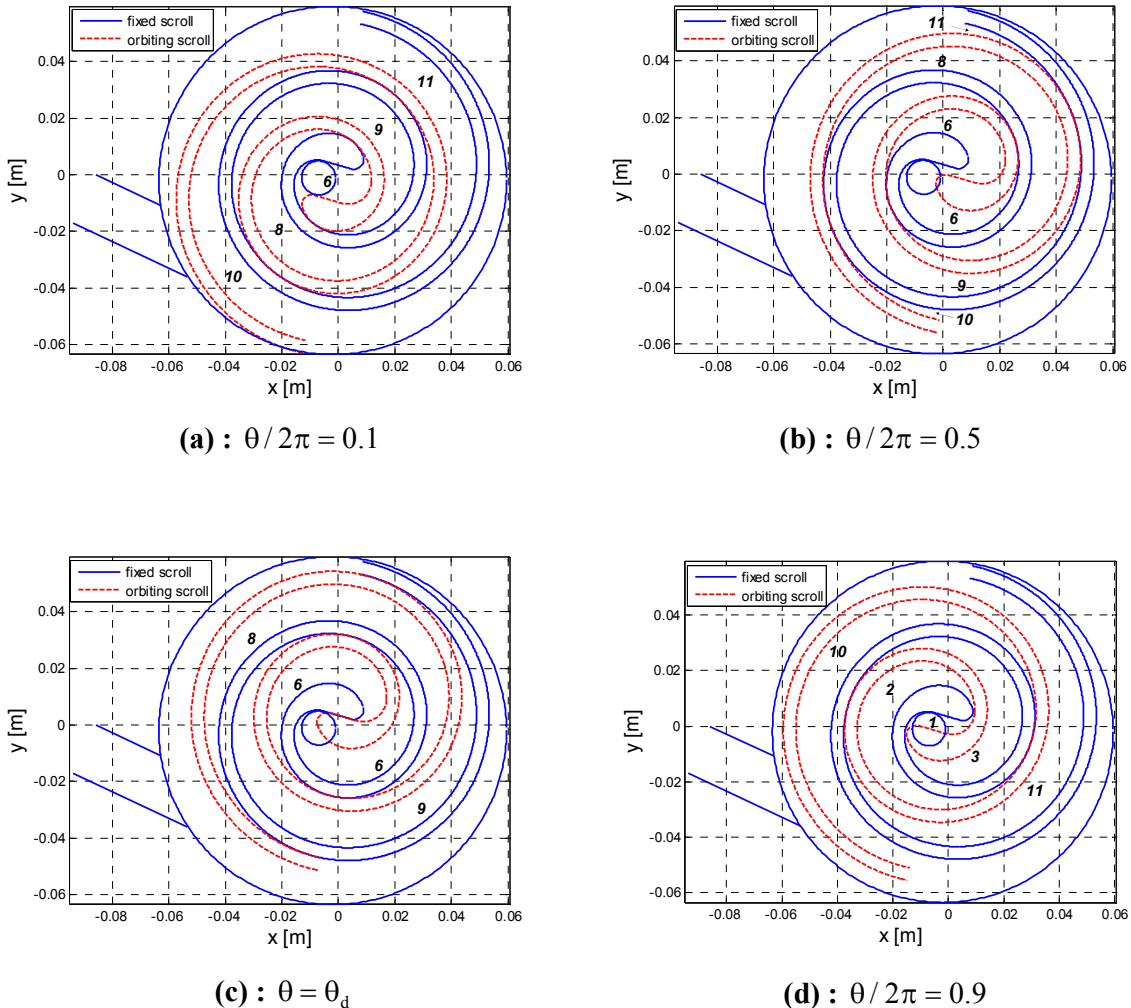


Figure 2-5: Relative position of the fixed and the orbiting scrolls at different steps of one entire revolution

2.4 Calculation of various chamber areas and volumes

2.4.1 Suction chambers

The suction chamber volume is defined as the height of the scroll multiplied by the area enclosed between the fixed and the orbiting scrolls, as depicted in Figure 2-4. Due to complex shape of the tip of both scrolls, an analytical expression of this area is difficult to establish: a numerical integration technique is thus used to calculate it. As mentioned by

Myszka (1998), the area enclosed within n-line segments of a curve whose coordinates are $[x_1 \ x_2 \ \dots \ x_n]$ and $[y_1 \ y_2 \ \dots \ y_n]$, can be calculated as (see Figure 2-6):

$$A = \frac{1}{2} \left\{ (x_1 y_2 + x_2 y_3 + \dots + x_{n-1} y_n + x_n y_1) - (x_2 y_1 + x_3 y_2 + \dots + x_n y_{n-1} + x_1 y_n) \right\} \quad (2-7)$$

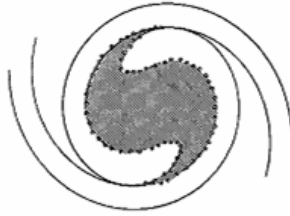


Figure 2-6: Calculation of the compressor suction chamber volume by a numerical technique (Myszka, 1998)

2.4.2 Expansion chambers

The volume of both expansion chambers is defined as the area enclosed by the involutes of the fixed and orbiting scrolls between two consecutive conjugate points (defined by conjugacy angles $\varphi_{conj,1}$ and $\varphi_{conj,2}$) multiplied by the height h of the scrolls. These volumes can be calculated analytically by the following relationship (Yanagisawa *et al.*, 1990)

$$V_e = h \left(\frac{1}{2} \int_{\varphi_{conj,1}}^{\varphi_{conj,2}} L_i^2 d\varphi - \frac{1}{2} \int_{\varphi_{conj,1}-\pi}^{\varphi_{conj,2}-\pi} L_o^2 d\varphi \right) = V_7 = V_8 \quad (2-8)$$

Solving the integral yields

$$V_e = -h\pi r_b^2 (\pi - \varphi_{i0} + \varphi_{o0}) (3\pi + 2\theta_d - 2\theta - 2\varphi_e + \varphi_{i0} + \varphi_{o0}) \quad (2-9)$$

Differentiation of this equation with respect to the orbiting angle θ gives

$$\frac{dV_e}{d\theta} = 2h\pi r_b^2 (\pi - \varphi_{i0} + \varphi_{o0}) \quad (2-10)$$

2.4.3 Discharge chambers

The volume of discharge *chamber 9* is defined as the height of the scroll h multiplied with the area enclosed by the fixed and the orbiting scrolls and a line segment connecting the end tip (corresponding to the ending involute angle) of the inner involute of the fixed scroll and the outer involute of the orbiting scroll and normal to the orbiting scroll. This volume is represented by the blue zone (“Low pressure chamber”) in Figure 2-1. The volume of *chamber 10* is equal to the one of *chamber 9*. These volumes can be calculated by integrating the area enclosed by the orbiting scroll from the involute conjugate angle φ_k to the involute ending angle φ_e and subtracting the area enclosed by the outer edge of the stationary scroll from $\varphi_k - \pi$ to $\varphi_e - \pi$ (Yanagisawa *et al.*, 1990). The result must be slightly corrected by a volume ΔV_d given by Halm (1997).

$$V_d = h \left(\frac{1}{2} \int_{\varphi_{\text{conj}}}^{\varphi_e} L_i^2 d\varphi - \frac{1}{2} \int_{\varphi_{\text{conj}} - \pi}^{\varphi_e - \pi} L_o^2 d\varphi \right) - \Delta V_d = V_9 = V_{10} \quad (2-11)$$

Solving this integral yields

$$\begin{aligned} V_d = & -\frac{1}{8} h r_b^2 (\pi - \phi_{i0} + \phi_{o0}) [-8 + 4\pi(\theta_d - \theta) + 4(\theta_d - \theta)^2 + 8\cos(\theta_d - \theta) \\ & - 8\pi\sin(\theta_d - \theta) + \pi\sin(2(\theta_d - \theta)) + 8(-\theta_d + \theta + \sin(\theta_d - \theta))\varphi_e + 4(\theta_d - \theta)\varphi_{i0} \\ & + 4(\theta_d - \theta)\varphi_{o0}] \end{aligned} \quad (2-12)$$

Differentiation of this equation with respect to the orbiting angle θ gives

$$\begin{aligned} \frac{dV_d}{d\theta} = & \frac{1}{4} h r_b^2 (\pi - \varphi_{i0} + \varphi_{o0}) [2\pi + 4(\theta_d - \theta) - 4\pi\cos(\theta_d - \theta) \\ & + \pi\cos(2(\theta_d - \theta)) - 4\sin(\theta_d - \theta) + 4(-1 + \cos(\theta_d - \theta))\varphi_e + 2\varphi_{i0} + 2\varphi_{o0}] \end{aligned} \quad (2-13)$$

2.4.4 Summary

The volumes of the different chambers calculated by the previous equations are plotted as function of the orbiting angle θ in Figure 2-7. It can be observed that, at the beginning of the

suction process ($\theta = 0 \text{ rad}$) the suction volume is not zero, but equal to a residual value (the clearance volume in compressor mode). This residual value is equal to the volume of *chamber 1* at the end of the suction process

$$V_6(0) = V_1(2\pi) \quad (2-14)$$

The expansion chambers (*chambers 7 and 8*) only exist for the period $0 - \theta_d$ of one entire revolution. At the discharge angle θ_d , the expansion chambers 7 and 8 open on the discharge channel and become the discharge chambers 9 and 10. The discharge process extends from θ_d to 2π , and from 0 to θ_d .

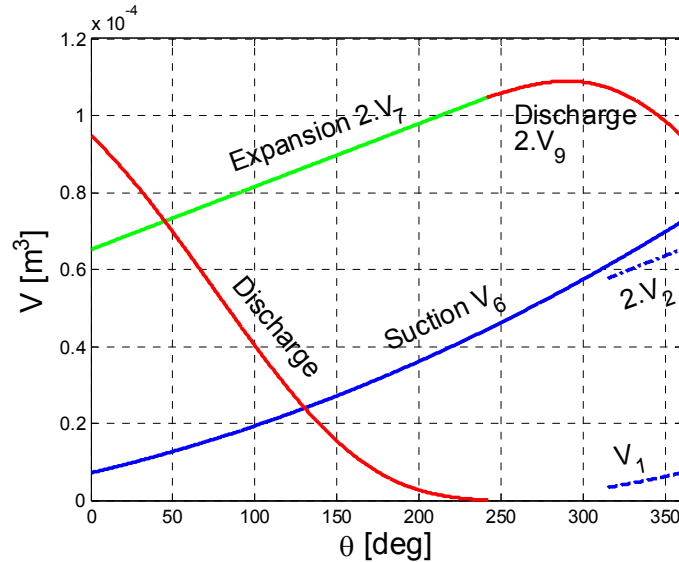


Figure 2-7 : Change of different chambers volume with respect to orbiting angle θ

In Figure 2-7, it can be observed that the volume of the discharge chambers first slightly increases before decreasing towards zero. This is an inherent characteristic of scroll machines. In compressor mode, this corresponds to the decrease in the volume of the suction chambers before the end of the suction process, resulting in the supercharging effect described by Nieter (1988).

2.5 Suction chamber supply port and discharge chambers' opening area

2.5.1 Calculation of the suction chamber supply port area

During part of the suction process, the suction chamber supply port is partially blocked by the tip of the orbiting scroll. The evolution of the effective area of the suction port with respect to the orbiting angle is shown in Figure 2-8. It can be observed that this area is sharply reduced at approximately 3 rad. It will be shown later than this is a source of pressure drops during the suction process. The blockage of the suction chamber inlet port at the end of the suction process is illustrated in Figure 2-5.

2.5.2 Calculation of discharge chamber's opening area

The fluid flows out of each of the discharge chambers through an opening of area A_d , defined by the length of the line connecting the inner and the outer scrolls multiplied by the scroll height h . This discharge area is represented in Figure 2-1 (“discharge section”). Halm (1997) proposed to calculate the area of that gap to a very good approximation by:

$$A_d = h r_o (1 - \cos(\theta_d - \theta)) \quad (2-15)$$

The variation of the discharge chambers' opening area with respect to the orbiting angle is shown in Figure 2-9.

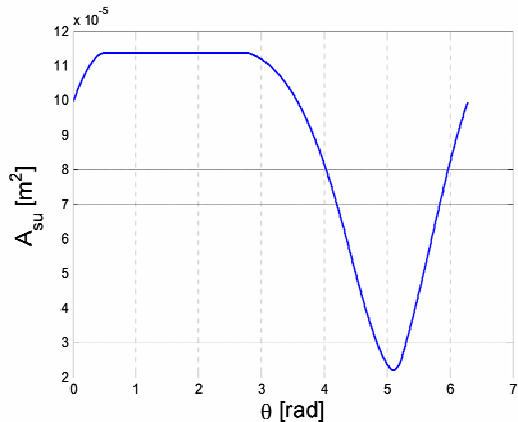


Figure 2-8: Change of suction chamber supply port area with the orbiting angle

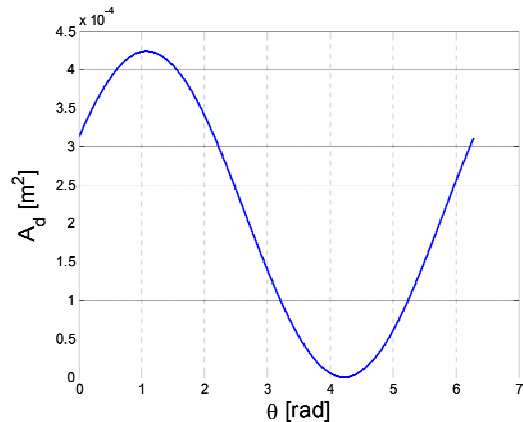


Figure 2-9: Variation of the discharge chamber opening area with the orbiting angle

2.6 Calculation of leakage areas

Leakages take place inside the expander through two different paths. The first path is formed by a clearance between the bottom (or the top) plate of the scroll and the wrap, and leads to “radial leakage”. The second path is formed by a clearance between the flanks of the two scrolls and leads to “flank leakages” (also called “axial leakages”). These two kinds of leakages are depicted in Figure 2-10.

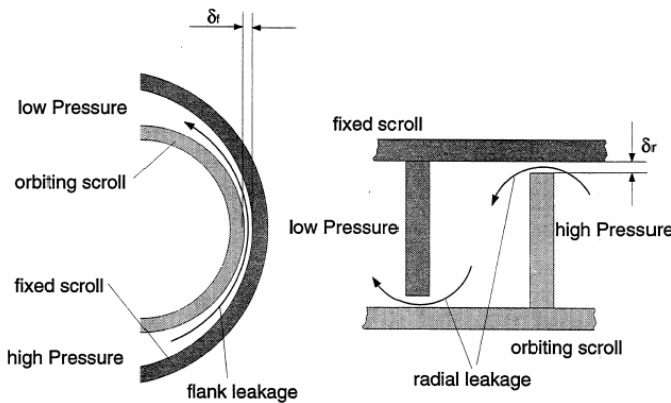


Figure 2-10: The two different leakage paths in a scroll machine (Halm, 1997)

The leakage area A_{leak} is equal to the product of the leakage gap δ by the leakage length L_{leak} . In the case of the flank leakage, the leakage length is simply the height h of the scroll wrap:

$$A_{leak,flank} = \delta_{flank} \cdot L_{leak,flank} = \delta_{flank} \cdot h \quad (2-16)$$

The radial leakage length between two chambers is the length of the portion of spiral separating these chambers.

$$A_{leak,rad} = \delta_{rad} \cdot L_{leak,rad} = \delta_{rad} \int_{\varphi_1}^{\varphi_2} L_o d\varphi = \delta_{rad} \cdot r_b \cdot \left[\frac{\varphi_2^2 - \varphi_1^2}{2} - \varphi_{oo} \cdot (\varphi_2 - \varphi_1) \right] \quad (2-17)$$

where φ_1 and φ_2 are the involute angles of the ending points of the separating portion of the spiral.

In the previous integral, L_i could be preferred to L_o depending on the direction of the leakage relative to the chamber (leakage flowing *into* or *out of* the chamber).

3 MODELING THE THERMODYNAMICS PROCESSES

The geometrical model introduced in the previous section is coupled to a thermodynamic model that actually describes the evolution of the fluid inside the expander from the beginning of the suction ($\theta = 0 \text{ rad}$) to the end of the discharge process ($\theta = 2\pi \text{ rad}$).

3.1 Differential equations governing the expansion process

The evolution of the fluid in the expander is modeled with each expander chamber considered as a control volume for which the governing equations of conservation of mass and energy are established and numerically solved.

The conservation of energy for an open control volume is:

$$\frac{dE_{CV}}{dt} = \dot{Q} + \dot{W} + \sum \dot{M}_{su} \left(h + \frac{v^2}{2} + gz \right)_{su} - \sum \dot{M}_{ex} \left(h + \frac{v^2}{2} + gz \right)_{ex} \quad (3-1)$$

where

$\frac{dE_{CV}}{dt}$ is the rate of total internal energy increase, W

\dot{Q} is the heat transfer, W

\dot{W} is the power, W

\dot{M} is the mass inflow or outflow rate, kg/s

$h + \frac{v^2}{2} + gz$ is the total enthalpy, J/kg

The mass balance for the control volume is:

$$\frac{dM}{dt} = \sum \dot{M}_{su} - \sum \dot{M}_{ex} \quad (3-2)$$

The kinetic and the potential energies can be neglected. Consequently, the “total” internal energy E_{CV} of the control reduces to its “static” internal energy value U_{CV} . The left hand side of Equation (3-1) can be written as:

$$\frac{dE_{CV}}{dt} = \frac{dU_{CV}}{dt} = M \frac{du}{dt} + u \frac{dM}{dt} \quad (3-3)$$

Introducing the expander rotation speed ω , the mass balance Equation (3-2) becomes:

$$\frac{dM}{d\theta} = \sum \frac{\dot{M}_{su}}{\omega} - \sum \frac{\dot{M}_{ex}}{\omega} \quad (3-4)$$

With

$$\omega = \frac{d\theta}{dt} \quad (3-5)$$

Assuming that the pressure and the temperature across each control volume are uniform (reversible expansion), the work term \dot{W} on the right hand side of Equation (3-1) can be expressed as:

$$\dot{W} = -P \frac{dV}{dt} \quad (3-6)$$

Combining the previous equations and operating the change of variable yields:

$$\frac{dU}{d\theta} = \frac{\dot{Q}}{\omega} - P \frac{dV}{d\theta} + \frac{1}{\omega} \sum \dot{M}_{su} \cdot h_{su} - \frac{h}{\omega} \sum \dot{M}_{ex} \quad (3-7)$$

Equations (3-4) and (3-7) constitute enough information for describing the crank angle evolution of the fluid properties in each chamber. Actually, solving these equations gives the mass $M(\theta)$ and the internal energy $U(\theta)$ and hence the specific internal energy $u(\theta)=U/M$. Knowing the volume $V(\theta)$ of the chamber, the specific volume $v(\theta)=V/M$ can be determined. Using the fluid state equations, the pressure P and the temperature T in the chamber can then be computed on the basis of $u(\theta)$ and $v(\theta)$ (Stošić, 2004).

However, for the *LFEC* expander investigated, it was found to be more convenient to derive the variations of the *pressure* and *temperature* with the crank angle. These equations are established as follows.

The change of the specific internal energy u for an open control volume is (Wark, 1995).

$$du = c_v dT + \left[T \left(\frac{dP}{dT} \right)_v - P \right] dv \quad (3-8)$$

The second term of the equation represents the non-ideal nature of the fluid.

Since the specific internal energy u can be rewritten as $u = h - P/\rho$, where h is the specific enthalpy, Equation (3-3) can be rewritten as:

$$\frac{dU_{cv}}{dt} = Mc_v \frac{dT}{dt} + T \left(\frac{dP}{dT} \right)_v \left[\frac{dV}{dt} - \frac{1}{\rho} \frac{dm}{dt} \right] - P \frac{dV}{dt} + h \frac{dm}{dt} \quad (3-9)$$

Associating Equation (3-7) and Equation (3-9), the first law of thermodynamics for the open control volume becomes:

$$Mc_v \frac{dT}{dt} + T \left(\frac{dP}{dT} \right)_v \left[\frac{dV}{dt} - \frac{1}{\rho} \frac{dM}{dt} \right] + h \frac{dM}{dt} = \dot{Q} + \sum \dot{M}_{su} h_{su} - \sum \dot{M}_{ex} h_{ex} \quad (3-10)$$

Recognizing that $h = h_{ex}$, and expressing the derivatives with respect to the change of orbiting angle θ rather than with respect to the change of time t , the expression becomes:

$$\frac{dT}{d\theta} = \frac{1}{Mc_v} \left[-T \left(\frac{dP}{dT} \right)_v \left(\frac{dV}{d\theta} - \frac{1}{\rho_w} (\dot{M}_{su} - \dot{M}_{ex}) \right) - \sum \frac{\dot{M}_{su}}{\omega} (h - h_{su}) + \frac{\dot{Q}}{\omega} \right] \quad (3-11)$$

For the *LFEC* expander, if the gas can be assumed to behave as an ideal gas, the term $T(dP/dT)_v$ reduces to the pressure P .

The expressions of the derivatives of the temperature and of the mass with respect to the orbiting angle θ can be used to calculate the properties of the mixture in each control volume throughout the expansion. However, instead of using the rate of variation of the mass, an expression similar to Equation (3-11) is established for the pressure:

Recognizing that:

$$\begin{aligned} \frac{dM}{dt} &= \frac{d(V\rho)}{dt} = \rho \frac{dV}{dt} + V \frac{d\rho}{dt} \\ &= \rho \frac{dV}{dt} + V \frac{dP}{dt} \frac{d\rho}{dP} + V \frac{d\rho}{dT} \frac{dT}{dt} \end{aligned} \quad (3-12)$$

the derivative of the pressure is:

$$\frac{dP}{dt} = \frac{1}{V \frac{d\rho}{dP}} \left[\frac{dM}{dt} - \rho \frac{dV}{dt} - V \frac{d\rho}{dT} \frac{dT}{dt} \right] \quad (3-13)$$

The expression of dT/dt developed previously can be introduced in the later expression of dP/dt . Finally, the change of properties is also expressed with respect to the change of orbiting angle rather than with the change of time. That is,

$$\frac{dP}{d\theta} = \frac{1}{V \frac{dp}{dP} c_v \rho} \left\{ \frac{\rho c_v}{\omega} \dot{M} - \rho^2 c_v \frac{dV}{d\theta} - \frac{dp}{dT} \left[-P \frac{dV}{d\theta} - \frac{1}{\omega} \sum \dot{M}_{su} u - \frac{1}{\omega} \sum \dot{M}_{ex} Pv + \frac{1}{\omega} \sum (\dot{M}_{su} h_{su}) + \frac{\dot{Q}}{\omega} \right] \right\} \quad (3-14)$$

The derivatives of the temperature and pressure constitute a system of differential equations which have to be solved numerically for each control volume.

3.2 Modeling the suction, expansion and discharge processes

The fluid is submitted to three main processes throughout the expander: suction, expansion and discharge. These processes are briefly described hereunder.

3.2.1 Suction process

Figure 2-7 shows that the volume of the suction chamber increases with increasing the orbiting angle. During the increase of the volume, the fluid at high pressure is drawn into the suction chamber. The suction chamber at the beginning of the suction process is *chamber 6*. Note that its volume is not equal to 0 at the beginning of the suction process. The volume of this chamber increases with increasing the orbiting angle, up to a point where the gap between the chamber in communication with the suction port (*chamber 1*) and two adjacent chambers (*chamber 2* and *3*) is large enough to create a pressure difference between the former and the two latter chambers. From this time, evolution of the pressure and the temperature in the 3 chambers are described independently. As the suction process goes on, the volume of *chamber 1* still increases to finally reach, at $\theta = 2\pi \text{ rad}$, the initial volume of the suction chamber (volume of *chamber 6* at $\theta = 0$). The pressure and the temperature of the fluid in *chamber 1* at the end of the suction process must be equal to the pressure and temperature in the *chamber 6* at the beginning of the suction process. After one revolution, *chambers 2* and *3* cease to be in communication with *chamber 1* and the expansion process starts. The evolution of the pressure during the suction process (pressures in chambers 6 and then 2) is shown in the P-V diagram in Figure 3-1 (between $V=0$ and $V=V_{s,exp}$).

3.2.2 Expansion process

The expansion process extends from $\theta = 0 \text{ rad}$ to $\theta = \theta_d \text{ rad}$, which is not a multiple of 2π as in other positive displacement machines (such as piston-cylinders). During this process, the fluid is expanded in a closed chamber (*chamber 7* and *8*, which are the former *chambers 3* and *2*). Actually, *chambers 7* and *8* are not closed, since flank and radial clearances will lead to fluid in-flowing or out-flowing from adjacent chambers. Internal leakages will be described in a later section.

3.2.3 Discharge process

The expansion chambers remain closed until the orbiting angle becomes equal to the discharge angle θ_d . At this time, the expansion chambers open up to the discharge region and the discharge process starts. At the beginning of the discharge process, the opening between the discharge chamber and the discharge region (*chamber 13*) is small and the in-going or out-going flow is restricted. The crank angle evolution of this opening was given in Figure 2-9. Consequently, the pressures in the discharge chambers and in the discharge region do not equalize instantaneously.

When the discharge chambers open up to the discharge region, the pressure in the chambers can be larger or lower than the one in the discharge region. In the first case, the fluid is *under-expanded*. Some fluid flows from the discharge chambers into the discharge region, until the pressures equalize. In the second case, the fluid is *over-expanded*. Some fluid has to flow from the discharge region to the discharge chambers until the pressures have equalized. Both under- and over-expansion processes therefore cause irreversibilities, which decreases the expander isentropic effectiveness.

When the pressure in *chambers 9, 10* and *13* have equalized, these three chambers are merged into one unique control volume, which is *chamber 14*. Both *chambers 13* and *14* communicate with the expander exhaust port.

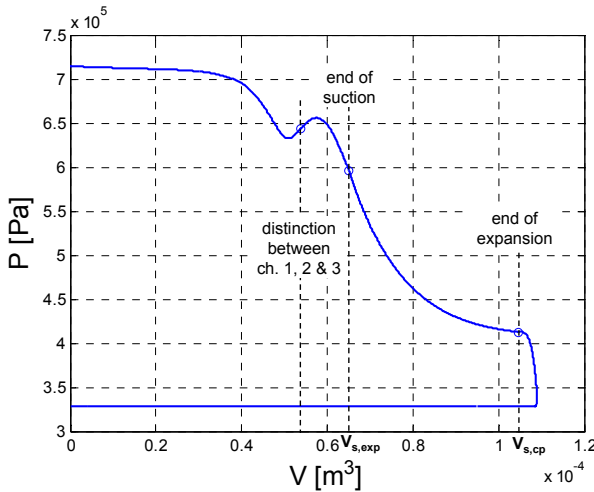


Figure 3-1: Example of P-V diagram for the global expansion process (LFEC expander)

3.3 Internal leakages

The most common way to compute the leakage flow rates between adjacent chambers is based on the equation for an isentropic flow through a nozzle, assuming that the fluid behaves as an ideal gas (Equation (3-15)). The nozzle throat area is corrected by a discharge coefficient C_d , accounting for the vena contracta.

$$\dot{M}_{\text{leak}} = C_d A_{\text{leak}} \sqrt{2P_h \rho_h} \sqrt{\frac{k}{k-1} \left[\left(\frac{P_l}{P_h} \right)^{\frac{2}{k}} - \left(\frac{P_l}{P_h} \right)^{\frac{k+1}{k}} \right]} \quad (3-15)$$

In this equation P_l is the pressure on the low pressure side and P_h is the pressure on the high pressure side. This flow is restricted by a critical pressure ratio P_l/P_h for choked flow conditions

$$\left(\frac{P_l}{P_h} \right)_{\text{crit}} = \left(\frac{2}{k+1} \right)^{\frac{k}{k-1}} \quad (3-16)$$

This equation will be used to model internal leakage flows inside the ORC expander. However for the LFEC expander, other equations accounting for the two-phase flow will be used. These equations have been introduced in Chapter 5.

Note that other flow equations might be used to describe the internal leakages. For instance, Caillat *et al.* (1988) suggested using a model including frictional effect for computing the radial leakages.

3.4 Thermal model

3.4.1 Definition of the lumped elements

As proposed by Chen (2000) for a scroll compressor, the expander and its components are split up into “lumped” elements associated to “lumped” temperatures. These lumped elements are shown in Figure 3-2. They are identified based on the following facts:

- The suction pipe cools the fluid and therefore increases its density;
- The expander scrolls cool the fluid in the suction chambers, heats or cools the fluid in the expansion chambers and heats the fluid in the discharge chambers;
- The fixed scroll is heated by the fluid in the plenum (a chamber located between the expander supply port and the suction chamber supply port);
- Heat gain from the ambient needs to be included in the overall energy balance of the expander

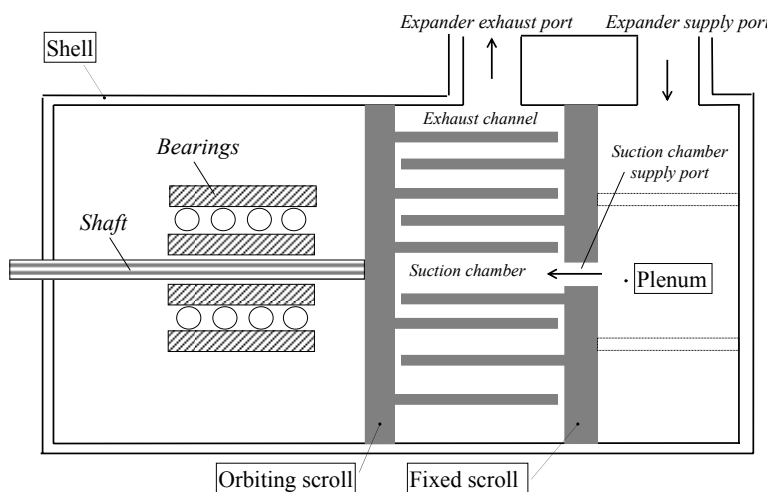


Figure 3-2: Definition of the lumped elements

In the early stages of model development, the lumped elements were the scrolls (whose mean temperatures were assumed equal), the shell, the ambient, the working chambers and the plenum. Results analysis revealed that the distinction between shell and scroll temperatures largely increased the computational time without significant impact on the predicted exhaust temperature. The reason is that temperature gradient inside the machine is small, because of the oil flooding. As a consequence, it was decided to merge the two scrolls and the shell into one isothermal element ($\bar{T}_{\text{orb}} = \bar{T}_{\text{fix}} = T_{\text{shell}}$).

3.4.2 Heat transfer between the fluid and the metal mass of the expander

In the different chambers, the fixed and the orbiting scrolls contact the refrigerant through the scroll wraps (also called “side walls” or “vanes”) and the scroll plates; which leads to either cooling-down or heating-up of the fluid, depending on both the temperatures of the fluid and the scrolls.

The temperature distribution in both the fixed and the orbiting scroll is obviously non-uniform. Based on a finite-element analysis, Halm (1997) showed that the temperature along the scrolls wraps can be assumed to vary linearly with the involute angle φ around a mean temperature \bar{T} . This temperature distribution can be written as:

$$T_{\text{fix}} = \bar{T}_{\text{fix}} + \left(\frac{\Delta T}{\Delta \varphi} \right)_{\text{orb}} \cdot (\varphi - \bar{\varphi}) \quad (3-17)$$

with the average involute angle given by

$$\bar{\varphi} = \frac{\varphi_1 + \varphi_2}{2} \quad (3-18)$$

The temperature distribution along the scrolls was recently measured by Jang and Jeong (2006), in the case of a compressor, by means of 13 thermocouples installed along the fixed scroll. Their study confirmed that the temperature decreases almost linearly with the involute angle (Figure 3-3).

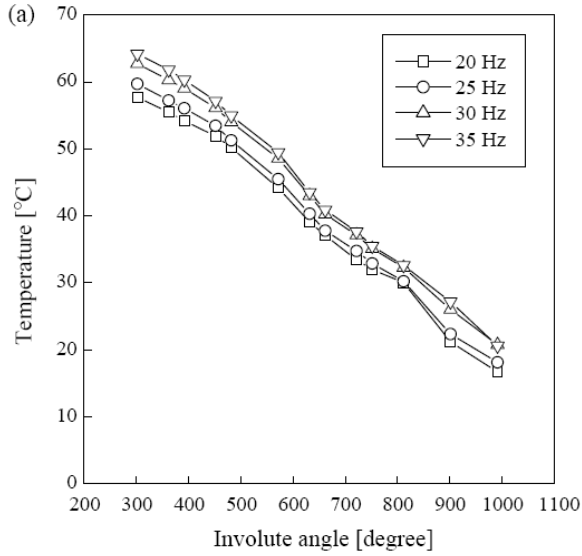


Figure 3-3: Temperature distribution in the fixed scroll (Jang and Jeong, 2006)

The average temperatures \bar{T}_{fix} and \bar{T}_{orb} of the fixed and the orbiting scrolls are obtained from an overall energy balance introduced later.

Heat transfers are computed as follows, through the plates of the *chambers 3, 7, 10*:

$$\dot{Q}_{plate,fix} = \frac{1}{2} h_c r_b^2 \left[\int_{\varphi_{k1}}^{\varphi_{k2}} [T_{fix}(\varphi) - T(i, k)] (\varphi - \varphi_{i0})^2 d\varphi - \int_{\varphi_{k1-\pi}}^{\varphi_{k2-\pi}} [T_{fix}(\varphi + \pi) - T(i, k)] (\varphi - \varphi_{o0})^2 d\varphi \right] \quad (3-19)$$

$$\dot{Q}_{plate,orb} = \frac{1}{2} h_c r_b^2 \left[\int_{\varphi_{k1}}^{\varphi_{k2}} [T_{orb}(\varphi - \pi) - T(i, k)] (\varphi - \varphi_{i0})^2 d\varphi - \int_{\varphi_{k1-\pi}}^{\varphi_{k2-\pi}} [T_{orb}(\varphi) - T(i, k)] (\varphi - \varphi_{o0})^2 d\varphi \right] \quad (3-20)$$

Through the plates of *Chambers 2, 8, 9*:

$$\dot{Q}_{\text{plate,fix}} = \frac{1}{2} h_c r_b^2 \left[\int_{\varphi_{k1}}^{\varphi_{k2}} [T_{\text{fix}}(\varphi - \pi) - T(i, k)] (\varphi - \varphi_{i0})^2 d\varphi - \int_{\varphi_{k1-\pi}}^{\varphi_{k2-\pi}} [T_{\text{fix}}(\varphi) - T(i, k)] (\varphi - \varphi_{o0})^2 d\varphi \right] \quad (3-21)$$

$$\dot{Q}_{\text{plate,orb}} = \frac{1}{2} h_c r_b^2 \left[\int_{\varphi_{k1}}^{\varphi_{k2}} [T_{\text{orb}}(\varphi) - T(i, k)] (\varphi - \varphi_{i0})^2 d\varphi - \int_{\varphi_{k1-\pi}}^{\varphi_{k2-\pi}} [T_{\text{orb}}(\varphi + \pi) - T(i, k)] (\varphi - \varphi_{o0})^2 d\varphi \right] \quad (3-22)$$

And through the walls:

$$\dot{Q}_{\text{wall,fix}} = h_c r_b h \int_{\varphi_{k1}}^{\varphi_{k2}} \left[T_{\text{fix}}(\varphi) - T(i, k) \right] (\varphi - \varphi_o) d\varphi \quad (3-23)$$

$T(i, k)$ is the temperature of the fluid in chamber i at the time step k . The total heat transfer from the fixed and orbiting scrolls to the refrigerant is given by:

$$\dot{Q}_{\text{orb}} = \dot{Q}_{\text{plate,fix}} + \dot{Q}_{\text{wall,fix}} \quad (3-24)$$

The average heat transfers from the fixed and the orbiting scrolls to the fluid are respectively calculated by:

$$\bar{Q}_{\text{fix}} = \frac{1}{2\pi} \sum_{k=1}^{\text{MAXN}} \dot{Q}_{\text{fix}}(k) \Delta\theta \quad (3-25)$$

$$\bar{Q}_{\text{orb}} = \frac{1}{2\pi} \sum_{k=1}^{\text{MAXN}} \dot{Q}_{\text{orb}}(k) \Delta\theta \quad (3-26)$$

In the previous equations, h_c is the convective heat transfer coefficient. It is calculated on the basis of a correlation established for spiral plate heat exchangers, in which the flow passage cross section is rectangular, with small aspect ratio. Tagri and Jayaraman (1962) have

reported experimental water-to-water heat transfer data for such exchanger. They identified the following correlation for $\text{Re}>6000$:

$$\frac{\text{Nu}}{\text{Nu}_{\text{DB}}} = K_c = \left(1.0 + 1.77 \frac{D_h}{R_c} \right) \quad (3-27)$$

Nu_{DB} is evaluated using the straight-tube Dittus-Boelter correlation, D_h is the hydraulic diameter of the spiral and R_c is the curvature radius of the spiral. For the inner involute, the curvature radius between conjugacy angles $\varphi_{\text{conj},1}$ and $\varphi_{\text{conj},2}$ is defined by:

$$R_c = r_b \frac{(\varphi_{\text{conj},i,2} - \varphi_{i,0}) + (\varphi_{\text{conj},i,1} - \varphi_{i,0})}{2} \quad (3-28)$$

In order to investigate the effect of the orbiting scroll motion on convection heat transfer in scroll wrap, Jang and Jeong (2006) measured the heat transfer in a rectangular duct with one oscillating wall. From this experimental study, they proposed the following correlation:

$$\text{Nu} = K_c K_{\text{st}} \text{Nu}_{\text{DB}} \quad (3-29)$$

In this expression K_{st} is a correction factor which accounts for the heat transfer enhancement due to the orbiting scroll motion. They proposed the following experimental correlation:

$$K_{\text{st}} = 1 + 8.48[1 - \exp(-5.35\text{St})] \quad (3-30)$$

The dimensionless parameter in this expression is the Strouhal number, defined as the ratio between the velocities in two directions: perpendicular and parallel to the flow:

$$\text{St} = \frac{fA}{U} \quad (3-31)$$

with,

- f frequency of the expander, rps
 A oscillation amplitude of the orbiting scroll, m
 U mean velocity of the fluid, m/s

3.4.3 Mechanical loss

As proposed by Yanagisawa (2001), mechanical loss is modeled by introducing a global mechanical frictional torque T_m . This loss accounts for friction between the scrolls as well as loss in the ball bearings. It is assumed that the whole mechanical loss is dissipated inside the expander's shell.

3.4.4 Heat transfer in the plenum

Probably in order to increase the rigidity of the assembly, a supporting element is nestled in the plenum. This element has a circular shape, with an opening on the top (as shown in Figure 3-4). Embedded in the plenum, this element creates a circular channel with a rectangular cross section.

Before reaching the suction chamber supply port, the fluid coming from the expander supply port has to flow around the supporting element. In order to estimate the heat flow rate given by the walls of the plenum to the fluid (Equation (3-32)), the convective heat transfer coefficient has to be evaluated.

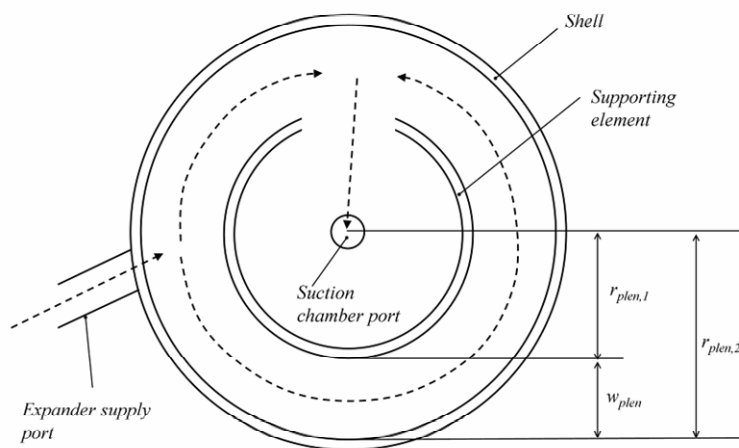


Figure 3-4: Circular channel in the plenum

This can be done by comparing the plenum to a circular channel with a rectangular cross-sectional area (Tagri and Jayaraman, 1962).

$$\dot{Q}_{\text{shell,plen}} = \varepsilon_{\text{shell,plen}} \cdot \dot{C}_{\text{plen}} \cdot (T_{\text{su,plen}} - T_{\text{shell}}) \quad (3-32)$$

3.4.5 Energy balances

Two energy balances must be performed in order to determine the temperatures of the scrolls and of the shell, respectively.

In steady state regime, the global energy balance of the scrolls and the shell assembly can be expressed as follows:

$$\dot{Q}_{\text{shell,plen}} + \dot{Q}_{\text{shell,su}} - \dot{Q}_{\text{shell,ex}} - \dot{Q}_{\text{shell,amb}} - \dot{Q}_{\text{shell,chan}} - \bar{\dot{Q}}_{\text{fix}} - \bar{\dot{Q}}_{\text{orb}} + \dot{W}_{\text{loss}} = 0 \quad (3-33)$$

The term $\dot{Q}_{\text{shell,chan}}$ represents the heat transfer from the shell to the fluid contained in the channel. It can also be computed by reference to a circular channel with a rectangular cross-sectional area.

The shell to ambient heat transfer is evaluated by

$$\dot{Q}_{\text{shell,amb}} = A U_{\text{shell,amb}} \cdot (T_{\text{shell}} - T_{\text{amb}}) \quad (3-34)$$

The average heat transfers from the fixed and the orbiting scrolls $\bar{\dot{Q}}_{\text{fix}}$ and $\bar{\dot{Q}}_{\text{orb}}$ were introduced previously. $\dot{Q}_{\text{shell,su}}$ and $\dot{Q}_{\text{shell,ex}}$ are the heat transfers between the shell and the fluid in the expander supply and exhaust ports. Convective heat transfer coefficients are computed with Dittus-Boelter relationship for a turbulent flow in a circular pipe.

3.5 Calculating the mass flow rate

The mass flow rate is calculated as the mass discharged through the expander exhaust port at each revolution divided by the corresponding time (Halm, 1997):

$$\bar{\dot{M}}_{ex} = \sum_{k=1}^{MAXN} \frac{\dot{M}_{ex}(k)\Delta\theta}{\omega} \cdot \frac{\omega}{2\pi} = \sum_{k=1}^{MAXN} \frac{\dot{M}_{ex}(k)\Delta\theta}{2\pi} \quad (3-35)$$

where

- $\dot{M}_{ex}(k)$ is the mass flow entering or exiting the channel at step k, kg/s
- $\Delta\theta$ is the orbiting angle step, rad
- MAXN is the number of steps used in the expansion process model, -
- ω is the expander rotational speed, rad/s

3.6 Calculating the average discharge temperature and enthalpy

The average enthalpy of the fluid at the exhaust of the expander can be calculated by (Halm, 1997):

$$\bar{h}_{ex} = \frac{\sum_{k=1}^{MAXN} \frac{\dot{M}_{ex}(k) \cdot h_{ex}(k) \cdot \Delta\theta}{\omega}}{\sum_{k=1}^{MAXN} \frac{\dot{M}_{ex}(k) \Delta\theta}{\omega}} = \frac{\sum_{k=1}^{MAXN} \dot{M}_{ex}(k) \cdot h_{ex}(k)}{\sum_{k=1}^{MAXN} \dot{M}_{ex}(k)} \quad (3-36)$$

where

$h_{ex}(k)$ is the enthalpy of the discharged mass flow at step k , J/kg

The average discharge temperature T_{ex} is then calculated on the basis of the average discharge enthalpy \bar{h}_{ex} and outlet pressure P_{ex} .

$$T_{ex} = T(P_{ex}, \bar{h}_{ex}) \quad (3-37)$$

3.7 Calculating the expansion work rate and the shaft power

Figure 3-5 shows the energy flow chart associated to a hermetic expander. The actual expansion work differs from the isentropic work due to heat transfer and internal leakages. The available shaft work is lower than the expansion work because of the mechanical loss dissipated across the expander. In the case of a hermetic machine, the shaft work is transformed into electrical work by means of a motor which is also subject to losses.

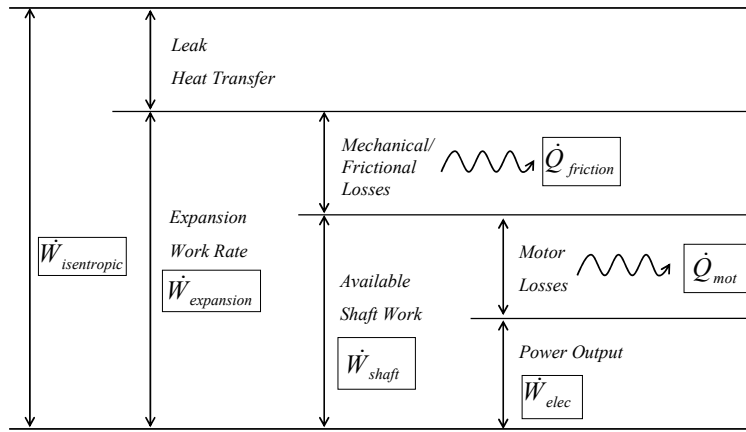


Figure 3-5: Expander energy flow chart

The shaft power can be calculated by expressing the heat balance across the expander:

$$\dot{W}_{\text{shaft}} = \dot{M} \cdot (h_{\text{su}} - \bar{h}_{\text{ex}}) - \dot{Q}_{\text{ambient}} \quad (3-38)$$

Alternatively, the shaft power can also be calculated from the expansion power, defined as

$$\dot{W}_{\text{expansion}} = \dot{M} \cdot (h_{\text{plen}} - h_{\text{channel}}) + \bar{Q}_{\text{fix}} + \bar{Q}_{\text{orb}} \quad (3-39)$$

by subtracting the mechanical loss

$$\dot{W}_{\text{shaft}} = \dot{W}_{\text{expansion}} - \dot{W}_{\text{loss}} \quad (3-40)$$

3.8 Numerical solution

The model described in the previous paragraphs has been implemented into a MATLAB simulation code. The program calculates the temperatures, pressures and masses in the different chambers of the scroll expander as a function of the orbiting angle θ for one entire revolution. It also calculates the temperatures of the different elements of the expander, the mean exhaust temperature of the fluid, the mass flow rate and the shaft power.

The entire revolution is divided into MAXN steps. The step length is chosen constant and is equal to $2\pi/MAXN$. When required, the calculation accuracy can be improved by adjusting the number of steps (and therefore the step length accordingly) for any parts of the expansion process.

The differential equations are solved by means of the Euler method, except for the simultaneous calculation of *chambers 1, 2 and 3* where Runge-Kutta fourth-order method is used. If X denotes M and U (or P and T , depending whether equations (3-4) and (3-7) or (3-11) and (3-14) are used), the Euler method can be expressed as

$$X(i, \theta_k) = X(i, \theta_{k-1}) + \left(\frac{dX}{d\theta} \right)_{k-1} \Delta\theta \quad (3-41)$$

The flow chart of the main program is shown in Figure 3-6. The simulation starts with the description of the expander geometry: crank angle evolution of the chambers' volumes, of the leakage lengths, heat transfer areas and the suction chamber supply port and discharge chamber opening.

Initial temperature and pressure are assigned to each working chamber. The corresponding initial mass of fluid is then computed. The suction, the expansion and the discharge processes are then successively described. The mass flow rate through the expander and the exhaust

temperature are calculated using Equations (3-35) and (3-36). All the previous steps are repeated until the exhaust temperature converges, which is expressed by

$$|T_{ex,j} - T_{ex,j-1}| < \varepsilon \quad (3-42)$$

where $T_{ex,j}$ and $T_{ex,j-1}$ denote the exhaust temperatures for two consecutive iterations. The convergence tolerance is set to 0.01K.

The secant method (Recktenwald, 2000) is used to compute the shell temperature and generally requires three iterations for convergence. Note that if more than one temperature node was introduced in the modeling, the Newton-Raphson method would be more appropriate to solve the associated set of non-linear equations.

The convergence criterion for the residual on the shell energy balance can be written as hereunder. Here, the convergence tolerance is set to 1 Watt.

$$\left| \dot{Q}_{shell,plen} + \dot{Q}_{shell,su} - \dot{Q}_{shell,ex} - \dot{Q}_{shell,amb} - \dot{Q}_{shell,chan} - \bar{\dot{Q}}_{fix} - \bar{\dot{Q}}_{orb} + \dot{W}_{loss} \right| < \varepsilon \quad (3-43)$$

Due to the periodicity of the process, the thermodynamics state variables in each chamber at the beginning of one rotation (*initial conditions*) must be equal to those determined at the end of previous rotation. This can be expressed by the following set of equations:

$$X(6,0) = X(1,MAXN) \quad (3-44)$$

$$X(7,0) = X(3,MAXN) \quad (3-45)$$

$$X(8,0) = X(2,MAXN) \quad (3-46)$$

(...) according to the number $NEXP$ of pairs of expansion chambers

$$X(7+2(NEXP-2),0) = X(7,0) \quad (3-47)$$

$$X(8+2(NEXP-2),0) = X(8,0) \quad (3-48)$$

$$X(7+2(NEXP-1),0) = X(7, 7+2(NEXP-2),MAXN) \quad (3-49)$$

$$X(8+2(NEXP-1),0) = X(8, 7+2(NEXP-2),MAXN) \quad (3-50)$$

For the discharge region, depending whether or not discharge chambers and discharge channel have merged (§3.2.3), the following equations can be written

$$X(13+2(NEXP-1),0) = X(13+2(NEXP-1),MAXN) \quad (3-51)$$

$$X(14+2(NEXP-1),0) = X(14+2(NEXP-1),MAXN) \quad (3-52)$$

Moreover, the relationships given hereunder must be imposed. If *BREAK12* denotes the step when *chamber 6* is divided into *chambers 1, 2 and 3*, it follows that

$$X(1,BREAK12+1) = X(2,BREAK12+1) = X(3,BREAK12+1) = X(6,BREAK12) \quad (3-53)$$

If *BREAK78* denotes the step when expansion chambers open up to the discharge region (discharge angle), we have

$$X(9+2(NEXP-1),BREAK78+1) = X(7+2(NEXP-1),BREAK78) \quad (3-54)$$

$$X(10+2(NEXP-1),BREAK78+1) = X(8+2(NEXP-1),BREAK78) \quad (3-55)$$

The *boundary conditions* to this system of differential equations are the expander supply pressure and temperature, the exhaust pressure, the rotational speed and the ambient temperature. In the case of the LFEC expander, an additional boundary condition is the mass fraction of liquid in the mixture.

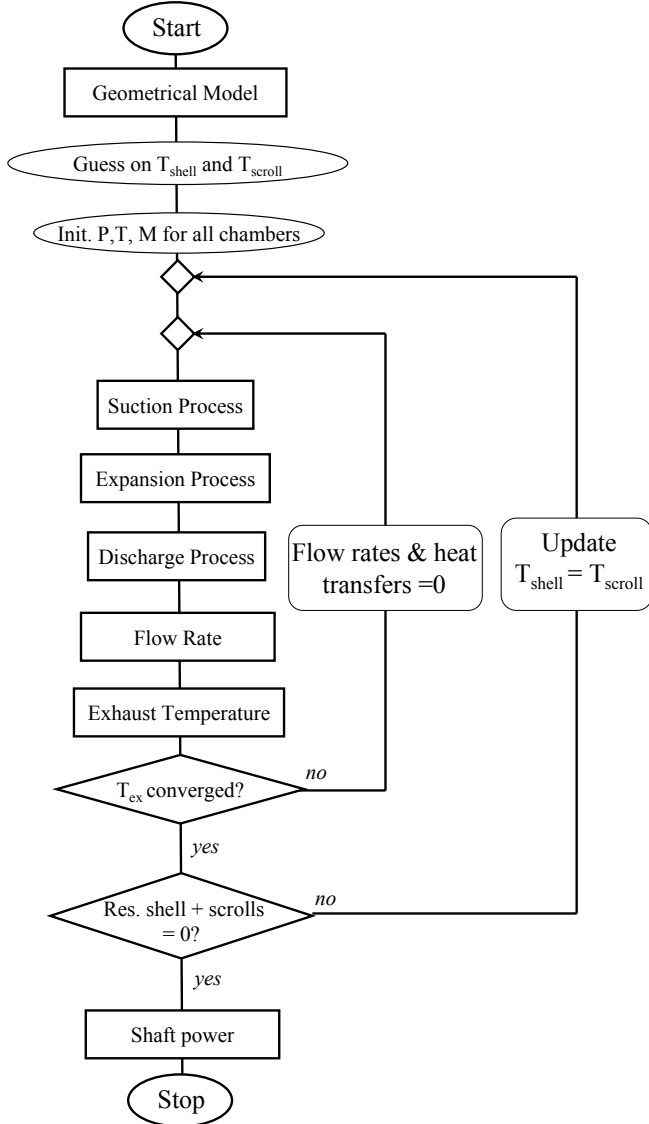


Figure 3-6: Flow chart for the main program

4 CONCLUSIONS

A comprehensive numerical model of the scroll expander has been established, based on an existing scroll compressor model (Halm, 1997). This adaptation demonstrated all the peculiarities of the operation in expander mode, such as the source of pressure losses during the suction process. It was shown that the model can easily be adapted to more than one pair of expansion chambers.

The development of this model is done in two steps. First, a *model describing the geometry* of the expander is built. This model determines the evolution of the volumes (and their derivatives) with the crank angle, but also the evolution of the internal leakage paths and the evolution of heat transfer areas with the crank angle. The model also accounts for other geometrical peculiarities of the machines which would impact on the expansion modeling (dimension of the ports, presence of a plenum between the inlet port and the suction chamber,...). Results generated by the geometrical model are then used in the *expansion process model*. This model describes the evolution of the temperature and the pressure in all the chambers of the expander with the crank angle. In the expansion process model, equations of conservation of energy and mass are solved numerically for each chamber.

For convenience, only modeling features associated to the *LFEC* expander have been presented in this chapter. Modeling features associated to the *ORC* expander and validation of the model for both expanders are presented in a subsequent chapter.

The detailed experimental validation of the expander deterministic model will be presented in Chapter 7 for both the ORC and the LFEC expanders.

REFERENCES

- Caillat, J.-L., S. Ni, M. Daniels. 1988. A computer model for scroll compressors, *Proceedings of the International Compressor Engineering at Purdue*: 47-55.
- Cengel, Y. A., and M.A. Boles. 2006. Thermodynamics, An engineering Approach, *Mc Graw Hill*.
- Chen, Y. 2000. Mathematical Modeling of Scroll Compressors, *Ph.D Thesis*, Purdue University.
- Creux, L. 1905, Rotary Engine, U.S. Patent no. 801182.
- Halm, N. P. 1997. Mathematical Modeling of Scroll Compressors, *Master Thesis*, Purdue University.
- Huff, H.-J., and R. Radermacher. 2003. CO₂ Compressor-expander analysis: Final Report, Air-Conditioning and Refrigeration Technology Institute, Arlington, VA, ARTI-21CR/611-10060-01.

- Jang, K., and S. Jeong. 2006. Experimental investigation on convective heat transfer mechanism in a scroll compressor. *International Journal of Refrigeration* 29: 744-753.
- Lee, G.H. 2002. Performance simulation of scroll compressors, Proc Instn Mech Engrs Vol 216 Part A: J Power and Energy: 169-179.
- Morishita, E., T. Inaba, T. Nakamura, and W. Works. 1984. Scroll Compressor Analytical Model. *Proceedings of the International Compressor Engineering Conference at Purdue*: 486-495
- Myszka, D.H. 1998. An analytical model for the discharge process in scroll compressors, *Proceedings of the International Compressor Engineering Conference at Purdue*.
- Nieter, J. 1988. Dynamic of scroll suction process, *Proceedings of the International Compressor Engineering Conference at Purdue*.
- Nieter, J.J., D.P., Gagne. 1992. Analytical modeling of discharge flow dynamics in scroll compressors. *Proceedings of the International Compressor Engineering Conference at Purdue*.
- Ooi, K. T., J. Zhu. 2004. Convective heat transfer in a scroll compressor chamber: a 2-D simulation, *International Journal of Thermal Sciences* 43: 677-688.
- Recktenwald G., Numerical Methods with Matlab, Implementation and Application, Prentice Hall, 2000, Upper Saddle River, New Jersey 07458
- Schein C., and R. Radermacher. 2001. Scroll compression simulation model, *Journal of engineering for Gas Turbines and Power*. ASME. 123: 217-225.
- Stošić, N. 2004. Screw Compressors in Refrigeration and Air Conditioning. HVAC&R Research, vol 10, 3: 242.
- Tagri, N.N., and R. Jayaraman. 1962. Heat Transfer Studies on a Spiral Plate Heat Exchanger, *Trans. Inst. Chem. Eng.*, Vol. 40: 161-168.
- Wang, B., X. Li, W. Shi. 2005. A general geometrical model of scroll compressors based on discretionary initial angles of involute, *Int. J. Refrigeration* 28: 958-966.
- Wang, B., W. Shi, X. Li and Q. Yan. 2007. Numerical research on the scroll compressor with refrigeration injection. *Applied Thermal Engineering*.
- Wark, K., *Thermodynamics*, Fourth edition, McGraw-Hill, 1983, pp. 669-671
- Xiaojun, G., L. Liansheng, Z. Yuanyang, S. Pengcheng. 2004. Research on a Scroll Expander Used for Recovering Work in a Fuel Cell. *International Journal of Thermodynamics* 7:1-8.

- Yanagisawa, T., M.C. Cheng, M. Fukuta, T. Shimizu. 1990. Optimum Operating Pressure Ratio for Scroll Compressor. Proceedings
- Yanagisawa, T., M. Fukuta, Y. Ogi, and T. Hikichi. 2001. Performance of an oil-free scroll-type air expander. *Proc. Of the ImechE Conf. Trans. On compressors and their systems:* 167-174.
- Yuanyang, Z., L. Liansheng, and S. Pengcheng. 2006. Thermodynamic simulation of scroll compressor/expander module in automotive fuel cell engine, *Proc. IMechE 220 Part D: J. Automobile Engineering.*

CHAPTER 7

VALIDATION OF THE SCROLL EXPANDER DETERMINISTIC MODEL

1	INTRODUCTION.....	224
2	RANKINE CYCLE EXPANDER	224
2.1	Data used for validation.....	224
2.2	Fluid thermodynamic properties	224
2.3	Geometrical description.....	225
2.3.1	Identification of the geometrical parameters	225
2.3.2	Definition of the working chambers.....	227
2.3.3	Ports and openings.....	229
2.4	Model verification.....	232
2.4.1	Identified parameters	232
2.4.2	Verification of the mass flow rate	234
2.4.3	Verification of the shaft power.....	234
2.4.4	Verification of the exhaust temperature.....	235
2.4.5	Verification of the isentropic effectiveness	237
2.5	Model analysis.....	238
2.5.1	Suction process	238
2.5.2	Expansion process	241
2.5.3	Discharge process	242
2.5.4	Heat transfers	244
2.6	Design modification.....	245
2.6.1	Reduction of the suction pressure drop	245
	Variation of the tip radial gap	245
	Variation of the suction chamber supply port	247
2.6.2	Variation of the radial and flank leakage gaps size	247
2.6.3	Variation of the mechanical loss torque	249
2.6.4	Variation of the heat transfer coefficients.....	250
2.6.5	Variation of the expander exhaust port diameter.....	251
2.7	Variation of the operating conditions	251
2.7.1	Pressure ratio	251
2.7.2	Rotational speed.....	252
2.8	Derivation of non-dimensional laws for the semi-empirical model	253
2.8.1	Expression of the laws.....	253
2.8.2	Comparative validation	256
2.9	Teardown inspection	258

3	ERICSSON CYCLE EXPANDER.....	258
3.1	Validation	258
3.1.1	Prediction of the mass flow rate.....	260
3.1.2	Prediction of the shaft power.....	261
3.1.3	Prediction of the exhaust temperature.....	262
3.2	Design modification.....	263
3.2.1	Decrease of the suction pressure drop.....	263
3.2.2	Variation of the flank and radial gap sizes.....	265
4	CONCLUSIONS	267
5	REFERENCES.....	269

NOMENCLATURE

A	Area, m ²
AU	Heat transfer coefficient, W/K
C	Discharge coefficient, -
d	Diameter, m
h	Scroll height, m
H	Height, m
h	Specific enthalpy, J/kg
h_c	Convective heat transfer coefficient, W/m ² .K
k	Specific heat ratio, -
L	Length, m
M	Mass, kg
\dot{M}	Mass flow rate, kg/s
N	Rotational speed, Hz
NEXP	Number of pair of expansion chambers, -
Nu	Nusselt number, -
P	Pressure, Pa
\dot{Q}	Heat transfer rate, W
r	Radius, m
r	ratio, -
$r_{v,in}$	Built-in volume ratio, -
rpm	Rotational speed, min ⁻¹
s	Specific entropy, J/kg-K
t	Scroll thickness, m
T	Temperature, °C
T	Torque, N-m
u	Specific internal energy, J/kg
U	Internal energy, J
\dot{V}	Volume flow rate, m ³ /s
V	Volume, m ³
W	Width, m

\dot{W} Power, W

Subscripts

amb	Ambient
b	Base circle
calc	Calculated
cp	Compressor
d	Discharge
dis	Discharge
e	Ending
ex	Exhaust
exp	Expander
exp	Expansion
f	Flank
fix	Fixed
leak	Leakage
loss	Mechanical loss
meas	Measured
n	Nominal
o	Outer, orbiting radius
orb	Orbiting
p	Pressure
s	Starting, swept, suction
su	Supply
suc	Suction
v	Constant volume

Greek and miscellaneous

ε	Effectiveness, -
δ	Gap, m
δ	Reduced density, -
Δ	Difference

ω	Rotational speed, rad/s
φ	Involute angle, rad
ρ	Density, kg/m ³
τ	Reduced temperature, -
θ	Orbiting (crank) angle, rad
0	Initial

1 INTRODUCTION

This Chapter presents the experimental validation of the deterministic model of the scroll expander. This validation is performed for two particular expanders: one integrated into the Organic Rankine Cycle system (*ORC expander*) and the other one into the Liquid Flooded Ericsson Cycle cooler (*LFEC expander*).

The main objectives of this chapter are to:

- 1) Validate the deterministic model introduced in the previous chapter.
- 2) Investigate the variation of the expanders' performance with the modification of their design and evaluate optimization potentials.
- 3) Check whether or not the parameters of the semi-empirical model have a physical meaning.

2 RANKINE CYCLE EXPANDER

2.1 Data used for validation

Data used for validation are thoroughly detailed in Chapter 4. This experimental data covers a wide range of operating conditions (Quoilin, 2007). In total 39 points were achieved. The influence of the following variables and parameters are investigated: the expander supply temperature and pressure (by controlling the refrigerant flow rate displaced by the pump, as well as the hot air flow rates and temperatures), the expander exhaust pressure (by adjusting the water flow through the condenser) and the expander rotational speed (set to 3 different values: 1771, 2296, 2660 min⁻¹).

2.2 Fluid thermodynamic properties

The equation of state the most frequently used to describe the properties of refrigerant R123 is the one established by Younglove and McLinden (1994). From this equation, Baehr and Tillner-Roth (1995) derived working equations which are almost as accurate and allow a drastic reduction in the computational time. For these reasons, these equations are used in the modeling presented hereunder. They are given as function of the reduced temperature τ (defined by $T_c[K]/T[K]$) and the reduced density δ (defined by ρ/ρ_c). The coefficients of these equations are given in the Appendix.

$$\frac{p(\tau, \delta)}{\rho RT} = 1 + \delta(b_1 + b_2\tau^{1/4} + b_3\tau^{7/2}) + 2\delta^2(c_1\tau^{-1/2} + c_2\tau^{-1/4}) \quad (2-1)$$

$$\begin{aligned} \frac{h(\tau, \delta)}{RT} &= a_1^*\tau + m_1 + \frac{1}{2}m_2\tau^{-1} + \frac{1}{3}m_3\tau^{-2} + \frac{1}{4}m_4\tau^{-3} \\ &+ \delta\left(b_1 + \frac{5}{2}b_2\tau^{1/4} + \frac{9}{2}b_3\tau^{7/2}\right) + \delta^2\left(\frac{3}{2}c_1\tau^{-1/2} + \frac{7}{4}c_2\tau^{-1/4}\right) \end{aligned} \quad (2-2)$$

$$\begin{aligned} \frac{s(\tau, \delta)}{R} &= a_0^* + (m_1 - 1)(1 - \ln \tau) - \ln \delta + m_2\tau^{-1} + \frac{1}{2}m_3\tau^{-2} + \frac{1}{3}m_4\tau^{-3} \\ &+ \delta\left(-b_1 - \frac{3}{4}b_2\tau^{1/4} + \frac{5}{2}b_3\tau^{7/2}\right) + \delta^2\left(-\frac{3}{2}c_1\tau^{-1/2} - \frac{5}{4}c_2\tau^{-1/4}\right) \end{aligned} \quad (2-3)$$

2.3 Geometrical description

2.3.1 Identification of the geometrical parameters

The design parameters of the scroll expander were retrieved by reverse engineering (Lee and Ree, 2007). This consisted in measuring one of the spirals by means of a 3-D measuring machine and tuning the geometrical parameters to match the geometry described by the model to the measured one. The result is shown in Figure 2-1. The tip geometry of the scroll machine under investigation differs obviously from that of a unique circular arc. It was observed that the tip of the scroll can be very accurately described by two circular arcs in series (dash lines in Figure 2-3).

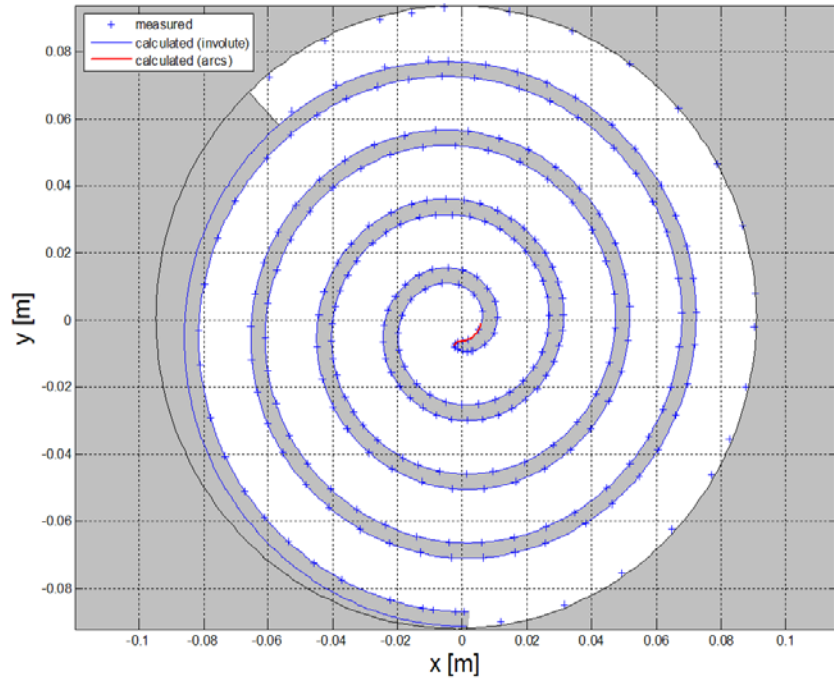


Figure 2-1: Comparison between the geometries measured and predicted by the model



Figure 2-2: View of the fixed scroll

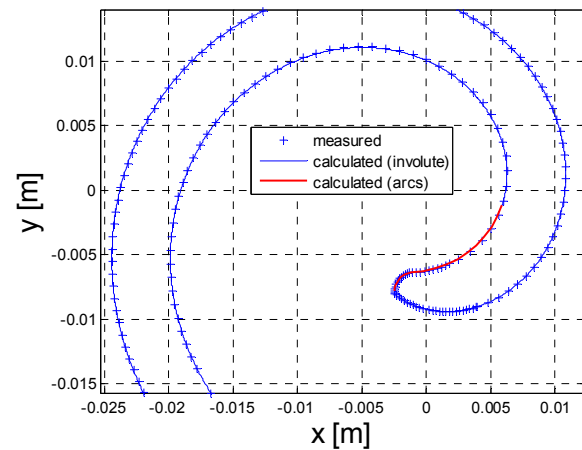


Figure 2-3: Prediction of the measured geometry : detail of the scroll tip

The identified geometrical parameters are given in Table 2-1.

Table 2-1: Identified geometrical parameters (ORC expander)

r_b	h	$\varphi_{o,0}$	$\varphi_{i,0}$	$\varphi_{o,s}$	$\varphi_{i,s}$	φ_e	r_o
[mm]	[mm]	[rad]	[rad]	[rad]	[rad]	[rad]	[mm]
3.264	28.65	0	1.3971	1.57	3.5	27.395	5.7

As shown in Table 2-2, the compressor swept volume predicted by the model is very close to the value announced by the manufacturer (148 cm^3). A volume ratio of 3.94 is predicted, which is a little bit lower than the value identified for the semi-empirical model. This yields a difference of 2.2% between the displacement predicted here and the one identified in the semi-empirical model.

Table 2-2: Comparison of the built-in volume ratio, swept volumes in compressor and expander modes predicted by the deterministic model and identified in the semi-empirical model

	Deterministic model	Semi-empirical model
$r_{v,in}$	3.94 [-]	4.05 [-]
$V_{s,cp}$	147.1 [cm^3]	148.0 [cm^3]
$V_{s,exp}$	37.36 [cm^3]	36.54 [cm^3]

2.3.2 Definition of the working chambers

The different working chambers corresponding to four steps during one entire revolution are represented in Figure 2-4. The suction chamber, which is in communication with the suction port is labeled *chamber 6*. The suction process starts when the orbiting angle θ is equal to 0. The relative position of the two spirals corresponding to this angle is shown in Figure 2-4 (a). The suction chamber 6, which is in communication with the suction port, is characterized by its minimal value. Note that the volume of the suction chamber is never reduced to zero, but to a residual clearance volume. The expansion chambers are *chambers 7, 8, 9, 10, 11* and *12*. *Chamber 7* is the expansion chamber that develops from *chamber 3* and *chamber 8* is the expansion chamber that develops from *chamber 2*. Expansion proceeds successively through *chambers 9* and *10* and *chambers 11* and *12*. The latter chambers only exist for the period $0 - \theta_d$.

Figure 2-4 (c) shows the relative position of the spirals, just after the expansion chambers 11 and 12 have opened onto the discharge channel (right after $\theta = \theta_d$). Chamber 13 is the discharge chamber that develops from chamber 11 and chamber 14 is the discharge chamber that develops from chamber 12. Both discharge chambers are connected to the discharge channel called chamber 17. In the case that the pressures in all three chambers 13, 14 and 17 have equalized, the entire control volume is treated as chamber 18.

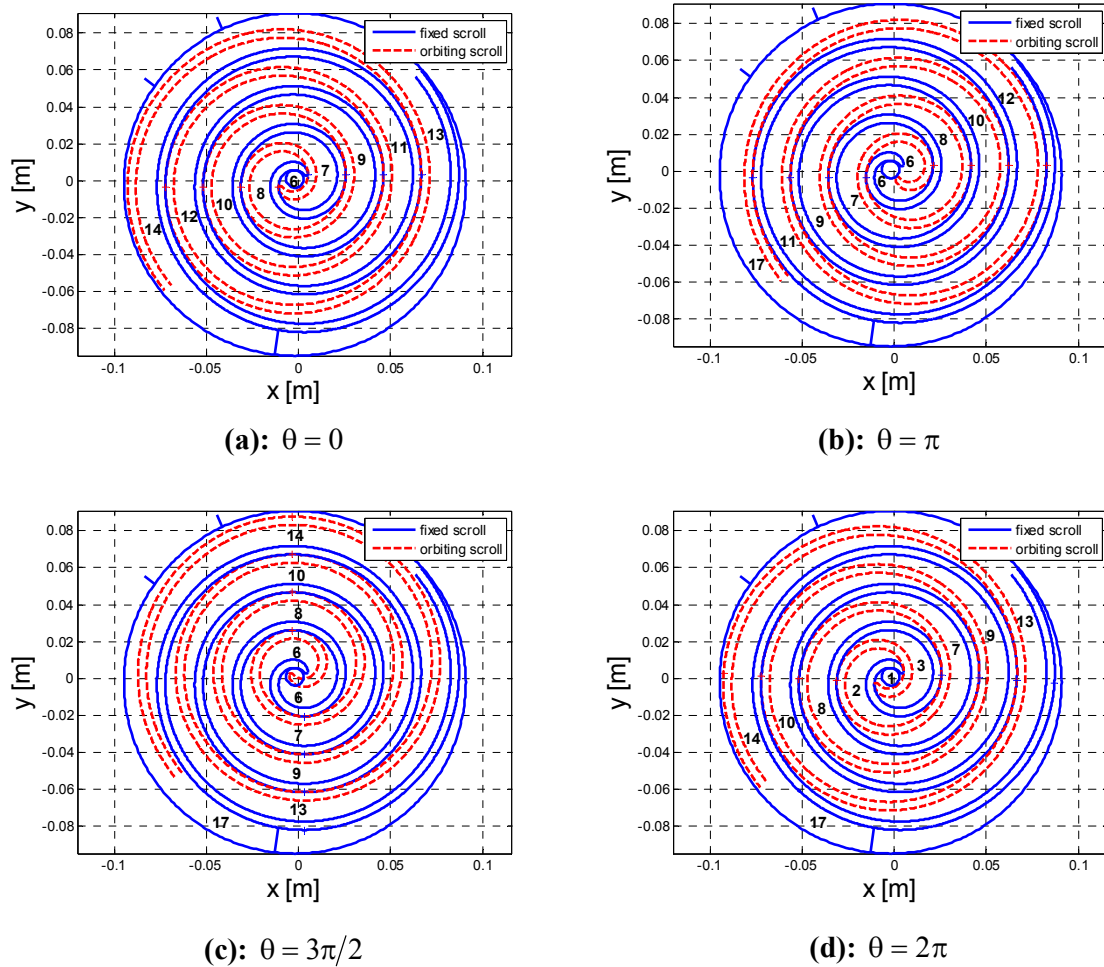


Figure 2-4: Definition of the expander working chambers

At the end of the suction process (Figure 2-4 (d)), the suction chamber 6 is fictitiously divided into chamber 1 and chambers 2 and 3. This sub-division is necessary to compute the

pressures in the three sub-chambers, since the latter communicate only by small gaps and cannot be supposed to be at exactly the same pressure.

The evolution of the volume of the different chambers with the crank angle is summarized in Figure 2-5. It can be observed that both the suction and the discharge processes extend over one entire revolution. The discharge process successively extends from θ_d to 2π , and from 0 to θ_d . The expansion process occurs during more than 2 revolutions (exactly during $4\pi + \theta_d$).

The ratio between the volume of the expansion chambers at the end of the expansion and the one at the beginning determines the built-in volume ratio of the machine. It can be observed that the expander under investigation is characterized by a large built-in volume ratio (~ 4.0), making it adapted to higher pressure ratios than a classical refrigeration compressor.

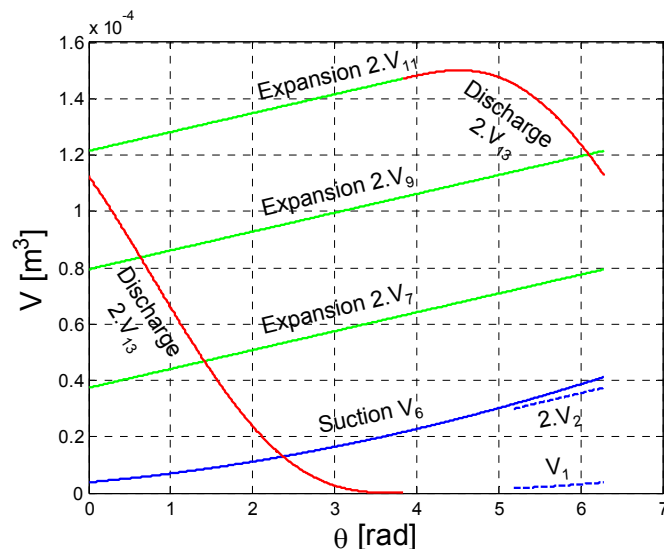


Figure 2-5: Crank angle evolution of the volumes of the different chambers

2.3.3 Ports and openings

For clarity, the following distinction must be made between the different ports and opening inside the expander:

- The *expander supply port* is the orifice through which the fluid coming from the supply line enters the expander. The internal diameter of the supply pipe is successively reduced from the expander supply port $d_{su,exp}$ to the intermediate supply

port diameter $d_{su1,exp}$ and finally to the suction chamber supply port diameter $d_{su,suc}$.

This is shown in Figure 2-6.

- The *suction chamber supply port* is the orifice through which the fluid enters the suction chamber. The expander and the suction chamber supply ports are connected by a short supply pipe whose length is $L_{su,exp}$.
- The *discharge chambers' openings* are the rectangular cross-sectional passageway through which the fluid leaves the discharge chamber.
- The *expander exhaust port* is the circular orifice of diameter $d_{ex,exp}$, which connects the discharge channel to the exhaust line. The portion of pipe of diameter $d_{ex1,exp}$ is included into the discharge channel volume.

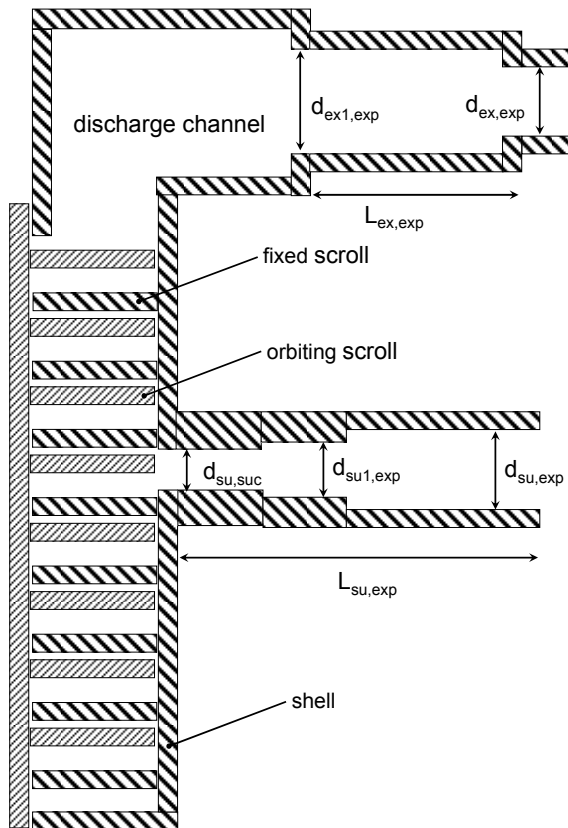


Figure 2-6: Definition of the expander supply and exhaust ports

Pressures and temperatures are measured in the supply and exhaust lines. All the dimensions mentioned hereunder are given in Table 2-3. This table also gives the approximate external dimensions of the machine with its insulation, as defined in Figure 2-7.



Figure 2-7: External dimensions of the insulated expander

Table 2-3: Measured external dimensions

$d_{su,exp}$ [mm]	$d_{su,l,exp}$ [mm]	$d_{su,suc}$ [mm]	$d_{ex,exp}$ [mm]	$L_{su,exp}$ [mm]	L_{ex} [mm]	L [m]	H [m]	W [m]
18.6	12.3	9.5	15.5	86	90	0.3	0.3	0.2

The crank angle evolution of the suction chamber supply port area is shown in Figure 2-8. This figure shows that the port area is reduced during part of the revolution, due to the blockage by the tip of the orbiting scroll. The crank angle evolution of the discharge chambers opening area is shown in Figure 2-9. This area presents a sinusoidal evolution going *theoretically* through zero at the discharge angle θ_d . Actually, this area never reaches zero because of the flank gap.

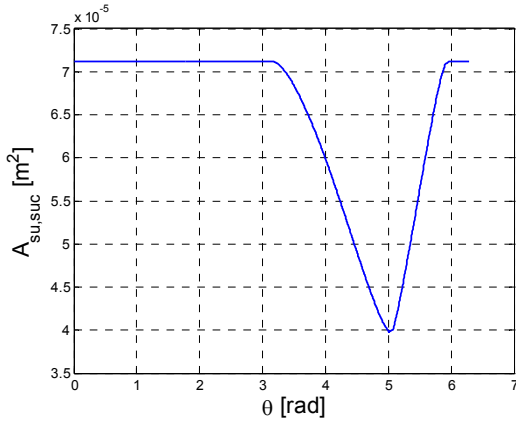


Figure 2-8: Crank angle evolution of the suction chamber supply port area

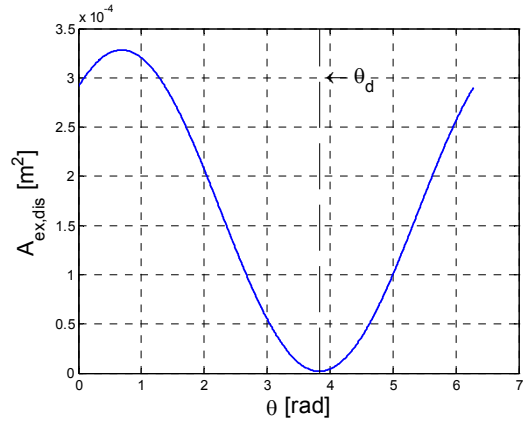


Figure 2-9: Crank angle evolution of the discharge chamber's opening area

2.4 Model verification

2.4.1 Identified parameters

The identified parameters of the deterministic model are given in Table 2-4. The radial leakage gap was set to 0 μm , assuming that the tip seals are working correctly. The identified flank gap is 70 μm .

Table 2-4: Identified parameters for the deterministic model

δ_f	δ_r	AU _{amb}	T _{loss}	C
[μm]	[μm]	[W/K]	[N.m]	[-]
70	0	4	1.0	0.66

These moving seals are embedded in a groove at the tip of each scroll (see Figure 2-10 and Figure 2-11). The internal surface of each seal is in contact with the high-pressure region of the compressor. Under action of the high pressure, each seal lifts and closes the gap between the base of one scroll and the tip of the other scroll, decreasing radial leakage. The tip seals wear in place of the scroll themselves (wear of 1 mm after 10,000 hours working). Each tip seal is made up of two parts with different materials: a high pressure and a low pressure tip seal.



Figure 2-10 : Fixed scroll



Figure 2-11 : Orbiting scroll

The identified values of the flank and radial leakage gaps ($70 \mu\text{m}$ and $0 \mu\text{m}$) are found to yield a good agreement between the measurements and the prediction by the model for the mass flow rate and for the shaft power. These two values are very close to those identified by Yanagisawa et al. (2001) who investigated experimentally and modeled a similar expander fed with steam and air.

The only parameters actually tuned are the external heat transfer coefficient AU_{amb} , the mechanical loss torque T_{loss} and a correction factor on the expander exhaust port cross-sectional area C_{ex} .

This latter correction factor introduced by Bell et al. (2008b) (for compressor operation) accounts for all the additional exhaust pressure losses, which are not described by the flow through the expander exhaust port. Among others, these additional pressure losses are due to:

- 1) the 180° bend encountered by the fluid flowing between the *chamber 14* and the exhaust port (see Figure 2-4 (c));
- 2) the small passageway from *chambers 13* and *14* during part of the discharge process.

The identified external heat transfer coefficient could be compared to the coefficient evaluated on the basis of the expander external dimensions and of the insulation

characteristics. As detailed in the Appendix, considering a global heat transfer coefficient of 10 W/m²-k (free convection + radiation), an insulation thermal conductivity of 0.036 W/m-K and an insulation thickness of 0.013 m yields an ambient heat transfer coefficient of 1.38 W/K. This value is much lower than the value identified in the deterministic model (4 W/K). The first reason for this disagreement might be that the calculation of the heat transfer coefficient doesn't account for the heat exchange by conduction through the metallic support on which the expander is bolted. The second reason might be that the deterministic model under-estimates the shell temperature.

2.4.2 Verification of the mass flow rate

Figure 2-12 compares the evolutions of the mass flow rate measured and predicted by the deterministic model with the expander supply specific volume, for the three different rotational speeds. The mass flow rate decreases with the specific volume of the refrigerant and increases with the rotation speed. It can be observed than the agreement between the measurement and simulation is good. The maximal deviation is of the order of 4%.

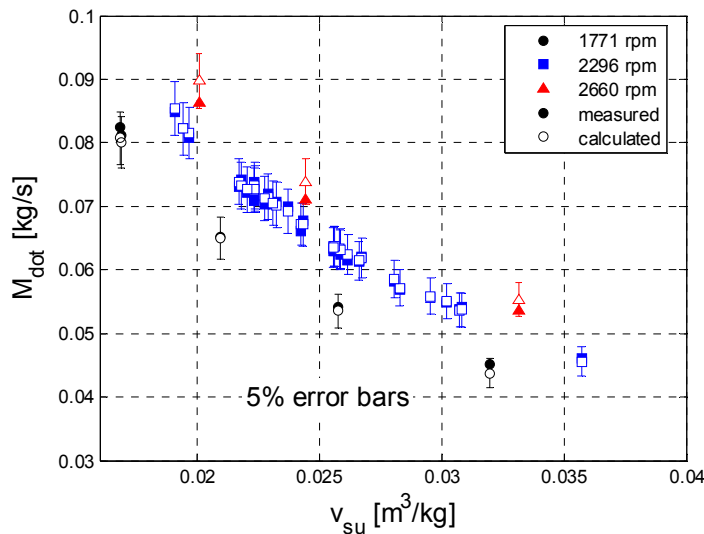


Figure 2-12: Verification of the mass flow rate (deterministic model)

2.4.3 Verification of the shaft power

A similar comparison is carried out for the shaft power. Figure 2-13 compares the evolutions of the measured and computed shaft powers as a function of the pressure ratio imposed to the expander. For almost all the points, the shaft power is predicted within 5%. The maximal

deviation between the predictions by the model and the measurements is 7.2%. The largest deviation is associated to the same point as for the flow rate and seems to be due to measuring problems associated to a two-phase regime at the expander supply.

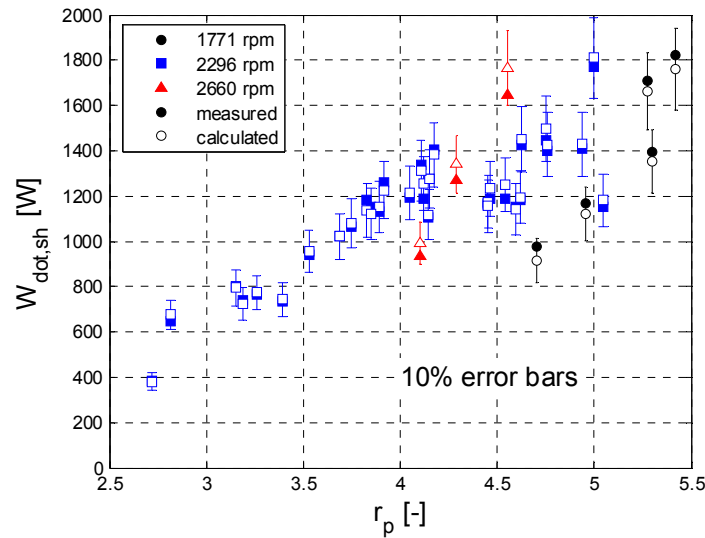


Figure 2-13: Verification of the shaft power (deterministic model)

2.4.4 Verification of the exhaust temperature

Comparison between the measured and the predicted exhaust temperature is shown in Figure 2-14. For most of the points, the exhaust temperature is predicted within 3K. The maximal deviation is 4.0 K. A same trend is observed as before, with the semi-empirical model: the lowest and the highest temperatures are respectively under- and over-predicted. Here also, the reason may be that the external heat transfer should not be calculated by reference to one unique temperature node as it is done in both models.

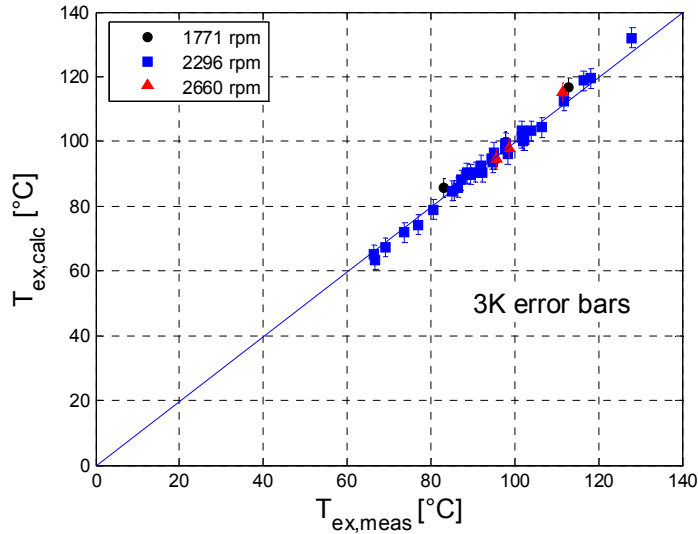


Figure 2-14: Verification of the exhaust temperature (deterministic model)

The evolution of the residual of the energy balance across the expander is shown in Figure 2-15. This evolution is consistent with results of Figure 2-14: the model seems to under-predict the shell temperature for the highest operating temperatures and over-predict it for the lower operating temperatures.

Further investigation should allow better characterization of the shell temperature. Up to now the latter is assumed uniform. Actually, not enough internal and external temperature measurements were done to validate a more detailed thermal model. In the present modeling, only one temperature node is introduced: the shell temperature is assumed to be equal to the mean temperatures of the fixed and the orbiting scrolls ($T_{\text{shell}} = \bar{T}_{\text{fix}} = \bar{T}_{\text{orb}}$). However, introducing an additional temperature node would largely increase the computational time. The agreement achieved here is judged satisfactory.

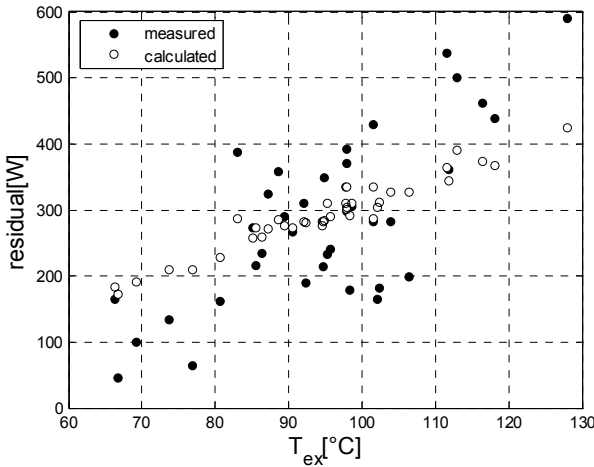


Figure 2-15: Measured and calculated energy residual on the expander (deterministic model)

2.4.5 Verification of the isentropic effectiveness

A comparison between isentropic effectivenesses determined from simulation and from measurements is shown in Figure 2-16. For most of the points, the global isentropic effectiveness is predicted within 2% absolute. However, the model slightly over-predicts the effectiveness for the highest rotational speed, which is correlated to the over-prediction of the shaft power.

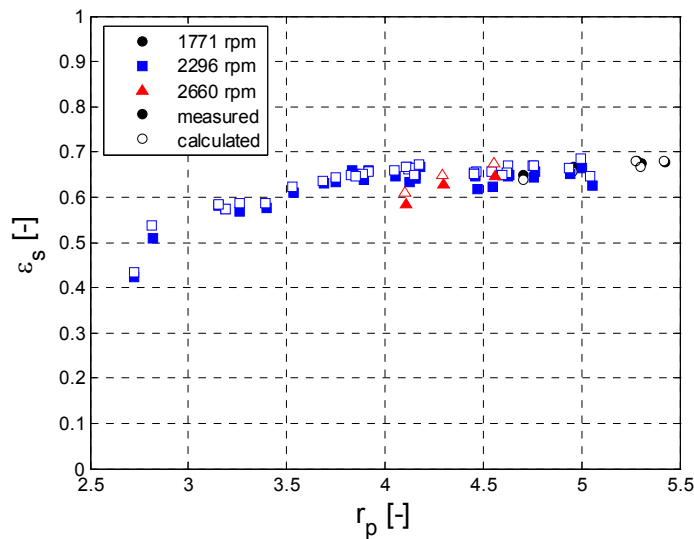


Figure 2-16: Verification of the global isentropic effectiveness (deterministic model)

2.5 Model analysis

This section gives a more comprehensive description of the main processes encountered by the fluid throughout the expansion.

Results are presented for two different operating points. The first point corresponds to under-expansion and is characterized by $P_{su} = 6.92$ bar, $P_{ex} = 1.38$ bar, $T_{su} = 145.6^\circ\text{C}$, $N = 2296 \text{ min}^{-1}$. The second point corresponds to over-expansion and is characterized by $P_{su} = 5.39$ bar, $P_{ex} = 2.00$ bar, $T_{su} = 121.0 \text{ C}$, $N = 2295 \text{ min}^{-1}$. The P-V diagrams associated to these two operating points are given in Figure 2-17 and Figure 2-18.

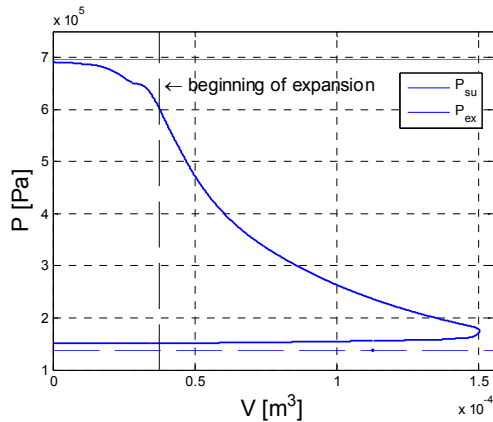


Figure 2-17: P-V diagram in the case of under-expansion

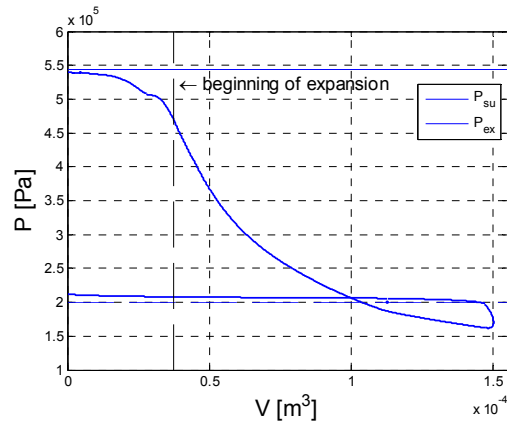


Figure 2-18: P-V diagram in the case of over-expansion

2.5.1 Suction process

Pressure at the beginning of the expansion process is lower than the supply pressure, because of the different pressure losses encountered by the fluid during the suction process. These pressure losses are due to (Yanagisawa, 2001):

- The flow through the suction chamber supply port. This pressure drop is exacerbated by the *blockage of the suction chamber supply orifice* by the tip of the orbiting scroll during part of the suction process.
- The *subdivision of the suction chamber*: at the end of the suction process, the flow passage (of cross-sectional area A_{12}) between the central portion of the suction

chamber and the two adjacent crescent-shaped portions is progressively reduced (see Figure 2-19).

The latter pressure drop is attenuated by the fact that the tip seal does not extend to the end of the scrolls, what increases the flow between the central and the adjacent chambers and attenuates the suction pressure drop. The radial gap $\delta_{r,tip}$ at the end of the two scrolls where the tip seal doesn't extend should be equal to the radial gap in the absence of tip seal (§2.4.1). A clearance of 250 μm was found to yield the best results for the prediction of the shaft power and mass flow rate. Note that another effect of the absence of the tip seal at the end of the scrolls is to increase the leakage flow rate between *chamber 6* and *chambers 7 and 8* at the beginning of the suction process.

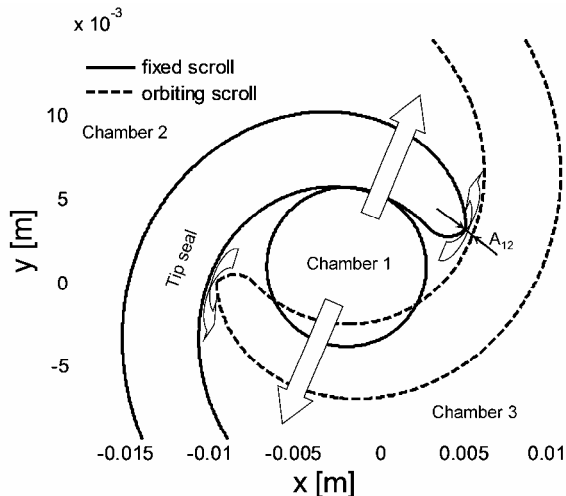


Figure 2-19 : Representation of the suction chambers at the end of the suction process

The evolution of the pressure in *chambers 6, 1* and *2* with the crank angle is shown in Figure 2-20. Pressure in chamber 6 gently decreases until approximately $\theta = 3$ rad. From this time, the sharper decrease in the pressure is due to the blockage of the suction chamber supply port. At $\theta = \theta_{12}$, *chamber 6* is divided into *chamber 1*, *chamber 2* and *chamber 3*. To prevent any numerical instability, this subdivision is simulated as if occurring when the flow passage area A_{12} is lower than the supply port area (at $\theta_{12} = 5.18$ rad). The crank angle evolution of the flow passage area A_{12} and suction chamber supply port area are compared in Figure 2-21. From this time, pressures in the 3 sub-chambers are followed independently. Pressure in

chamber 1 starts to increase again, because the suction chamber supply port is progressively uncovered. Pressure in *chamber 1* at the end of one entire revolution is equal to the pressure in *chamber 6* at the beginning of the suction process. Pressures in *chambers 2* and *3* continue to decrease till the end of the suction process.

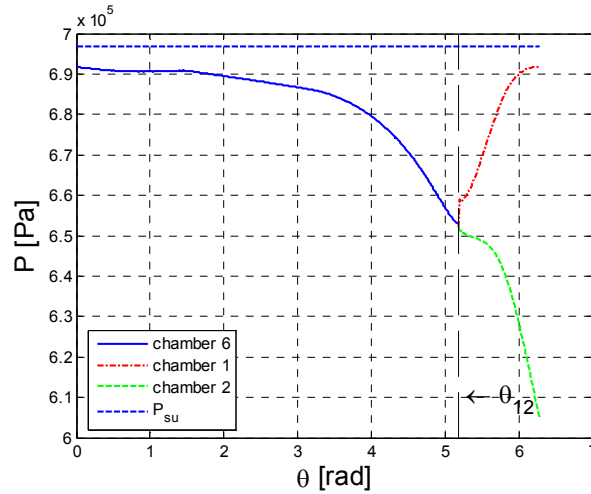


Figure 2-20 : Crank angle evolution of the pressure in the suction chambers

For this operating point, the deterministic model predicts a suction pressure drop of 13.24% (the supply pressure is 6.92 bar and the pressure at the beginning of the expansion is 6.05 bar). For the same operating point, the semi-empirical model predicts a pressure drop of 10.15% (Chapter 4). Hence, the value of the fictitious supply diameter introduced in the semi-empirical model can be considered as physically meaningful.

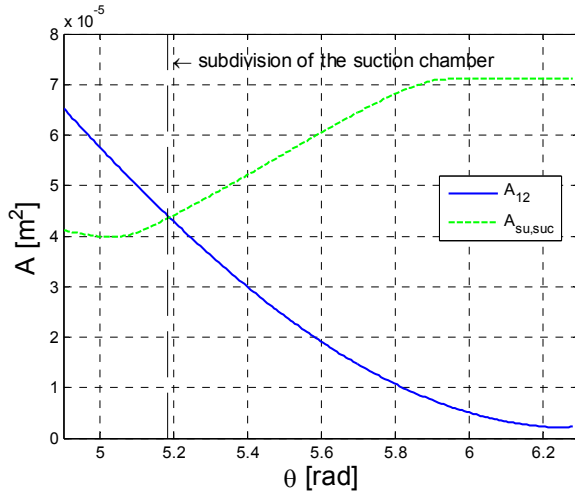


Figure 2-21: Crank angle evolution of the opening area connecting central *chamber 1* to the adjacent *chamber 2* (or *3*)

The physical meaning of the leakage area identified in the semi-empirical model can also be verified. The actual leakage area corresponds to the flow passage between *chamber 6* (or *2 & 3*) and *chambers 7* and *8*. Since the identified radial leakage gap δ_r is equal to zero, the leakage area reduces to

$$A_{\text{leak}} = 2h_{\text{scroll}}\delta_f \quad (2-4)$$

The measured actual leakage area is 4.01 mm^2 . This value is very close to the value identified in the semi-empirical model (4.6 mm^2).

2.5.2 Expansion process

The crank angle evolution of the pressure in the expansion *chambers 7, 9 and 11* is shown in Figure 2-22. Note that most of the pressure decrease is achieved in the first pair of expansion chambers (7 and 8).

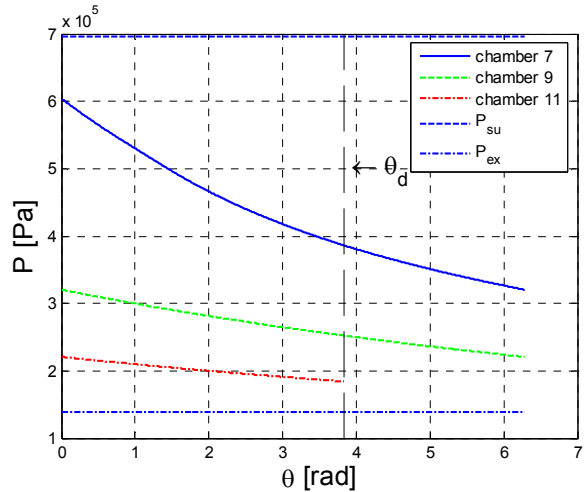


Figure 2-22: Crank angle evolution of the pressure in the expansion chambers (under-expansion)

2.5.3 Discharge process

Figure 2-20 shows the evolution of the fluid pressure during the discharge process in the case of *under-expansion*. At the discharge angle θ_d , the pressure in the discharge chamber 14 (the former expansion chamber 12) is higher than the pressure in the discharge channel (*chamber 17*). Hence, some fluid flows from *chamber 14* into *chamber 17* until the pressures of the latter two chambers have equalized. When the pressures in *chambers 13, 14 and 17* are within 1% the three chambers are merged into one unique chamber (*chamber 18*). The difference between the pressure in the discharge channel (*chamber 17* or *18*) and the exhaust pressure P_{ex} is due to the pressure drop through the expander exhaust orifice and to the additional exhaust pressure losses already described in §2.4.1.

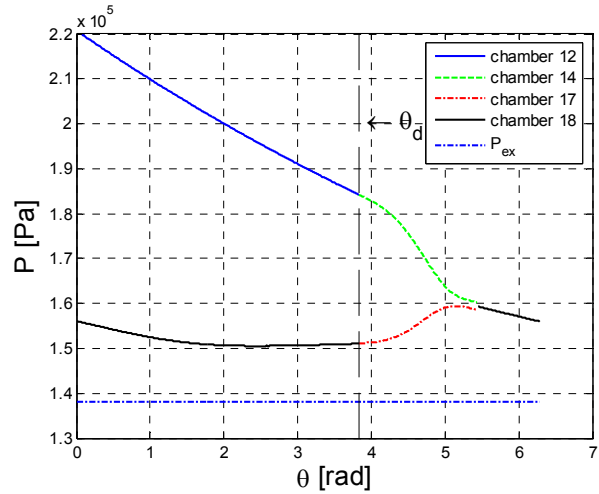


Figure 2-23: Crank angle evolution of the pressure in the discharge chambers (under-expansion)

The description is similar in the case of *over-expansion*. In this situation, the pressure in the discharge chambers (13 and 14) is lower than the pressure in the discharge channel (*chamber 17*). Some fluid flows from the discharge channel back into the discharge chambers until the pressures in all three chambers have equalized. This situation is represented in Figure 2-24.

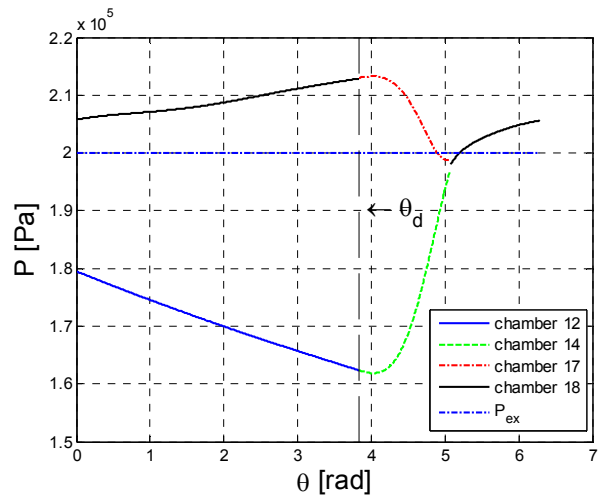


Figure 2-24: Crank angle evolution of the pressure in the discharge chambers (over-expansion)

2.5.4 Heat transfers

The evolutions of the heat transfer rates during suction, expansion and discharge processes according to the crank angle are shown in Figure 2-25. Negative and positive values correspond to cooling and heating of the fluid respectively. The largest heat transfer rate is the cooling-down in the suction chambers. The average heat transfer rates during suction, expansion and discharge are evaluated by integrating the curves in Figure 2-25:

$$\dot{Q}_{\text{suc}} = -144 \text{ W}$$

$$\dot{Q}_{\text{exp}} = 11 \text{ W}$$

$$\dot{Q}_{\text{dis}} = 66 \text{ W}$$

These values are compared with the heat transfer rates computed in the semi-empirical model for the same operating point. The semi-empirical model only accounts for the supply cooling-down and exhaust heating-up. It assumes that the expansion is adiabatic. The higher cooling rate identified in the semi-empirical model might be explained by the smaller expander displacement considered in the semi-empirical model.

$$\dot{Q}_{\text{su}} = -405 \text{ W}$$

$$\dot{Q}_{\text{exp}} = 0 \text{ W}$$

$$\dot{Q}_{\text{ex}} = 69 \text{ W}$$

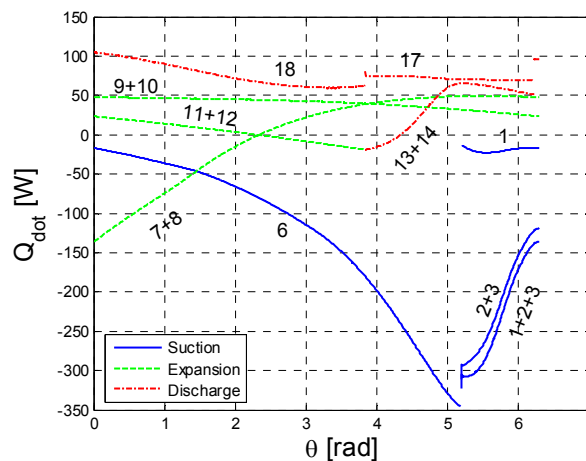


Figure 2-25: Heat transfer rates during suction, expansion and discharge processes

2.6 Design modification

Using the validated expander simulation model, the variation of the expander performance with some of the design parameters has been investigated. This parametric study aims at investigating the potential ways to improve the expander's performance.

2.6.1 Reduction of the suction pressure drop

As mentioned hereunder, the suction pressure drop is mainly due to the combined effect of the blockage of the suction chamber supply port and the subdivision of the suction chamber. However, this pressure drop is attenuated by the fact that the tip seal doesn't extend to the end of the scroll. The radial gap where the tip seal is not present is $\delta_{r,tip}$.

Variation of the tip radial gap

The sensitivity of the expander's performance to the tip radial gap $\delta_{r,tip}$ is investigated by multiplying the nominal tip radial gap $\delta_{r,tip,n}$ (250 μm) by a scaling factor ranging from 0 to 8.

The deformation of the P-V diagram with the tip radial gap is shown in Figure 2-26. Increasing the tip radial gap reduces the suction pressure drop. As shown in Figure 2-28, this yields an increase in the shaft power. However, the leakage flow rate between the suction chamber 6 and the expansion chambers 7 and 8 increases in the mean time. This leakage flow explains the slight pressure decrease which can be observed at the beginning of the suction process (upper-left corner of the P-V diagram). A direct consequence of this leakage flow rate is the increase of the mass flow rate displaced by the expander (Figure 2-27).

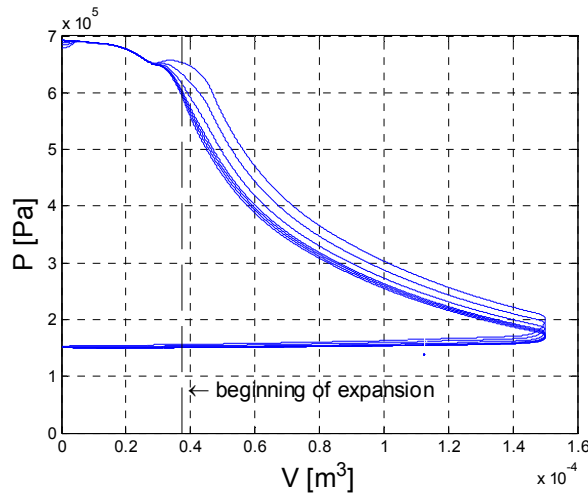


Figure 2-26: Deformation of the P-V diagram with the tip radial gap ($P_{su}=6.98$ bar, $P_{ex}=1.38$ bar, $T_{su}=145.6^\circ\text{C}$, $\text{rpm}=2296 \text{ min}^{-1}$)

As a consequence of the simultaneous increase of the shaft power and leakage flow, the isentropic effectiveness of the expander remains almost constant (ranging from 64.5 to 64.6%). Hence, it is concluded that increasing the tip radial gap is not an appropriate way to improve the expander performance.

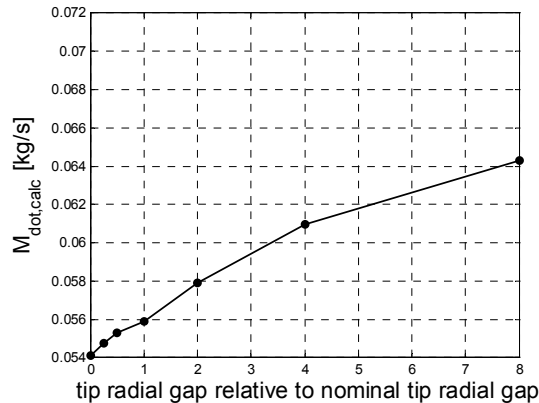


Figure 2-27: Evolution of the mass flow rate with the tip radial gap

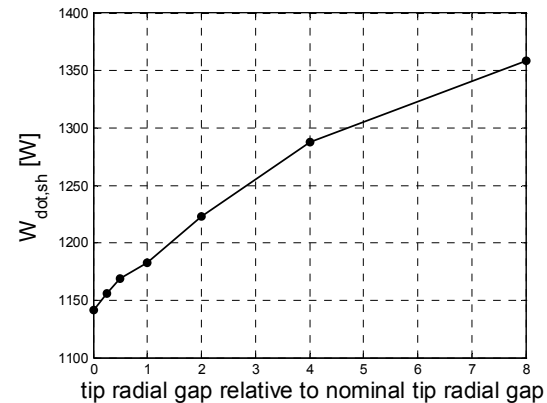


Figure 2-28: Evolution of the shaft power with the tip radial gap

Variation of the suction chamber supply port

The effect of the suction chamber supply port diameter on the expander's performance is investigated by increasing it by 50% (Figure 2-29). This yields a very limited effect on the suction pressure drop. For the same operating point, the shaft power and the isentropic effectiveness are only slightly increased (1180 W and 64.6% for the original design and 1219 and 65.5 % for the modified design). The main source of suction pressure losses is actually the subdivision of the suction chamber.

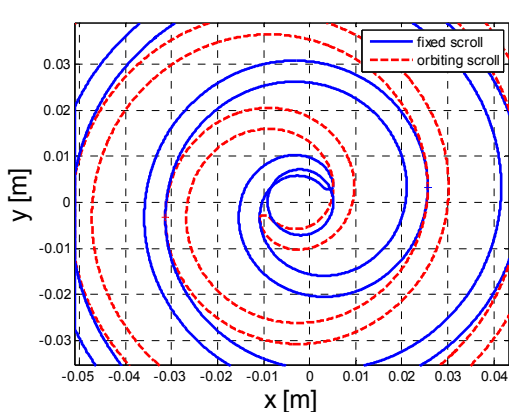


Figure 2-29: View of the expander with a larger suction chamber supply port

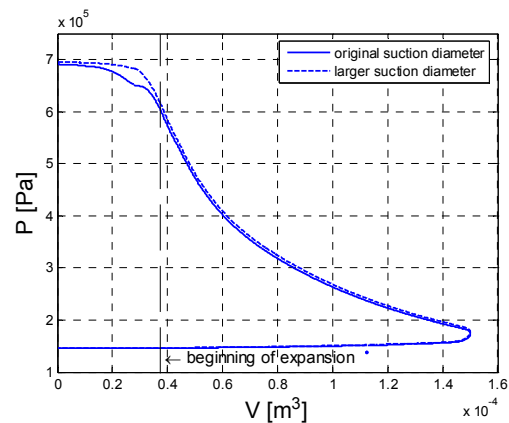


Figure 2-30: Modification of the P-V diagram with the increase of the suction chamber supply port diameter

2.6.2 Variation of the radial and flank leakage gaps size

Figure 2-31 gives the evolution of the delivered shaft power with the gap size relative to the nominal *flank* leakage gap size (70 μm). It can be observed that the shaft power increases with the flank leakage gap size, while it decreases with the radial leakage gap size. These opposite evolutions can be explained by examining Figure 2-33 and Figure 2-34.

Flank leakages tend to increase the area of the P-V diagram (modification of the slope of $P=f(V)$). However, they simultaneously increase the suction pressure drop, because of the larger flow rate through the suction chamber supply port. The net effect of these two phenomena is an increase in the P-V diagram area and hence in the shaft power.

Radial leakage lengths are larger than the flank leakage length. Hence, radial leakages are more sensitive to the leakage gap than flank leakages. As a consequence, internal leakages strongly increase with the radial gap, causing large suction pressure drops. This is shown in Figure 2-32. Therefore, it is crucial to reduce as much as possible the radial leakage gap. This is even more important for the scroll machines characterized by large internal built-in volume ratio, since the radial leakage length increases with the ending involute angle.

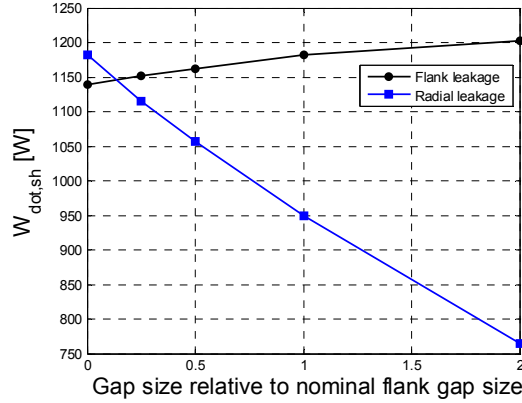


Figure 2-31: Evolution of the delivered shaft power with the gaps' size

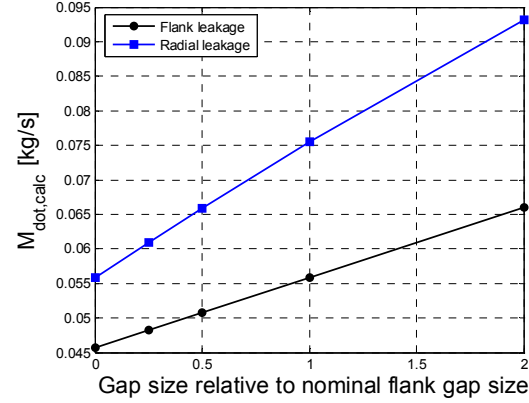


Figure 2-32: Evolution of the displaced mass flow rate with the gaps' size

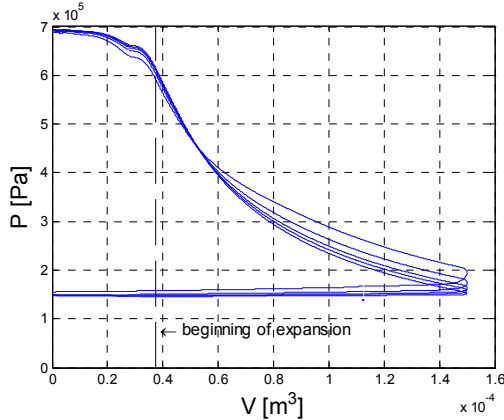


Figure 2-33: Deformation of the P-V diagram with the flank leakage gap size

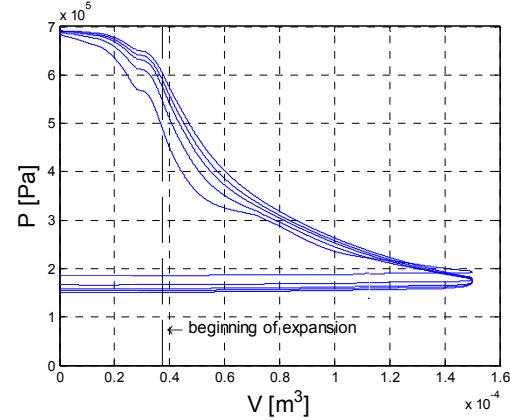


Figure 2-34: Deformation of the P-V diagram with the radial leakage gap size

Figure 2-35 shows that internal leakages strongly influence the expander exhaust temperature. The evolution of the global isentropic effectiveness with the leakage gaps is shown in Figure 2-36. Even if the shaft power increases with the flank gap, it has a negative

impact on the global isentropic effectiveness because of the increase in the mass flow rate. The performance can be substantially increased by decreasing the flank gap. For instance, by reducing by half the flank gap, the isentropic effectiveness would increase by 5%.

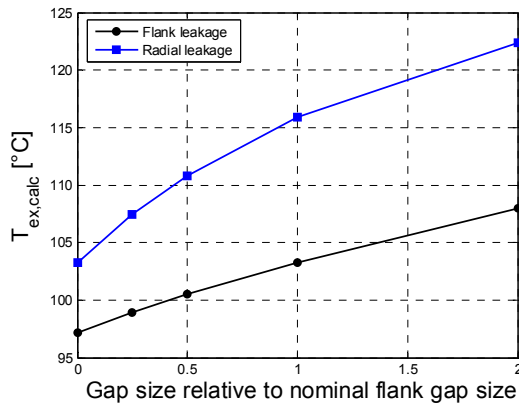


Figure 2-35: Evolution of the exhaust temperature with the gap size

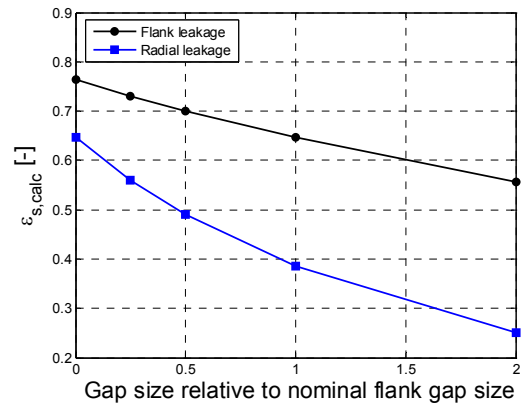


Figure 2-36: Evolution of the global isentropic effectiveness with the gap size

2.6.3 Variation of the mechanical loss torque

Figure 2-37 shows the evolution of the delivered shaft power with the mechanical loss torque. As it has already been mentioned by Yanagisawa et al. (2001), mechanical loss is one of the main factors affecting the performance of the expander. The mechanical loss has two origins: the loss in the bearings and the friction loss due to the contact between the tip seal and the scroll plates.

Further investigation is required in order to determine to what extend this loss could be reduced (by using more adapted tip seals for instance).

It is interesting to observe that the mechanical loss torque identified in the semi-empirical model is smaller than the one identified in the deterministic model. The underlying reason was given in the previous paragraph: the expansion work is increasing with the flank leakage, which cannot be described by the semi-empirical model. Hence, a smaller mechanical loss torque must be introduced in the semi-empirical model in order to predict the same shaft power.

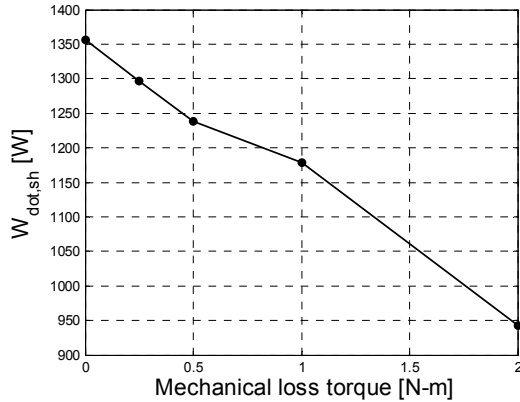


Figure 2-37: Evolution of the delivered shaft power with mechanical loss torque

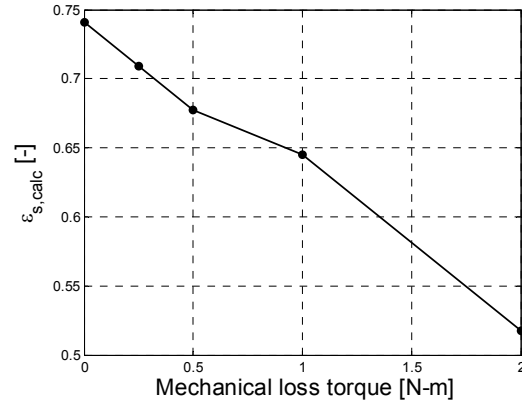


Figure 2-38: Evolution of the global isentropic effectiveness with mechanical loss torque

2.6.4 Variation of the heat transfer coefficients

The impact of the *internal* heat transfers has been investigated by introducing a scaling factor in the correlation used to compute the convective coefficient between the fluid and the scrolls. It can be observed that the effect of the internal heat transfer is limited: multiplying by 8 the actual heat transfer coefficients only increases by 3.7% the mass flow rate in the expander and by 1.4 K the exhaust temperature.

As shown in Figure 2-15, the impact of the *external* heat transfer is more important.

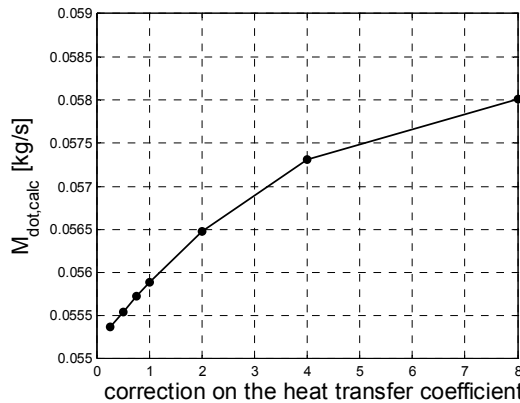


Figure 2-39: Evolution of the displaced mass flow rate with the correction factor on the heat transfer coefficient

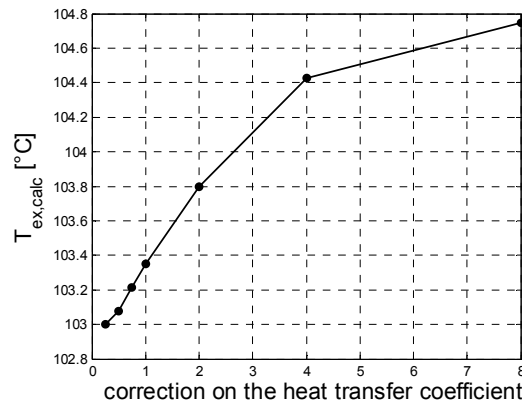


Figure 2-40: Evolution of the exhaust temperature with the correction factor on the heat transfer coefficient

2.6.5 Variation of the expander exhaust port diameter

Figure 2-23 and Figure 2-24 show that the pressure in the discharge channel is higher than the exhaust pressure because of the pressure drop in the exhaust port and other sources of discharge pressure losses. Figure 2-41 and Figure 2-42 show that the expander performance could be significantly improved by increasing the exhaust port diameter.

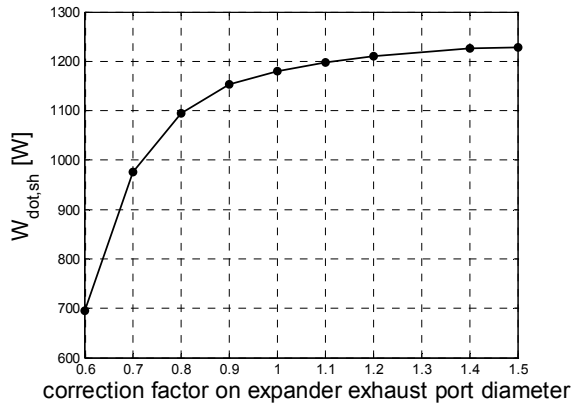


Figure 2-41: Evolution of the delivered shaft power with the expander exhaust port diameter

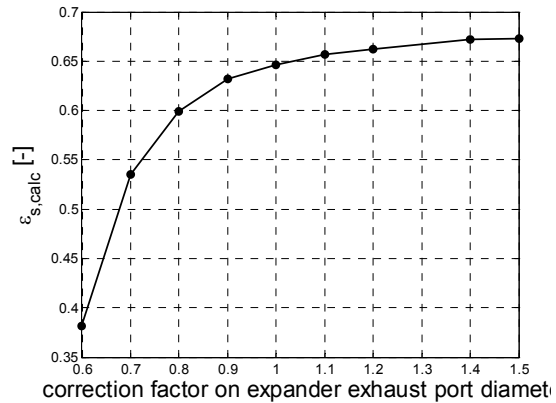


Figure 2-42: Evolution of the global isentropic effectiveness with the expander exhaust port diameter

Note that this modification is very easy: it only necessitates increasing the exhaust pipe diameter (which is under-sized in the actual test rig).

2.7 Variation of the operating conditions

2.7.1 Pressure ratio

The evolution of the global isentropic effectiveness with the pressure ratio is shown in Figure 2-43 for two situations: with the actual flank gap size and with a flank gap size equal to zero. In this latter limit case, the effectiveness would increase by 10% absolute. Reducing the flank leakage can be achieved by radial compliance, which necessitates lubrication and probably increases mechanical loss. The height of the scroll might also be reduced in order to decrease the flank leakage gap. Note that, according to Preissner (2001), the scroll height is constrained by material strength (the ratio scroll height/thickness shouldn't exceed 3.5) and machining (the ratio scroll height/ distance between two walls should be smaller than 2 to avoid deflection of the milling tool).

This figure shows also that the penalty of under-expansion is actually pretty limited (in comparison with over-expansion). Hence, under size and cost constraints (such as for mobile applications), using an expander with a built-in volume ratio slightly under-sized is a good option, which is currently applied for scroll compressors used in automotive air-conditioning.

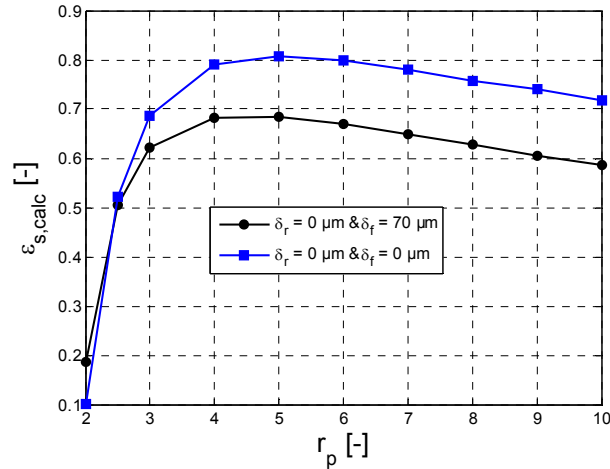


Figure 2-43: Evolution of the expander global isentropic effectiveness with the pressure ratio
($P_{su}=10 \text{ bar}$, $T_{su}=150^\circ\text{C}$, $\text{rpm}=2296\text{min}^{-1}$)

2.7.2 Rotational speed

Figure 2-44 shows the evolution of the global isentropic effectiveness with the rotational speed for different pressure ratios.

First of all, this figure demonstrates that the optimum pressure ratio is comprised between 4.0 and 5.0, whatever the rotational speed.

This figure also shows that there is an optimal rotational speed which is close to 2000 min^{-1} for almost all the pressure ratios, except when the fluid is over-expanded. In this particular case the optimal speed is lower, probably because of the positive impact of the internal leakages, which strongly reduce the effect of over-expansion.

The optimum results from two competing effects of the speed: on one hand it increases the suction and the discharge pressure losses and on the other hand it decreases the relative impact of the leakages.

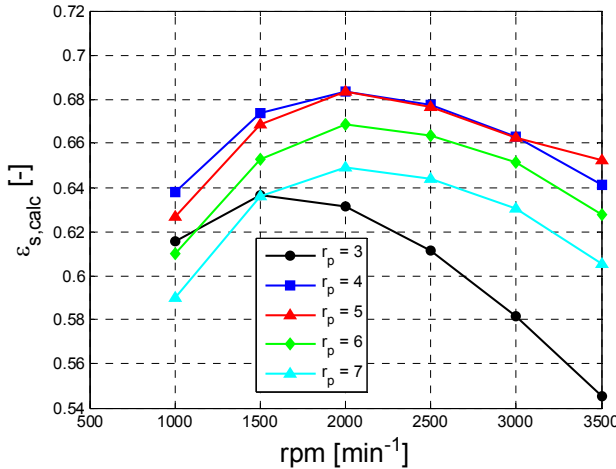


Figure 2-44: Evolution of the global isentropic effectiveness with the rotational speed for different pressure ratios ($P_{su}=10$ bar, $T_{su}=150^{\circ}\text{C}$)

2.8 Derivation of non-dimensional laws for the semi-empirical model

In the pre-design process of a thermal system comprising a scroll expander, it is useful to estimate how the performance of the expander varies with its size. The purpose of this paragraph is to develop sizing laws related to the expander semi-empirical model.

2.8.1 Expression of the laws

In the case of a scroll machine, the most appropriate characteristic dimension is its eccentricity r_o (or the basis circle radius r_b). However, the latter dimension is not easily “accessible”, and it is more convenient to express the parameters of the semi-empirical model as a function of the displacement V_s . If the geometry of the expander is simply scaled in order to modify its displacement, the following relationship can be written

$$\frac{r_o}{r_{o,n}} = \left(\frac{V_s}{V_{s,n}} \right)^{1/3} \quad (2-5)$$

This can be demonstrated considering that:

- 1) the displacement is given by $V_s = h\pi r_b r_o (3\pi - \varphi_{i,0} + 2\varphi_{o,s} - \varphi_{o,0})$

- 2) the relationship between the eccentricity and the basic circle radius is $r_o = r_b(\pi - \varphi_{i,0} + \varphi_{o,0})$ and
- 3) if the expander geometry is scaled, the special involute angles φ_{i0} , φ_{o0} , φ_{is} and φ_{os} are conserved
- 4) if the expander geometry is scaled, the scroll height h is proportional to the basic circle radius r_b and hence to the eccentricity r_o .

The lumped parameters of the semi-empirical model can be expressed as function of the expander displacement.

For instance, assuming that the friction torque is proportional to the friction surfaces area, it follows:

$$T_{\text{loss}} = T_{\text{loss},n} \left(\frac{r_o}{r_{o,n}} \right)^2 = T_{\text{loss},n} \left(\frac{V_s}{V_{s,n}} \right)^{2/3} \quad (2-6)$$

Similarly, the ambient heat transfer can be expressed as:

$$A_{\text{amb}} = A_{\text{amb},n} \left(\frac{r_o}{r_{o,n}} \right)^2 = A_{\text{amb},n} \left(\frac{V_s}{V_{s,n}} \right)^{2/3} \quad (2-7)$$

The supply and the exhaust heat transfer coefficient can still be estimated by the same equations as those introduced previously. Considering the dependency of the heat transfer area A with the eccentricity and the dependency of the convective heat transfer U coefficient on both the mass flow rate and the eccentricity gives:

$$\begin{aligned} AU_{\text{su}} &= A_{\text{su},n} \left(\frac{r_o}{r_{o,n}} \right)^2 U_{\text{su},n} \left(\frac{\dot{M}}{\dot{M}_n} \right)^{0.8} \left(\frac{r_{o,n}}{r_o} \right)^{1.8} \\ &= AU_{\text{su},n} \left(\frac{V_s}{V_{s,n}} \right)^{0.2/3} \left(\frac{\dot{M}}{\dot{M}_n} \right)^{0.8} \approx AU_{\text{su},n} \left(\frac{\dot{M}}{\dot{M}_n} \right)^{0.8} \end{aligned} \quad (2-8)$$

The dependency of the heat transfer coefficient U on the mass flow rate and the eccentricity can be established considering that

$$Nu = K Re^{0.8} \Leftrightarrow \frac{Ur_o}{k} = K \left(\frac{\dot{M}}{\mu r_o} \right)^{0.8} \quad (2-9)$$

The leakage area introduced in the semi-empirical model is the product of a fictitious leakage length and the leakage gap:

$$A_{leak} = L_{leak} \cdot \delta_{leak} \quad (2-10)$$

If the geometry of the expander is scaled, the leakage length L_{leak} is proportional to r_o . Because of limitation in machining technique, the leakage gap δ_{leak} doesn't vary linearly with the r_o . Persson (1990) mentioned that the machining tolerance varies the characteristic dimension of the machine exponent $1/3$.

$$\delta = \delta_n \left(\frac{r_o}{r_{o,n}} \right)^{1/3} \quad (2-11)$$

That is,

$$A_{leak} = L_{leak,n} \cdot \frac{r_o}{r_{o,n}} \delta_{leak,n} \cdot \left(\frac{r_o}{r_{o,n}} \right)^{1/3} = A_{leak,n} \cdot \left(\frac{r_o}{r_{o,n}} \right)^{4/3} = A_{leak,n} \cdot \left(\frac{V_s}{V_{s,n}} \right)^{4/9} \quad (2-12)$$

The fictitious supply diameter introduced in the semi-deterministic model is assumed to vary proportionally with the characteristic dimension:

$$d_{su} = d_{su,n} \frac{r_o}{r_{o,n}} = d_{su,n} \left(\frac{V_s}{V_{s,n}} \right)^{1/3} \quad (2-13)$$

2.8.2 Comparative validation

In order to check the validity of the simple laws introduced hereunder, the performance predicted by the semi-empirical model has to be compared to the performance predicted by the deterministic model for different expander displacement. These displacements are defined by scaling the expander geometry. This is achieved by modifying the basic circle radius r_b (from 0.5 $r_{b,n}$ to 2.0 $r_{b,n}$, where $r_{b,n}$ is the nominal basic circle radius given in Table 2-1) and conserving all the following ratios:

$$h^* = \frac{h}{r_b} \quad (2-14)$$

$$V_s^* = \frac{V_s}{r_b^3} \quad (2-15)$$

$$d_{suc}^* = \frac{d_{suc}}{r_b} \quad (2-16)$$

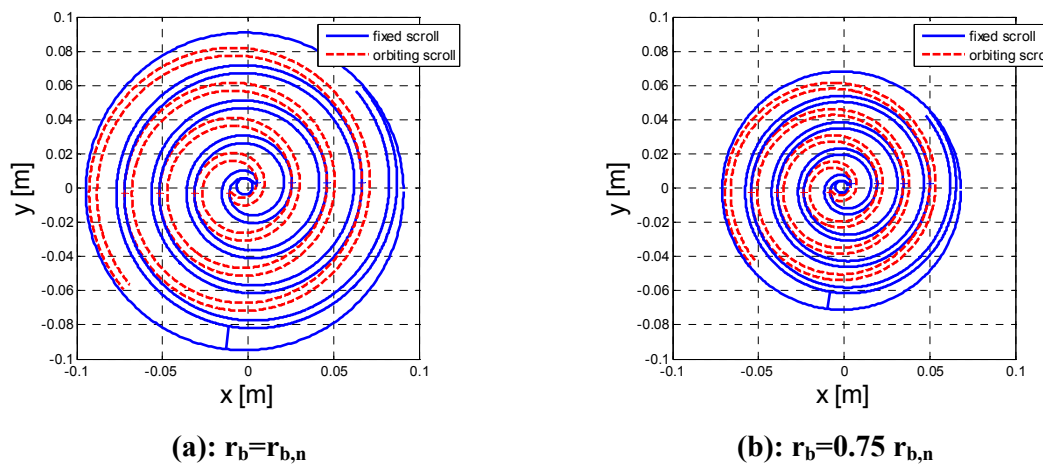


Figure 2-45: Scaling the expander geometry

In the semi-empirical model, the mechanical loss torque and the ambient heat transfer coefficient are imposed to vary according to Equations (2-6) and (2-7). The flank leakage varies according to Equation (2-11).

Figure 2-46 and Figure 2-47 compare respectively the mass flow rate and the shaft power predicted by the semi-empirical model to those predicted by the deterministic model. Operating conditions corresponds to $P_{su}=6.97$ bar, $P_{ex}=1.46$ bar, $T_{su}=145.6^\circ\text{C}$, $T_{amb}=34.8^\circ\text{C}$ and $N=2296 \text{ min}^{-1}$.

It can be observed that the deviation between the semi-empirical model and the deterministic model increases with the expander displacement. However, even for the highest displacement (299 cm^3 , which is probably an unrealistic size) both the mass flow rate and the shaft power are predicted within 10%. Figure 2-48 shows that the deviation between the semi-empirical model and the deterministic model for the exhaust temperature is lower than 1K.

For displacements ranging from half to twice the nominal displacements, the agreement is far better (the deviation is lower than 5%). Hence, the simple non-dimensional laws proposed here seem appropriate to investigate the performance of the thermal system with variation of the expander size (for instance, with a view of pre-designing the system).

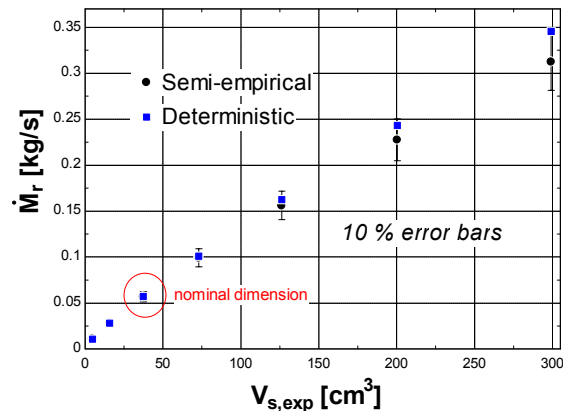


Figure 2-46: Comparison between the mass flow rate predicted by the semi-empirical and the deterministic models

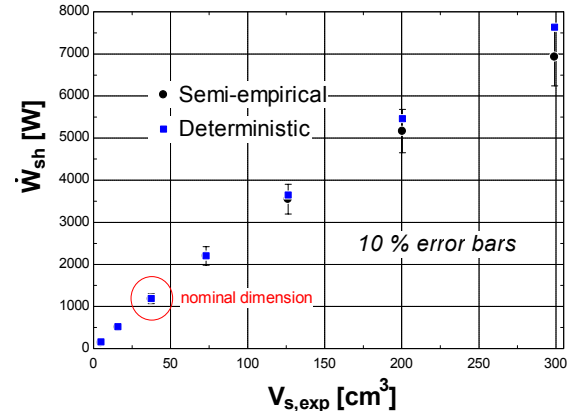


Figure 2-47: Comparison between the shaft power predicted by the semi-empirical and the deterministic models

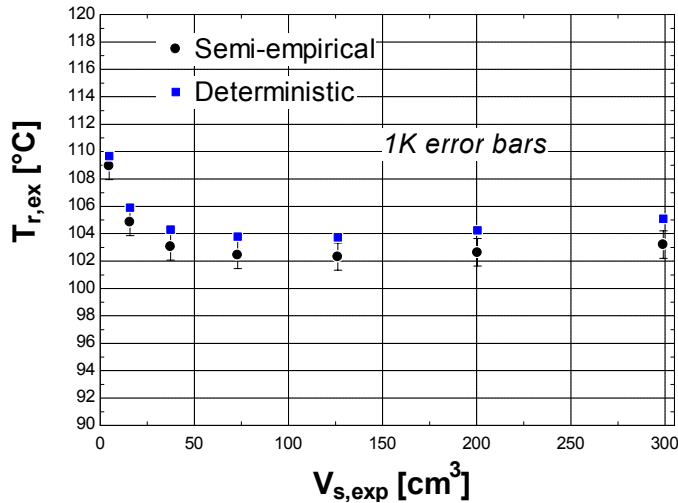


Figure 2-48: Comparison between the shaft power predicted by the semi-empirical and the deterministic models

2.9 Teardown inspection

At the end of the testing program, the expander was disassembled to inspect the condition of the internal components.

Globally, the spirals were found to be in good conditions. Some punctual damages were observed on the spirals' flanks. They are probably due to some contamination getting between the spirals.

The two high pressure tip seals were moving freely in their grooves. Moreover they have worn a little bit thinner than expected. Hence, the assumption that the tip seal were functioning correctly tends to be confirmed. On the other hand excessive wearing means that more adapted tip seals should be installed. The two low pressure seals were also moving freely except in two points, where they seemed to be stuck into their groove. However, it shouldn't have had a big impact on volumetric effectiveness, since these points are located at high involute angles (closer to the scroll periphery).

3 ERICSSON CYCLE EXPANDER

3.1 Validation

The data used for the experimental validation and the description of the fluid properties have been presented and analyzed in Chapter 5.

The inputs of the model are the supply and the exhaust pressures P_{su} and P_{ex} , the supply temperature T_{su} and the mass fraction of liquid in the mixture x_l . The outputs of the model are the gas flow rate \dot{M}_g , the exhaust temperature T_{ex} and the shaft power \dot{W} . Some model parameters are measured (such as the geometric parameters of the machine, as shown in Chapter 6) and others need to be tuned using experimental data (the axial and radial leakage gaps, the heat transfer coefficient with the ambient and the mechanical losses).

The global heat transfer coefficient between the expander and the ambient is adjusted to best fit the calculated exhaust temperature to the measured one. The identified heat exchange coefficient is equal to 1 W/K. The mechanical losses are computed as a function of the expansion power. A same approach has been used for validating a deterministic model of the compressor (Bell et al., 2008b). Note that no strong correlation is found between the mechanical loss and the supply temperature.

$$\dot{W}_{\text{loss}} = \dot{W}_{\text{loss},0} + \alpha \dot{W}_{\text{in}} \quad (3-1)$$

The flank and radial clearances are the most difficult parameters to identify. As for the semi-empirical model (Chapter 5), it appears that a leakage gap varying with the operating conditions should be introduced in the model. The best agreement between model predictions and experimental measurements for the flow rate and the mechanical power is found by tuning the flank gap rather than the radial gap. As shown in Figure 3-1, the identified flank leakage gap decreases with the pressure ratio and with the rotational speed. A similar trend has already been observed with the semi-empirical model (Chapter 5).

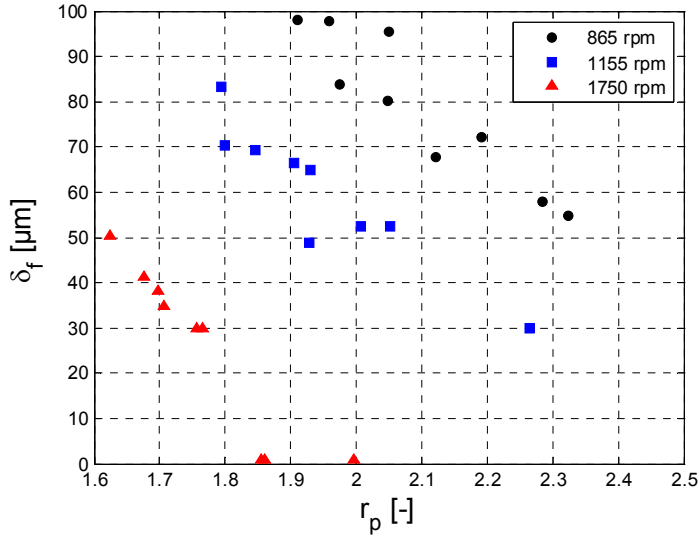


Figure 3-1: Evolution of the identified flank leakage gap with the pressure ratio for the three rotational speeds

Identified parameters of the models are summarized in Table 3-1. As for the ORC expander, the cross-sectional area of the expander exhaust port is corrected (by a factor C) to account for additional exhaust pressure drops which are not described in the modeling.

Table 3-1: Identified parameters for the deterministic model (LFEC expander)

δ_f	δ_r	AU _{amb}	$\dot{W}_{loss,0}$	α	C
[μm]	[μm]	[W/K]	[W]	[-]	[-]
varying	10	1	55	0.059	0.5

3.1.1 Prediction of the mass flow rate

In the validation presented hereunder, a linear relationship between the flank gap and the pressure ratio is considered for each rotational speed. For the calculation of the suction, discharge and internal leakage flows, it is observed that the separated flow model with liquid entrainment (Chapter 5) yields good results.

Figure 3-2 compares the measured and calculated gas mass flow rates. For all the points, except one, the gas mass flow rate is predicted within 5%. The error bars are specified for reference.

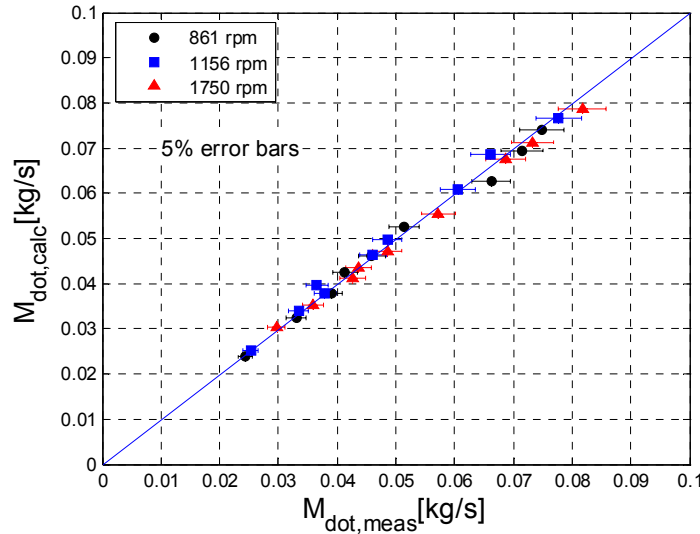


Figure 3-2: Verification of the gas mass flow rate (deterministic model)

3.1.2 Prediction of the shaft power

The internal power \dot{W}_{in} is roughly identified by running the simulation assuming no mechanical loss. The “measured” mechanical loss is the difference between the internal power and the measured shaft power. The evolution of the measured mechanical loss with the internal power is given in Figure 3-3. The parameters of Equation (3-1) are *roughly* identified by drawing a linear regression through the points. It is not possible to correlate the “stand-by” loss $\dot{W}_{loss,0}$ with the expander rotational speed.

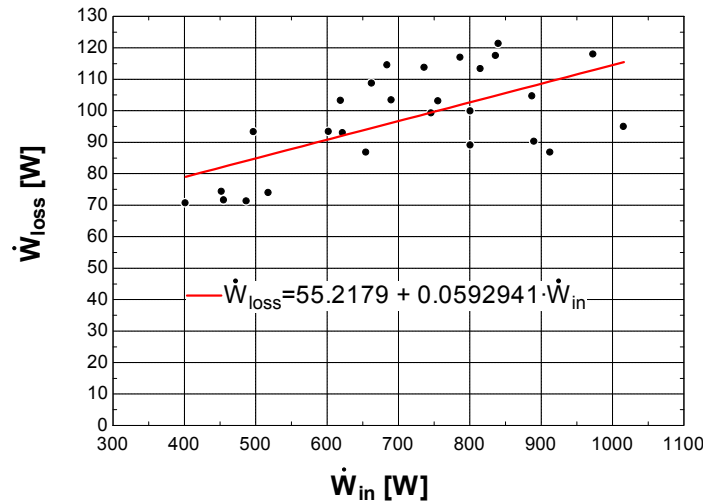


Figure 3-3: Evolution of the measured mechanical loss with the internal power

The measured and calculated shaft powers are compared in Figure 3-4. The maximum deviation between the model predictions and the measurements is 5.0%. Here also, error bars are specified for reference.

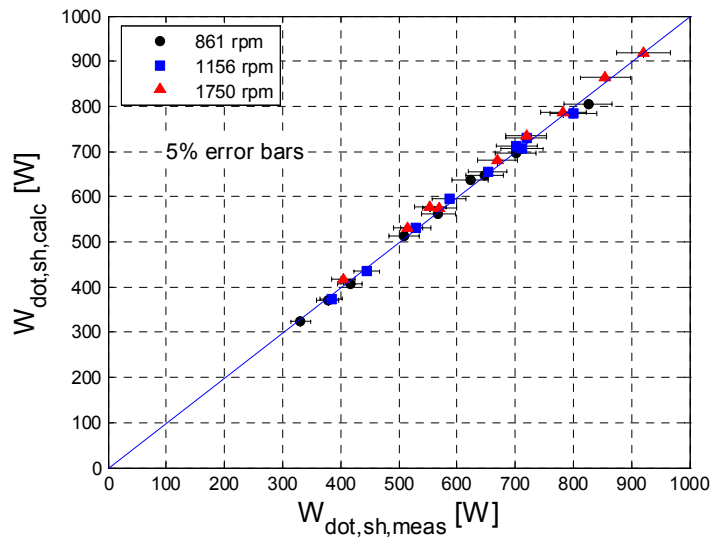


Figure 3-4: Verification of the shaft power (deterministic model)

3.1.3 Prediction of the exhaust temperature

The comparison between calculated and measured exhaust temperatures is given in Figure 3-5. For all the points, except two of them, the exhaust temperature is predicted within 1K.

Deviations for the two points are explained by a bad prediction of the gas mass flow rate (the leakage is probably under-predicted).

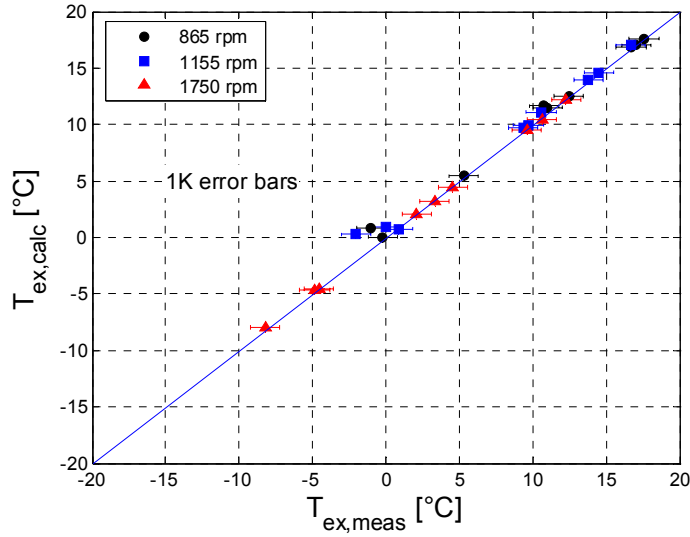


Figure 3-5: Verification of the exhaust temperature

3.2 Design modification

3.2.1 Decrease of the suction pressure drop

The suction process causes a non-negligible suction pressure drop due to the partial blockage of the suction port by the tip of the orbiting scroll (see Figure 3-6). Moreover, at the end of the suction process, this pressure drop is reinforced by the decreasing flow path A_{12} between *chamber 1* and *chambers 2 and 3*. This suction pressure drop also increases with the oil fraction, which is an undesirable feature of the expander geometry. In order to investigate the potential improvement of the expander performance by reducing the suction pressure drop another scroll geometry, represented in Figure 3-6 (at position $\theta/2\pi=0.9$), is defined. This new geometry is characterized by a thinner tip of the scroll (so that the suction port blockage is reduced) and a suction port diameter 10% larger than the initial one. The model parameters are those given in Table 3-1, except for the flank leakage which is imposed to 10 μm (assuming that it is well controlled).

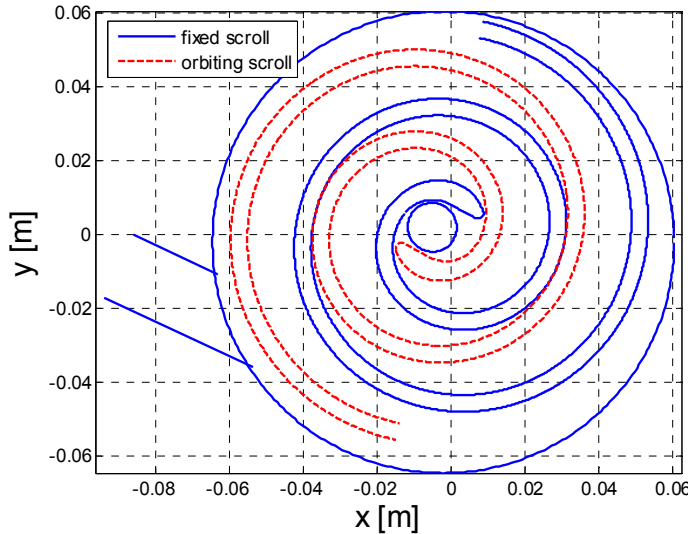


Figure 3-6: Modified geometry of the innermost portion of the scrolls

Figure 3-7 and Figure 3-8 compare the P-V diagrams associated to the initial design and the modified design, for a point characterized by low rotational speed. The new geometry yields a slight increase of the shaft power (from 827 W to 851W). Also it allows a decrease of the internal leakage (which is driven by the pressure difference between the suction chambers and the expansion chambers): the displaced mass flow rate decreases from 54.3 g/s to 52.3 g/s. As a consequence, the global isentropic effectiveness increases from 62.0% to 66.1%.

Examination of Figure 3-7 and Figure 3-8 also reveals that the expander performance could be improved by increasing its built-in volume ratio (equal to 1.6 for the actual machine) so that under-expansion losses would be reduced.

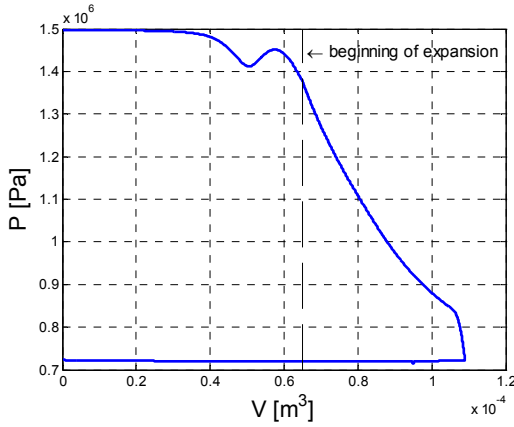


Figure 3-7: P-V diagram : $P_{su} = 15$ bar, $P_{ex} = 7.17$ bar, $T_{su} = 9.68^\circ\text{C}$, $x_l = 60\%$, $\text{rpm} = 892 \text{ min}^{-1}$ (original geometry)

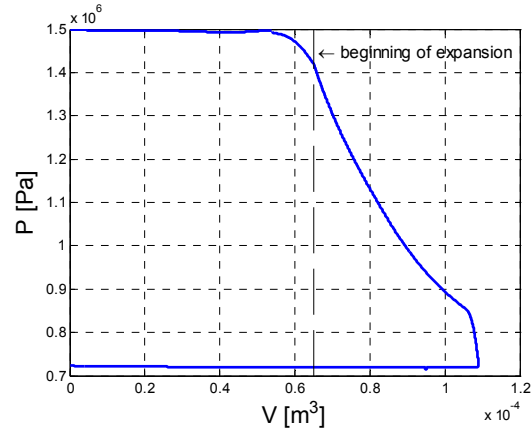


Figure 3-8: P-V diagram : $P_{su} = 15$ bar, $P_{ex} = 7.17$ bar, $T_{su} = 9.68^\circ\text{C}$, $x_l = 60\%$, $\text{rpm} = 892 \text{ min}^{-1}$ (modified geometry)

The increase of the expander's performance with the new design is even more significant at higher expander speeds. This is shown in the comparison between Figure 3-9 and Figure 3-10. The shaft power increases from 583W to 664W. The reduction of the pressure drop here results in an increase of the displaced mass flow rate, from 66.0 g/s to 68.0 g/s. The global isentropic efficiency is increased from 64.7% to 71.4%.

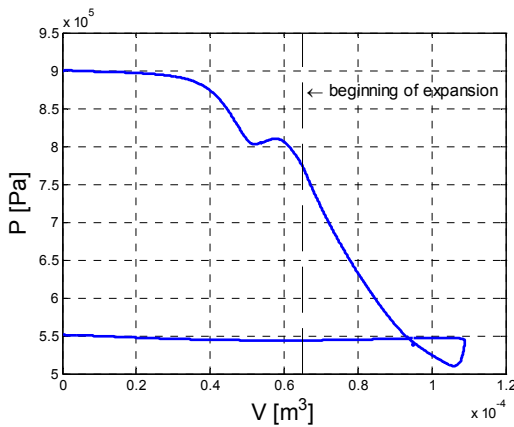


Figure 3-9: P-V diagram $P_{su} = 9.05$ bar, $P_{ex} = 5.39$ bar, $T_{su} = 15.3^\circ\text{C}$, $x_l = 69\%$, $\text{rpm}=1751 \text{ min}^{-1}$ (original geometry)

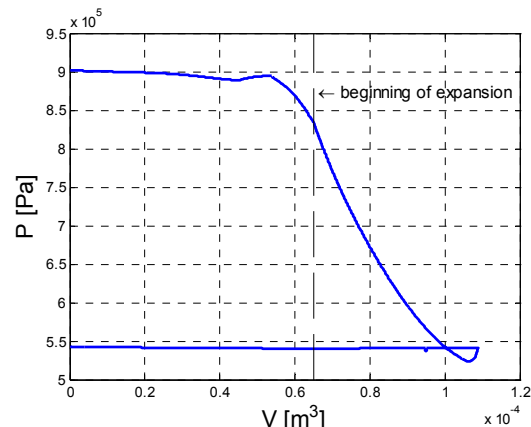


Figure 3-10: P-V diagram $P_{su} = 9.05$ bar, $P_{ex} = 5.39$ bar, $T_{su} = 15.3^\circ\text{C}$, $x_l = 69\%$, $\text{rpm} = 1751 \text{ min}^{-1}$ (modified geometry)

3.2.2 Variation of the flank and radial gap sizes

Simulations for different radial and flank leakage gap sizes are performed in order to

investigate the sensitivity of the expander performance with respect to the leakages (for this simulation, the operating conditions are: $P_s = 13.9$ bar, $P_d = 7.27$ bar, $T_s = 13.9$ °C, $x_l = 59\%$, $\text{rpm} = 865 \text{ min}^{-1}$). The standard flank gap size is 10 μm and the standard radial gap size is 10 μm .

The evolution of the gas mass flow rate with the flank and radial gap sizes is displayed in Figure 3-11. As already explained in §2.6.2, the displaced mass flow rate is more sensitive to the variation of the radial gap size than of the flank gap size. The shaft power decreases with the leakage gaps size because of the increase of the suction pressure drops due to higher mass flow rate (Figure 3-12). For this simulation, the flank leakage curve shows an optimal value. This is due to the fact that, even if they exacerbate the suction pressure drops, leakage flows can slightly improve the P-V diagram. The evolution of the global isentropic effectiveness with both gap sizes is given in Figure 3-13.

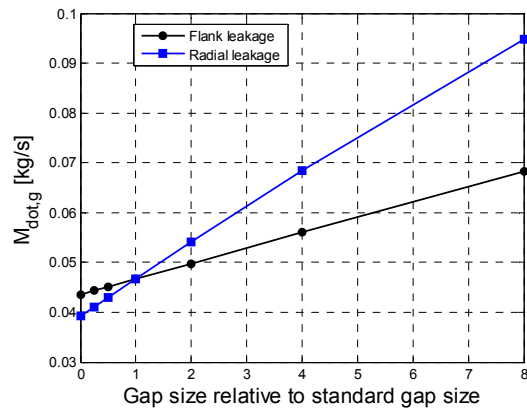


Figure 3-11: Evolution of the gas flow rate with the gaps' size

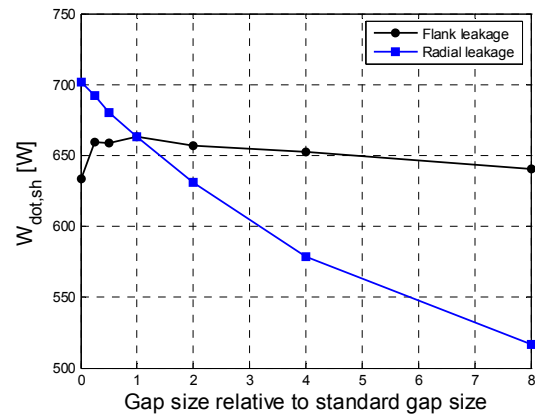


Figure 3-12: Evolution of the shaft power with the gaps' size

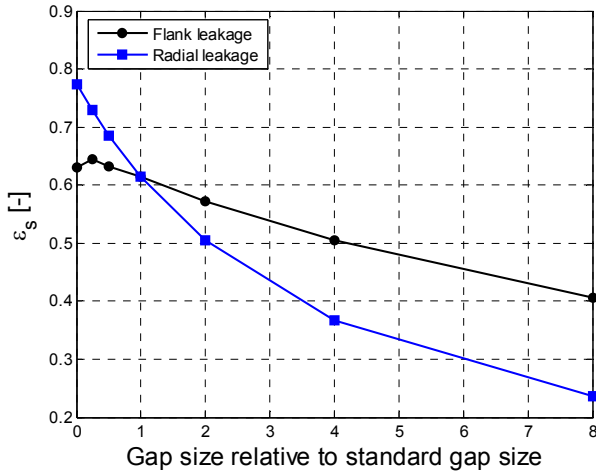


Figure 3-13: Evolution of the global isentropic effectiveness with the gap size

4 CONCLUSIONS

The expander deterministic model allows for better characterization the different sources of inefficiency of the machine. As already observed in Chapter 4 the main sources of inefficiency are the suction pressure losses and the internal leakages.

For the ORC expander, the identified flank and radial gaps are 70 μm and 0 μm respectively. The radial gap equal to zero means that the tip seals are working correctly. This is confirmed by the teardown inspection of the scrolls. It must be probably difficult to reduce the flank gap, because of the mechanism employed to create the orbital motion of the orbiting scroll (15 bearings) without causing contact between the scrolls.

For the LFEC expander, it is observed that the identified leakage area is varying with the operating parameters. At this point, it is still not possible to determine the underlying reason (mechanical deformation, play in the orbiting scroll, ...).

As already observed by Yanagisawa et al. (2001), the suction pressure drop is an inherent characteristic of the scroll expander. It is mainly due to the covering of the suction chamber supply port by the tip of the orbiting scroll and the subdivision of the suction chamber (in three different sub-chambers) at the end of the suction process.

Using the validated deterministic model, parametric studies were carried out to investigate the variation of the expander performance with variation of the scroll expander design and operating parameters. The results of the analysis can be summarized as follows:

- 1) For the ORC expander, it does not seem feasible to substantially reduce the *suction pressure* drop and increase the isentropic effectiveness. The effect of attenuating the supply port blockage was investigated by enlarging the supply port diameter by 50%. For the considered operating point, this only yields an increase of the isentropic effectiveness by 1%. Actually, the main contribution to the suction pressure drop is the subdivision of the suction chamber at the end of the suction process. This pressure drop could be attenuated by increasing the flow passage between the central chamber and the adjacent chambers, but at the cost of an increase of the leakage flow rates during suction. As a consequence, both the shaft power and the displaced mass flow rate increase and the isentropic effectiveness remains almost unchanged. For the LFEC expander, the suction pressure drop can be more substantially reduced by enlarging the supply port and making the tip of the scrolls thinner.
- 2) For the ORC expander, the exhaust pressure drop is not negligible. It could be reduced by simply enlarging the exhaust port area.
- 3) Internal leakage is a main source of inefficiency of both expanders.

For the ORC expander, radial leakages are well controlled by tip seals. Simulation has shown that in the limiting case of canceling the flank leakages, isentropic effectiveness would increase by 10%. However, at this point of the investigation, it is not possible to determine how much these dimensions can be reduced. Some technical information is needed, such as machining tolerance, material strength, machining constraints and differential thermal expansion.

For the LFEC expander, further experimental work should allow understanding the reason for the large and non constant flank leakage gap.

- 4) The impact of the internal heat transfer in the modeling was investigated by introducing a multiplication factor in the expression used to compute the convective heat transfer coefficient. It was observed, that the uncertainty on the convective heat transfer coefficient does not have a substantial impact on the prediction of the mass flow rate and the exhaust temperature.

- 5) Under cost and size constrains, slightly under-sizing the expander built-in volume ratio is a good option, since it does not largely cut down the global isentropic effectiveness.
- 6) The ORC scroll expander is characterized by an optimal rotational speed (maximizing the global isentropic effectiveness) close to 2000 min^{-1} , for most of the pressure ratios. This optimum results from the increase of the suction and discharge pressure drops with the rotational speed and the simultaneous decrease of the relative impact of the internal leakages.
- 7) Performance can be slightly improved by reducing the mechanical loss. For the ORC expander, this could be achieved by using tip seals more adapted to the working conditions. Actually, teardown inspection of the scroll machine showed that they wore a little bit thinner than expected.

The analysis of the results generated by the *deterministic* model shows that the values of the parameters of the semi-empirical model identified in Chapter 4 have a physical meaning. The mechanical loss torque identified in the *semi-empirical* model is smaller than the one identified in the deterministic one. The underlying reason seemed to be that the semi-empirical model is not able to predict the increase of the expansion work with the flank leakage.

Non-dimensional laws were derived for the semi-empirical model. These laws express the variation of the model's parameters with the expander displacement. A validation of these laws was carried out by comparing predictions by the semi-empirical model to those by the deterministic model. These laws are accurate enough to be used in early design stages of a thermal system comprising a scroll machine.

5 REFERENCES

Baehr, H.D., R. Tillner-Roth. 1995. Thermodynamic Properties of Environmentally Acceptable Refrigerants. *Springer-Verlag*. Berlin Heidelberg: 23.

- Bell, I., V. Lemort, J. Braun, E. Groll. 2008a. Development of Liquid-Flooded Scroll Compressor and Expander Models. *Proceedings of the 19th International Compressor Engineering Conference at Purdue University*: Paper 1283.
- Bell, I., V. Lemort, J. Braun, E. Groll. 2008b. Analysis of Liquid-Flooded Compression Using a Scroll Compressor. *Proceedings of the International Compressor Engineering Conference at Purdue University*: Paper 1263.
- Lee, J.N., and R.S. Lee. 2007. Geometric Modelling and NC Machining of Scroll Profiles Using Circular Biarcs Fitting. *Proceedings of the 35th International MATADOR Conference*, 3: 41-44.
- Persson, J.-G. 1990. Performance mapping vs design parameters for screw compressors and other displacement compressor types. *VDI Berichte*, nr. 859, Düsseldorf.
- Preissner, M. 2001. Carbon Dioxide Vapor Compression Cycle Improvements with Focus on Scroll Expanders. *Ph.D. Thesis*, University of Maryland, College Park.
- Yanagisawa, T., M. Fukuta, Y. Ogi, and T. Hikichi. 2001. Performance of an oil-free scroll-type air expander. *Proc. Of the ImechE Conf. Trans. On compressors and their systems*: 167-174.
- Younglove, B.A., and M.O. McLinden. 1994. An International Standard Equation of State for the Thermodynamic Properties of Refrigerant R123. *Journal of Physical and Chemical Reference Data*, Vol. 23, No. 5: 731-779.

CHAPTER 8

GENERAL CONCLUSIONS AND RECOMMENDATIONS

Testing and modeling scroll machines

This thesis has presented different experimental and modeling investigations on scroll compressors and expanders used in various thermal systems.

Experimental investigations

Two open-drive scroll expanders have been tested. Both of them are derived from off-the-shelf compressors. Performances of the expanders have been measured and analyzed under different operating conditions.

ORC expander

The first expander tested is used in an Organic Rankine Cycle (ORC) power system working with R123. It is originally an oil-free open-drive air scroll compressor. The scroll machine is characterized by a large built-in volume ratio (close to 4.0), which makes it better adapted to the achieved pressure ratio than refrigeration scroll compressors. The fact that the expander does not need lubrication was also a primary selection criterion. Lubrication of the expander would have required an oil separator and an oil pump, which would have increased the cost and the complexity of the system. The experimental study confirmed that the scroll expander is a good candidate for an ORC application. The prototype tested presented good performances: the maximum global isentropic effectiveness achieved is 68%.

Despite its good performance, the expander showed a few drawbacks:

- The machine is not tight, which caused large refrigerant losses during the test campaign.
- The machine cannot withstand pressures higher than 10 bar. For ORC systems working at similar heat source temperatures, this restricts the choice of the working fluid (for instance, R245fa and R134a couldn't be used).

LFEC expander

The second expander tested was integrated into a Liquid Flooded Ericsson Cycle cooler (LFEC). Such a system uses the liquid flooding of the compressor and of the expander to approach isothermal compression and expansion processes. The refrigerant in the system was nitrogen and the flooding liquid was alkyl-benzene oil. The performances of a compressor integrated into the same system have also been measured and analyzed. Both machines are originally automotive air-conditioning compressors. The experimental investigation revealed that the isentropic effectiveness of both machines was decreasing with the oil mass fraction, which is an undesirable feature for the global system. It was also observed that the volumetric effectiveness of the expander was very low compared to the effectiveness achieved with the compressor.

Modeling investigations

Compressor and expander semi-empirical models

A semi-empirical model of a *scroll expander* is proposed. The model involves a limited number of parameters which describe the main physical features of the expander. Due to its accuracy, low computational time and robustness, the model can easily be associated to the models of other components (such as heat exchangers) in order to describe a larger thermal system.

The model parameters were identified for both expanders. For the ORC expander, the model predicts with a very good agreement the variables of first importance such as the mass flow rate, the shaft power and the discharge temperature. For the LFEC expander, it was observed that the identified leakage area is varying with the operating parameters. At this point, it is still impossible to determine the underlying reason (mechanical deformation, play in the orbiting scroll, problems with the tip seals,...).

An existing hermetic *scroll compressor* semi-empirical model has been modified to account for the *discharge valve*. This valve is used in scroll compressors working at high pressure ratios to decrease the loss associated to under-compression. The presence of the discharge valve is described in terms of re-expansion of the clearance volume of the scroll compressor and pressure drop through the discharge opening. Two additional parameters are introduced

in the original model of the hermetic scroll compressor. The modified model has been validated on the basis of published manufacturer data for a heat pump scroll compressor. This modification of the model strongly impacts on the prediction of the electrical consumption, but not on the refrigerant mass flow rate prediction. Consequently, introducing the two parameters does not increase the complexity of the parameters identification process. The compressor model, without discharge valve, has also been validated in the case of an air-conditioning compressor (based on published manufacturer data) and in the case of the LFEC compressor (with experimental data). In both cases, predictions by the model agree very well with measurements.

Expander deterministic model

A *deterministic model* (comprehensive numerical model) of the scroll expander has been established and validated for both the ORC and the LFEC expanders. The model associates a geometrical description of the machine with a thermodynamic description of the expansion process. The reason for developing such a model was to identify and quantify the different sources of inefficiency of the machine.

The ORC expander model predicts with a good agreement the mass flow rate, the shaft power and the exhaust temperature. The identified flank and radial leakage gaps are 70 µm and 0 µm respectively. For the LFEC expander, a flank gap varying with the rotational speed and the pressure ratio was found to yield good results.

For both expanders, the main sources of inefficiency are the supply pressure drop and the internal leakage. The supply pressure drop is explained by the covering of the suction chamber supply port by the tip of the orbiting scroll and the subdivision of the suction chamber (in three different sub-chambers) at the end of the suction process.

Using the validated deterministic model, parametric studies have been carried out to investigate the variation of the performance of both expanders with modification of their design and with the operating parameters. The results of the analysis can be summarized as follows:

Investigation of the design

For the ORC expander, it did not seem feasible to substantially reduce the *suction pressure drop* by enlarging the supply port diameter by 50%. Actually, the suction pressure drop is mainly due to the subdivision of the suction chamber in three sub-chambers at the end of the suction process. This pressure drop could be attenuated by increasing the flow passage between the central chamber and the adjacent chambers, but at the cost of an increase of the leakage flow rates during the suction process. As a consequence, both the shaft power and the displaced mass flow rate increase and the isentropic effectiveness remains almost unchanged. For the LFEC expander, it was found that the suction pressure drop can be more substantially reduced by enlarging the supply port and making the tip of the scrolls thinner.

Under cost and size constrains, slightly under-sizing the expander *built-in volume ratio* is a good option since it does not largely cut down the global isentropic effectiveness.

Internal leakage is a large source of inefficiency for both expanders. In the case of the ORC expander, radial leakages seem to be well controlled by tip seals: the identified radial leakage gap of 0 μm is confirmed by the teardown inspection of the machine. Simulation has shown that in the limiting case of canceling the flank leakages, isentropic effectiveness would increase by 10%. However, at this point of the investigation, it is not possible to determine how much the flank leakage gap can be reduced. Some technical information is needed, such as machining tolerance, material strength, machining constraints and differential thermal expansion.

Performance can be slightly improved by reducing the *mechanical loss*. For the ORC expander, this could be achieved by using tip seals more adapted to the working conditions. Actually, teardown inspection of the scroll showed that they wore a little bit thinner than expected.

Investigation of the operating conditions

The ORC expander is characterized by an optimal rotational speed (maximizing the global isentropic effectiveness) close to 2000 min^{-1} , for most of the pressure ratios. This optimum

results from the increase of the suction and discharge pressure drops with the rotational speed and the simultaneous decrease of the relative impact of the internal leakages.

Deterministic model versus semi-empirical model

Analysis of the results generated by the deterministic model demonstrated that the values of the parameters of the semi-empirical model identified in Chapter 4 have some physical meaning.

Non-dimensional laws were derived for the semi-empirical model. These laws express the variation of the model's parameters with the expander displacement. Validation of these laws was carried out by comparing predictions by the semi-empirical model to those by the deterministic model. These laws are accurate enough to be used in the early stages of the sizing of a thermal system comprising a scroll expander.

Recommendations

For the validation of the expander deterministic model, internal measurements of the pressure in the different chambers would be useful.

For some applications it would be more convenient that the expander produces directly electricity and not mechanical power. Hermetic scroll expanders would be appropriate. A similar experimental characterization should be carried out in order to measure their performance and identify the different sources of irreversibility.

Other types of open-drive expanders, working in the same range of power, such as piston-cylinder, screw and vane expanders, should also be characterized.

Testing and modeling thermal systems with scroll machines

The thesis also investigated the scroll machine from the point of view of its integration into a thermal system. Two systems have been studied: an ORC power system and an air-cooled chiller.

Testing and modeling an air-cooled water chiller

Published manufacturer data is often the only one information available for modeling HVAC components. Some information is usually lacking to accurately validate the components models. As a consequence, rational assumptions and idealizations must be proposed. This was illustrated in this thesis in the case of an air-cooled scroll compressor chiller.

The thesis presents the parameters identification process based on manufacturer data. First the compressor model parameters were identified, using compressor's performance. Then the heat exchangers model parameters were identified, using the chiller's performance. The only difficulty encountered was the characterization of the fan control model, since information was lacking to identify its parameters.

Results of an experimental investigation carried out on the same chiller integrated into an existing cooling plant were finally presented. The instrumentation was mainly limited to simple measurements such as the secondary fluids temperatures, the glycol water flow rate, the compressor suction and discharge pressures and the chiller electrical consumption (with distinction between fan and compressors consumption).

The compressor model was used as refrigerant flow meter. Comparison between simulation and experimental data revealed that the chiller model with its parameters identified based on manufacturer data was not able to correctly predict the cooling capacity (deviations up to almost 30%). The analysis of the experimental data allowed a better understanding of the chiller's operation and a better identification of the model parameters (such as the fan control model). Moreover a simple but realistic model of the condenser hot gas bypass was introduced. As a result, deviations between predictions by the model and the experimental data were considerably reduced. The total cooling energy and the total electrical consumption over a four-day simulation period (minute by minute) agree with experimental data within respectively 4% and 1%.

Recommendations

The compressor performance tables should always be given as part of the chiller performance data.

In the frame of the commissioning of a chiller, if there is no measurement of the refrigerant flow rate, the validated scroll compressor model could be used as an accurate flow meter.

Testing and modeling an organic Rankine cycle system

An experimental study has been carried out on an ORC power system, working with R123 and characterized by a boiler thermal power ranging from 10 to 20 kW.

In order to select the most appropriate fluid, the performances achieved with four fluids were compared. The comparison accounted for the main characteristics of the expander, such as its built-in volume ratio and displacement.

The maximum achieved cycle and second law efficiencies were 7.2% and 21.2% respectively.

The cycle simulation model was only partly validated. Using the expander and the cycle simulation models, parametric studies were performed to investigate the variation of the expander and the cycle performances with the operating conditions and the expander design. It was shown that the performance of the expander could be largely improved by reducing both the internal leakage and the suction pressure drop. The performance of the cycle mainly suffers from the expander internal leakage and liquid subcooling at the condenser exhaust. This subcooling can be reduced by controlling the charge of refrigerant inside the cycle.

Recommendations

The instrumentation of the test rig could be improved. For instance, additional instrumentation would be necessary to better characterize the heat exchanger's performance.

The design of the present test rig should be optimized to increase its performance. The optimization must determine the size and the configuration of the heat exchangers as well as

the operating parameters (such as pump/expander rotational speeds or the charge of refrigerant in the system).

The potential working fluids for ORC applications appeared to be limited. Environmental friendly fluids with good thermal properties should still be developed.

APPENDIX

1	APPENDIX TO CHAPTER 2.....	280
1.1	Development of the expression of the internal power in the case of an expander	280
1.1.1	Suction power	280
1.1.2	Expansion power	281
1.1.3	Throttling	281
1.1.4	Discharge power	282
1.1.5	Internal power	282
2	APPENDIX TO CHAPTER 3.....	283
2.1	Coefficients used in the equations for the compressor performance data.....	283
2.2	Definition of quasi-steady state points	284
2.3	Control of the chiller's compressors (Felsmann, 2008).....	287
2.4	Control of the condensers' fans	289
3	APPENDIX TO CHAPTER 4.....	290
3.1	Performance points for the expander	290
4	APPENDIX TO CHAPTER 5.....	291
4.1	The Ericsson cycle	291
4.2	Problems encountered with RTD's	291
4.3	Thermal properties of alkyl-benzene oil.....	295
4.4	Derivation of an equation for two-phase flow pressure drop through an orifice by conservation of momentum	296
4.5	Expander isothermal effectiveness	297
5	APPENDIX TO CHAPTER 7.....	298
5.1	Coefficient of the equations of Baehr and Tillner-Roth (1995) for R123	298
5.2	Comparison of the R123 properties tabulated in EES and given by the equations of Baehr and Tillner-Roth (1995) for R123	298
5.3	Equations describing the scroll tip	299
5.4	Estimation of the external heat transfer coefficient	300

1 APPENDIX TO CHAPTER 2

1.1 Development of the expression of the internal power in the case of an expander

The relative position of the fixed and the orbiting scrolls defines different chambers, which can be divided up into suction chambers, expansion chambers and discharge chambers

One working cycle of the scroll expander includes three processes: suction, expansion and discharge. During the suction process, the suction chamber is in communication with the suction port and fluid flows into the chamber. The expansion is initiated when the suction chamber ceases to be in communication with the suction port. Discharge begins when the discharge chambers are in communication with the discharge channel.

The internal power \dot{W}_{in} produced by the expansion is the summation of the suction power \dot{W}_{suc} , the expansion power \dot{W}_{exp} and the discharge power \dot{W}_{dis} :

$$\dot{W}_{in} = \dot{W}_{suc} + \dot{W}_{exp} + \dot{W}_{dis} \quad (1-1)$$

1.1.1 Suction power

The energy balance across the suction chamber, between the beginning and the end of the suction process, can be expressed in the rate form by:

$$\dot{M}_{in} u_{su,2} = \dot{M}_{in} h_{su,2} - \dot{W}_{suc} \quad (1-2)$$

The suction power can be expressed as a function of the expander displacement

$$\dot{W}_{suc} = \dot{M}_{in} P_{su,2} v_{su,2} = P_{su,2} \dot{V}_{s,exp} \quad (1-3)$$

The suction power corresponds to the area a-b-h-g in the diagram (pressure versus rate of change of the volume) given in Figure 1-1.

1.1.2 Expansion power

Writing the energy balance between the beginning and the end of the expansion process yields

$$\dot{M}_{in}(u_{ad} - u_{su,2}) = -\dot{W}_{expan} \quad (1-4)$$

By definition of the enthalpy,

$$\dot{W}_{expan} = \dot{M}_{in}(h_{su2} - P_{su2}v_{su2} - h_{ad} + P_{ad}v_{ad}) \quad (1-5)$$

The expansion power corresponds to the area b-c-i-h in the diagram (pressure versus rate of change of the volume) given in Figure 1-1.

1.1.3 Throttling

- *Under-expansion* occurs when the internal pressure ratio imposed by the expander is lower than the system pressure ratio (Figure 1-1 (a)). The pressure in the expansion chambers at the end of the expansion process (P_{ad}) is higher than that of the discharge reservoir. In order to equalize the pressures the discharge chambers (the former expansion chambers) and in the discharge reservoir, some fluid has to flow from the discharge chamber out-of the expander. This is achieved at the instant when the discharge port becomes uncovered.

At the end of this “throttling” process, it is assumed that the fluid in the channel is in thermodynamic equilibrium with the fluid in the discharge reservoir.

The energy balance over the discharge chamber can be expressed as follow:

$$(\dot{M}_{in} - \Delta\dot{M}_{in})u_{ex,3} - \dot{M}_{in}u_{ad} = -\Delta\dot{M}_{in}h_{ex,3} \quad (1-6)$$

- *Over-expansion* occurs when the internal pressure ratio imposed by the expander is higher than the system pressure ratio (Figure 1-1 (b)). The energy balance over the discharge chamber is similar to the one for the under-expansion process.

$$(\dot{M}_{in} + \Delta\dot{M}_{in})u_{ex,3} - \dot{M}_{in}u_{ad} = \Delta\dot{M}_{in}h_{ex,3} \quad (1-7)$$

There is no work associated to the under- and over-expansion process.

1.1.4 Discharge power

As for the suction process, the equation of conservation of energy is applied on the discharge chamber between the beginning and the end of the discharge process.

$$-(\dot{M}_{in} \pm \Delta\dot{M}_{in})u_{ex,3} = -\dot{W}_{dis} - (\dot{M}_{in} \pm \Delta\dot{M}_{in})h_{ex,3} \quad (1-8)$$

$$\dot{W}_{dis} = -(\dot{M}_{in} \pm \Delta\dot{M}_{in})P_{ex,3}V_{ex,3} = -r_{v,in}P_{ex,3}\dot{V}_{s,exp} \quad (1-9)$$

The discharge power corresponds to the area d-e-g-i in the diagram (pressure versus rate of change of the volume) given in Figure 1-1.

1.1.5 Internal power

The internal power can be found by combining Equations (1-3), (1-5) and (1-9).

$$\dot{W}_{in} = P_{su,2}\dot{V}_{s,exp} + \dot{M}_{in}(h_{su,2} - h_{ad}) + \dot{M}_{in}(r_{v,in}P_{ad}V_{su2} - P_{su2}V_{su,2}) - r_{v,in}P_{ex,3}\dot{V}_{s,exp} \quad (1-10)$$

After some algebra, Equation (1-10) can be written as follows:

$$\dot{W}_{in} = \dot{M}_{in}(h_{su2} - h_{ad}) + \dot{M}_{in}P_{ad}r_{v,in}V_{su2} - r_{v,in}P_{ex,3}\dot{V}_{s,exp} \quad (1-11)$$

Recognizing that $\dot{V}_{s,exp} = \dot{M}_{in}V_{su,2}$,

$$\dot{W}_{in} = \dot{M}_{in} ((h_{ad} - h_{su,2}) + r_{v,in} \cdot v_{su2} (P_{ad} - P_{ex,3})) \quad (1-12)$$

By expressing the steady-flow energy balance on the expander (assumed to be adiabatic), the internal power can be expressed as a function of initial and final enthalpy states.

$$\dot{W}_{in} = \dot{W}_{suc} + \dot{W}_{expan} + \dot{W}_{dis} = \dot{M}_{in} (h_{su,2} - h_{ex,3}) \quad (1-13)$$

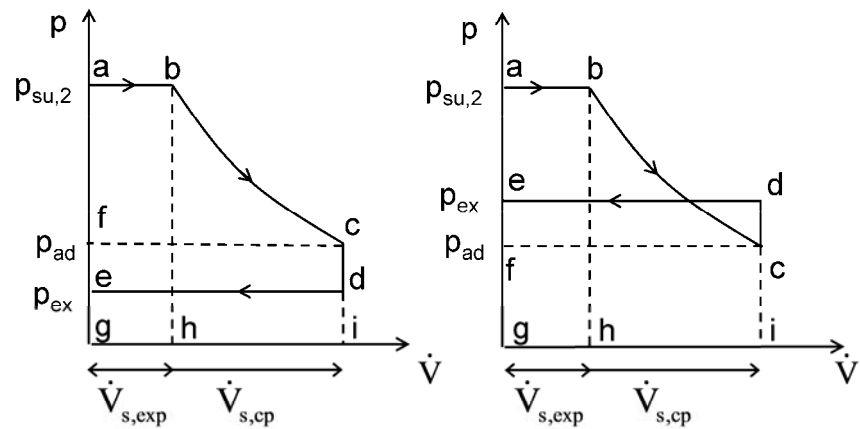


Figure 1-1: Representation of the entire process in the pressure-volume diagram

2 APPENDIX TO CHAPTER 3

2.1 Coefficients used in the equations for the compressor performance data

CAPACITY:		C0	C1	C2	C3	C4	C5	C6	C7	C8	C9
		55070.1268	1015.759132	-670.9283618	8.366942721	-4.292080418	5.652055068	0.035482911	-0.036895584	0.011956878	-0.02093168
POWER:		P0	P1	P2	P3	P4	P5	P6	P7	P8	P9
		899.8284616	20.82344535	9.768848299	-0.008466594	-0.279296311	0.080915998	-4.25228E-05	0.000833453	0.000458658	0.000713569
AMPS:		A0	A1	A2	A3	A4	A5	A6	A7	A8	A9
		3.370385621	-0.003505257	0.030809052	-0.00022633	0.000373509	-0.000280016	-1.49094E-06	4.49923E-06	-3.89537E-06	2.86122E-06
MASS FLOW:		M0	M1	M2	M3	M4	M5	M6	M7	M8	M9
		687.6230367	11.07418464	-10.3357279	0.070086666	-0.050875571	0.106697334	0.000412451	-0.000193216	0.000319303	-0.00039856

2.2 Definition of quasi-steady state points

The identified quasi-steady state points are represented (by the vertical red lines) in the following Figures, giving the time evolutions of the evaporator brine temperatures, condenser air temperatures and chiller total consumption.

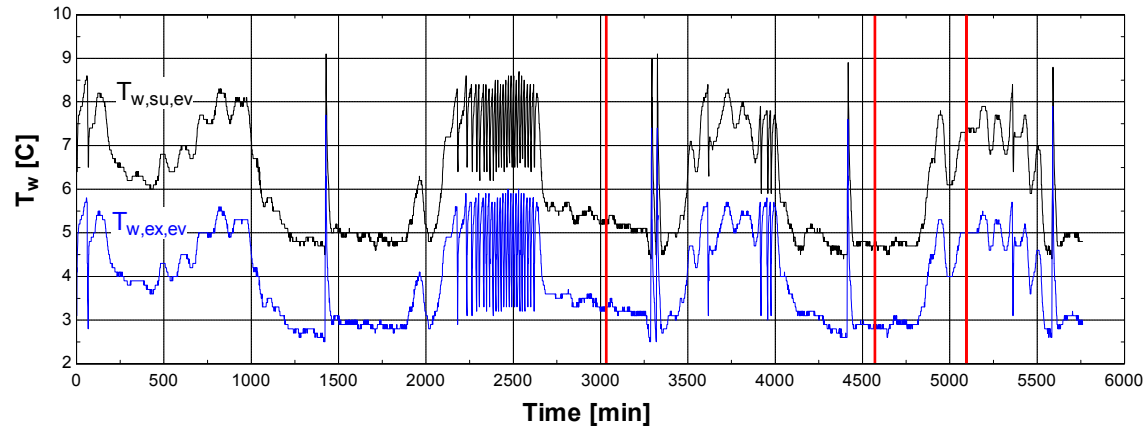


Figure 2-1: Time evolution of the evaporator brine temperatures (Empirical test II cold dry)

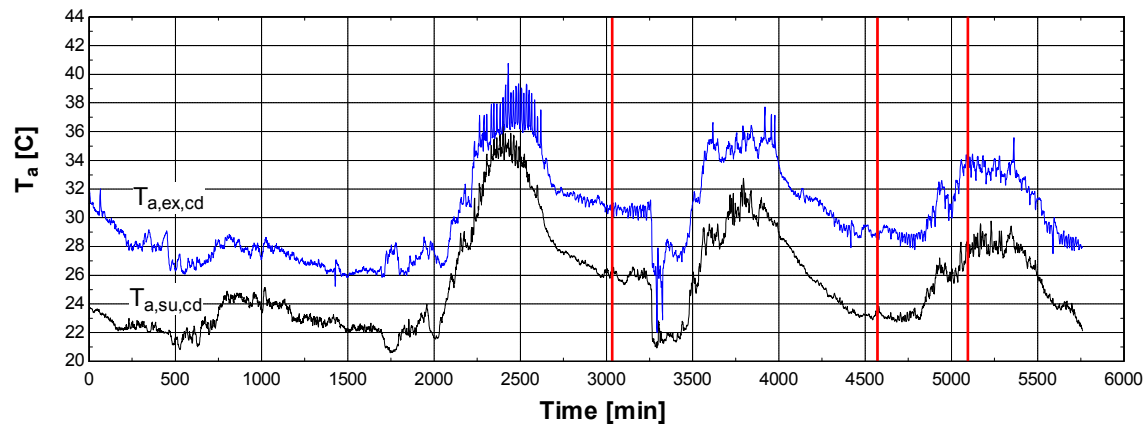


Figure 2-2: Time evolution of the condenser air temperatures (Empirical test II cold dry)

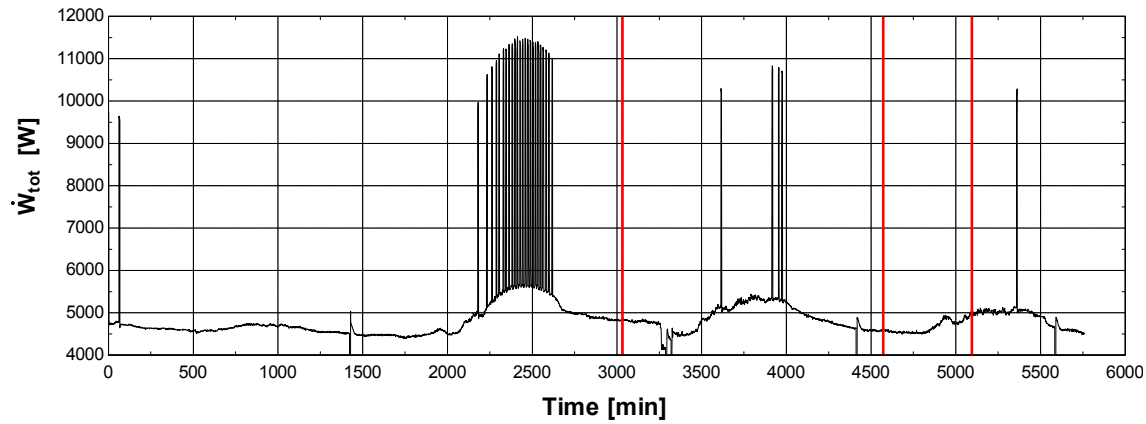


Figure 2-3: Time evolution of the chiller electrical consumption (Empirical test II cold dry)

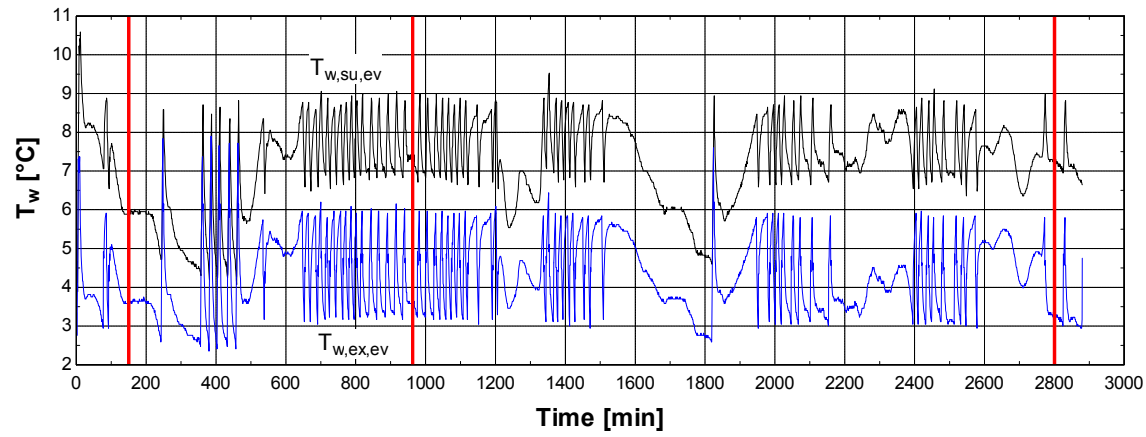


Figure 2-4: Time evolution of the evaporator brine temperatures (Empirical test II outside air)

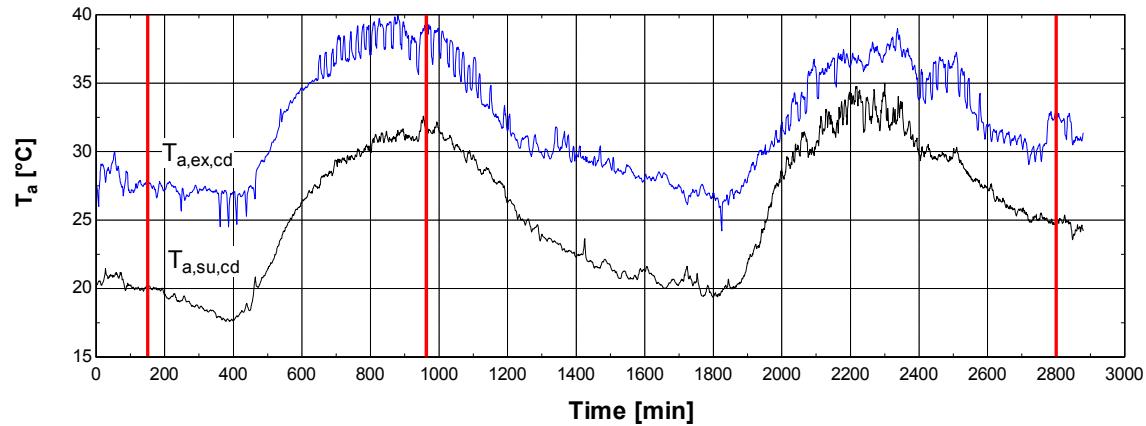


Figure 2-5: Time evolution of the condenser air temperatures (Empirical test II outside air)

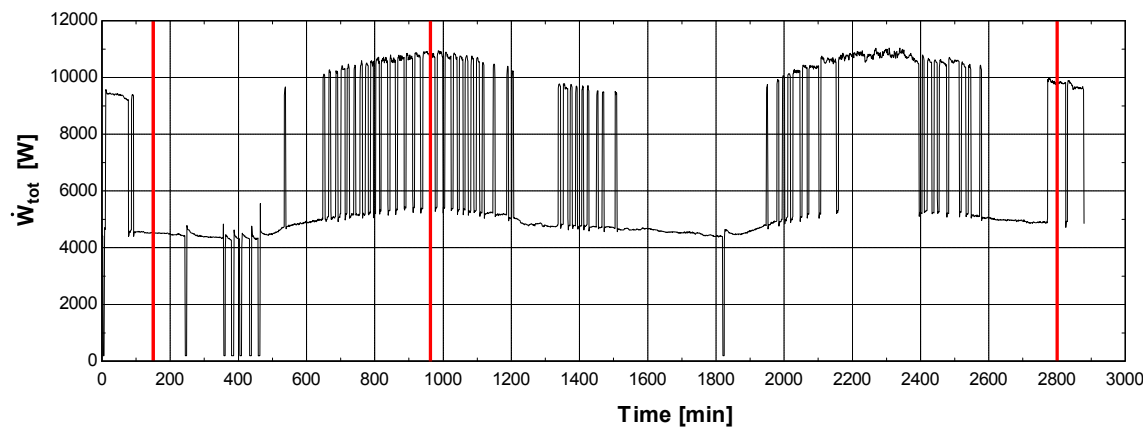


Figure 2-6: Time evolution of the chiller electrical consumption (Empirical test II outside air)

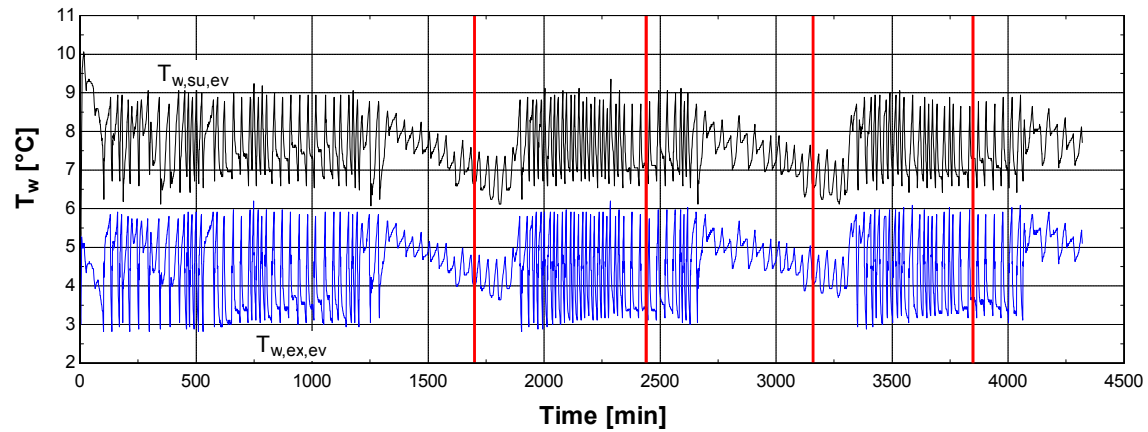


Figure 2-7: Time evolution of the evaporator brine temperatures (Empirical test II cold humid)

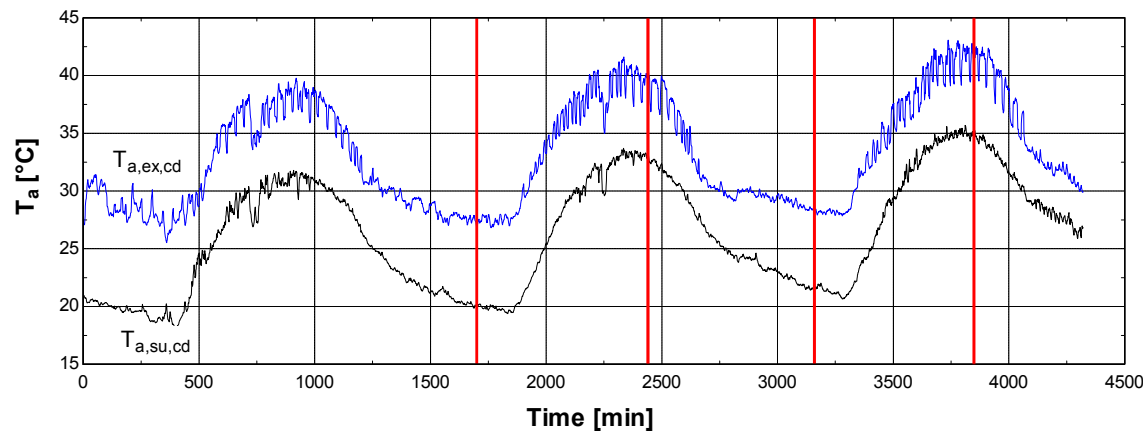


Figure 2-8: Time evolution of the condenser air temperatures (Empirical test II cold humid)

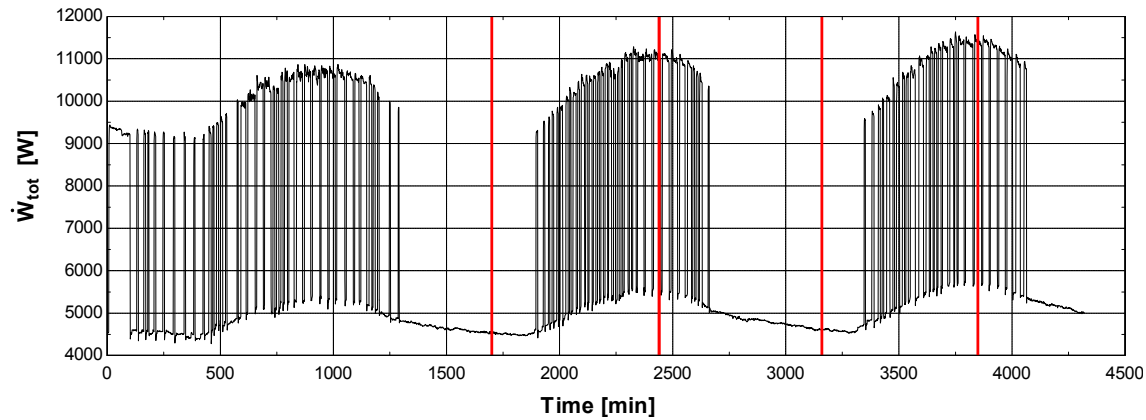


Figure 2-9: Time evolution of the chiller electrical consumption (Empirical test II cold humid)

2.3 Control of the chiller's compressors (Felsmann, 2008)

The chiller is controlled depending on leaving water temperature. According to the control scheme given in Figure 2-10, the compressor stages are switched on and off.

The dead band is automatically set of 60% of the user defined temperature difference between chiller entering water temperature and the leaving water temperature set point.

$$T_{DB} = 0.6 \times \Delta T_{Evap}$$

$$\Delta T_{Evap} = T_{EWT} - T_{LWT, set}$$

Compressor start and stop is determined by the dead band and ΔT_{Start} settings. ΔT_{Start} is the number of degrees above the temperature setting that determines when the lead compressor starts.

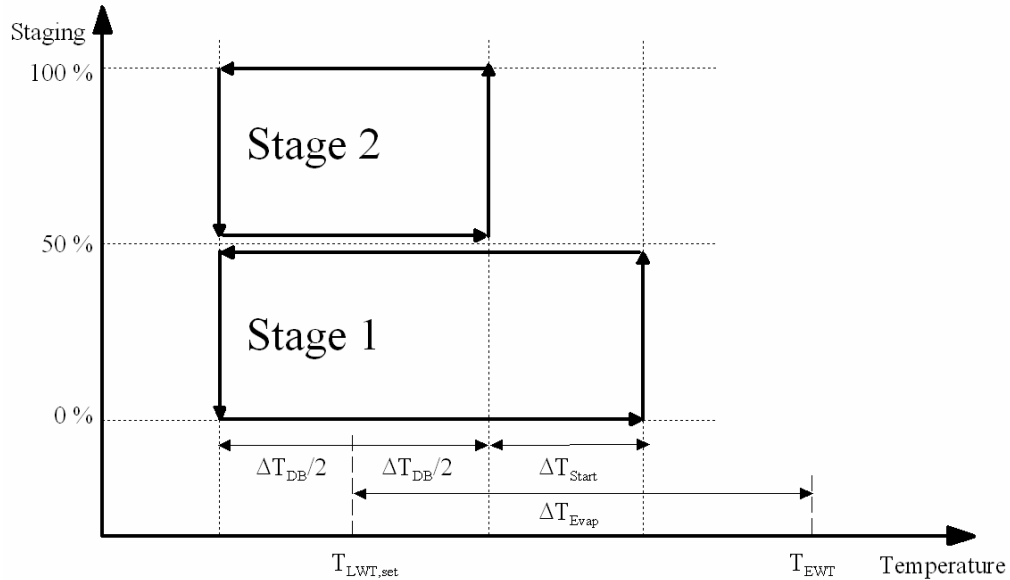


Figure 2-10: Chiller control scheme

For a warm start-up the lead compressor will start at any temperature above $T_{LWT,se} + 0.5\Delta T_{DB} + \Delta T_{Start}$. The lag will start after the start interval Δt_{up} has timed out. The chilled water temperature will begin to be pulled down. At $T_{LWT,se} - 0.5\Delta T_{DB}$ the lag compressor will shut off. If the temperature climbs above $T_{LWT,se} - 0.5\Delta T_{DB}$ within a limited time range Δt_{down} , the lead compressor will remain on. This would be normal operation. If for some reason the temperature does not rise, the lead compressor will also shut off. The lead compressor will start again when the chilled water temperature reaches $T_{LWT,se} + 0.5\Delta T_{DB} + \Delta T_{Start}$. The compressor designated as the lead will be the first to start and the last to shut off. Lead/lag designation is switched based on the number of starts. After 10 starts on Compressor #1 as lead, Compressor #2 starts as Lead for 10 starts, and then the cycle is repeated. Table 2-1 summarizes the rules for staging the compressors.

The time delays Δt_{up} and Δt_{down} are fixed as follows:

$$\Delta t_{up} = 240 \text{ s}$$

$$\Delta t_{down} = 30 \text{ s}$$

Table 2-1: Compressor staging rules

Description	Occurs When:	Action Taken	
		Lead Compressor	Lag Compressor
Stage #1 ON	$LWT > T_{LWT, set} + (\Delta T_{DB}/2) + \Delta T_{Start}$	ON	OFF
Stage #2 ON	$\Delta t > \Delta t_{up}$ $LWT > T_{LWT, set} + (\Delta T_{DB}/2)$	ON	ON
Stage #2 OFF	$\Delta t > \Delta t_{down}$ $LWT < T_{LWT, set} - (\Delta T_{DB}/2)$	ON	OFF
Stage #1 OFF	$\Delta t > \Delta t_{down}$ $LWT < T_{LWT, set} - (\Delta T_{DB}/2)$	OFF	OFF

2.4 Control of the condensers' fans

Condenser fan motors are automatically cycled in response to condenser pressure by a standard method of head pressure control called FanTrol. This function is controlled by the microprocessor, maintains head pressure and allows the unit to run at low ambient air temperatures down to 1.7°C (35°F). Fans are normally staged as follows:

Stage 1: On 1034 kPa (150 psig)

Off with unit

Stage 2: On 2000 kPa (290 psig)

Off 1172 kPa (170 psig)

Fan #1 is on with first compressor above 24°C (75°F).

The SpeedTrol method of head pressure control operates in conjunction with FanTrol by modulating the motor speed on system #1 fan in response to condenser pressure. By reducing the speed of the last fan as the condensing pressure falls, the unit can operate down to -18°C (0°F) ambient air temperature.

3 APPENDIX TO CHAPTER 4

3.1 Performance points for the expander

	\dot{M}_r	\dot{W}_{exp}	N_{exp}	$T_{r,su,exp}$	$T_{r,ex,exp}$	$P_{r,su,exp}$	$P_{r,ex,exp}$	$T_{amb,exp}$
	[kg/s]	[W]	[min ⁻¹]	[°C]	[°C]	[Pa]	[Pa]	[°C]
1	0.04615	382.2	2295	121	94.92	545000	200000	30.96
2	0.05697	736.9	2296	109.8	80.66	644945	189890	30.84
3	0.07086	1188	2296	122.6	85.05	825000	200000	33.07
4	0.06613	1065	2296	128.1	92.01	784558	209116	33.08
5	0.05384	737.4	2296	143.9	111.8	669945	210000	34.57
6	0.05407	767.2	2296	152.2	118.1	685000	210000	36.52
7	0.06767	1184	2296	136.5	102.1	805000	210000	35.49
8	0.07070	1276	2296	134.4	98.28	831292	200000	35.99
9	0.05487	801.8	2295	165.2	128	723784	229405	34.73
10	0.06995	1259	2296	141.9	106.4	838117	213851	34.48
11	0.07199	1340	2296	139	102.4	855486	208081	35.02
12	0.07376	1404	2296	142.7	103.9	883696	211529	34.68
13	0.07307	1134	2296	110.1	76.93	806801	207130	33.61
14	0.07025	1191	2296	123.2	86.42	814187	200807	33.48
15	0.06293	1021	2296	134.6	97.89	759516	205802	34.86
16	0.06198	1150	2296	156.4	116.4	787972	204490	36.91
17	0.05565	1154	2296	145.6	101.6	697817	138111	34.81
18	0.07030	1412	2296	132.2	92.35	829313	167705	35.58
19	0.08086	1446	2296	112.9	73.7	882277	185458	34.31
20	0.08231	1426	2296	107.7	69.23	873096	188519	34.22
21	0.07169	1401	2296	129.2	87.18	844089	177256	35.04
22	0.08476	1769	2296	141.6	97.77	1.007E+06	201314	36.46
23	0.07418	1189	2296	101.7	66.79	777838	173962	33.89
24	0.07220	1187	2296	103.8	66.4	777334	170965	33.41
25	0.06155	1181	2295	130.1	88.56	739967	159953	32.91
26	0.06241	1166	2296	128.8	89.37	744539	166962	34.27
27	0.06298	1106	2296	127.9	90.55	748831	180330	34.43
28	0.06301	939.1	2296	128.1	94.54	748796	211940	35.44
29	0.06326	647.4	2296	128.1	101.6	750045	266086	36.22
30	0.06129	1164	2296	132.5	94.74	734577	164709	36.19
31	0.05822	1151	2296	138	97.89	713676	155097	35.93
32	0.06519	1394	1771	130.3	82.99	894388	168581	31.35
33	0.05423	1167	1771	143.5	97.89	782226	157715	32.38
34	0.04513	974.8	1771	160.6	113	678479	144161	34.28
35	0.08246	1820	1771	141.2	95.34	1.112E+06	204911	35.7
36	0.08118	1708	1772	130.8	85.51	1.068E+06	202267	34.83
37	0.08625	1648	2660	138.9	98.58	956117	209715	34.63
38	0.07110	1269	2660	132.5	95.73	791276	184132	34.72
39	0.05358	934.2	2659	152.4	111.5	641749	156229	35.72

4 APPENDIX TO CHAPTER 5

4.1 The Ericsson cycle

The Ericsson cycle tends to get a Coefficient of Performances (COP) close to the COP of the Carnot cycle by imposing isothermal compression and expansion. The $T\text{-}s$ and $P\text{-}v$ diagrams of this cycle are shown in Figure 4-1. This cycle is made up of four totally reversible processes (Cengel and Boles, 2006): 1-2: isothermal compression; 2-3: constant pressure regeneration (heat rejected to the low temperature stream); 3-4: isothermal expansion; 4-1 constant pressure regeneration (heat absorbed from the high temperature stream).

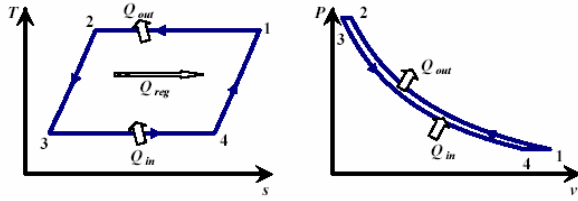


Figure 4-1: T-s and P-v diagrams for the ideal Ericsson cycle cooler (Cengel and Boles, 2006)

4.2 Problems encountered with RTD's

Some preliminary tests were performed in order to check that the system was working correctly and more especially to control all the measurement devices. One of the challenges of this experimental investigation is to achieve a high accuracy on the temperature measurements. This would improve the accuracy of the heat balances across the compressor, the expander and the heat exchanger when temperature differences are small.

Large energy residuals across the entire system were observed. The measured mechanical power was first thought to be incorrect. The calibration of the four torque-meters was checked, but appears to be very accurate. The RTD's were then suspected not to be reliable anymore due to excessive vibrations in the early tests. New vibration-resistant RTD's were installed at the inlet and the outlet of both the compressor and the expander.

A few tests were reproduced with thermocouples installed on the two heat exchangers in place of the RTD's. The comparison between measurements with RTD's and those with thermocouples highlighted some problems associated with the use of RTD's. Among other things, these problems are (Sandborn, 1972):

- *Joule ("self"-)heating effects.* The amount of current sent into the RTD has to be limited to 1 mA.
- *Calibration uncertainty.* The calibration of the RTD's was checked by means a calibrator
- *Conduction of heat to the supports.* All the fittings were carefully insulated. The effect of the insulation of the fitting is shown in Figure 4-3. The insulation on the fitting of RTD T_7 was temporarily removed, leading to a considerable increase of the measured temperature.
- *Impact of lead resistance.* A 4-wires connection scheme is used. This configuration is represented in Figure 4-2. A current is injected through wire resistance 1, the *RTD* and wire resistance 2. Wire resistances 3 and 4 are connected to a very high impedance differential amplifier. Because there is no current flowing through wire resistances 3 and 4, there is no voltage drop across them and the amplifier inputs sees only the voltage directly across the *RTD*. This method is not affected by the difference in wire and connection resistances. Therefore this is a good choice for sensors with non-equal lead lengths or with connections resistances that could change over time.
- *Time lag.* The duration of the test should be long enough to reach steady state regime.

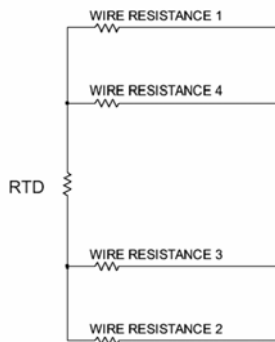


Figure 4-2 4-wires RTD configuration

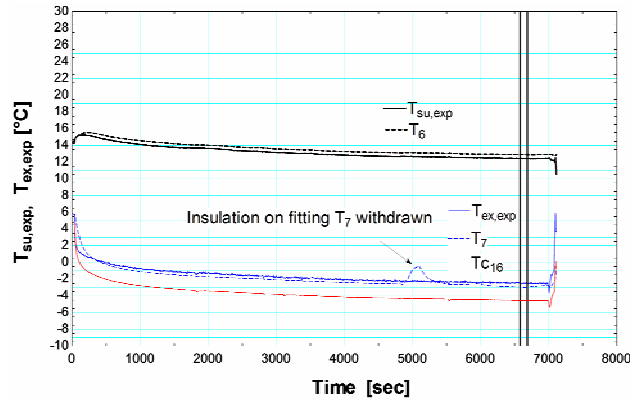


Figure 4-3 Evolution with time of temperatures at the inlet and the outlet of the expander and at the inlet of the heat exchanger: effect of the insulation on the fittings

Another main problem associated with two phase flow temperature measurement is the non thermal equilibrium between the two phases. Figure 4-4 shows a summary of what are the measurements (in blue) and the calculated values (in red) for the entire test rig. On this figure, it can be observed that the temperature at the exhaust of the expander (measured by thermocouple $T_{ex,exp}$ and RTD T_7) is higher than the temperature at the inlet of the cold heat exchanger (measured by RTD T_{16}). These temperatures are lower than 0°C and the ambient temperature is close to 25°C. Consequently, only an increase of the temperature between the expander outlet and the heat exchanger inlet was expected, due to heat gains. The apparent temperature drop is probably due to a measurement problem. One plausible explanation is that, straight after the expander outlet, the two phases in the mixture are not in thermal equilibrium (oil would be warmer than nitrogen) and the temperature measurement devices measure a temperature closer to the one of oil. Temperatures of the phases equalize along the pipe (more than 1 meter long) between the expander and the heat exchanger. It was also observed that the temperature drop increases as the mass fraction of oil decreases. To check that the RTD T_{16} at the inlet of the heat exchanger was working correctly, similar tests were achieved with thermocouples, leading to the same observation. For the very last tests, a thermocouple T_{c7} was finally installed between the expander and the heat exchanger. It was observed that the measured temperature was lower than the temperature at the expander

outlet and a little bit lower (a few tenths of a degree) than the temperature at the heat exchanger inlet. The latter difference of temperature is probably due to ambient heat gains. The evolution of the temperatures at the inlet and the outlet of the expander and the inlet of the heat exchanger are shown in Figure 4-5.

When expressing the heat balance across the expander, the temperature at the outlet of the expander will be considered equal to the temperature at the heat exchanger inlet (RTD T_{16}).

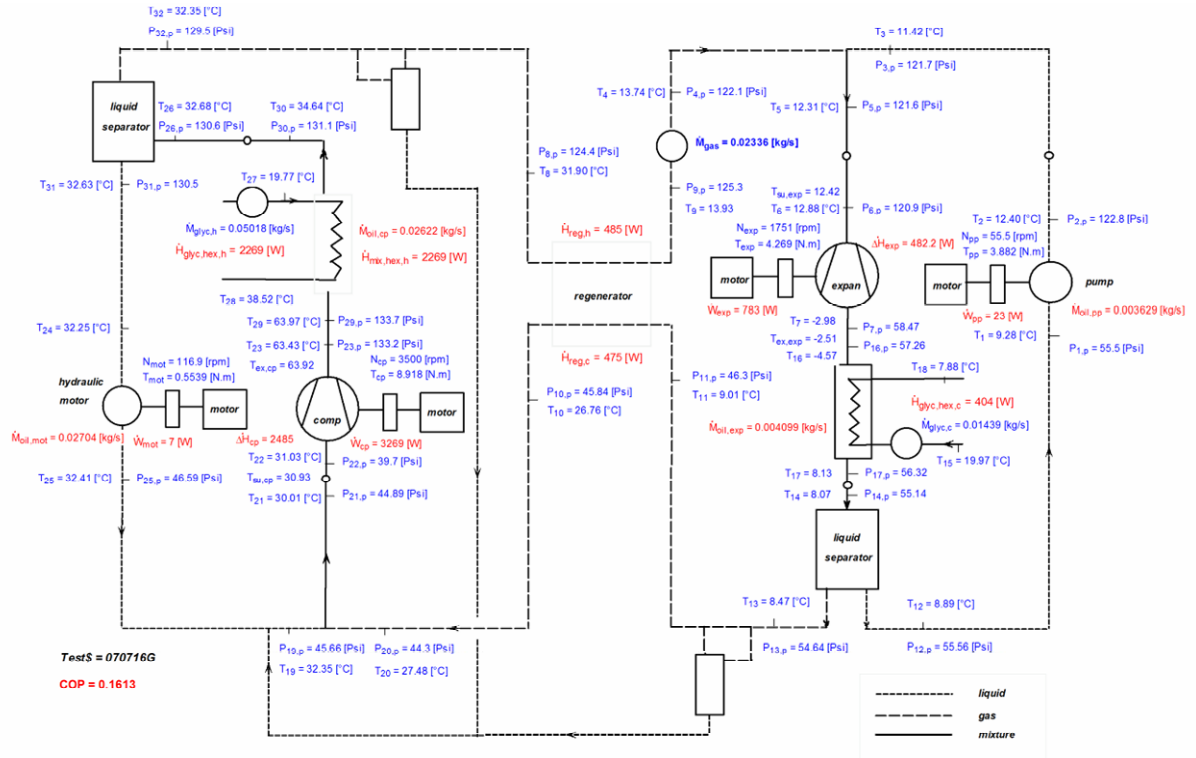


Figure 4-4: Summary of measurements (in blue) and calculated values (in red) for the entire rig

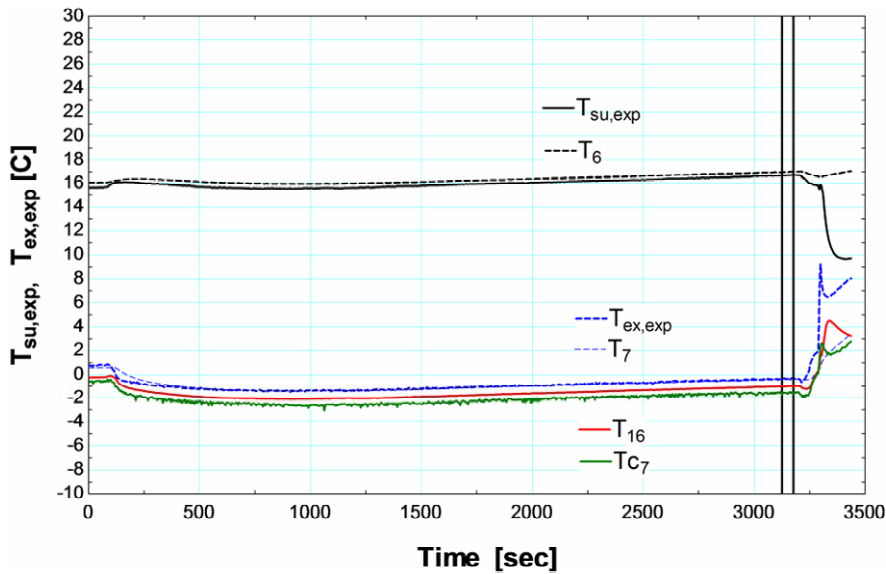


Figure 4-5 Evolution with time of temperatures at the supply and the exhaust of the expander and at the supply of the heat exchanger

4.3 Thermal properties of alkyl-benzene oil

In the experimental study presented in Chapter 5, nitrogen is selected as the refrigerant and alkyl-benzene oil (Zerol 60) is the liquid used to flood the compressor and the expander. Another gas and/or another liquid could have been used. The choice of these two fluids results from recommendations of Hugenroth's work (2006).

The specific heat and the density of the alkyl-benzene oil are given as a function of the temperature by the following correlations based on laboratory measurements.

$$c_l = 5.186(T + 273.15) + 337.116 \text{ [J/kg-K]} \quad (4-1)$$

$$\rho = -0.667(T + 273.15) + 1050.865 \text{ [kg/m}^3\text{]} \quad (4-2)$$

The viscosity of the oil is not known accurately but the following information has been provided by the manufacturer:

Viscosity @ 40°C = 11,16 cSt

Viscosity @ 100°C = 2,475 cSt

Viscosity Index = 4,48

No data about the thermal conductivity of the oil has been found. The thermal conductivity of similar oil has therefore been considered.

4.4 Derivation of an equation for two-phase flow pressure drop through an orifice by conservation of momentum

If the velocity ratio is assumed constant along the flow path, a simple theoretical solution is obtained. From a force balance on the flowing mixture:

$$-Adp = \dot{M}du_e \quad (4-3)$$

which can alternatively be written

$$-dp = \dot{G}du_e \quad (4-4)$$

The effective velocity u_e of the mixture is given by

$$u_e = \dot{G}v_e \quad (4-5)$$

Associating Equation (3.47) and (3.48) yields to

$$-\nu_e dp = u_e du_e \quad (4-6)$$

which leads to (since the gas is compressible)

$$\dot{G}_2^2 = - \frac{-2 \int v_e dp}{v_e^2 \left[1 - \left(\frac{A_2 v_{e1}}{A_1 v_{e2}} \right)^2 \right]} \quad (4-7)$$

4.5 Expander isothermal effectiveness

The expander isothermal effectiveness doesn't give more indication about the expander's performance than the shaft power and the global isentropic effectiveness. However, for information, evolution of the expander isothermal effectiveness with the oil mass fraction is given in Figure 4-6. The isothermal effectiveness is defined as

$$\varepsilon_t = \frac{\dot{W}_{\text{exp}}}{\dot{M}_g \cdot r \cdot T_{\text{su,exp}} (K) \ln \left(\frac{P_{\text{su}}}{P_{\text{ex}}} \right) + \dot{M}_{l,\text{exp}} v_{l,\text{su,exp}} (P_{\text{su,exp}} - P_{\text{ex,exp}})} \quad (4-8)$$

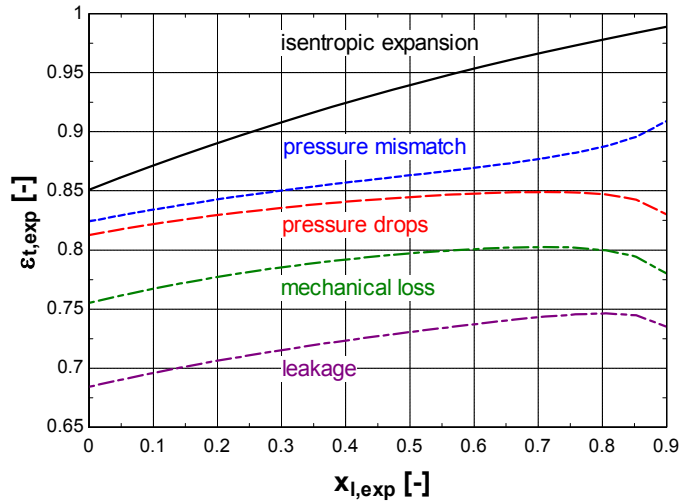


Figure 4-6: Evolution of the predicted expander isothermal effectiveness with the oil mass fraction

5 APPENDIX TO CHAPTER 7

5.1 Coefficient of the equations of Baehr and Tillner-Roth (1995) for R123

$$\begin{array}{llll} b_1 = 4.6367330 & b_2 = -5.3773427 & b_3 = -0.54677089 & c_1 = -2.8206711 \\ c_2 = 3.1091167 & a_0^* = 13.23249393 & a_1^* = 10.94800494 & \\ m_1 = 2.046009 & m_2 = 22.231991 & m_3 = -11.658491 & m_4 = 2.691665 \end{array}$$

5.2 Comparison of the R123 properties tabulated in EES and given by the equations of Baehr and Tillner-Roth (1995) for R123

The temperature evolution of the enthalpy, for a pressure of 5 bar, predicted by the equation of Younglove and McLinden (1994) and the one of Baehr and Tillner-Roth (1995) is compared to the evolution obtained using EES thermodynamics library¹.

It can be observed that the enthalpy predicted by EES is slightly higher than the one predicted by the two other equations. For an expansion between *state 1* defined by $P_1=10\text{ bar}$, $T_1=150^\circ\text{C}$ and *state 2* defined by $P_2=1\text{ bar}$, $T_2=50^\circ\text{C}$, the difference of enthalpy predicted by EES (69212 J/kg) is 4.2% higher than the one predicted by Younglove and McLinden (66283 J/kg).

¹ According to EES literature, R123 properties are described by a fundamental equation of state proposed by Reiner Tillner-Roth (1998). The latter equation is a refit of the equation established by Younglove and McLinden (1994).

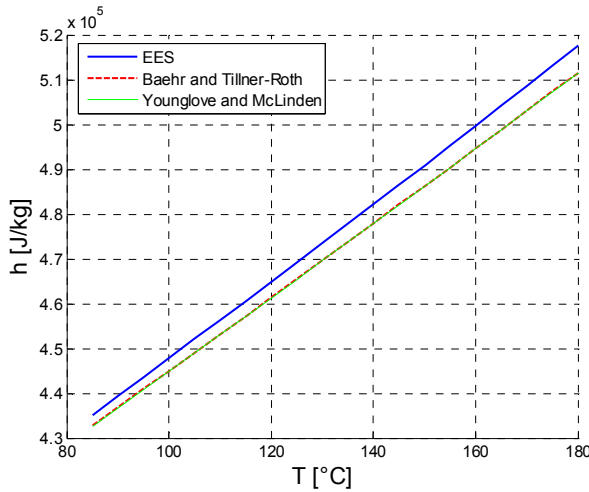


Figure 5-1: Temperature evolution of the enthalpy (for a pressure of 5 bar) predicted by the equation of Younglove and McLinden (1994), the one of Baehr and Tillner-Roth (1995) and EES

5.3 Equations describing the scroll tip

As shown in Figure 5-2, the shape of the tip of the scroll cannot be described anymore by the involute of a circle. Actually, the involutes forming the scroll start at an inner starting angle φ_{is} and an outer starting angle φ_{os} and can be connected by different geometries, of which the simplest is a circular arc. The tip geometry of the scroll machine under investigation differs obviously from that of a unique circular arc. It was observed that the tip of the scroll can be very accurately described by two circular arcs in series. The tangency between the first arc and the inner involute is verified by imposing

$$-(x_1 - x_a)/(y_1 - y_a) = \tan(\varphi_{is}) \quad (5-1)$$

There is no tangency imposed between the outer involute and the second arc. Points 1 and 2 belong to the first arc and points 2 and 3 belong to the second arc, which is expressed by

$$(x_1 - x_a)^2 + (y_1 - y_a)^2 = r_a^2 \quad (5-2)$$

$$(x_2 - x_a)^2 + (y_2 - y_a)^2 = r_a^2 \quad (5-3)$$

$$(x_2 - x_b)^2 + (y_2 - y_b)^2 = r_b^2 \quad (5-4)$$

$$(x_3 - x_b)^2 + (y_3 - y_b)^2 = r_b^2 \quad (5-5)$$

The values of x_2, y_2 and r_b are tuned in order to bring the two arcs as close as possible to the actual measured shape. The other values are computed by solving the system of Equations hereunder.

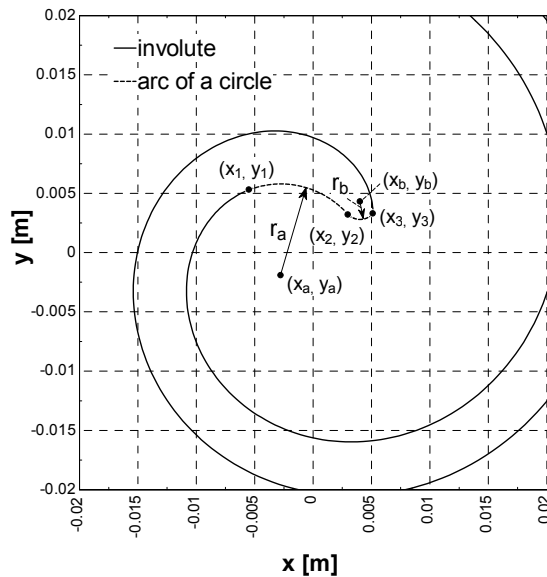


Figure 5-2: Description of the scroll tip by two arcs of a circle in series

5.4 Estimation of the external heat transfer coefficient

The insulated expander can be compared to a parallelepiped, whose dimensions L, H, W are given in Chapter 4, insulated on 5 of its 6 sides. The insulated surface area is given by

$$A_1 = 2LH + 2WH + WL \quad (5-6)$$

The non-insulated surface area is given by

$$A_2 = WL \quad (5-7)$$

The heat transfer resistance between the expander surface and the ambient through the insulated surface is

$$R_1 = \frac{1}{A_1 h} + \frac{e}{A_1 k} \quad (5-8)$$

The heat transfer resistance between the expander surface and the ambient through the insulated surface is

$$R_1 = \frac{1}{A_2 h} \quad (5-9)$$

The ambient heat transfer coefficient is finally given by

$$AU_{amb} = \frac{1}{R_1} + \frac{1}{R_2} \quad (5-10)$$